National and Kapodistrian University of Athens

Faculty of Geology and Geoenvironment

Department of Mineralogy and Petrology

Serpentinization and Metasomatism

Constraints to their relationship through mineralogical, petrological and geochemical study of rodingitized dykes intruded ultramafic rocks of Kimi district, Evia, Greece

Christos Karkalis

MSc Thesis

Supervisor Prof. Andreas Magganas

2018

Three-Member Committee

Professor Andreas Magganas (Supervisor)

Assistant Professor Panagiotis Pomonis

Professor Konstantinos Kyriakopoulos

Contents

Abstract

In Kimi (Central Evia, Greece) the Cretaceous-Paleogene flysch consists of schists, sandstones, cherts and ophicalcites, along with serpentinized peridotite bodies underlying Upper Cretaceous limestone intercalations with peridotite fragments. Serpentinized peridotites are intruded by rodingite dykes of a possibly gabbroic origin and they are thought to represent cretaceous ophiolitic remnants of the Vardar Ocean inside flysch, being obducted onto the Pelagonian platform. Based upon their petrographical, mineralogical and geochemical data Kimi rodingites have been divided into two groups according to the presence of calcite or not. A further discrimination concerns the three distinct zones that have been observed in rodingite dykes from both field and laboratory examination and include chlorite-diopside rich Marginal Zones (MZ), garnet-vesuvianite rich Core Zones (CZ) and Transitional Zones (TZ) which include the aforementioned mierals in various amounts. Rodingitization was a continuous metasomatic process strongly related with serpentinitzation and occurred under alkaline conditions. It was evolved in two main metasomatic events with low and high XCO_2 conditions respectively. Each metasomatic event could further subdivided into several stages as it is confirmed by the existence of distinct zoning within the rodingite dykes. Each stage corresponds to the gradual infiltration of metasomatic fluids through the mafic dyke with a gradual increasing of water/rock ratio and decreasing of CO_2/H_2O ratio and T conditions. Whole rock chemical analyses exhibit CaO enrichment and silica-alkali depletion. Ca^{2+} derives from clinopyroxene dissolution and is strongly mobilized during serpentinization, while Si loss is attributed to feldspar breakdown of the mafic protoliths. Vesuvianite formation took part in later metasomatic stages of the first event, when the metasomatic fluids were Ca^{2+} and OH^- rich with low CO_2/H_2O ratios. Apatite formation is indicative of seawater participation and CO_2 increase. These final are followed by the second metasomatic event of lower T and high CO_2 conditions. This event coincides with ophicalcite formation in OCT (Ocean Continent Transitional Zone) where brittle conditions cause serpentinite breakdown. These cracks usually begin from the chloritic margins and crosscut the whole rodingite dyke, permitting the CO_2 hydrous rich fluids to crystallize calcite. LREE deposition is observed in apatite and allanite. LREE mobilization took part mainly via CO_3^{-2}, while apatite presence and Zr mobility could also support the presence of PO_4^--LREE and LREE-OH^- and complexes as well. Stable isotope chemistry data of C and O in calcite samples form rodingite, ophicalcite and red mudstones of Kimi flysch show a combination of sedimentary and mantle derived processes in the metasomatic fluids. Based upon whole rock chemical data from rodingites and serpentinites, spinel chemistry, the presence of vesuvianite and hydrogarnets we conclude that the metasomatic processes possibly took part in a SSZ geological setting. Chemical similarities of Kimi rodingites with those of Skyros are indicative of an elongated ophiolitic Zone within Vardar Ocean. The closure of this Upper Cretaceous Vardar basin coincides with the flysch formation resulting in the westwards thrusting of Kimi flysch onto the Pelagonian platform and the entrance of peridotitic olistostromes within flysch.

***Keywords*:** vesuvianite, grossular, REE, Ca-metasomatism, chloritite, rodingite zoning, carbonization

Περίληψη

Στην περιοχή της Κύμης ο φλύσχης του Άνω Κρητιδικού-Παλαιοκαίνου αποτελείται από σχιστόλιθους, ψαμμίτες, οφειτασβεστίτες μαζί με σώματα υπερβασικών πετρωμάτων τα οποία υπόκεινται Άνω Κρητιδικών ασβεστόλιθων, οι οποίοι συχνά περιέχουν εγκλείσματα υπερβασικών τεμαχίων. Οι σερπεντινιωμένοι περιδοτίτες συχνά διασχίζονται από φλέβες ροδιγκιτών με διαστάσεις που κυμαίνονται από μερικά εκατοστά έως αρκετά μέτρα. Οι ροδιγκίτες αυτοί παρουσιάζουν μία πιθανή γαββρική προέλευση, ενώ τα οφιολιθικά τεμάχη αντιπροσωπεύουν υπολείμματα του ωκεανού του Αξιού τα οποία βρίσκονται μέσα στο φλύσχη της Πελαγονικής. Βασισμένοι στα πετρογραφικά, ορυκτολογικά και γεωχημικά δεδομένα, οι ροδιγκίτες διακρίνονται σε δύο ομάδες ανάλογα με την ύπαρξη ή την απουσία ανθρακικών ορυκτών και κυρίως ασβεστίτη. Μια περεταίρω διάκριση αφορά στη δημιουργία διαφορετικών ζωνών μέσα στις ροδιγκιτικές φλέβες οι οποίες χαρακτηρίζονται από την επικράτηση συγκεκριμένων ορυκτών και είναι οι ακόλουθες: Περιθωριακή Ζώνη (MZ) στην οποία επικρατεί ο χλωρίτης και ο διοψίδιος, Ζώνη Πυρήνα (CZ) στην οποία επικρατούν ο βεζουβιανίτης και ο γρανάτης και Μεταβατική Ζώνη (TZ) στην οποία συνυπάρχουν οι 4 προαναφερθείσες φάσεις σε διαφορετικές αναλογίες. Η ροδιγκιτίωση ήταν μία συνεχής διαδικασία άμεσα συσχετιζόμενη με τη διαδικασία της σερπεντινίωσης και έλαβε χώρα σε γενικά αλκαλικές συνθήκες. Δύο κύρια μετασωματικά επεισόδια μπορούν να διακριθούν, από τα οποία το πρώτο αφορά συνθήκες φτωχές σε CO_2, ενώ το δεύτερο αφορά ρευστά πλούσια σε CO_2. Κάθε μετασωματικό γεγονός μπορεί να διαιρεθεί σε επιμέρους μετασωματικά στάδια όπως επιβεβαιώνεται και από την ύπαρξη διακριτών ζωνών στους ροδιγκίτες. Το κάθε στάδιο αφορά τη βαθμιαία εισχώρηση των ένυδρων ρευστών διαλυμάτων από το περιθώριο προς τον πυρήνα της μαφικής φλέβας με ταυτόχρονη αύξηση του λόγου H_2O/πέτρωμα, μείωση της θερμοκρασίας και του λόγου CO_2/H_2O. Δεδομένα από τη χημεία ολικού πετρώματος δείχνουν ξεκάθαρο εμπλουτισμό του CaO από το περιθώριο προς τον πυρήνα των φλεβών, ενώ αντίθετα τα αλκάλια και το SiO_2 μειώνονται. Το ασβέστιο προέρχεται από τη διάλυση των κλινοπυρόξενων στο υπερβασικό πέτρωμα κατά τη σερπεντινίωση, ενώ η απώλεια Si και αλκαλίων οφείλεται στη διάλυση των αστρίων των μαφικών πρωτόλιθων. Η δημιουργία του βεζουβιανίτη σχετίζεται με τα τελευταία στάδια της πρώτης μετασωματικής φάσης καθώς τα ρευστά προχωρούν προς τον πυρήνα και με ένυδρες συνθήκες χαμηλού λόγου CO_2/H_2O και χαμηλότερες θερμοκρασίες, ενώ η δημιουργία απατίτη είναι ενδεικτική της συμμετοχής θαλάσσιου νερού στο σύστημα. Τα τελευταία αυτά στάδια ακολουθούνται από ένα δεύτερο μετασωματικό επεισόδιο χαμηλότερων θερμοκρασιών και συνθηκών πλούσιων σε CO_2. Το στάδιο αυτό συμπίπτει με τη δημιουργία οφειτασβεστιτών κοντά στο OCT όπου επικρατούν οι συνθήκες θραυσιγενούς παραμόρφωσης. Σε αυτές τις συνθήκες δημιουργούνται ασυνέχειες στο σερπεντινιτικό πέτρωμα οι οποίες επιτρέπουν στα ένυδρα πλούσια σε CO_2 ρευστά να εισέλθουν και να κρυσταλλώσουν ασβεστίτη. Ο εμπλουτισμός των ροδιγκιτών σε ελαφριές σπάνιες γαίες μέσα στον αλλανίτη και στον απατίτη οφείλεται στη μεταφορά τους μέσω ανθρακικών κυρίως συμπλόκων στα μετασωματικά ρευστά. Επιπλέον η ύπαρξη του απατίτη καθώς και η κινητικότητα του Zr θα μπορούσαν να δικαιολογήσουν την ύπαρξη φωσφορικών και ένυδρων συμπλόκων σπανίων γαιών. Χημικά δεδομένα σταθερών ισοτόπων O-C σε ασβεστιτικά δείγματα από ροδιγκίτες, οφειτασβεστίτες και ερυθρούς πηλόλιθους μας δείχνουν τη συμμετοχή υδροθερμικών διαλυμάτων ιζηματογενούς και μανδυακής προέλευσης στα μετασωματικά ρευστά. Η χημεία των ροδιγκιτών και των υπερβασικών πετρωμάτων καθώς επίσης και η

ορυκτοχημεια των σπινέλιων, η ύπαρξη βεζουβιανίτη και υδρογρανατών είναι ενδεικτικές της πετρογένεσης των ροδιγκιτών σε συνθήκες υποβύθισης με παράλληλη λειτουργία ωκεάνιας λεκάνης (SSZ). Επιπρόσθετα οι χημικές ομοιότητες των ροδιγκιτών της Κύμης με αυτούς της Σκύρου είναι ενδεικτικές της ύπαρξης μίας ενιαίας επιμήκους οφιολιθικής ζώνης μέσα στον ωκεανό του Αξιού η οποία στην περίπτωση της Κύμης αφορά σε μία ωκεάνια λεκάνη που συνέχισε να λειτουργεί στο Άνω Κρητιδικό. Το κλείσιμο της κρητιδικής αυτής λεκάνης συμπίπτει με την έναρξη της φλυσχογένεσης και την τοποθέτηση των περιδοτιτικών ολισθοστρωμάτων μέσα στο φλύσχη κατά την τοποθέτησή του πάνω στην πλατφόρμα της Πελαγονικής.

<u>Λέξεις Κλειδιά:</u> βεζουβιανίτης, γροσουλάριος, σπάνιες γαίες, μετασωμάτωση ασβεστίου, χλωριτίτης, ζώνωση ροδιγκιτών, ανθρακοποίηση

Acknowledgments

I would like to express my sincerest thanks to Professor Mr. Andreas Magganas, for his help and guidance. He is a real mentor for me and a real teacher since the undergraduate program and we have an excellent collaboration through all these years, inspiring me to continue the study and research in the scientific fields of Igneous and Mantle Petrology and Geochemistry. His help, his scientific knowledge and his support was very decisive and valuable.

I would also like to thank Professor Mr. Panagiotis Pomonis, who always helps me through all these years and especially in my post-graduate Diploma Thesis. He was always willing to help me and guide me through the complicated scientific fields that I was studying, giving me useful advices and communicated me his knowledge.

Another person that I would like to thank is Professor Mr. Konstantinos Kiriakopoulos, for all his knowledge that he transmitted to me during the post-graduate program and for his useful and crucial comments in the present research.

Professor Marianna Kati really helped with her special knowledge in ophicalcites.

All the professors who involved in my post-graduate studies played an important role in the configuration and evolution of my scientific knowledge, helping me to enter the complicated and exciting fields of Petrology-Mineralogy and Geochemistry. More specifically I would like to thank the following Professors: Andreas Magganas, Athanasios Katerinopoulos, Konstantinos Kiriakopoulos, Panagiotis Voudouris, Athanasios Gondelitsas, Panagiotis Pomonis, Marianna Kati and Vlachou Tsipoura Maria. The total knowledge that I gained through my post-graduate studies helped me to become a better geologist and to combine the knowledge from different fields of Petrology, Mineralogy and Geochemistry in order to study special geological issues.

I would also like to thank all the technicians of the Laboratory of Petrology and Mineralogy Department of the National and Kapodistrian University of Athens.

I would like to express my appreciation to Dr. Chavez from ACME Labs and to Prof. Michael Joachimski from Geozentrum Nordbayern for the whole rock chemical and stable isotope analyses respectively.

I would like to express my real thanks to Dr. George Economou who helped me with the mineral chemistry analyses using the SEM-EDS of the Institute of Geological and Metallurgical Research of Greece (IGME), as well as the technician Mr Sakalis for his help and support.

Finally, I would like to express my sincerest thanks to my mother and especially to my father, who supported me through all these years to study the Science that I love and to make my dreams come true. They always stand by my side, even in the hardest moments for them, supporting me and giving me the capability to study Geology and to be specialized in the excited fields of Petrology, Geochemistry and Mineralogy.

1 Introduction

Serpentinization is a very important process for the planet Earth and elsewhere since it has been linked among others and with the origin of life, as well as with the global greenhouse phenomenon caused by CO_2 emissions (Oze and Sharma, 2005; Schulte et al., 2006; Power et al., 2013). As carbonate minerals are naturally produced during serpentinization, the development of industrial strategies that mimic this natural serpentinization for CO_2 sequestration is a modern task worldwide. On the other hand, rodingitization, that is the formation of rodingites, is a metasomatic process that is considered widely to be related to serpentinization.

In particular, rodingites are rocks that are thought to have mostly resulted from the interaction of serpentinization fluids with parent rocks along the contact with serpentinites (Pirajno, 2013). These parent rocks, which include mafic to felsic lithologies e.g. gabbro, granite, greywacke, quartzite and argillite (Coleman, 1967; Schandl and Mittwede, 2001; Hatzipanagiotou et al., 2003; Li et al. 2007), are mainly enriched in CaO and depleted in SiO_2 and Na_2O during rodingitization (Piranjo, 2013). Rodingitization mainly occurs in seafloor environments and more rarely in subduction environments (Koutsovitis et al., 2013 and references therein).

In Kimi Evia there is a strong relationship in space and time between rodingites and serpentinites. This relationship implied from the formation of rodingite dykes themselves, as well as the reaction zones developed near the contact of the rims of rodingites with the serpentinite host rocks. Rodingites are present as dykes inside serpentinites, both of which in turn are located as large blocks within the Maestrichtian-Paleocene(?) flysch of Pelagonian Zone (Katsikatsos et al., 1970).

Rodingites and serpentinites of Kimi area have not been studied in the past 45 years. The first report on Kimi's rodingites and serpentinites was made by Papastamatiou (1945). He stated the serpentinitic bodies found within flysch are the result of intrusion of a peridotitic magma which penetrated it, whereas the rodingite dykes are rocks rich in Ca-silicate minerals.

Marakis (1972a,b), referred to clinochlore and vesuvianite-rich rodingite dykes inside serpentinitic rocks, in an area which lies north of Kimi and in Kalimeriani village, few km away of Kimi towards SW. He studied especially the clinochlore using X-Ray and microscopic examinations in order to explain its conditions of formation. He reported that the rodingites are metamorphosed Al-rich limestones mostly consisting of chlorite, vesuvianite and calcite. He attributed their formation to metamorphic events which affected the primary marly limestones. Paraskevopoulos and Kanakis (1972), studied the Kimi ophicalcites, which appear in Choneftiko area near Kimi. They stated these ophicalcites are parts of the serpentinitic margins and consist of calcite veins which crosscut serpentinite, whereas calcite can also appear as thin layers inside the serpentinitic mass. They also recognized another ophicalcite group, which consists of slightly metamorphosed marbles, that are present as inside serpentinites and their formation is attributed to an ultrabasic magma which penetrated to the uppermost limestones and distracted limestone fragments, which were metamorphosed into marbles.

From the above it is clear that there is not any detailed and modern petrological geochemical and mineralogical study of the rodingite-serpentinite rock association occurring in the Kimi area. The suggested petrogenesis for this association is far from what we presently know for similar occurrences elsewhere. Thus, my aim is to cover

the gap to our petrological and geochemical knowledge for the rodingite-serpentinite rocks using expert classical petrographical microscopic methods, modern tools such as XRD evaluation, SEM-EDS mineral chemical analyses, ICP-MS geochemical data, as well as stable isotopes. I will also focus to the relation between the metasomatic processes of rodingitization and serpentinization in this particular case, trying to find evidences that link them, such as the physicochemical conditions under which they have been formed, when this metasomatism was realized and which are the chemical reactions that the mineral assemblages formed. Moreover, I shall try to conclude about the protolith of rodingites and the geotectonic setting under which, serpentinization and metasomatic processes occurred, firstly considering that they might be realized within or close to the oceanic floor of Vardar Ocean. Finally, a very notable task which I will try to explain is the discovered relatively high REE abundances in many rodingite samples from the study area, and to compare them with similar REE enrichments occurring elsewhere in the world.

2 Serpentinization and Metasomatism – State of the Art

2.1 Description of metasomatism and metamorphism

Harlov and Austrheim (2013), following the definition of the International Union of Geological Sciences (IUGS), refer to **metasomatism** as a process that chemically changes the whole rock or a part of that in solid state and results from the interaction of the rock with chemical solutions. During these interactions chemical components are removed off or/and entered the two phases. On the other hand, **metamorphism** is a process of mineral and microstructural changes of rocks remaining is solid state (Harlov and Austrheim, 2013). These two processes can coexist.

2.2 Metasomatic features

According to Zharikov et al. (2007), metasomatism is characterized by:

- Ion by ion replacement in minerals of a rock in solid state.
- Addition or subtraction of major components other than H_2O and CO_2.
- Formation of zones that represent chemical equilibrium between two rocks or a rock and an infiltration liquid.

2.3 Metasomatic processes

According to Zharikov (2007), there are five types of metasomatic processes:

- **Diffusional metasomatism, which occurs** when a solute is diffused due to the chemical gradient between the fluids and the rock in pores and does not require the movement of the fluid,
- **Infiltrational metasomatism, which occurs** where an infiltrated fluid under pressure transfers material.
- **Autometasomatism** such as albitization is a post-magmatic process, appearing in igneous intrusions.
- On the other hand, near the contact of two different lithologies the activity of the fluid gradients leads to **boundary metasomatism**, which is very often in blackwall alterations and rodingitization processes, while
- **Contact metasomatism** is divided into endo-contact and exo-contact and concerns the changes that evolve an igneous intrusion and all the wallrock. An example of contact metasomatism is the formation of skarns**.**

**Chemical gradient is the concentration difference of a chemical component between two areas. As a result, activate particles move from areas with high concentrations to those with low ones.*

2.4 Metasomatism associated with ultramafic rocks

Metasomatism associated with ultramafic rocks mainly includes serpentinization and carbonization. Blackwall alteration, steatitization, diopsiditization and rodingitization

are metasomatic processes also associated with ultramafic rocks, but they usually require mafic rocks, which may intrude the ultramafics or are in immediate contact with them. The serpentinization leads to the formation of serpentinite and carbonization produces ophimagnesite, ophicalcite and listwanite. Blackwall alteration forms mainly talc- and chlorite-schist and chloritite, steatitization creates also talc-schist, a variety of which is soapstone or steatite, diopsiditization forms diopsidite and rodingitization rodingite.

From the serpentinization of Fe-Mg silicates the fluids that derive cause the metasomatism of the mafic rocks and their contacts with their host rocks. The serpentinization ranges from T < 100 ^{o}C with lizardite being the mineral that occurs phase that occurs to 500 ^{o}C (antigorite). The common minerals of the serpentinization are lizardite, chrysotile, brucite and magnetite as a byproduct of serpentinization due to the release of Fe from Fe-Mg silicates and its oxidation to Fe^{3+}. In shallow depths (<20 Km) lizardite is stable, while chromite turns to lizardite. With the increasing of P-T lizardite turns to antigorite at almost 400 ^{o}C. During the subduction serpentinites are prograde metamorphosed and dehydrated causing the antigorite breakdown (Deschamps et al., 2013)

2.5 Serpentinization

Serpentinization is a process, where ultramafic rocks are hydrated and anhydrous Fe-Mg silicate minerals are converted to hydrous ones of serpentine group. During this process the rock density changes from 3,2 g/cm^3 to 2,4 g/cm^3, which corresponds to 30% mass loss and almost 40% volume gain. Serpentinization as an isochemical process has been observed by many researches in the past (e.g. Page, 1976; Ashley, 1973), while many other authors refer to serpentinization as a chemical process in which chemical changes occur (e.g. Engin and Hirst, 1970b; Coleman and Keith, 1971), but serpentinization is nowadays considered as a complex process in which both volume and chemical changes can occur and for their exact calculation many mathematic models are possibly required (Karkanas, 1987). Wicks & Whittaker (1977), divide serpentinization into 8 types according to the increase or decrease of temperature, while O'Hanley et al. (1989a), initially distinguish this process into retrograde (with a decrease in T) and progressive (with an increase in T).

2.5.1 Geotectonic environments of serpentinization

The Penrose model suggests that the oceanic crust has a layer cake structure in which: Layer 1 is a sediment cover of the magmatic crust. Layer 2 consists of basalts I form of pillow lavas or sheeted dikes. Layer 3 comprises gabbro. All these layers are seismically defined (Klein, 2009). In an average of six kilometers beneath the ocean floor the MOHO is present separating the crust from the underlying peridotitic mantle. Thus, these peridotites seem difficult to be exposed on the sea floor. However, today it is well known after many detailed studies, such as Deep-Sea Drilling Project, deep faults allow mantle rocks usually serpentinized to be exposed (e.g. Schroeder, 2007).

Deschamps et al. (2013), distinguish three groups of serpentinites according to their geotectonic setting: abyssal or oceanic, subducted and mantle wedge serpentinites (Fig. 1).

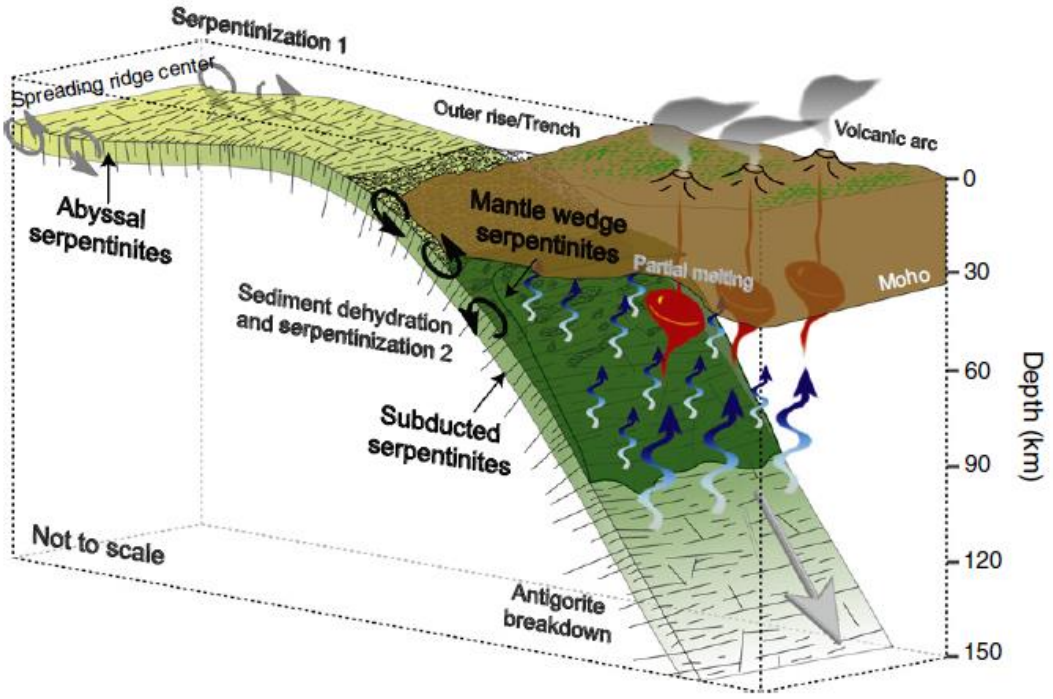

Figure 1. Division of three serpentinite groups based upon their geotectonic setting (abyssal or oceanic, subducted and mantle wedge serpentinites). (Deschamps et al., 2013).

2.5.1.1 Abyssal or oceanic serpentinites

At slow (1 to 5 cm/year) to ultraslow (<2 cm/year) spreading ridges the crust is relatively thin (1 to 7 km) and there are many faults permitting the intrusion of circulating fluids and the serpentinization of the oceanic lithosphere (e.g. Mevel, 2003). Because of the thin crust, the seawater hydrates the abyssal peridotites through faults (transformation faults) and scraps. This is confirmed by O and H isotopic analyses (Deschamps et al., 2013). Thus, serpentinites play the role of a water sink holding on average of 13% H_2O in serpentine minerals until the T is between 600 to 700 ^oC (Ulmer and Trommsdorf, 1995; Wunder and Schreyer, 1997). On the other hand, the fast spreading ridges (> 9 cm/year) present a very notable magmatic activity, forming 7 to 10 km thick crust preventing the serpentinization of abyssal peridotites, since they cannot outcrop on the seafloor (Sinton and Detrick, 1992; Deschamps et al., 2013).

Serpentinization in oceanic environments can be attributed to fractures (Andreani et al., 2007), which permit the fluid transfer. Based on isotopic studies and the stability of serpentine minerals, abyssal peridodite serpentinization appears at 7 km depth (Escartin et al., 1997) and T_{max}: 450-500 ^oC (Evans et al., 1976), while their texture is mainly pseudomorphic (Deschamps et al., 2013).

2.5.1.2 Mantle wedge serpentinites

Mantle wedge is the part of the mantle between the upper part of the subducted lithosphere and the lower part of the crust of the overlying plate. This wedge is percolated by fluids derived from the subducted slab (sediments, basalts and serpentinites). These water rich fluids hydrate the mantle and cause its serpentinization at T<700 ^oC, but due to the lower viscosity and density of these rocks

compared to those of pure peridotites, serpentinites can be exhumed in accretionary prisms (Deschamps et al., 2013 and references therein).

2.5.1.3 Subducted serpentinites

These serpentinites are divided into two groups according to their protolith. The first group is the oceanic serpentinites, while the second group includes the continental peridotites which are hydrated during rifting. They are both emplaced in accretionary complexes or suture zones. When a slab of oceanic or continental serpentinized mantle reaches near the trench area seawater fluids interact with these mantle rocks along cracks and faults, causing a second serpentinization (Contreras-Reyes et al., 2007; Ranero et al., 2003, 2005).

2.5.2 Serpentinite Subduction Channel

The serpentinite channel is placed between the dry slab and the mantle wedge. It comprises abyssal serpentinites, HP rocks of the subducted slab, serpentinized rocks from the mantle wedge. This unit can be exhumed within this channel and to be accreted as an ophiolitic mélange (Deschamps et al., 2013). The dehydration in subduction related systems occurs in the first 100 to 170 Km and the subducted channel is 5 to 10 m thick extending from ca 20 to 80 Km depth (Hilairet and Reynard, 2009; Schwartz et al., 2001).

2.5.3 The chemical process of serpentinization

It is under debate whether serpentinization is an isovolumetric process with mass transfer or just a hydration with an increase in volume. The chemical reaction of serpentinization for olivine and pyroxene respectively are the following (Klein, 2009):

$2Mg_2SiO_4 + 3H_2O \rightarrow Mg_3Si_2O_5(OH)_4 + Mg(OH)_2$

(Forsterite) (Chrysotile) (Brucite)

$3MgSiO_3 + 2H_2O \rightarrow Mg_3Si_2O_5(OH)_4 + SiO_2(aq)$

(Enstatite) (Chrysotile)

Their $\Delta_r V$ equals to 52% and 16% respectively.

According to Klein (2009) the serpentinization of harzburgite with 1:1 molar ratio of olivine to orthopyroxene increases its volume of 45%.

$Mg_2SiO_4 + MgSiO_3 + 2H_2O \rightarrow Mg_3Si_2O_5(OH)_4$

(Forsterite)(Enstatite) (Chrysotile)

but with Si and Mg removal in isovolumetric processes the reaction is:

$6Mg_2SiO_4 + 2MgSiO_3 + H_2O + 10H^+ \rightarrow 3Mg_3Si_2O_5(OH)_4 + 5Mg^{2+} + 2SiO_2(aq)$

(Forsterite) (Enstatite) (Chrysotile)

Serpentinization is a reducing process (e.g. Mc Collom and Bach, 2009), in which many changes occur such as the oxidation of Fe^{2+} in olivine and pyroxene to Fe^{3+} in magnetite. The last process releases H^+ as described from the reactions below:

$3Fe_2SiO_4 + 2H_2O \rightarrow 2Fe_3O_4 + 3SiO_2(aq) + 2H_2(aq)$

(Fayalite) (Magnetite) and

$3FeSiO_3 + H_2O \rightarrow Fe_3O_4 + 3SiO_2(aq) + H_2(aq)$,

(Ferrosilite) (Magnetite)

Olivine is usually replaced, except by serpentine, by carbonated minerals and Fe-talc (Andreani et al., 2009; Bach et al., 2013), while other times olivine is replaced by calcite (Kelemen et al., 2004; Bach et al., 2013; Klein, 2009). These are the results of CO_2 metasomatism. The extent of mineral carbonation depends on the protolith composition, the CO_2 activity of the fluid, T and fluid flux (Bach et al., 2013), while the carbonation is an example of the coexistence of infiltration and diffusion.

On the other hand, serpentinites can also be metasomatized by silica. They have very low silica activities under sub-greenschist phases, but near magmatic intrusions (e.g. gabbro), the silica content increases due to their hydrothermal alteration (Bach et al., 2013 and references therein).

2.5.4 Serpentinite deformation

Pseudomorphic serpentine presents brittle deformations, while in P=1.5-3.0 Kbar a transition between brittle and ductile features occur (Raleigh and Paterson, 1965). Brittle deformation dominates at P<3 Kbar and temperatures lower than that of serpentinization. On the other hand, ductile is the main deformation type at P> 4 Kbar and temperatures between 500-600 ^oC. Finally, according to Norrell et al. (1989), lizardite serpentinites sustain brittle deformation during or after the ophiolite obduction at T<30 ^oC.

2.6 Carbonization of ultramafic rocks

2.6.1 Magnesites - Ophimagnesites

Magnesite is usually the result of CO_2-metasomatic processes that take place in the seafloor and they are associated with serpentinization. According to Klein and Garrido (2011), a peridotite infiltrated by CO_2 rich fluid will form some distinct zones changing its mineral assemblage. At 200 ^oC and 100 MPa a serpentine-brucite protolith (Fig. 2), with progressive CO_2 metasomatism will create magnesite, talc and quartz, whereas in partly serpentinized rocks the relict olivine and pyroxenes will be replaced by magnesite and serpentine or magnesite and talc. The extent of the carbonation depends on the CO_2 activity of the fluid, the flux of the fluid and the temperature (Bach et al., 2013). CO_2 metasomatism is a mixed diffusional and infiltrational process and is the result of the interaction of CO_2-rich fluids with serpentinite in temperatures between 150 to 300 ^oC.

There are to main opinions concerning magnesite deposition, which support either the hydrothermal origin of magnesite from magmatic waters or the origin of magnesite from meteoric water, while in modern theories a mixture of both magmatic and meteoric water is suggested, explaining CO_2 derivation (Skliros, 2013).

According to Pohl (1990), hydrothermal magnesite derives from low salinity rich in CO_2 hydrothermal metamorphic derived fluids, which dissolve olivine crystals and produced fluids rich in SiO_2 and $Mg(OH)_2$. These waters move through cracks in the ultramafic rocks and crystallized magnesite in vein forms near the surface in alkaline

and reducing conditions (pH: 7.5-9.5, Eh: -70 to -120 mV) conditions and (Pohl, 1990).

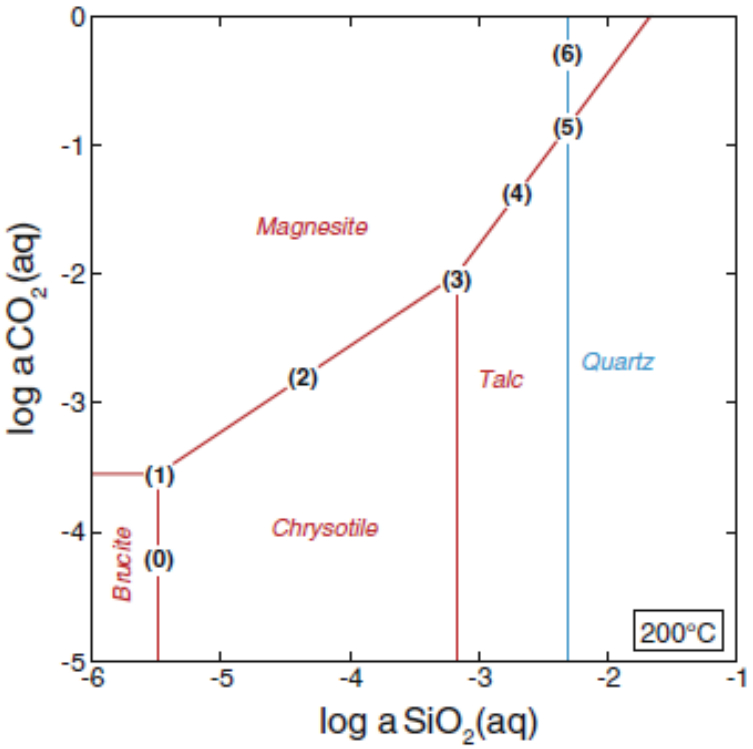

Figure 2. Phase diagram of the system MgO-SiO_2-H_2O-CO_2 with predicted mineral assemblages labeled, modified from Klein and Garrido (2011), (Bach et al., 2013).

The main chemical reactions for magnesite formation are the following:

Mg_2SiO_4 (Forsterite) + $2CO_2$ (aq) → $2MgCO_3$ (magnesite) + SiO_2 (aq) + 64 KJ/mole, in which magnesite occurs as a metasomatic product, deriving form forsterite hydration in CO_2 rich conditions.

There are also two other chemical reactions describe both magnesite, serpentine and talc formation during CO_2 metasomatism during serpentinization:

$2Mg_2SiO_4$ (Forsterite) + $2H_2O$+ CO_2 → $Mg_3Si_2O_5(OH)_4$ (Serpentine) + $MgCO_3$ (Magnesite)

$2Mg_3Si2O_5(OH)_4$ (Serpentine) + H_2O+ $3CO_2$ → $Mg_3Si_4O_{10}(OH)_2$ (Talc) + $3MgCO_3$ (Magnesite).

Many theories have been proposed for the origin of CO_2, suggesting either an organic or a biotic origin, or a magmatic origin (Abu-Jaber & Kimberley, 1992). Other authors state that CO_2 clearly state it has a meteoric origin (e.g. Kelemen and Matter, 2008; Kelemen et al., 2011). They based on isotopic studies, the low or zero REE concentrations, the $\Sigma(CO_2)$ concentrations in alkaline conditions and the pH-Depth relations (Palinkaš et al., 2012).

In some metasomatic processes the hydrothermal fluids which are evolved in ophicalcititization (see Chapter 2.6.2) can be Ca as well as Mg-rich (Capedri, 1973). The crystallization of calcite, dolomite and magnesite from such Ca-Mg-rich solutions is mainly related with T and Ca, Mg concentration in the fluids.

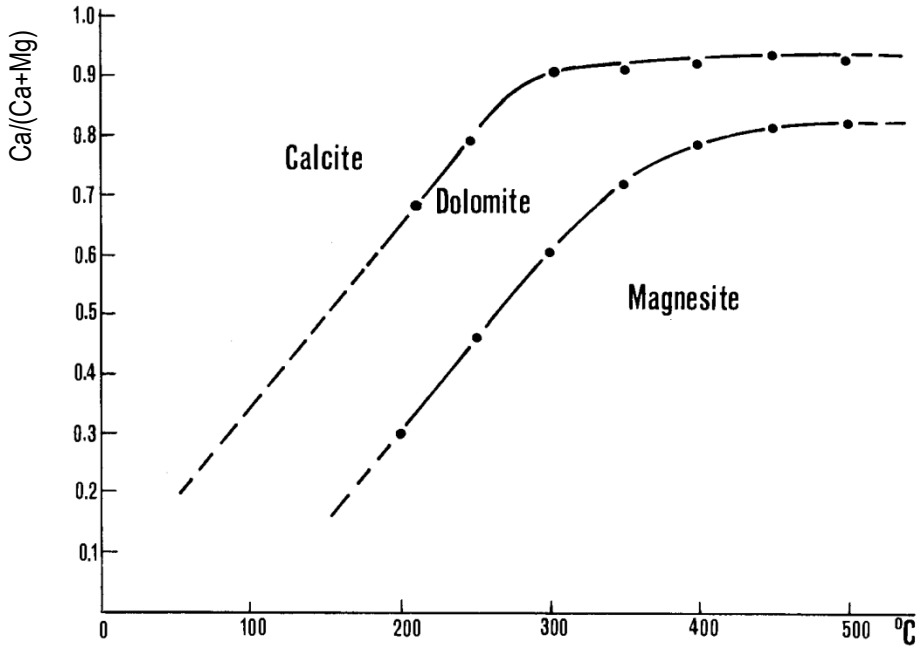

Figure 3. Stability field of calcite, dolomite and magnesite, related with Ca/(Ca+Mg) and the T of the solutions (Johannes, 1970).

From the above diagram (Fig. 3) it is clear that for T = 400-500 ^{o}C magnesite is the most usual carbonated mineral for a wide range of Ca/(Ca+Mg) ratios, compared to dolomite and calcite, while magnesite seems to be the first carbonate phase producing from Mg rich solutions with decreasing Ca/(Ca+Mg) ratios and then follows dolomite and calcite (Capedri, 1973). From the aforementioned data it is clear that ophimagnesite formation can also occur, depending on the T and Ca/(Ca+Mg) values.

2.6.2 Ophicalcites

Ophicalcites are mixed tectono-sedimentary brecciated rocks or cataclastites with serpentinite fragments and calcite matrix. Their formation is a result of exposure of the oceanic mantle to or near to ocean floor due to tectonic processes (Bernoulli et al., 2003 and references therein). They can be divided into two groups, with the first group including those types which derive from chemical hydrothermal processes, while the second type includes those ophicalcites which come from re-sedimentary processes, such as sediment gravity flows and debris flows. They can also be distinguished into two other groups, with the first group represented by massive serpentinites with dense mesh of calcite-filled fractures, while the second includes sedimentary breccias with a calcitic matrix, often deposited above the previous ophicalcite group (Clerc et al., 2014; Lemoine et al., 1987).

Their main mineral assemblage mostly consists of calcite, dolomite, magnesite and siderite, while serpentine can occur as chrysotile, antigorite or lizardite.

Accessory minerals include chromite, spinel, magnetite, tremolite, chlorite, hematite and sulfides. Aragonite is unstable and turns into calcite above 200 ^{o}C, while in T<150 ^{o}C calcite doesn't form. As a result, aragonite is indicative of low T conditions. Magnetite forms in T> 400 ^{o}C and siderite can form from reactions that substitute Ca^{2+} with Fe^{2+} (Johannes, 1970; Capedri et al., 1973).

The geotectonic environments of their formation are the ocean-continent transition zones (Fig. 4) and the ocean ridges and transition faults and normal faults in slow spreading ridges, whereas their formation is related with brittle deformations and the exhumation of the oceanic lithospheric mantle in subduction zones (Bernouli and Jenkyns, 2009).

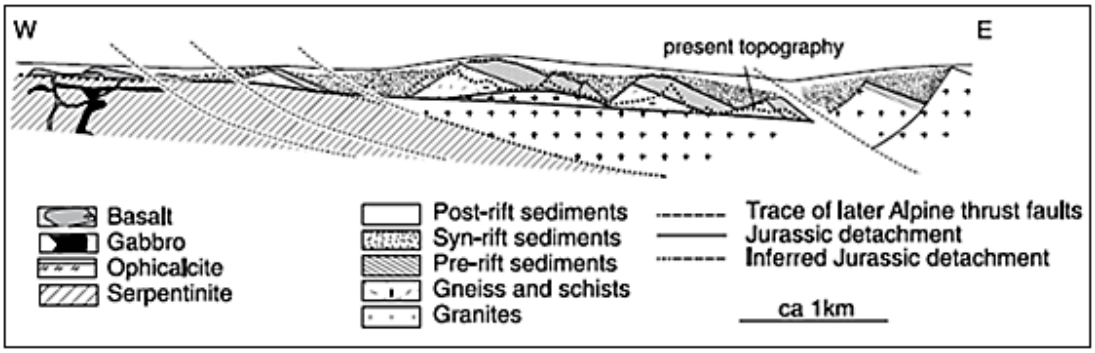

Figure 4. Geological cross section of the ocean-continent transition zone. Mantle rocks have been exhumed from low angle detachment faults. Ophicalcites correspond the transition between the detachment fault and the exhumed mantle (Bernoulli et al., 2009).

2.6.3 Listwanite

Listwanites are carbonate metasomatized ultramafic rocks, which mainly include magnesite, ankerite, ankerite, quartz and fuchsite (chromian muscovite) (Halls and Zhao, 1995), while they can also include varying amounts of serpentine, talc, chlorite phlogopite and they are usually related with lode Au and Ag mineralization (Pirajno, 2013).

Brownlow (1995), suggests that in neutral to slightly acidic pH values SiO_2 dissolution is reinforced in its amorphous rather than in its crystallized state. During this process both SiO_2 and CO_2 react with water producing H_4SiO_4 and HCO_3^- respectively, while H^+ is released from CO_2 hydration as well (Skliros, 2013 and references therein). This chemical process, which leads to listwanitation from the above chemical solutions, occurs at T between 290 to 340 ^oC and P between 1-4 Kbar and is characterized by SiO_2 release and by the replacement of Fe-Mg minerals in the ultramafic rock by Fe-Mg carbonates, described below:

$(Mg,Fe)_3Si_2O_5(OH)_4 + 3CO_2 \rightarrow 3\ (Mg,Fe)CO_3 + 2SiO_2 + H_2O.$

Listwanite demands a high K influx to be formed and due to this strong K metasomatism Cr is leached from the chromite and/or other Cr-bearing silicates of the ultramafic rock, leading to the formation of chromian muscovite (Pinjaro, 2013).

Hinsken et al (2017), studied Tinos listwanites using petrographical, whole rock chemical, isotopic and geochronological data. Tinos listwanite occurrences are associated with phyllites, talc-schists, meta-gabbros and serpentinites. They occur as sheeted like bodies along low angle normal faults, due to their higher resistance in alteration processes compared to that of their neighbor schistose and phyllitic talc-rich rocks. Their main mineral assemblage consists of magnesite and quartz, which occur as secondary veinlets, as well fuchsite, chlorite, albite, chromite, magnetite and other opaque minerals, which are present in small amounts. Listwanitation is an isochemical process and can be attributed to fluid infiltration and distribution via the aforementioned normal faults, leading to serpentinite carbonation and fuchsite

formation, under CO_2-rich and K-bearing conditions. Based on Rb-Sr mineral isochrons and chlorite thermometry the metasomatic process took place at T between 250-350 ^oC at ages 16 Ma and 19 Ma. Sr isotopic features in magnesite combined with C and O isotopic data indicate a marine environment, where infiltrated seawater fluids participated in the functioning hydrothermal system (Hinsken et al., 2017).

2.6.4 Ophicalcites Listwanites and Magnesites in Evia

Paraskevopoulos and Kanakis (1972), studied the ophicalcites and refer to a serpentinitic appearance in strong association with flysch north of Kimi area. Ophicalcites occur at the margins of the serpentinitic masses in Choneftiko area. These ophicalcite are described as serpentinites crossed by calcite veins, whereas calcite can be also mixed with serpentine in the rock mass. Calcite can also form thin layers inside serpentinite. Another ophicalcite type described by Paraskevopoulos and Kanakis (1972), concerns weakly metamorphosed marble bands and lenses inside serpentinites, interpreted as fragments of the uppermost limestones trapped inside the ultramafic magma. The authors divide the ophicalcites into two groups, with the first group called serpentinitic ophicalcite, mostly consisting of antigorite and calcite veins, whereas chrysotile, magnetite, chromite, pentlandite and pyroxene can also occur. The second group concerns ophicalcites which derived from an intruded ultramafic magma inside carbonated rocks. Their matrix mainly consists of calcite, while serpentine occurs in the form of veins, or mixed with calcite. Chlorite, chromite and magnetite are also present.

Listwanites and ophicalcites in the Central part of Evia between Pyxaria and Kandili mountains ophicalcite and listwanite occurrences appear (Capedri, 1973). In this area both unaltered and serpentinized ultramafic rocks were affected by hydrothermal activity, especially in Mantoudi area, where a lot of magnesite ores have been detected (Capedri, 1973). Listwanites differ from ophicalcites consisting of carbonated phases which are not found in ophicalcites, whereas metasomatic alteration has affected the mineralogy and chemistry of the ultramafic parts of listwanites. On the other hand, the ultramafic parts of the ophicalcites have not been affected by any mineralogical or chemical transformation (Capedri, 1973).

In the following paragraphs we present the main characteristics of listwanites and ophicalcites in Central Evia, as they were described by Capedri (1973):

Central Evia listwanites contain three zones, which correspond to successive alteration stages of a fresh ultramafic harzburgitic body. An inner green zone is consisting of green chlorite along with some quartz. This zone turns to an intermediate yellowish zone containing montmorillonite, quartz and abundant carbonates in vein forms. The outer zone is red colored and includes many carbonated crystals and vein, as well as hematite. Talc occurs in the yellowish zone, while tremolite is present in all three zones. Magnetite and clay minerals are present in small amounts, while serpentine is absent. Listwanitation took part when hydrothermal solutions changed the initial mineralogical composition, characterized by a great MgO and SiO_2 mobilization from the ultramafic protolith to the solution, thus Fe was strongly mobilized during metasomatism, it was concentrated in the listwanites.

Ophicalcites consist of abundant carbonated veins and completely or partly serpentinized clasts. Apart from serpentine and carbonated minerals they also include

quartz in veins and cement, while carbonated phases usually substitute the ultramafic minerals forming pseudomorphs. From the whole rock chemistry of the ultramafic fragments and the carbonate veins is easily understood that no chemical transformation occurred during ophicalcitization.

Magnesite occurs in the form of sills, veins or sub-spherical bodies, dolomite which also forms veins and is usually associated with calcite, building the outer bands of the veins, whereas calcite concentrates in the center of them. Other carbonate phases include calcite, siderite and aragonite.

Gartzos (2004), studied the magnesite deposits of North Evia hosted in Alpine rocks, conducting stable C and O isotopes, strongly suggesting a meteoric water involvement and an organic derived carbon in their formation as well. The most important magnesite deposits are mainly hosted in non- or partly-serpentinized peridotites, which are dismembered ophiolitic parts, missing the upper units.

2.7 Blackwall alteration and steatitization

They are mixed metasomatic processes, where both infiltration and diffusion exist. They usually occur in the contact of zones of serpentinized ultramafic rocks with diverse compositions and mainly consists of talc, chlorite, biotite and amphibole. The reactions take place during backwall alteration cause usually the formation of monomineralic zones-shells that developed along the contact of the ultramafic bodies with the surrounding mafic rocks.

Steatization is a kind of Mg-metasomatism that occurs within the oceanic lithosphere and is a result of chemical exchanges between the rocks of the lithosphere and seawater. In heterogeneous oceanic crust mass transfer between basaltic lithologies and peridotite is very common and results to the steatitization of serpentinites usually when in contact with gabbroic intrusions, due to the strong differences in the activities of major solutes in the intergranular fluids near the contact of these different lithologies (Bach et al., 2013). Contacts between mafic and ultramafic lithologies present a greater hydration compared to that of uniform mafic and ultramafic masses (Bach et al., 2013). As a result, steatitization which occurs in the contacts of different lithologies and depends on the fluid solute is reinforced.

Bach et al. (2013), describe steatitization as a process where intergranular fluids reacted with gabbro, will cause the steatitization of the adjacent serpentinites, just like intergranular fluids of serpentinite cause the rodingitization of the mafic protolith. The chemical process of steatitization includes an enrichment in SiO_2 and water and talc ($Mg_3(OH_2)(Si_2O_5)_2$) formation. Furthermore, steatitization includes the removal of Mg^{2+} from the fluids which is counterbalanced by the leaching of Ca^{2+} from the basalts, while at T>150 ^oC, SiO_2 is leached from the mafic rocks, with quartz saturation at T: 150-500 ^oC (Pirajno, 2013). The chemical Mg-metasomatic reaction of steatitization is described by Seyfried et al. (1988):

$$3Mg^{2+} + 4SiO_2 + 4H_2O \rightarrow \underset{\text{(talc)}}{Mg_3(OH_2)(Si_2O_5)_2} + 6H^+$$

2.8 Diopsiditization

Diopsidites, described for first time in Oman ophiolite by Python et al. (2007), comprise monomineralic-diopside dykes intruding mantle rocks. Nephrite, the host rock of diopsidites, displays various amounts of tremolite/actinolite, which increase closer to the diopsidite dykes (Python et al., 2011). These diopsides present low TiO_2 Al_2O_3 and Cr_2O_3 contents, whereas some of these dykes are anorthite bearing (Python et al., 2011). Based upon their chemical and mineralogical features they are of a hydrothermal ocean floor origin (Python et al., 2007). More specifically these authors describe diopsiditization as a process that gabbroic dykes interact with serpentinization fluids. In these processes the driving forces for the formation of monomineralic veins or not are the nature of the parent rock and the physicochemical conditions such as fO_2 and XCO_2.

In the field examination diopsidites present either sharp or progressive contacts with their host-rocks and a few centimeters to 1 m width (Python et al., 2011). They are mineralogically homogenous, especially in their cores, while their rims near the contact with their host rocks rarely contain olivine and chromian-spinel crystals (Python et al., 2011). On the other hand, anorthite bearing diopsides mainly consist of anorthite and diopside, while accessory minerals such as titanite, rutile, zircon, corundum are present, with diopside forming earlier than anorthite as it is indicated by inclusions of the first inside large anorthite crystals (Python et al., 2011).

Compositionally similar diopside rich veins are also present inside rodingite masses in the Oman ophiolite (e.g. Python et al., 2011 and references therein), while many Oman rodingites generated from the transformation of anorthite-diopsidites (Python et al., 2011).

Python et al. (2011), propose two metasomatic alterations leading to diopsitization, both related with serpentinization. The first type of metasomatism concerns rodingitic dykes, while the second alteration concerns harzburgites close to the diopsidite dykes. In this second type of alteration, Python et al (2011), suggest that diopsides derived from a strong Ca metasomatism of the mantle. During this process CaO-SiO_2 rich fluids reacted with mantle harzburgite, producing nephrites and diopsides, while the water was enriched in Mg and Fe. These chemical exchanges can be mineralogically attributed to tremolite formation from clinopyroxene and olivine transformation.

Concluding it is easily understood that diopsides and rodingites may share some common petrological and chemical features but they have been originated by different metasomatic processes concerning both their protolith and the Ca source (Python et al., 2011).

2.9 Rodingitization

2.9.1 Rodingite definition

According to Coleman (1967), rodingites are those calc-silicate rocks that typically contain hydrogarnet, diopside, vesuvianite and chlorite and represent the metasomatism of gabbros and basalts.

Based on the SCMR[1] definition, rodingitization is a metasomatic process in which basic rocks within serpentinized ultramafic bodies are replaced by grossular-andradite garnet and calcic pyroxene-rich rocks, called rodingites. Other accessory minerals include vesuvianite, epidote, scapolite and iron ores. Rodingites original protoliths are mainly basic dykes or inclusions, while they sometimes originate from other basic rocks such as volcanic rocks and amphibolites.

2.9.2 Chemistry of rodingitization & rodingites' formation

Rodingites are metasomatic rocks enriched in CaO (increase in CaO) and depleted in silica and Na_2O (Pirajno, 2013), while they usually present a Mg^{2+} enrichment (Coleman, 1977).

Three main hypotheses have been proposed for rodingite formation (Koutsovitis et al., 2013 and references therein). In the first scenario alkaline, Ca-rich and silica poor fluids deriving from serpentinization, infiltrate the rodingite parent rock, in the second scenario alkali and Si loss from the mafic protolith predominates the Ca addition from the serpentinization related fluids. In the third scenario rodingitization is an autometasomatic process, which is not related with serpentinization at all and it is thought to result from post-magmatic fluids released from a cooling magma.

Since rodingitization is strongly related with serpentinization significant explanations have been given for the gains and losses of each element from the parent rock, during its interaction with serpentinization-related fluids.

Ca^{2+} derives from dissolution of the clinopyroxene of the ultramafic during serpentinization (Coleman, 1977), producing Ca-OH-rich, high pH (>11) waters (Barnes et al., 1967; Barnes and O'Neil, 1969; Barnes et al., 1972). Silica release is the result of the breakdown of the anorthite of the dykes during their reaction with serpentinization fluids (Frost et al., 2008). Alkalis and more specifically, Na^+ can be also released from the interaction of the mafic protolith with fluids. These kinds of reactions release a high number of mobile elements in the reacted fluids, such as Ca, Na and Si. In such reactions Na, but also Si and Ca can be released by plagioclase of the dyke according to the following reaction (Li et al., 2008):

$$Pl + Cpx + H_2O \rightarrow (Hgrs–Hadr) + Chl + Di \pm C_m,$$

where C_m are the mobile elements (Na, Si, Ca).

Mg is possible to derive from the reaction of Mg-rich serpentinization fluids with the mafic rocks. During serpentinization the olivine breakdown can release Mg^{2+} in the metasomatic fluids which react with the mafic protoliths and enrich them in MgO (Tsikouras et al., 2009).

Some authors state that rodingitization depends more to the silica activities of the mafic protolith compared to those of the ultramafic rock, rather than to the intrusion of Ca rich fluids deriving from serpentinization (e.g. Frost and Beard, 2007; Frost et al., 2008; Bach and Klein, 2009; Bach et al., 2013). In such a scenario low α_{SiO_2} serpentinization fluids are the main factors of metasomatism and not a Ca addition, with the stability of Ca-silicate minerals (e.g. garnets) at low SiO_2 activities playing the most important role (Bach et al., 2013).

[1] *The Subcommission on the Systematics of Metamorphic Rocks (SCMR) is a branch*

2.9.3 Physicochemical Conditions of rodingitization

Rodingitization takes place at T between 250 ^{o}C and 450 ^{o}C (Schandl and Mittwede, 2001). Experimental studies by many researchers have given a variety of data concerning the T, P conditions under which rodingites occur. Palandri and Reed (2004) simulated rodingitization processes and produced typical rodingite assemblages at T 300 ^{o}C and 100 bar. On the other hand, Bach and Klein (2009), conducted experimental petrological research, using serpentinization fluids which reacted with mafic protoliths. The experimental results showed that rodingite formation takes place at temperatures between 200 and 300 ^{o}C. Finally, Li et al. (2007) conducted a pioneering experiment, studying rodingite formation by the interaction of serpentinization fluids with an eclogite parent rock. The results of this experiment show that rodingitization of eclogite began at 430-410 ^{o}C and completed at 250-200 ^{o}C at pressures equivalent of 7-6 km depths.

Pyroxene and olivine dissolution of ultramafics leads to OH^- production, producing alkaline fluids with high pH values, while oxidation of olivine and pyroxene Fe^{2+} to Fe^{3+}, produces reducing conditions especially at slow spreading ridges, while reducing conditions have not been confirmed in subduction zones (Koutsovitis et al., 2013 and references therein). Additionally, Palandri and Reed (2004), suggest that decreasing water/rock ratio, fluid pH decreases, while SiO_2 and Al fluid concentrations increase. Al decreases at higher w/r ratios following a pH decrease as well. Alteration reactions tend to neutralize pH, which is almost 5.6 at dry up conditions.

Koutsovitis et al. (2013), studied the physicochemical condition at East Othris rodingites and found out that rodingitization took place in three successive stages, with the first stage being more acidic and oxidizing with increased CO_2/H_2O ratio. The second stage included alkaline and reducing fluids with decreasing CO_2/H_2O ratio, while the final rodingitization stage was alkaline and characterized by the recovery of oxidizing conditions and even lower CO_2/H_2O ratio.

2.9.4 Rodingitization and serpentinization

Rodingites are closely related with serpentinites and it is believed to generate when fluids that have been affected by ultramafic rocks interact with mafic to felsic lithologies (e.g. Coleman, 1967; Bach et al., 2013). As a process, it involves a mass transfer in which silica removes from the rodingitized rock and Ca^{2+} is added in it (Coleman, 1967).

The formation of rodingites or not, depends on the P-T conditions of serpentinitic fluids. At P ~500 bar rodingites occur at T<300 ^{o}C, where serpentinization fluids are buffered by brucite-serpentine-diopside equilibrium (Bach and Klein, 2009).

Bach et al. (2013), conclude that rodingites form due to diffusional metasomatism because of gradients in protons and silica activity in the serpentine-brucite-diopside equilibrium and albite-quartz-tremolite-clinozoisite equilibrium for ultramafic and mafic rock respectively, while the Ca gradient is zero, suggesting that rodingites do not originate from Ca-rich serpentinitic fluids, whereas Si loss is controlled by decrease of αSiO_2 and not Ca^{2+} addition according to Frost et al. (2008) and Frost and Beard, (2007).

2.9.5 Mineralogy and mineral chemistry of rodingites - Stages of rodingitization

As we have already mentioned rodingite is primarily composed of grossular-andradite garnet/hydrogarnet and calcic pyroxene (mostly diopside); vesuvianite, epidote, scapolite and iron ores are usual accessories. Hydrogarnet is also with prehnite, wollastonite, chlorite and nephrite (tremolite-actinolite). Assuming the formation of hydrogarnet from the breakdown of the Ca-plagioclase of the original mafic dyke the following chemical reactions can be suggested (Rice, 1977):

$3\text{anorthite} + Ca^{2+} + 2H_2O \rightarrow 4\text{zoisite} + 2H^+$

$4\text{zoisite} + 5Ca^{2+} + 13H_2O \rightarrow 3\text{hydrogarnet} + 1.5SiO_2 + 10H^+$

Serpentinization-derived waters are supersaturated in diopside and tremolite. Coleman (1977), explains rodingitization as a result of the incompatibility of Ca-OH rich waters in such minerals. The percolated aqueous fluids are H_2 rich due to magnetite formation, though H_2 has been very rarely detected in fluid inclusions in metamorphic environments (Ferrando, 2010).

Metasomatic reactions tend to complete by the increase of Ca^{2+} in the fluid, while the main source of Ca^{2+} needed for the garnet formation is originated from the breakdown of clinopyroxene during serpentinization. The formation of hydrogarnet can also be attributed by the hydration of garnet by the following reaction (Frost and Beard, 2007)

$Grs + 2xH_2O \rightarrow Hgrs + xSiO_2(aq)$ - fluid

Garnet can be also formed by the reaction of anorthite with amphibole with the presence of lime (CaO) and water as described below (Koutsovitis et al., 2013):

$5An + Am + 3H_2O + 5\ Lm \rightarrow 4Grs + Chl + 3Qtz$

According to Coleman (1967), hydrogrossular can also derive from prehnite as described by the following reaction:

$2Prh + 2Ca^{2+} \rightarrow 2Hgrs + Si^{4+}$

or from the reaction of clinopyroxene with plagioclase with the presence of water, as is described by Li et al., (2007)

$Pl + Cpx + H_2O \rightarrow (Hgrs\text{-}Hadr) + Chl + Di \pm C_m$, where C_m is for mobile elements Ca^{2+}, Na^+ and Si^{4+}.

As we can see from the previous chemical reaction both hydrogrossular and hydroandradite can be produced. Grossular is restricted to liquids with $XCO_2<0.2$ and $T = 500\ ^oC$ (Rice, 1983). Hydroandradite can also have a hydrogrossular origin as the result of hydrogrossular reaction with diopside and water along with the presence of mobile elements (Li et al., 2008)

$Hgrs + Di + H_2O \pm C_m \rightarrow Hadr + Chl$

Prehnite formation can be described by the dissolution of anorthite with the presence of Ca^{2+} following the reaction below (Coleman, 1967):

$1{,}5\ An + 2Ca^{2+} + 1{,}5H_2O \rightarrow Prh + 0{,}5\ Al_2O_3 + H^+$

Vesuvianite is most likely formed in very low CO_2 conditions with water rich fluids, at 300-400 ^oC (Li et al., 2004; Hatzipanagiotou et al., 2003; Li et al., 2008, Koutsovitis et al., 2013) and its formation can be described by the following reactions (Li et al., 2004, 2008)

$Hgrs + Chl + H_2O \rightarrow Ves + C_m$

$Hgrs + Chl + Ca^{2+} \rightarrow Ves + H_2O$

Calcite is present when large quantities of aqueous fluid exist and the physicochemical conditions are appropriate so that Ca^{2+} can react with HCO_3^- to form calcite both in peridotites and rodingite.

Chlorite is replacing hydrogrossular by the following reaction with decreasing of temperature (Li et al., 2008; Buse et al., 2010; Koutsovitis et al., 2013).

$Hgrs + Di + H_2O \pm C_m \rightarrow Hdr + Chl$

Bach et al. (2013), heated seawater equilibrated with harzburgite at T= 200 ^oC and P= 1kbar and then they equilibrated this serpentinitic fluid with gabbro. The main mineral assemblages of this experiment with increasing distance from the gabbro-peridotite contact to the core of gabbro with water/rock ratio decreasing present the following conversions: Garnet zone is converted to garnet, chlorite zone which turns to clinopyroxene, garnet, chlorite zone, turning to clinopyroxene, garnet, chlorite and biotite zone, while the final zone consists of prehnite, clinopyroxene, chlorite, garnet and biotite. These authors also refer to the conversion of talc and chlorite to tremolite and Na-plagioclase. From the above experiment we observe that garnet formation mostly occurs in rodingite rims, while clinopyroxene and chlorite appear gradually moving from rim to core, that is towards a lower water/rock ratio. Finally, epidote and prehnite concentrate at the core, whereas neither, vesuvianite or calcite, were formed.

Bach and Klein (2009), simulated rodingitization at 300 ^oC and 500 bar, and found the following mineral transitions (from rodingite rim to core): clinopyroxene + garnet → garnet + clinopyroxene + chlorite → garnet + clinopyroxene + chlorite + epidote-ss (clinozoisite-epidote solid solution) → clinopyroxene + epidote-ss + chlorite →clinopyroxene + epidote-ss + tremolite → clinopyroxene + epidote-ss + tremolite + prehnite → prehnite + epidote-ss + tremolite → prehnite + epidote-ss + tremolite + plagioclase. Thus, garnet is mostly present near the rodingite rims, while clinopyroxene is present almost all the way from rim to core. Epidote minerals appear from the transition zone near the rodingite rims and dominate in the rodingite core, while tremolite, prehnite and plagioclase occur in the core. Bach and Klein (2009), also state that epidote-ss is dominant at 300 ^oC, while at 200 ^oC it disappears.

In the experiment of Palandri and Reed (2004), who used a pyroxene bearing protolith reacting with a rich in Al and Ca serpentinization fluid at 300 ^oC and 100 bar, the mineral assemblages observed with water/rock decreasing are the following: vesuvianite-chlorite-grossular turns to grossular, chlorite and prehnite which turns to prehnite, grossular and diopside, prehnite, diopside prehnite and wairakite. When the smallest w/r condition occurs, diopside is dissolved and prehnite, wairakite and chlorite are the dominant minerals. Waikarite is a very special mineral, which is not usually observed in rodingites and in physical systems occurs under zeolite faces of metamorphism. As for the physicochemical conditions the authors found out that at small w/r ratios fluids are Ca depleted with decreasing alkalinity.

2.9.6 Derodingitization and Metarodingites

Rarely rodingites can be derodingitized or metamorphosed. Derodingitization occurs at the late metasomatic stages and results from Mg-rich metasomatic fluids, changing the rodingitic mineral assemblage and converting it into Mg-rich (e.g. Koutsovitis et

al., 2013). In East Othris a derodingitization episode took place immediately after the final rodingitization stage, characterized by significant Ca decrease and Mg enrichment, as seen by the high MgO contents in some minerals and the Mg-chloritic marginal zones between rodingites and serpentinites (Koutsovitis et al., 2013). The mineral assemblage in many rodingites changed and Fe-rich pumpellyite as well as Mg-chlorite were formed, due to the clinopyroxene and hydrogarnet breakdown, possibly reacting with Mg-rich and Ca-poor metasomatic fluids (Barnes and O'Neil, 1969; Li et al., 2004; Koutsovitis et al., 2013).

Evans et al. (1979), studied the eclogite-metarodingite suite of Cima di Gagnone, Valle Verzasca, Ticino, Switzerland. Their study area lies in the Central Alpine metamorphic belt consisting of metacarbonated rocks as well as amphibolites, semi-pelitic gneisses and ultramafic rocks with a lherzolitic composition. The metamorphism mainly comprises two episodes, with the first concerning an HP eclogite phases, while the second was a lower pressure amphibolite episode (Evans et al., 1979). Metarodingites form boudinaged sheets inside and foliation inside the ultramafic rocks, while transitional rocks between metarodingites and eclogites occur inside the ultramafic rocks. Metarodingites mainly consist of garnet, pyroxene (mainly diopside and some jadeitic), epidote, secondary hornblende, accessory sphene and rutile, whereas their boudins are surrounded by amphibole rich contact reaction zones. More specifically, Evans et al. (1979), recognize three reaction zones from metarodingite to the ultramafic side. The first zone includes hornblende-epidote symplectite and diopside, the second zone mainly consists of hornblende and epidote, while the third zone includes actinolite and chlorite. The eclogite-metarodingite transition is characterized by Ca increase and Na depletion. As for their formation Evan et al. (1979), suggest that serpentinization related fluids caused rodingitic metasomatism possibly prior to the eclogitic metamorphic event. After that in a subduction setting the partially serpentinized rocks were affected by an early eclogitic metamorphic episode following a subsequent Barrovian regional metamorphism during the upward movement of rock fragments.

Stucki et al. (2001), studied a rare mineral called zirconolite ($CaTi_2ZrO_7$), found inside metarodingite rocks in Central Alps. These metarodingites are parts of metamorphic ophiolitic relics along with meta-peridotites, gneisses and amphibolites and they are found as boudinaged dykes inside the meta-peridotites. They display a magmatic origin, mainly having a gabbroic or basaltic protolith, while rarely they have been generated from oceanic plagiogranites. Zirconolite presents high REE and Y values and is accompanied by clinopyroxene, magnesian ilmenite, spinel, chlorite and titanian clinohumite pseudomorphs (Stucki et al., 2001). REE and Y usually substitute Ca and Ti in zirconolite, explaining its high REE and Y contents.

Laborda Lopez et al. (2015), studied petrographically and geochemically the metarodingites of Cerro del Almirez in South Spain, which were enclosed as boudinaged lenses within antigorite serpentinites and chlorite harzburgites. The antigorite-serpentinite hosted metarodingites present magmatic ophitic textures and mainly consist of grossular, Mg-chlorite, diopside, amphibole and titanite, while ilmenite, magnetite, zircon, allanite and apatite are the accessory minerals. Metarodingites in chlorite harzburgites include epidote and amphibole, diopside, Mg-chlorite and titanite, while some relict garnets also occur. Accessory minerals are ilmenite, magnetite, zircon and apatite. The petrogenetic model for these antigorite serpentinite hosted rodingites suggests a seafloor metamorphism, where plagioclase was replaced by Ti-grossular, which was enriched in Fe and depleted in Ca during the

metamorphic processes. Finally, the mineralogical differences between the two rodingite types are explained by the hydration reactions in each type (garnet + H_2O → epidote + diopside for antigorite serpentinite hosted metarodingites and diopside + H_2O → epidote + amphibole for chlorite harzburgite hosted metarodingites).

2.9.7 Rodingite occurrences in Greece

Many rodingite occurrences have been reported in Greece. The majority of them have been detected within ophiolitic ultrabasic rocks as dikes or pods, while only Samothraki rodingite formation is attributed to non-serpentinization related processes (Hatzipanagiotou and Tsikouras, 2001). More specifically:

Koutsovitis et al. (2013), studied the rodingites from the ophiolitic complex of East Othris in Central Greece. Othris is one of the most well-known ophiolitic complexes and consists of mafic volcanic rocks, dolerites, gabbros, ultramafic and serpentinized ultramafic rocks. The whole sequence also includes an ophiolitic mélange. The rodingites in East Othris occur mostly as fine-grained displaced or folded dykes in sharp contact with the host serpentinized harzburgite. They are white-colored and divided into two groups, with Type-1 rodingites being prehnite rich, while Type-2 rodingites mainly include garnet and vesuvianite. Type-1 rodingites mainly include prehnite, clinopyroxene, amphibole, chlorite, hydrogarnet, pumpellyite, white mica and calcite, while the main mineral assemblage of Type-2 rodingite consists of hydrogarnet, garnet, clinopyroxene, chlorite and vesuvianite. Finally, they conclude that rodingites in East Othris involve subducted carbonate sediments in an intra-oceanic subduction environment unlike the commonly accepted theory for most rodingites that have been formed close to an ocean-floor environment. Rodingitization occurred during the exhumation of the mafic/ultramafic mantle wedge and evolved in three stages with successively decreasing of CO_2/H_2O ratio. Metasomatic processes were strongly related to rich in Ca, Mg and Ni serpentinization fluids having increased pH values. Hydrothermal fluids circulated through dolerites and gabbros and during the late stage of rodingitization seawater was possibly added in the metasomatic fluid. After the final rodingitization stage derodingitization immediately followed.

Tsikouras et al. (2009), who studied rodingites occurring within ultramafic ophiolitic rocks of West Othris, divide them in two groups according to the presence or not of calcite. The calcite-bearing samples preserve a few relict igneous textures, while the calcite-free samples show intense deformation with later cataclastic textures and no relict igneous minerals preserved. The mineral assemblages in both groups mainly include hydrogrossular and diopside and differ in the presence of calcite and apatite. They suggest that the calcite-bearing rodingites indicate a transition, between meta-dolerite and rodingite, while the calcite-free ones are indicative of a late phase of the metasomatic alteration. The authors conclude that rodingitization occurred under rich CO_2-fluids, possibly implying a subduction related origin rather than an ocean-floor episode. Rodingitization was related with serpentinization of the surrounding peridotites. Both CO_3^{-2} and PO_4^{-3} behaved as ligands for REE, while CO_2 and PO_4^{-3} behaved as ligands for Ti and Zr as well in successively increasing pH values.

Tsikouras et al. (2013), studied Iti and Kallidromon ophiolites. Iti mountain lies south of the Othris mountain and includes rodingitic rocks in the forms of fragments, thrust sheets within the ophiolite mélange, or as pods or dykes within serpentinized rocks of the ophiolitic nappe. They are divided into mantle derived and gabbroic ones

including garnet, chlorite, diopside, prehnite, tremolite ± vesuvianite ± epidote with granoblastic, lepidoblastic and locally cataclastic textures and chlorite + garnet + diopside + prehnite + tremolite ± clinozoisite ± talc with relict granular textures respectively. In Kallidromon Mountain which lies to the north of Parnassos Mountain in Central Greece, rodingitized gabbroic and doleritic dykes are mainly observed, mostly displaying a greenish chloritic blackwall. These rodingites are dolerite derived and contain grossular garnet, epidote, clinozoisite, prehnite, tremolite/actinolite, with preserved granular to subophitic textures. As far as their metasomatic processes concerns, Tsikouras et al. (2013), conclude that many types of processes can be observed and they strongly suggest that rodingitization is not a unique process and that it was controlled by the composition of the protolith and the fluids. It is most possible that the rodingitization was triggered by fluids which passed through the serpentinized peridotite and then circulated from the lower ultramafic rocks to the upper mafic ones.

In Rodiani area, which lies north of mountain Vourinos, rodingitized dykes occur along with other separate bodies of dunite with chromite ore, gabbro and pyroxenite within serpentinized harzburgite (Christidis et al., 1998). Rodingite mainly comprises hydrogrossular, vesuvianite and epidote, while angular chromite fragments occur inside the rodingite. Moreover, chlorite bodies are present in the tectonic contact of the serpentinitic rocks with the chromite ores near the contact with rodingite dykes. These chlorite bodies host among others, perovskite and pseudobrookite, which can be probably related to rodingite formation.

In Skyros Island rodingites are observed as dykes, which intrude massive or highly deformed serpentinites of the Eohellenic ophiolitic nappe (Karkalis et al., 2016). They consist of hydrogarnet, vesuvianite, chlorite (brunsvigite), diopside and prehnite. Involvement of subduction-related fluids during the formation of the rodingites is suggested. The whole ophiolitic sequence as well as the rodingites that are included in is believed to have formed in a supra-subduction zone geotectonic environment of the Jurassic – Lower Cretaceous Vardar Ocean (Karkalis et al., 2016).

In Koziakas ophiolitic complex, in western Thessaly, rodingites occur as dykes intruded ultramafic rocks (serpentinitic harzburgites) of the ophiolitic mélange of the sequence (Pomonis et al., 2008). They are homogenous, white colored medium to coarse grained with sharp contacts with the ultramafic rocks and occur in places with high shearing displaying two main directions (NE-SW and N-S to NNW-SSE). Their mineral assemblage mostly consists of hydrogrossular, diopside (new or relict), chlorite, clinozoisite-epidote, calcite, prehnite and accessory titanite and magnetite, while their texture is granular, plastic and mylonitic due to their high deformation (Pomonis et al., 2008). According to their geochemical and mineralogical features, Koziakas rodingites are similar to many Phanerozoic rodingite formations, associated with subgreenschist metamorphism and reducing conditions. The chemical exchanges during rodingitization occurred by infiltrational mass. Their petrogenetic model suggests that rodingitization was concomitant with serpentinization and ocean floor metamorphism/metasomatism during Lower Jurassic at $T< 650\ ^{o}C$ with alkaline H_2O-rich fluids of gabbro as indicated by their minerals which also include albite, tremolite, chlorite, calcite, epidote, titanite and magnetite.

Rodingites from Samothraki ophiolite are fine grained leucocratic rocks with reddish garnet which have been found enclosed in diorite (Hatzipanagiotou and Tsikouras, 2001). They are present only near shear zones and they lack reaction contacts with the

country doleritic rocks. According to their mineralogy they were divided into two groups, with the first group including garnet and vesuvianite and lacking of chlorite and albite, whereas the second group includes chlorite and albite and lacks vesuvianite and garnet. Their mineral assemblages are similar to many other Phanerozoic rodingite around the world, associated with high pH conditions and greenschist metamorphism. Finally, Hatzipanagiotou and Tsikouras (2001), conclude that these rodingite rocks possibly formed by heating in water rich fluids at possible T< 500 ^{o}C during oceanic metamorphism. From the above is clear that this rodingitization is not necessarily related with serpentinites and Samothraki rodingite boudins and pods have a dioritic origin formed in the upper plutonic ophiolite members.

2.9.7.1 Kimi rodingites

The present study is the first detailed petrological, mineralogical and geochemical study concerning rodingites of Kimi. Four studies have been accomplished the last 72 years, but since 1972, no studies have been reported. In the next paragraphs we present the main results of these studies.

The first reference for Kimi rodingites appears in Papastamatiou (1945), who describes calc-silicate, calcite bearing rocks hosted inside serpentinitic bodies in Choneftiko area. According to Papastamatiou (1945), the occurrence of peridotite bodies inside flysch is interpreted by peridotitic magma intrusions inside flysch formation, causing metamorphic episodes.

Marakis (1972a), describes the rodingites as light-colored small lenses, bands or irregular bodies inside serpentinites, which in turn occur within a sedimentary formation. Their sizes ranges from 10 cm to 3-6 m, while their mineral assemblage consists of vesuvianite, calcite, chlorite, antigorite, epidote, zoisite and diopside. He found also dark green bands between serpentinitic host rocks and rodingites, which were interpreted as reaction zones. As far as their petrogenesis concerns, the author suggests the firstly an intrusion of a peridotitic magma in sediments, cutting and trapping fragments of sedimentary rocks, mainly marly Al-rich limestones. Afterwards and under of regional metamorphic conditions the marly Al-rich limestones converted into rodingites. Vesuvianite formation was attributed to high Ca concentrations of the initial limestone parent rock. In cases that Al was not enough to form vesuvianite, chlorite, diopside and antigorite were formed instead. Finally, Marakis (1972a), supports that the formation of Kimi rodingites by contact metamorphic processes should not be excluded.

In another study, Marakis (1972b), studied the clinochlore crystals of Kimi rodingites. The author concludes that both vesuvianite and clinochlore crystals indicate the same P, T metamorphic conditions of formation for Kimi rodingites under contact or regional metamorphic conditions. Furthermore, he suggests the presence of diopside crystals in rodingitic rocks and its absence from the adjacent ones, further supports the assumption of rodingite formation under conditions of contact metamorphism. Clinochlore formation mostly depended on Al availability, while Al and Ca took part in vesuvianite formation.

As for the Kimi rodingite occurrences Paraskevopoulos and Kanakis (1972), adopt also the theory of an ultramafic magma intrusion in limestone protoliths, producing rodingites, which consist of vesuvianite, epidote, zoisite, diopside and clinochlore. Diopside occurs as crystals inside rodingite matrix, whereas diopside veins usually

occur. They also suggest a strong CO_2 participation in rodingite petrogenetic processes which most probably resulted from a contact metamorphic event. Finally, rodingite formation is in agreement with that of ophicalcite rocks, since both petrogenetic processes involved the intrusion of a peridotitic magma in fragments of the uppermost limestones.

3 Geological Background

3.1 Geological division of the Hellenides

Hellenides (Fig.5) are part of the Alpine-Himalayan mountain chain. They are traditionally divided into several subparallel tectono-stratigraphic zones which trend NNW-SSE.

These two main zones comprise the External Hellenides in the west and the Internal Hellenides in the east. The external Hellenides form a part of Greater Apulia (De Bono, 1998) and their carbonated platform lies in the western part of Greece, comprising many non-metamorphosed and metamorphosed units such as Paxos, Ionian, Gavrovo and Tripoli, which are dominated by Mesozoic and Cenozoic cover rocks (Anders, 2005), and Mani, Western Crete, Olympos and Almyropotamos respectively. Their flysch is of a Late Eocene to Oligocene age (Godfriaux, 1968, Fleury, 1980; De Bono, 1998).

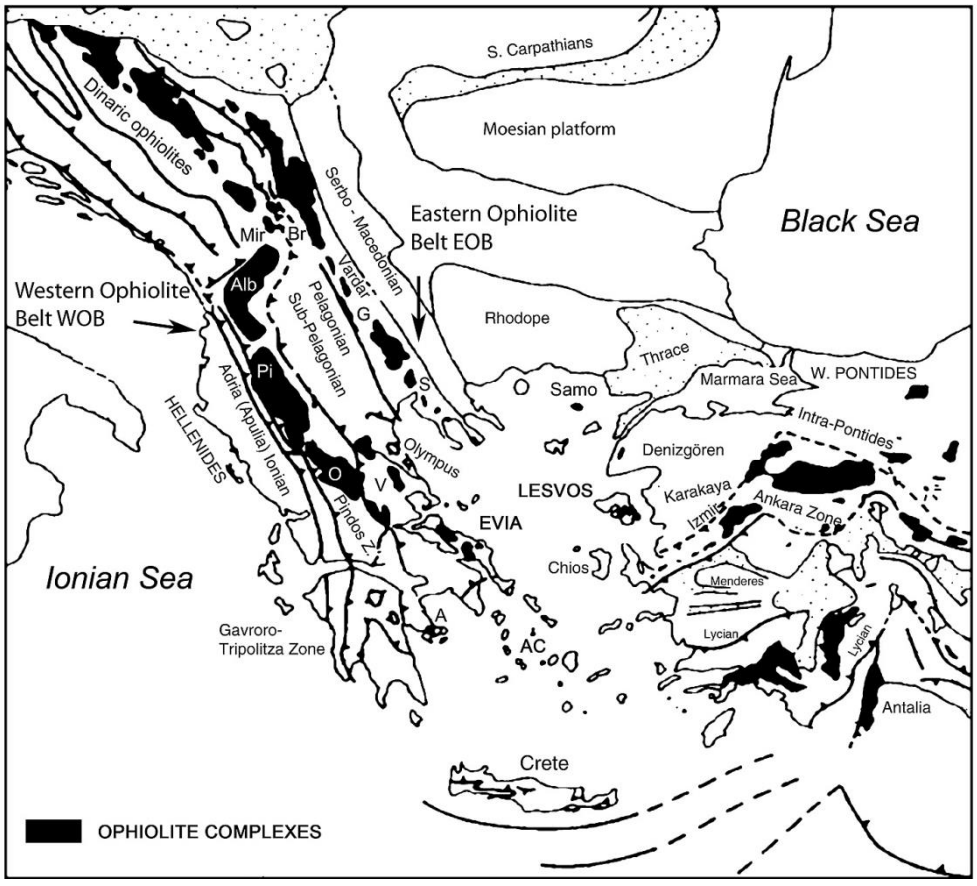

Figure 5. Distribution of ophiolite complexes in the Dinarides, Hellenides and Taurides of western Turkey. The tectonic sketch map is modified after Robertson and Shallo (2000). WOB: Western Ophiolite Belt, EOB: Eastern Ophiolite Belt, Ophiolite complexes: A for Argolis, AC for Attico-Cyclades, Alb for Albanian, BR for Brezovica, EVIA, G for Guevgueli, Mir for Mirdita, LESVOS, O for Othris, Pi for Pindos, S for Sithonia, Samo for Samothraki, V for Vourinos (Gartzos, 2009).

On the other hand, the Pelagonian Zone, the Attico-Cycladic Massif, the Vardar Zone, the Serbo-Macedonian Massif and the Rhodope Massif form from east to west the Internal Hellenides. The Pelagonian and Vardar Zone represent the western part of the Internal Hellenides, while the Vardar Zone has long been regarded as an ophiolite

suture zone separating the Pelagonian Zone to the west and the Serbo-Macedonian Massif to the east (Anders, 2005).

Papanikolaou (1989), describes the Internal Hellenides platform as the Late Cretaceous transgression which covers the Parnassos, Beotia and Pelagonian terrains after their previous tectonic event (Stampfli, 1996, Stampfli et al., 1998)

On the other hand, Aubouin et al. (1970), described the internal Hellenides as these zones that have been tectonized and metamorphosed before the Late Cretaceous such as Pelagonian and Maliac-Othris Zones.

They are deformed and metamorphosed during Late Jurassic to Early Cretaceous age, following the westward obduction of Vardar Ocean onto the Pelagonian Zone (Schermer, 1993; Most, 2003; Kilias et al., 2010; Nirta et al., 2015).

The External Hellenides have undergone Late Cretaceous to Eocene HP metamorphism as documented by the presence of Olympos tectonic window and in the Pelion Peninsula (Schermer et al., 1990; Lips et al.,1998; Kilias et al., 2010; Nirta et al., 2015).

Finally, the Internal and External Hellenides are separated by a deep-sea water basin since Middle Triassic between Gavrovo-Tripoli and Pelagonian, which is called Pindos-Olonos Zone and some of its ophiolitic remnants are found in the Pindos realm having a Vardar or Pindos origin (De Bono, 1998 and references therein).

The Jurassic ophiolites of Hellenides can be divided into an Eastern Ophiolite and Western Ophiolite Belt respectively (Spray et al., 1984; Ferrière et al., 2012; Nirta et al., 2015). The Eastern ophiolites correspond to the Vardar Zone and they are overthrusted above the Eastern Pelagonian margin, while the Western ophiolites were thrusted above the Western margin of Pelagonian Zone. There are two main theories concerning the origin of the Western ophiolites: in the first theory they derive from Pindos Ocean, while in the second theory both Eastern and Western ophiolites belong to the unique Vardar ocean (Nirta et al., 2015 and references therein).

3.2 Pelagonian Zone

Aubouin (1959), describes the Pelagonian Zone as the total of the metamorphosed rocks in Western Macedonia, Eastern Thessaly, Evia, Attica and Cyclades, including the overthrusted sedimentary formations of a neo-Paleozoic and Mesozoic age and places it between Axios and Pindos trough in the eastern and western parts respectively. The same author refers to Sub-Pelagonian as the Pelagonian ridge to the deep-sea basin. This theory has been rejected since it was based on the existence of ophiolitic magmas (Koutsovitis, 2009).

The Pelagonian Zone is either regarded as the eastern continental margin of the Adria Plate or the continent between the Vardar and Pindos ocean basins to the east and west respectively (Nirta et al., 2015).

Katsikatsos (1992), regards Pelagonian and Sub-Pelagonian as a uniform Zone which is distinguished according to the grade of metamorphism and divides it into *''Pelagonian Zone of metamorphosed or non-metamorphosed formations''*.

Geodynamically, Pelagonian is regarded as a detached fragment of Eurasian which drifted away during the Permian or Early Triassic age and was overthrusted by

ophiolitic thrusts of a Vardar origin, which belong to the Eohellenic orogenic phase during the Middle Triassic (De Bono, 1998).

3.3 Vardar Zone

The Vardar Zone is a suture zone east of the Pelagonian Zone (Anders, 2005) and in Greece it is situated between the Serbo-Macedonian Zone to the East and the Pelagonian zone to the West. In Macedonia, the Vardar Zone is divided into Peonia, Paikon and Almopia units. During the Eohellenic orogeny the Vardar Ocean overthrusts on the Pelagonian and Pindos realms as an ophiolitic tectonic nappe (De Bono, 1998).

For some researchers, Vardar Zone was the ocean separating the Apulia Gondwana-related units such as the Pelagonian, from the Eurasian units (Dercourt et al., 1993), while others (Stampfli et al., 1998; Stampfli, 2000) support that the Vardar ocean is a marginal basin, which was developed behind an earlier Palaeotethyan-oceanic basin beneath the Pindos suture, with the Jurassic ophiolites being obducted from a Vardar marginal basin over the Pelagonian continent (Robertson, 2002).

3.4 Attico-Cycladic Complex

The Attico-Cycladic Complex is divided into the following three units: The Basal Unit, the Cycladic Blueschist Unit and the Upper Unit (e.g. Papanikolaou, 1984; Shaked et al., 2000; Xypolias & Kokkalas, 2003). The Basal Unit is believed to be part of the External Hellenides and consists of metasedimentary and metavolcanics rocks of Permian-Tertiary age (e.g. Avigad et al.,1997; Baziotis, 2008). The Blueschist Unit is the mostly exposed one and includes metamorphosed rocks such as schists, marbles and metavolcanics (Baziotis, 2008). It has been affected by a blueschist to eclogitic metamorphic episode (50-54 Ma, P: 2GPa, T: 600 ^{o}C) (Schmädicke & Will, 2003) and a retrograde greenschist or/and amphibolitic episode 20-25 Ma (P: 0,7 GPa, T: 450-600 ^{o}C).

A final episode is recorded 15-9 Ma, due to a meocenic igneous intrusion. This unit is exposed in many greek areas such as Evia, Cyclades and East Attica.

Finally, the Upper Unit consists of non-metamorphosed formations of a Permian-Triassic age along with serpentinites and meta-basalts and meta-gabbros. They have affected by greenschist metamorphism 70 Ma (Maluski et al.,1987; Avigad and Garfungel, 1989; Bröcker,1990; Bröcker et al., 1993; Patzak et al., 1994; Katzir et al.,1996; Baziotis, 2008).

3.5 Evia geological setting

According to Katsikatsos et al. (1986) and Katsikatsos (1992), three units crop out in Evia. The uppermost of them is the Pelagonian Unit, which lies on the northern and central part of the island and consists of metamorphic and non-metamorphic rocks of the Internal Hellenides. The southern part of the island includes HP/LT metamorphic rocks which are equivalent to those of middle Cycladic blueschist unit and is called “South Evia Blueschist Belt”, while under this unit the para-autochthonous Almyropotamos Unit is exposed as a tectonic window (Shaked et al., 2000). This unit

has experienced LP metamorphism and is considered to be part of the External Hellenides (Dürr et al. 1978; Papanikolaou, 1984, 1986; Katsikatsos et al. 1986; Okay, 1989; Shaked et al., 2000).

In opposite to the above division De Bono (1998), describes the geological structure of Evia as consisting of the following six tectonic units from South to North: the Ochi mountain formation, the Styra unit, the Almyropotamos unit, the Liri unit, which occurs only in Central Evia and it is a Triassic flyschoid sequence consisting of limestone and granitoid olistholiths, called *"Liri Granites"*, the Stropones limestones unit, which outcrops in northern and central Euboea and finally the Pelagonian zone formations, which overthrust the Attic-Cycladic Zone in Euboea.

3.6 Southern Evia

Almyropotamos Unit (Fig.6) is mainly composed of marbles that are overlain by meta-quartzites and meta-pelites with some marble horizons. The whole sequence is interpreted as a meta-flysch (Shaked et al., 2000). The South Evia Blueschist Belt consists of the following three units, which are from bottom to top: Tsaki, Styra and Ochi formations. They have all experienced HP metamorphism as it is suggested by its mineral assemblage (Katsikatsos, 1991 a,b; Shaked et al., 2000). The Tsaki Formation mainly includes mica-chlorite-schists with impure marble intercalations. It is distinguished from the underlying Almyropotamos flysch by metamorphosed serpentinitic and metabasic blocks along with schists, while its structural position is debatable with some researchers grouping it with the higher Styra formation (e.g. Katsikatsos et al. 1986; Jacobshagen, 1986), while others include it in the Almyropotamos flysch (Chenevart and Katsikatsos, 1967). Styra formation mainly includes impure marbles with quartzite horizons and schists, while a few metabasic bodies are found near the base and top of this formation (Shaked et al., 2000).

The uppermost Ochi formation consists of quartzites, meta-tuffs, and metabasic rocks intercalations with metabasites and serpentinites, near the contact with the underlying Styra formation (Shaked et al., 2000).

3.7 Central-Northern Evia and Kimi Geological Setting

According to Katsikatsos (1992), the northern and central parts of Evia consist of the following Pelagonian formations from the lower to the upper parts (Fig. 7): a Paleozoic crystalline basement, including gneisses and schists, neo-Paleozoic formations including sandstones, schists and phyllites, Lower to Middle Triassic volcano-sedimentary rocks, carbonates of Upper Jurassic-Lower Cretaceous age, ophiolitic nappe formations along with their accompanying sediments, Upper Cretaceous limestones, Paleocene flysch and the Neogene formations. In central Greece, including Evia, the Pelagonian has experienced only low-grade metamorphism (Mountrakis, 1986). Its continental basement consists of Upper Paleozoic granite, while the carbonated platform is overthrusted by ophiolitic thrusts during the Upper Jurassic – Early Cretaceous (Rassios & Moores, 2006). The stratigraphic sequence ends up with a new redeposition episode during the Early Cretaceous (Mountrakis, 1986).

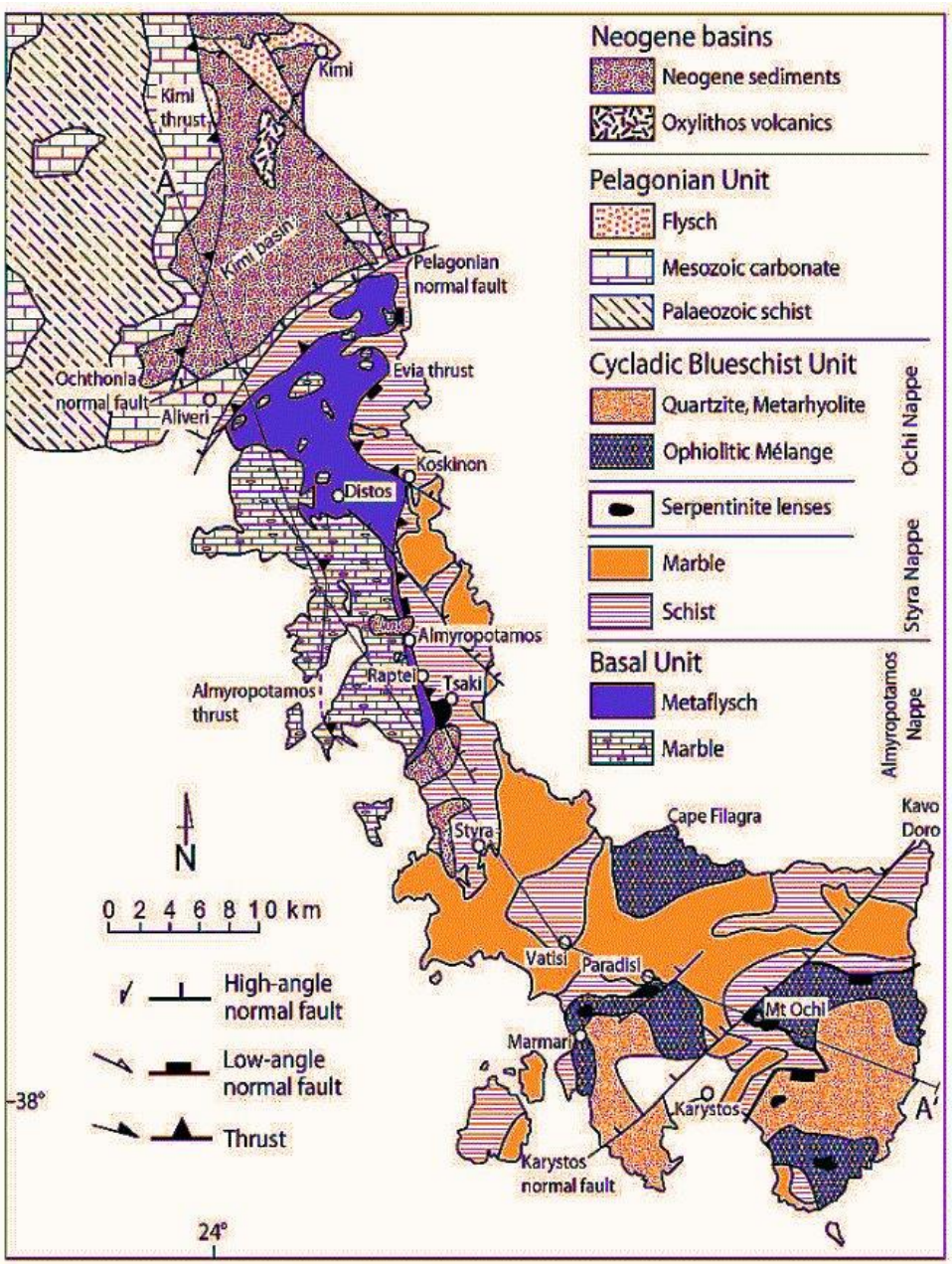

Figure 6 . Geological map of southern Evia (Ring et al., 2007)

Kimi is part of central Evia and presents the aforementioned stratigraphic sequence, consisting from bottom to top, of the following Pelagonian formations (Figs 8 and 9) (Katsikatsos et al., 1970):

Triassic thick to medium bedded crystalline limestones with dolomitic limestone intercalations, clastic materials and basic igneous bodies. The clastic materials mainly include greywakes and breccio-conglomertes. In the upper parts of Triassic limestones iron nickel lateritic ores and bauxite deposits (both in the form of leuticular layers on an eroded footwall) underlie the Upper Cretaceous limestones. Iron nickel ores are pisolithic and compact, while the bauxitic deposits are usually compact with limestone breccias in palces.

Cenomanian-Maestrichtian transgressive limestones marly in their lower parts with numerous fossils such as Chrysalidina cf. and Rudist fragments. Their middle parts are karstic and Rudist-bearing, while their upper parts are marly limestones of Upper Senonian-Maestrichtian age.

Upper Senonian – Maestrichtian thin bedded microcrystalline marly limestones, including many fossils such as Globotruncana stuarti and Globotruncana arca.

Maestrichtian-Paleocene flysch, which contains alterations of shales, sandstones, breccio-conglomerates and limestone intercalations with Globotruncana, as well as diabase and more or less serpentinized peridotite bodies. The total thickness is up to 500m.

Neogene formations, containing basal conglomerates, which are overlain by Lower Neogene sediments, consisting of marls, marly limestones and intercalations of clays, sandstones and conglomerates. The sequence ends up with alterations of conglomerates, sandstones, clays and clayly marls with volcanic tuff layers.

Kimi-Aliveri basin lies south of Kimi and comprises Early to Middle Miocene terrestrial sedimentary rocks along with felsic volcanics. The following three sedimentary groups can be distinguished (Bradley, 2005): The Prinias Group which consists of marls, silts, with alluvial and delta conglomerates and the Mantzari Group deposited uncomfortably onto the Prinias group and consisting of lacustrine, alluvial fan delta, and fluvial sediments (Bradley, 2005). These rocks were derived from the erosion of a low-grade metamorphic terrane situated to the east of the Kimi-Aliveri basin. The Koustoumalou Group consists of alluvial conglomerates, whereas both Prinias, Mantzari, and lower Koustoumalou groups were intruded by Oxylithos volcanic complex almost 14 Ma (Bradley, 2005).

In northern Evia (Fig. 7), a mélange called Pagondas complex structurally occurs between the Triassic-Jurassic carbonated platform of Pelagonian Zone and an overriding harzburgitic ophiolite (Robertson, 1990). The Pagondas Complex includes remnants of Neotethyan oceanic lithosphere, overlain by radiolarites, hemipelagic carbonates and calci-turbidites, derived from a Mesozoic carbonate platform. The volcano-clastic sediments reflect a post-volcanic erosion of the ocean floor, where the tholeiites erupted during Triassic-Jurassic age at spreading axes (Robertson, 1990).

This mélange is interpreted as remnant of Pindos Ocean, developed westwards of the Pelagonian Zone, within the Neotethyan Ocean (Robertson, 1990). It mainly consists of basic to intermediate volcanic rocks, serpentinites, limestones and other sedimentary rocks such as cherts, sandstones and shales. The ophiolites that were probably formed in a marginal basin or forearc setting have been weathered forming bauxite and Fe-Ni-sediments (Guernet & Robert, 1973).

The overthrusted Evia peridotite is structurally underlain by a dismembered metamorphic sole that mainly consists of serpentinite, amphibolites and greenschists.

At Pilion-North Evia, amphibolite sole rocks plot in the MORB and VAB fields (Simantov et al., 1990), while amphibolites from Prokopion area (North Euboea) plot in the WPB field (Robertson, 1990). However, as the structural data from the sole is not conclusive, Robertson (1990) proposes an eastwards emplacement of the ophiolite.

As the westwards intraoceanic subduction of Pindos Ocean continued, an accretionary complex was developed and the majority of the Neo-Tethyan oceanic lithosphere was subducted. Finally, the supra-subduction zone Evia ophiolite was thrusted eastwards over the accretionary complex, creating the high-temperature amphibolite sole (Robertson, 1990).

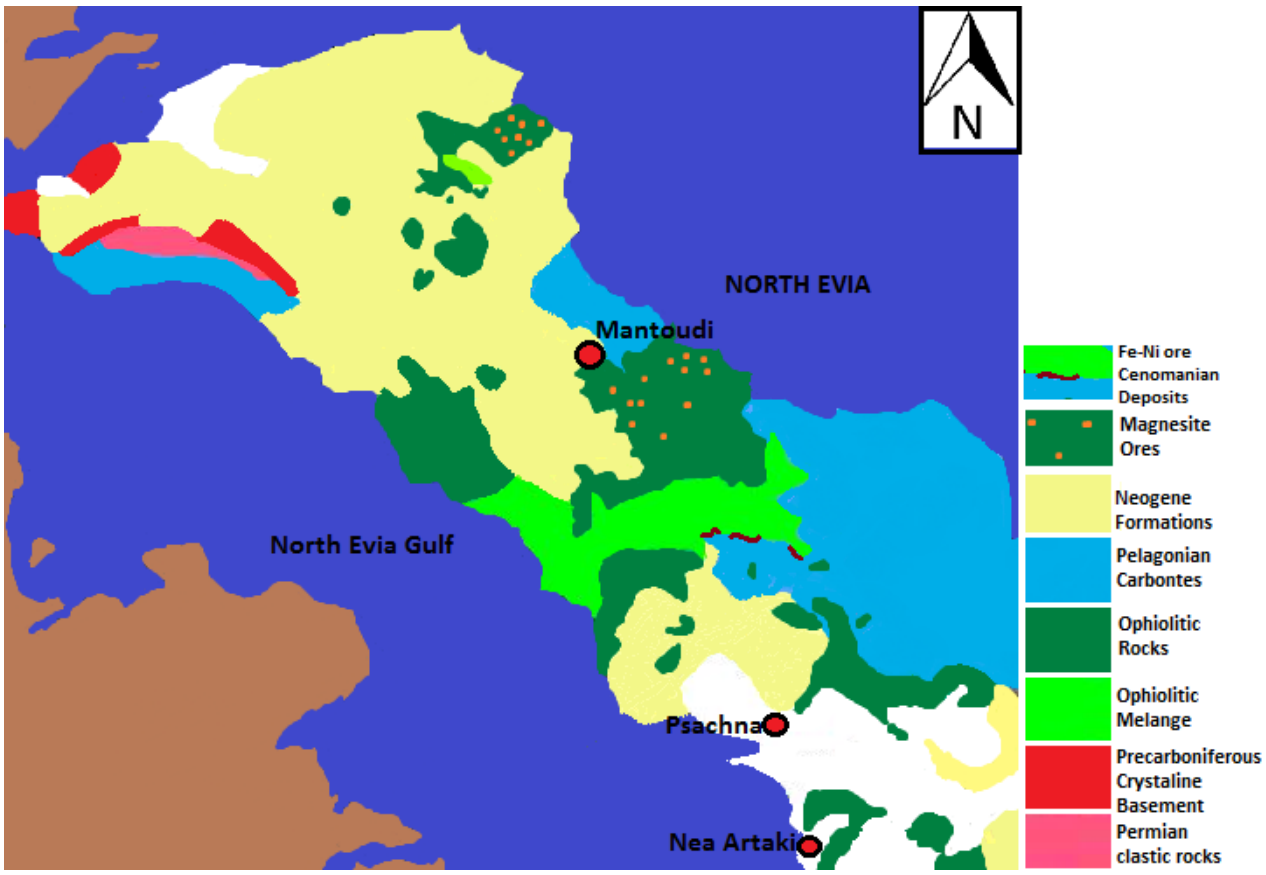

Figure 7. Northern Evia simplified geological map.

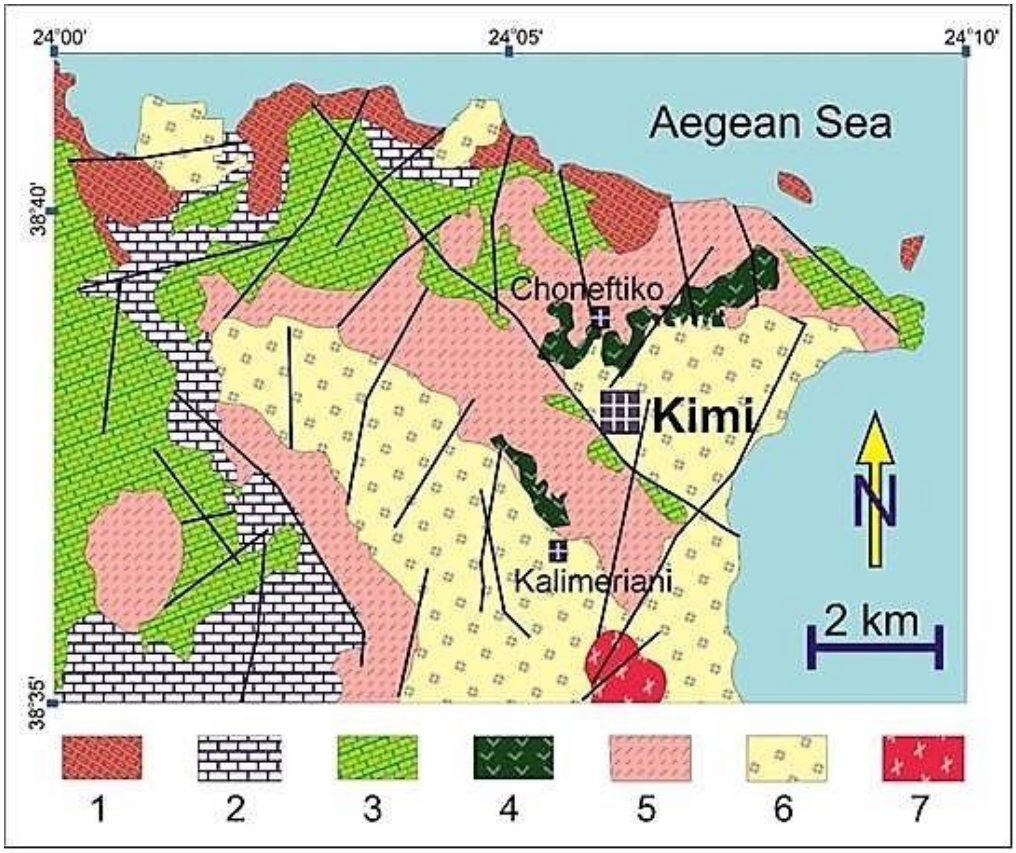

Figure 8. Simplified geological map of Kimi area (modified after Anastopoulos, 1962, Katsikatsos et al., 1970). 1. Triassic Limestones and Clastic Sedimentary Rocks, 2. Jurassic – L. Cretaceous Limestones, 3. U. Cretaceous Limestones, 4. Ultramafic Rocks and Rodingites, 5. U. Cretaceous – Paleocene Flysch, 6. Neogene and Quaternary Rocks, 7. Miocene Volcanics. Black lines: faults and possible faults.

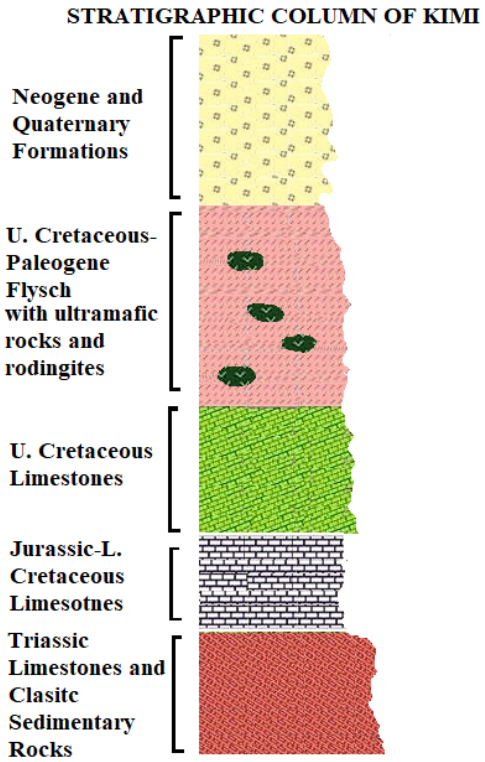

Figure 9. Stratigraphic Column of Kimi (after after Anastopoulos, 1962, Katsikatisos et al., 1970 IGME).

3.8 The Kimi flysch

In Kimi the stratigraphic sequence of Pelagonian Zone ends up with the Maestrichtian to Paleocene flysch (Figs 8, 9 and 10). According to Katsikatsos et al. (1970), the flysch consists of shales, sandstones, and limestone intercalations, while it further includes serpentinized peridotite bodies and diabases. The flysch comprises siliclastic sandstones, shales and limestone blocks.

Roberston (1990), states that Kimi flysch has an Upper Cretaceous age. It consists of shales, sandstones with deformed zones, Maestrichtian limestone blocks, serpentinitic ultramafic bodies, ophicalcites and mafic lavas. The ultramafic rocks mainly include blocky or highly sheared serpentinites, and highly sheared serpentinized harzburgites as well. The blocky serpentinites are either overlain by the sheared ones or by ophicalcites filled with sparry calcite or pink limestone.

Faupl et al. (1996), studied the heavy minerals of the Kimi flysch sediments. They suggest that the flysch, is characterized predominantly by different mixtures of the zircon, titanite, rutile and apatite. That was interpreted that the flysch is associated with the closure of a Neotethyan Ocean in the Vardar Zone along the eastern margin of the Pelagonian Unit during the Early Tertiary, as has been described in the model of Robertson 1990. In Robertson's model the flysch corresponds to an accretionary prism which was emplaced above the eastern Pelagonian margin via a westwards tectonic movement In Robertson's model the flysch corresponds to an accretionary prism which was emplaced above the eastern Pelagonian margin via a westwards tectonic movement. However, the ophiolitic complexes in many Greek areas such as Evia have not been tectonically evolved to a high extent and as a result their mineral composition was minor influenced by the aforementioned Tertiary heavy minerals.

According to many researchers (e.g. Bernoulli and Laubscher, 1972; Kilias et al., 2010; Ferrière et al., 2012), the Western ophiolites in Greece are far travelled nappes that belong to Vardar Zone. In this scenario all the ophiolitic thrusts are Vardar-derived and so we could assume for the ophiolitic fragments/slices inside flysch formations. Such a flysch formation is the Beotian flysch in which many ophiolitic fragments have been recognized.

The Beotian basin was possibly placed between Pelagonian and Parnassos platforms, lying on the Western tip of Pelagonian microcontinent (Nirta et al., 2015 and references therein). The Beotian flysch in Levadia, Parnassos and Iti areas includes two turbiditic systems: the Lower Beotian flysch which presents a Jurassic-Cretaceous to Early Aptian age and the "Upper Beotian flysch" which has a Cenomanian to Coniacian age. In Levadia the flysch mainly includes calcareous turbiditic beds, calcarenites, marls and siliceous limestones, with minor serpentinized and chloritized ophiolitic fragments. From Levadia to Amfissa the Berriasian flysch includes debris flows dominated by ophiolitic rocks, while the transition between Parnassos Lower Aptian flysch and Levadia flysch, is characterized by debris flows rich in ultramafic

and radiolaritic fragments. According to Nirta et al. (2015), these three areas include the Lower Beotian flysch. On the other hand, the Upper Beotian flysch is exposed in Levadia-Amfissa transition and presents either a Late Albian or a Turonian to Coniacian age. In the first case it consists of sandstones, micritic limestones and conglomerates with serpentinitic fragments, while in the second case it includes reddish sandstones with marly and ophiolitic material as well.

But while Beotian flysch is of U. Jurassic – U. Cretaceous age, another flysch zone related to the Vardar Ocean and of Cretaceous–Paleocene age occurs in the other side of the Aegean and opposite to Evia, in western Turkey. This flysch zone is named the Bornova Flysch Zone and is an olistostrome–mélange belt located between the İzmir–Ankara Tethyan suture in northwest and the Menderes Massif in the southeast (Okay et al., 2012). The Bornova flysch consists of a sandstone-shale matrix and clasts, ranging from grains to blocks. The blocks are mainly Mesozoic limestones radiolarites and ophiolites. The ophiolites consist of serpentinized peridotites as well as gabbros and diabases. Based on geochemical data and stratigraphic features, the Bornova flysch was probably formed in a Tethyan oceanic basin. The ocean island type alkali basalts (Aldanmaz et al., 2008), as well as the presence of radiolarite blocks are indicative of an oceanic accretionary complex (Okay et al., 2012). Furthermore, the chert ages suggest that the İzmir–Ankara (Vardar) ocean was active during Cretaceous (Okay et al, 2012). Ankara subduction related ophiolitic mélange presents many similarities with Kimi flysch, since it consists of both continental sedimentary and oceanic material blocks, such as serpentinites (Festa et al., 2009).

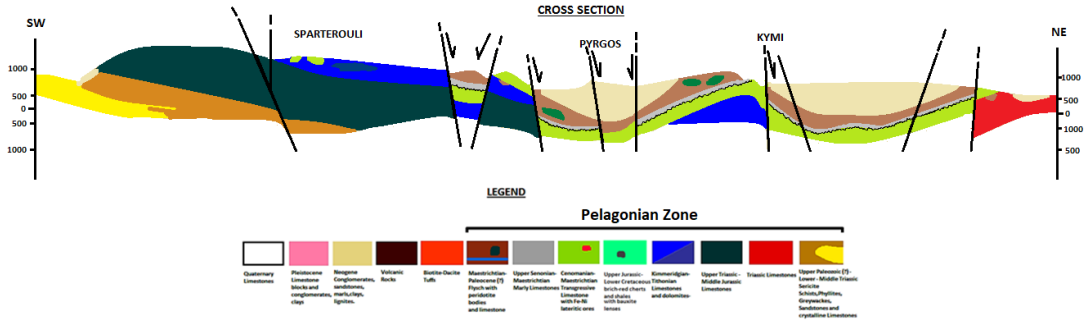

Figure 10. Geological SW-NE cross section and legend of Kimi (after Anastopoulos, 1962, Katsikatisos et al., 1970 IGME).

4 Field Work

Our field study was mainly focused on the ophiolitic ultramafic rocks (mostly serpentinites and serpentinitic harzburgites) associated with the Maestrichtian – Paleocene flysch and the rodingitic dykes that crosscut the ultramafic rocks in Choneftiko and Kalimeriani-Grammatikiani areas. Neither mafic dykes nor any kind of unaltered veins were found, whereas the volcanic rocks that Robertson (1990), described were not detected. The flysch succession consists of shales and sandstones and it is characterized by the presence of peridotitic bodies and limestone intercalations (Katsikatsos et al, 1970; Robertson, 1990), which is also consistent with our field study. Red colored shales overlie the white ones, while white colored shales overlie red colored mudstones (Fig. 14c). The typical sedimentary flyschoid lithologies overlie highly sheared serpentinitic bodies and usually alternate with small sized layers of red colored shales. Moreover, ophicalcite bodies including calcite veins of many generations were detected in Choneftiko area, as described by Paraskevopoulos and Kanakis (1972) and Robertson (1990). Ophicalcites usually contain lenses of red colored mudstones or underlie them, while they usually underlie Upper Cretaceous limestones. We also come to agreement with Robertson's observations, where highly sheared, clastic serpentinite overlies massive blocky serpentinite and underlies pelagic limestone successions, which are usually folded or chert layered. Serpentinized harzburgites are in contact with red colored sedimentary rocks and highly sheared serpentinitic blocks. The flysch presents a chaotic structure since there is no a clear strata continuity and presents many common features with an ophiolitic mélange that will be described below.

Figure 11. Kimi photograph from Choneftiko sampling location.

4.1 Sedimentary Rocks of Flysch

The studied sedimentary rocks in Kimi are parts of the U. Cretaceous-Paleocene flysch and include mainly shales of 5 to 7m thickness (Figs 12b, 14a and 15a,b), sandstones of 3m thickness (Fig. 14b), cherts and limestones. Carbonate rocks are mainly matrix supported limestones of 20m thickness, which are of an Upper Cretaceous age (Robertson, 1990) (Figs 12a and 13a) and they are present as intercalations in flysch. Limestones are often deformed and folded (Fig. 13a) and rarely enclose serpentinitic fragments (Fig. 13b), which means that the serpentinite was form earlier than limestone, that is earlier or during Upper Cretaceous. They overlie highly sheared serpentinitic bodies and underlie the brecciated limestone blocks. In their higher parts, siliceous limestone successions are present as well (Fig. 12c). Chert formations are red colored, including many subparallel quartz veins (Fig. 14d) and they are in contact with the highly sheared serpentinite presenting features of an ophiolitic mélange. Red colored turbiditic slumps are also present (Fig. 12d).

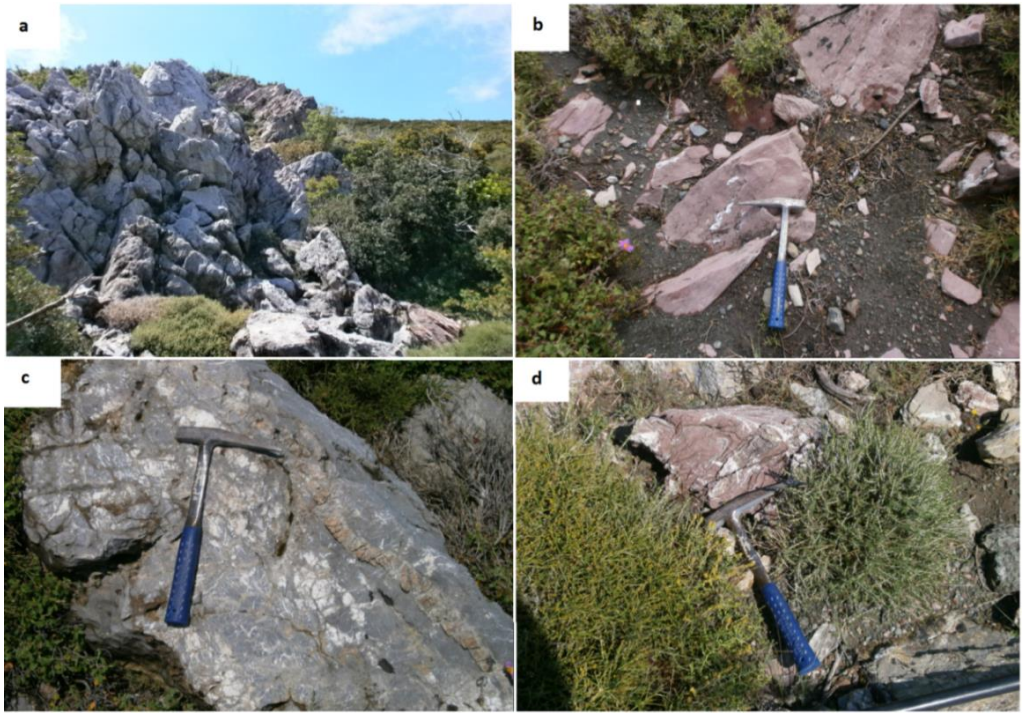

Figure 12. a. Brecciated Cretaceous limestones underlying limestones with red shale layers, b. red colored limestone, c. chert-layered limestones, d. Turbiditic slumps.

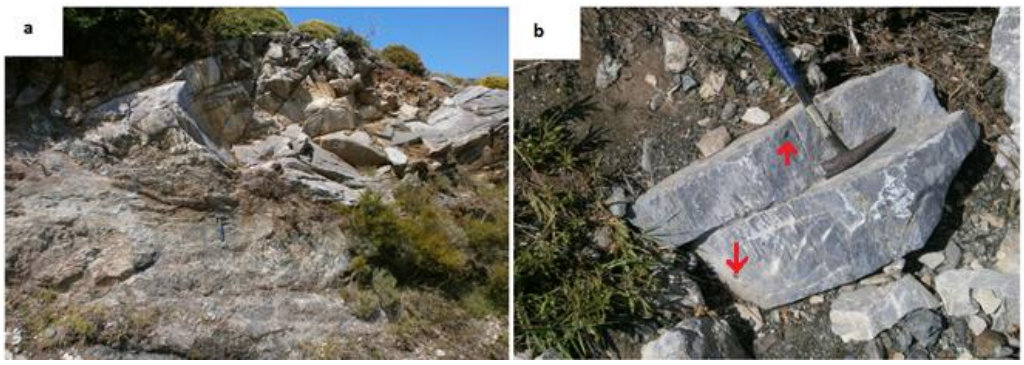

Figure 13. a. Upper Cretaceous folded neritic limestone overlying highly sheared serpentinite, b. Upper Cretaceous neritic limestone with serpentinitic breccias, near the contact with the underlying serpentinite body.

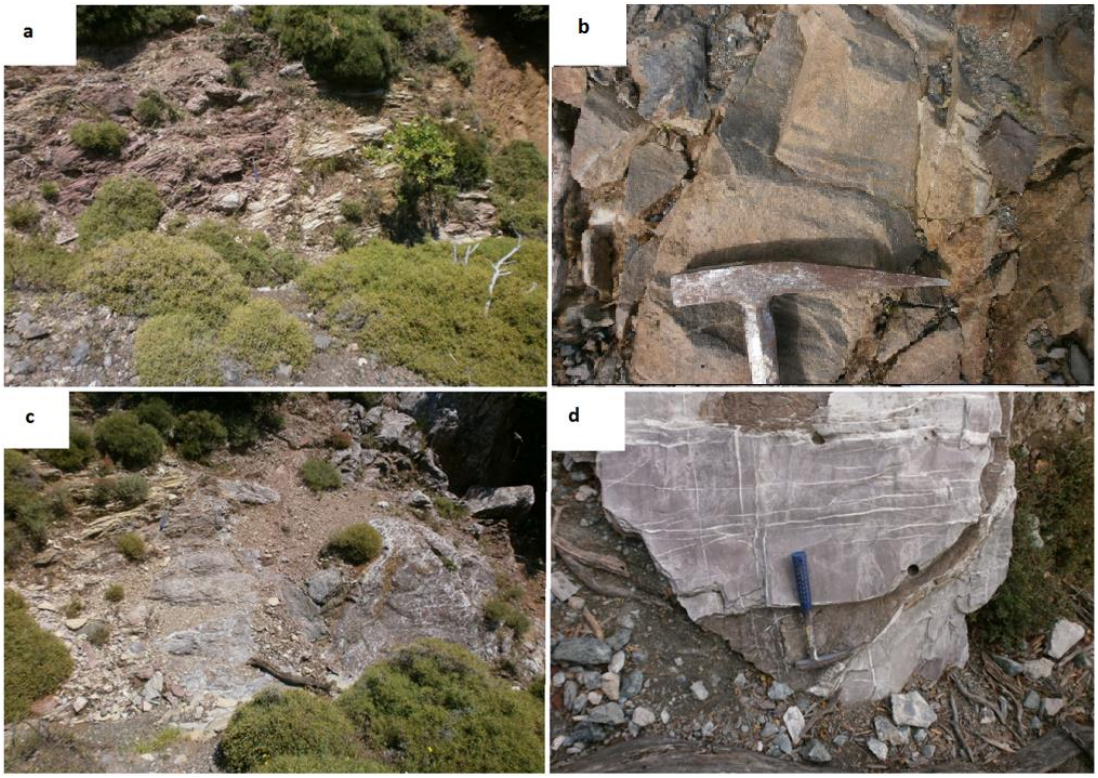

Figure 14 a. Red and white shales in contact, b.sandstone c., white shales overlying red colored mudstones, d. massive chert formation intruded by quartz veins of two generations

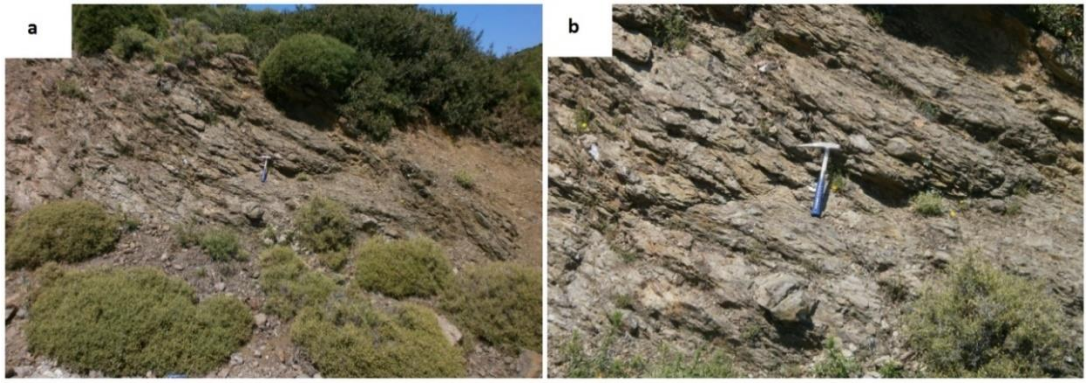

Figure 15 a.,b. Typical flysch formation consisting of red colored and white colored shales.

4.2 Ultramafic Rocks

The ultramafic rocks are serpentinized peridotites circa 200m thick, metasomatized serpentinites and chloritites. Serpentinized peridotites correspond to areas relatively away from the rodingitic dykes, while metasomatized serpentinites and chloritites correspond to areas near the contact with the rodingitic dyke. In Choneftiko area serpentinized peridotites appear as green to black colored deformed blocks presenting massive or cataclastic textures and containing numerous subparallel shear zones (Figs 16e,f and 17b,c,d). They include magnesite (Fig. 16c), pyroxenite (Fig 16d), and chrysotile veins (Fig. 16a), while dark-colored serpentinite is also developed within mylonitic zones of peridotitic blocks (Fig. 19a,b). On the other hand, serpentinized

peridotites in Kalimeriani-Grammatikiani are brown to yellow colored highly altered-lateritized with cataclastic textures (Figs 17a and 18). Chloritites thickness ranges from 15 cm to 0.5 m. They are massive and green colored exhibiting a gradual transition to the rodingite dyke. They are usually crosscutted by later formed calcite veins, or alternate with relict serpentine-rich zones of 2cm thickness. Chloritites can also contain garnet-fragments from the marginal rodingite zone, whereas numerous chlorite rich veinlets crosscut their matrix vertically to the dyke direction. On the other hand, the contact between the rodingite dyke and the metasomatic serpentinite is very sharp, while serpentinites are highly sheared and green colored, presenting mylonitic textures near the contact with the rodingite dyke.

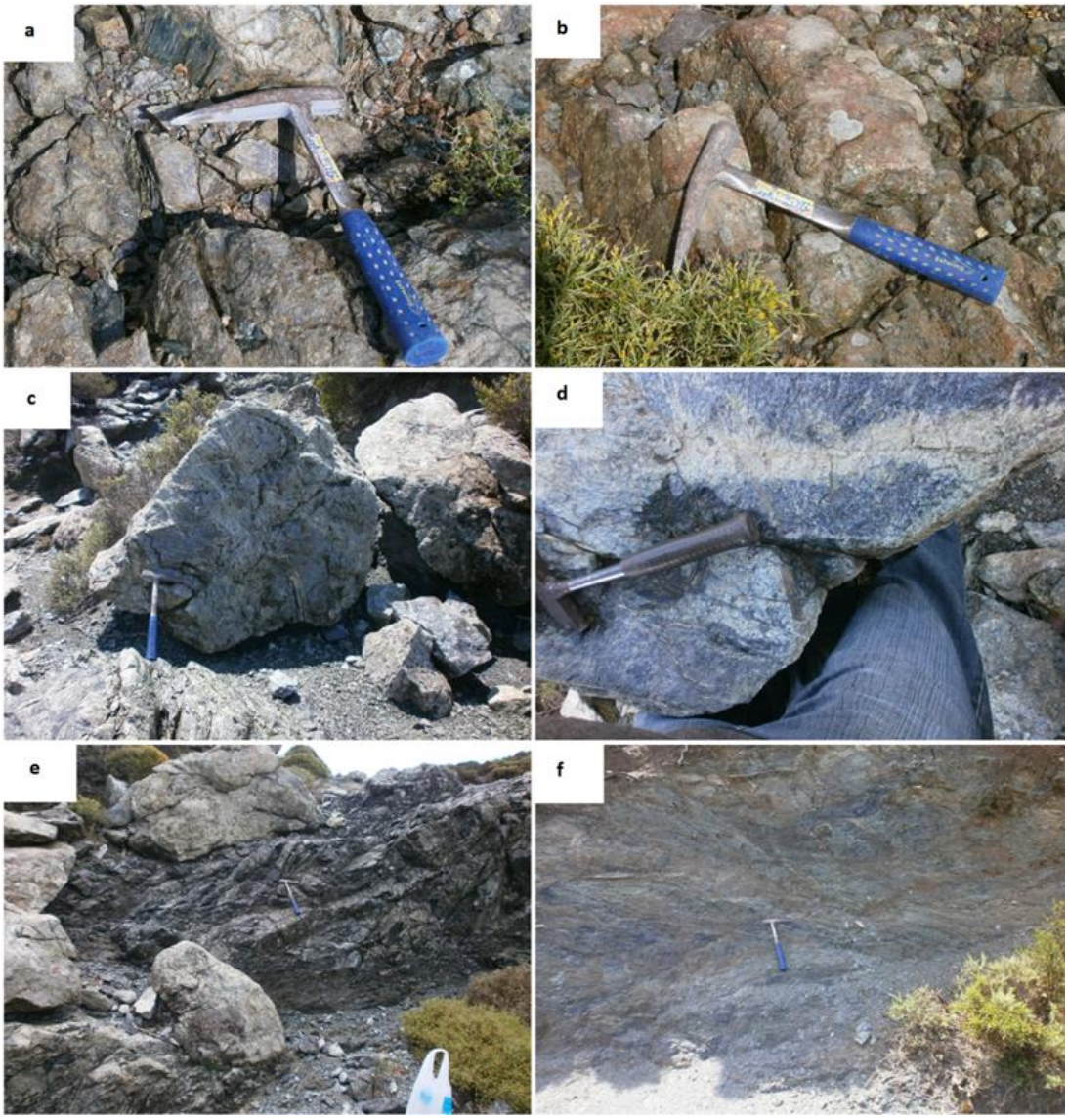

Figure 16. a. Green colored serpentinite with cross-fiber veins, b. serpentinite with bastite grains, c. green colored serpentinite with magnesite veins, d. pyroxenite vein inside a serpentinite body, e, f. highly sheared serpentinites.

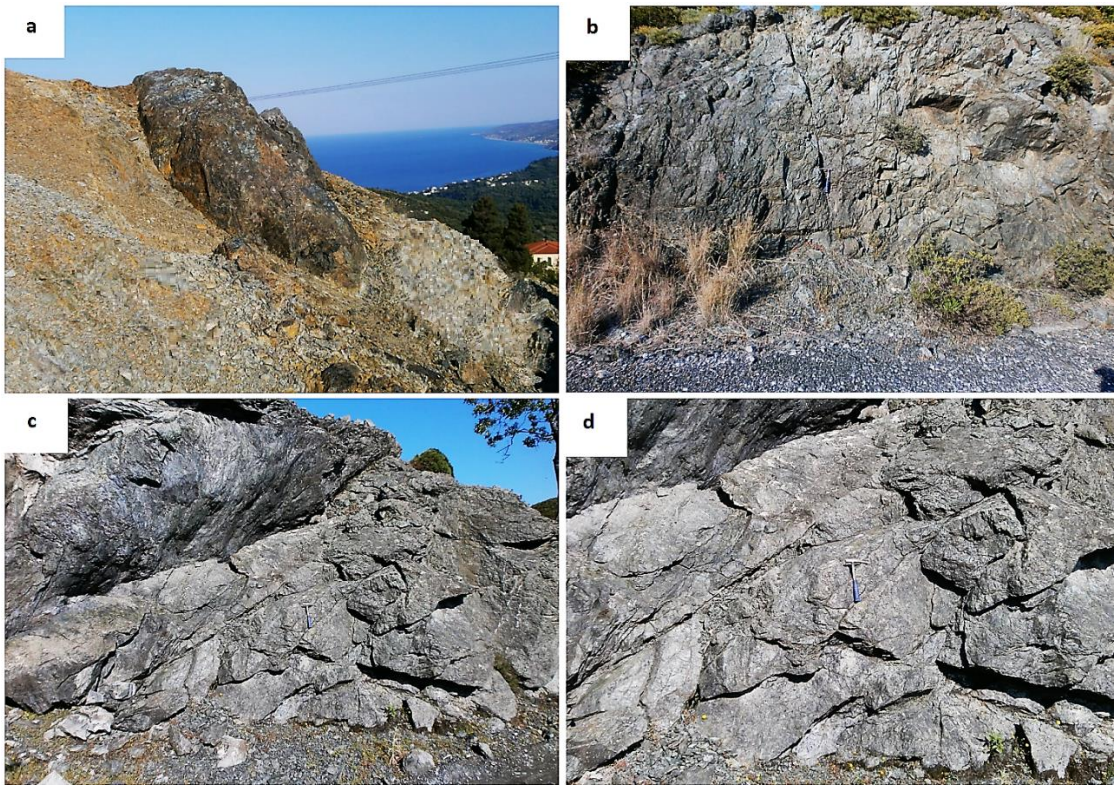

Figure 17. a., Massive serpentinite lens inside a cataclastic serpentinite mass, b. massive serpentinite body in Kalimeriani area, c.,d., shear zones in a serpentinitic mass.

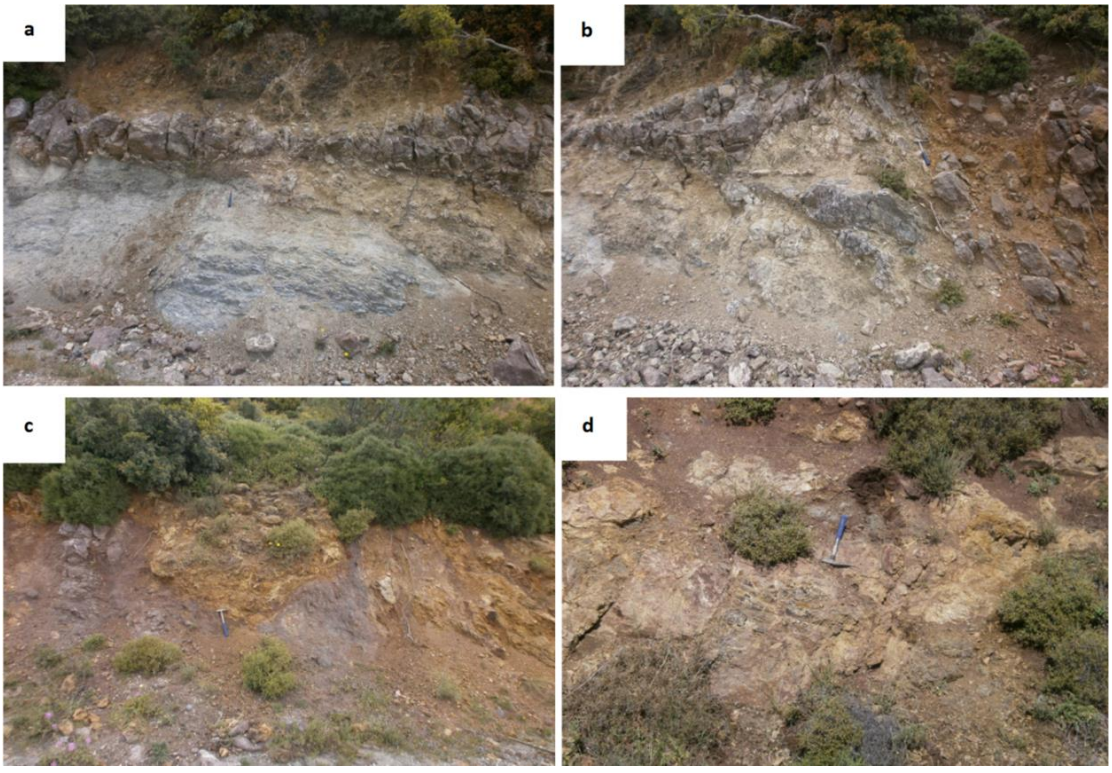

Figure 18. a.,b., Serpentinized peridotites overlying red colored mudstones and highly sheared serpentinite bodies. Serpentinitic bodies usually host red colored mudstone lenses. c.,d., Yellow to brown colored serpentinitic harzburgite with loose texture and lateritized surfaces

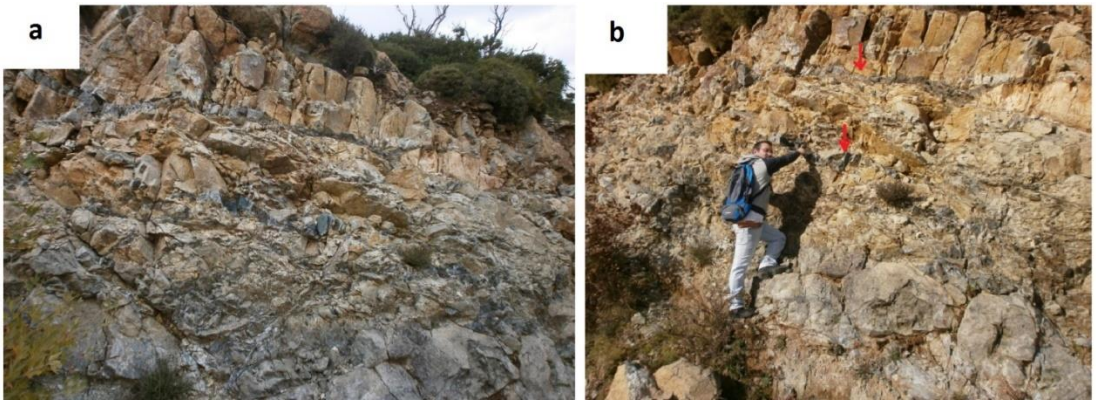

Figure 19 a,b, Highly altered dark colored serpentinite veins in mylonitized zone (Sample SERPVT) within a serpentinized peridotitic mass.

4.1 Ophicalcites

Ophicalcites (Figs 20 and 21) are massive green to black serpentinites crosscut by calcite veins of different generations, sizes and directions (Fig. 20d). Their thickness is ranging from 2.5 to 4.5 m.They are closely related with red colored brecciated mudstones, which are either in contact (Fig. 20a) or trapped within them giving a chaotic structure. According to their texture ophicalcites can be divided into three types. The first type includes typical ophicalcite rocks with numerous calcite veinlets (Figs 20b,c and 21a). The second type includes ophicalcites of 1.3 large veins (Fig. 20d), while the third one includes ribbon-type ophicalcites (Fig. 21d).

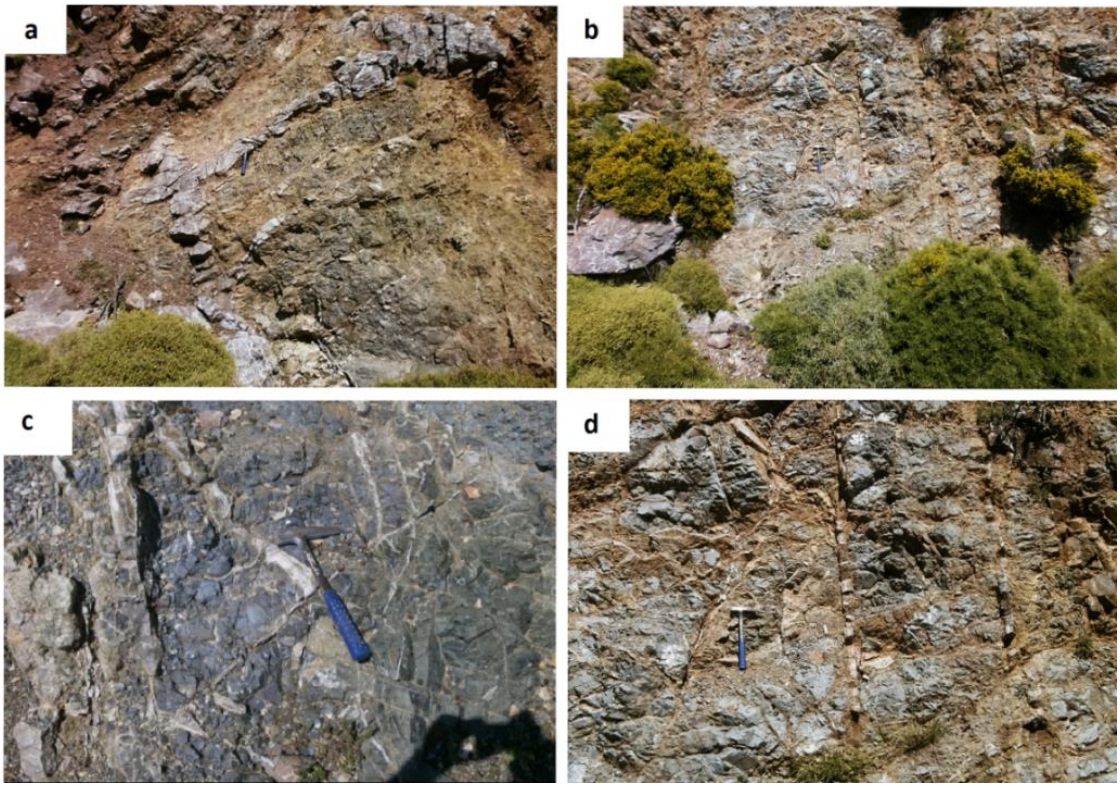

Figure 20 a. Ophicalcite (Sample SOPHAcc) overlain by red colored mudstones (Sample CAREDcc), b. an ophicalcite outcrop, c. calcite veins in an ophicalcite mass, d. ophicalcite with big sized veins of later generations.

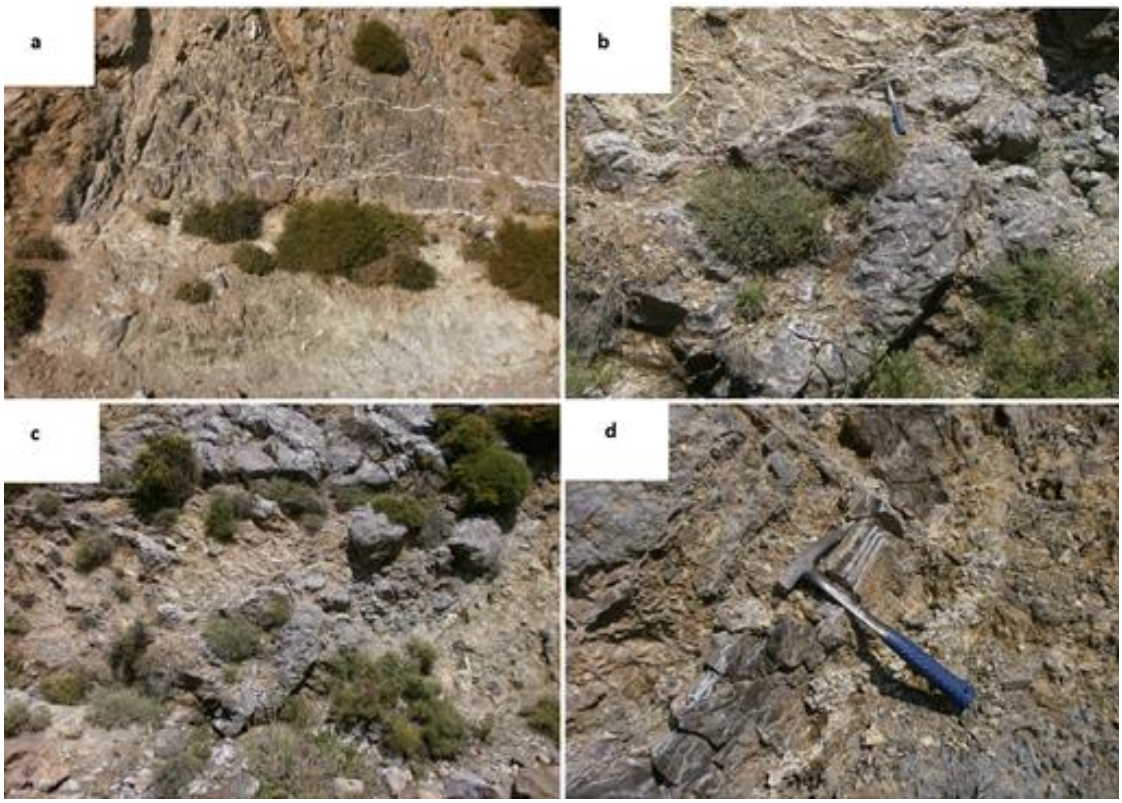

Figure 21. a., Sheared ophicalcite overlain by U. Cretaceous dark colored limestones with calcite veins, b., c. red colored limestone lenses inside an ophicalcite mass, d. ribbon-type ophicalcite (Sample ZTOPHcc).

4.2 Rodingites

Rodingite samples have been collected from Choneftiko and Kalimeriani/Grammatikiani areas near Kimi in four sampling sites. They appear as in situ dykes or smaller veins in serpentinitic bodies presenting NNE-SSW (Figs 22 and 27) or almost horizontal E-W (Figs 23 and 26) directions. Their thickness is ranging from 15cm to 2m. Rodingites are coarse-grained (usually rich in miarolitic calcite and chlorite crystal bearing cavities Fig. 30c,d) to aphanitic (mostly), zoned or patched in different colors, and consist mainly of garnet, vesuvianite, chlorite, diopside and occasionally calcite. As zoning seems to relate to various mineral assemblages, three different zones with gradual contacts were distinguished (Fig. 29). The core zone (CZ), where garnet and/or vesuvianite predominate, the marginal zone (MZ), which comprise assemblages enriched in chlorite and/or diopside, and the intermediate or transitional zone (TZ) consisting of all these four mineral phases. In most thick dykes all three zones are developed, whereas the transitional zone mainly occurs in thinner dykes or veins, where no different colored and well defined cores or margins exist. In some dykes euhedral or hypidiomorphic calcite crystals of sparitic size are abundant. Veinlets of different generations and mineralogical assemblages (mono-minerallic or not) are usually crosscut the rodingite dykes. These veinlets are usually developed perpendicular to the margins of the dykes, although veinlets of any random direction occur. In vesuvianite-rich dykes the cores tend to be white with pink or purple colored patches due to the high amounts of garnet and vesuvianite respectively. Rodingites are found as massive-hard rocks (e.g. Fig 28), brecciated (Fig. 24b), sheared (Fig. 24a) or heavily cataclastic (Figs 26c,d and 27). The last three types of rodingite indicate deformation of dykes in a brittle environment following the metasomatic event. On

the other hand, the massive dykes seem to be rich in vesuvianite and calcite, while the cataclastically fractured ones vesuvianite and calcite are in very low amounts or completely absent.

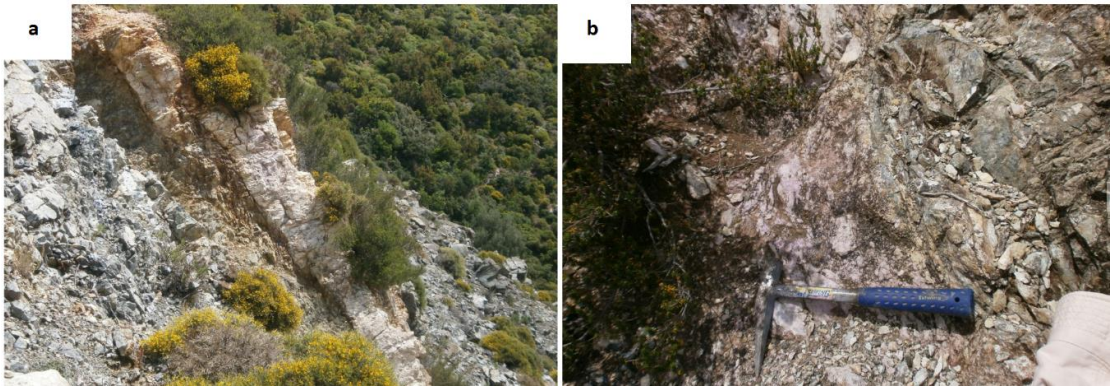

Figure 22. In situ rodingite vein with NNE-SSW direction, in a serpentinitic body in Choneftiko area. b. pink colored rodingite core in Choneftiko area with cataclastic texture.

Figure 23. In situ rodingite vein rich in calcite, in a serpentinitic body in Choneftiko area with E-W direction and massive texture (SamplesEROD26).

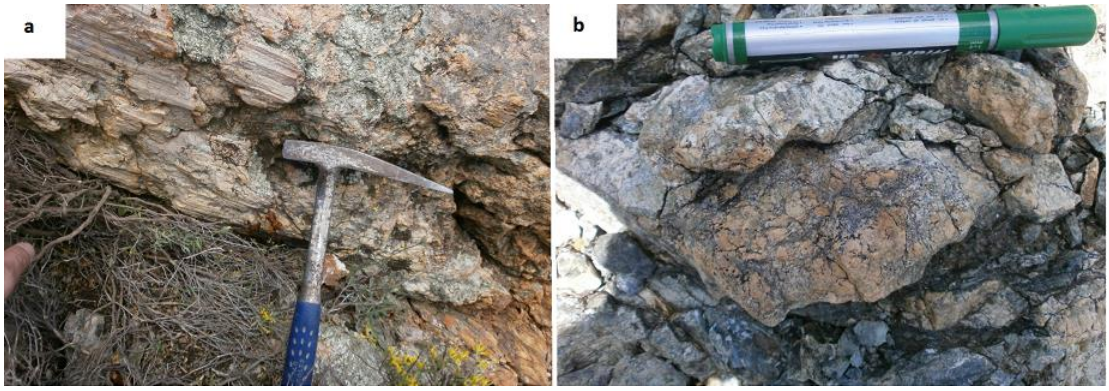

Figure 24. a. Shears in rodingite body, b. Brecciated rodingite in Choneftiko village.

Figure 25. . Rodingite bodies in Choneftiko area presenting oxidized brown colored crust surface

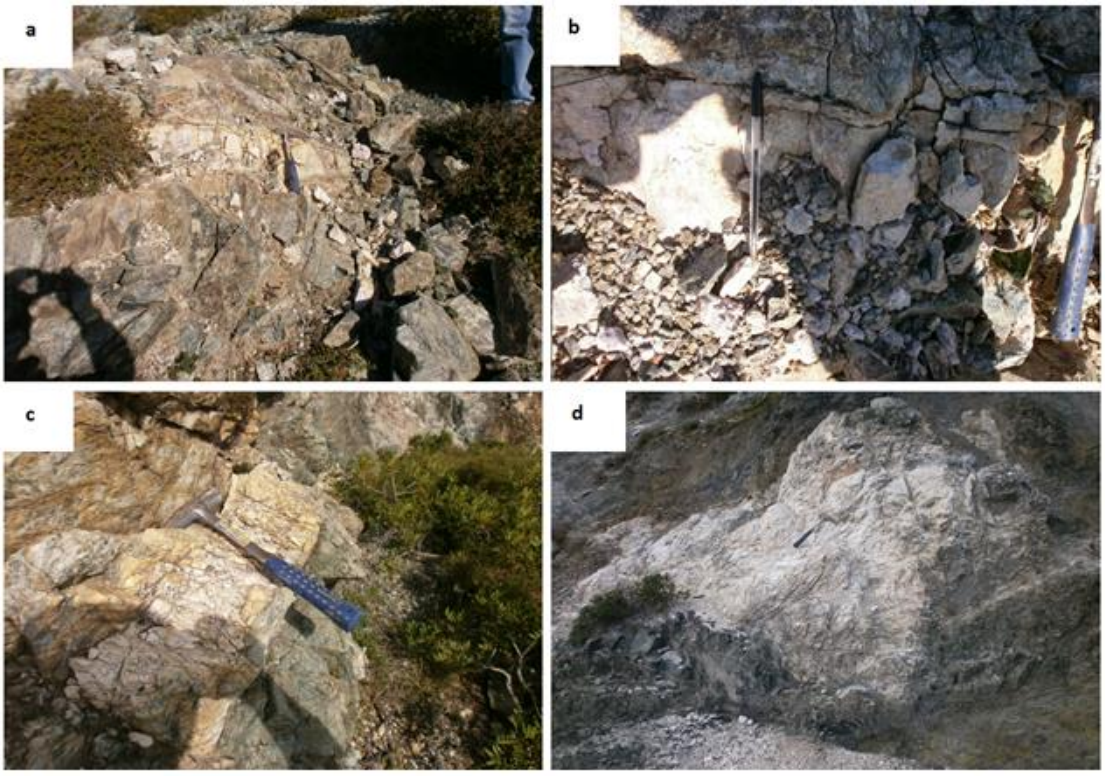

Figure 26a, b. E-W rodingite vein rich in chlorite (Samples EROD22), with cataclastic texture in Choneftiko area., c. E-W rodingite vein (Samples EROD23) with cataclastic texture rich in garnet and diopside, in Choneftiko area d. E-W Rodingite vein (Sample EROD18) with cataclastic texture rich in garnet and diopside in Choneftiko area.

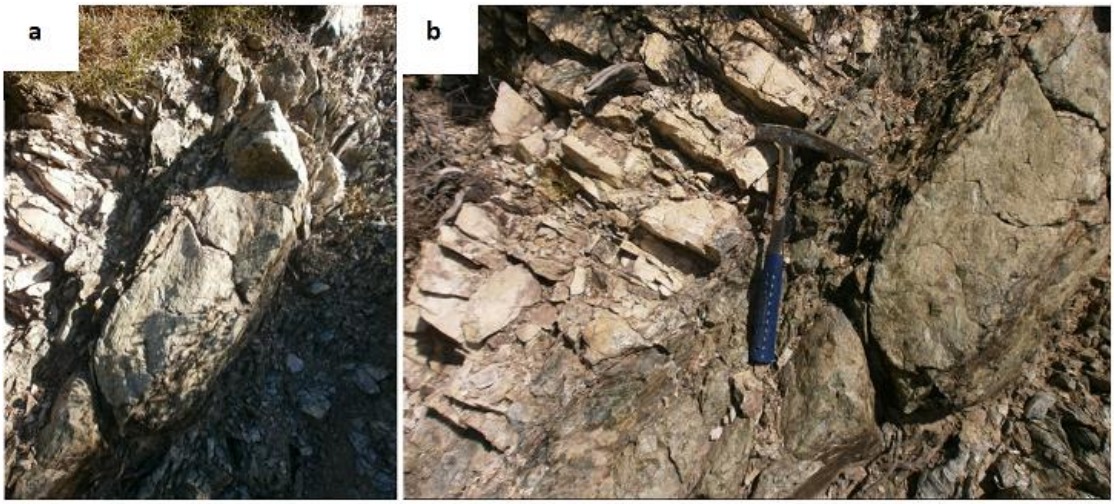

Figure 27.a., b., NNE-SSW Rodingite vein (Marginal Sample EROD6-Core Sample EROD7) rich in garnet and vesuvianite with massive texture inside serpentinitic body (Sample SERP6-7).

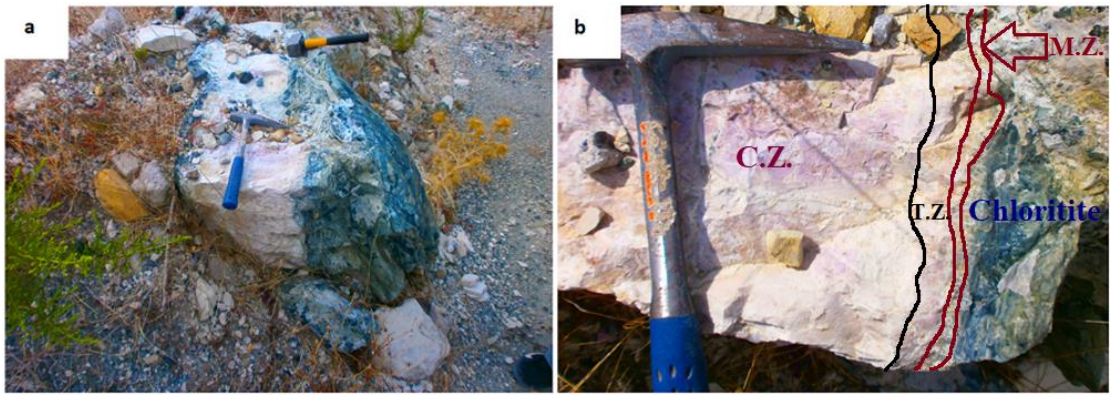

Figure 28. Rodingite dyke (Samples EROD7S) in serpentinitic body in Kalimeriani-Grammatikiani area, b. Close up of the rodingite dyke showing zoning, veinlets and patches. A green-chlorite rich marginal zone is followed gradually by a yellowish garnet-diopside rich zone and a purple and white vesuvianite-garnet-rich core. The thickness of the external zones is variable 1 to 3 cm, while the inner one is greater occupying most of the rodingite dyke. The core is inhomogeneous consisting of white/garnet-rich and purple/vesuvianite-rich patches and veinlets. M.Z.: Marginal Zone, T.Z.: Transitional Zone, C.Z.: Core Zone.

For a more detailed study of the zones and other internal features of the rodingite dykes, several big samples were collected and large slabs where studied macroscopically (Figs 30, 31, 32 and 33). Thus, it is furthermore confirmed the vast majority of Kimi rodingites are highly zoned. The zones are usually inhomogeneous, consisting of patches of different prevailing minerals with characteristic colors.

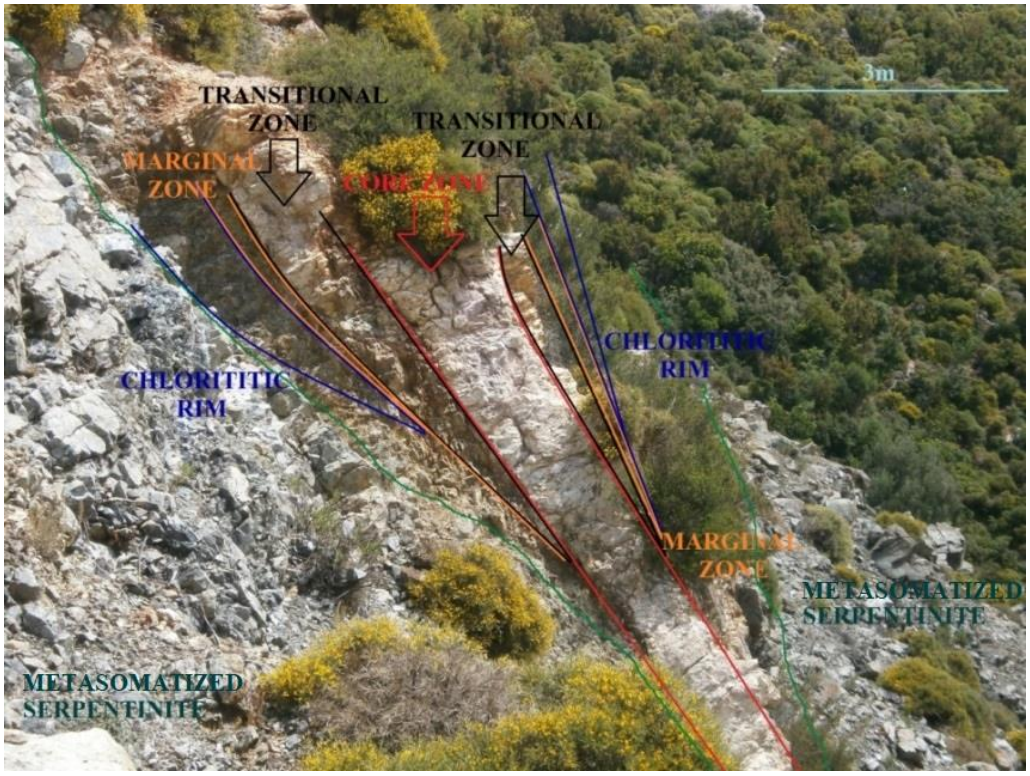

Figure 29. Complete rodingite zoning with garnet-vesuvianite rich core, garnet-vesuvianite-diopside-chlorite rich transitional zone and chlorite-diopside rich marginal zone. Chloritititic rim and metasomatized serpentinite host rock are also observed.

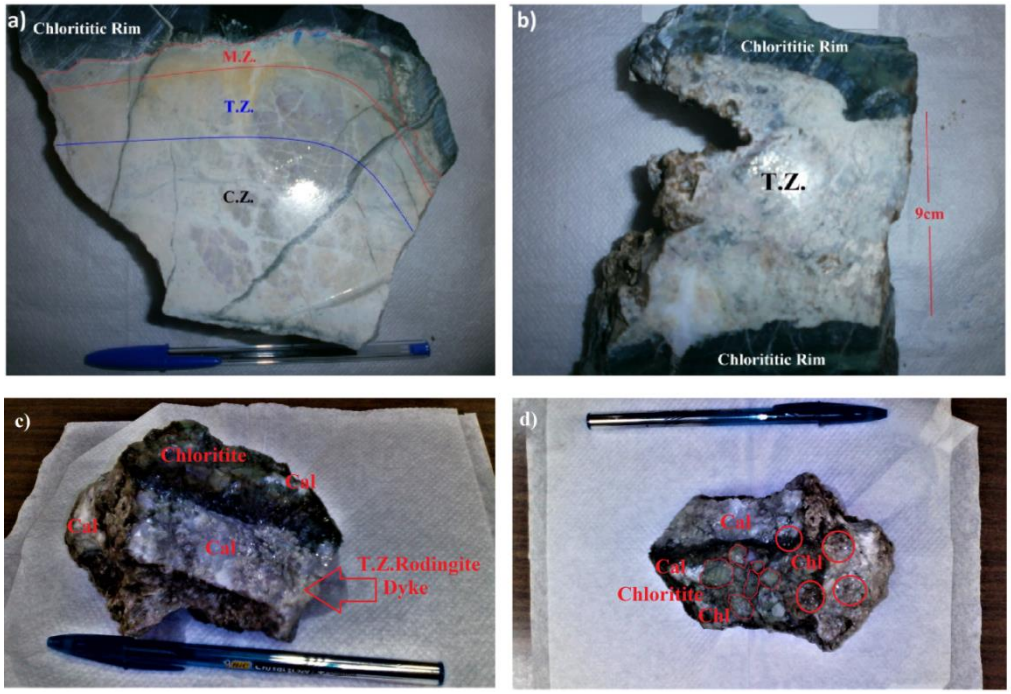

Figure 30. Macroscopic examination of sample EROD7S and EROD12 from Kalimeriani-Grammatikiani and Choneftiko are respectively. Chl for chlorite, Di for diopside, Grt for garnet and Ves for vesuvianite. M.Z.: Marginal Zone, T.Z.: Transitional Zone, C.Z.: Core Zone. c,d. TZ Rodingite dyke (Sample EROD12) consisting of calcite (Cal) cavities. Chlorite (Chl) appears in the chloritititic rims as green colored crystals or as silver colored small sized booklet chlorite grains.

Figure 31. Macroscopic image of rodingite with vesuvianite (purple) and garnet rich points (white colored) (Sample EROD11).

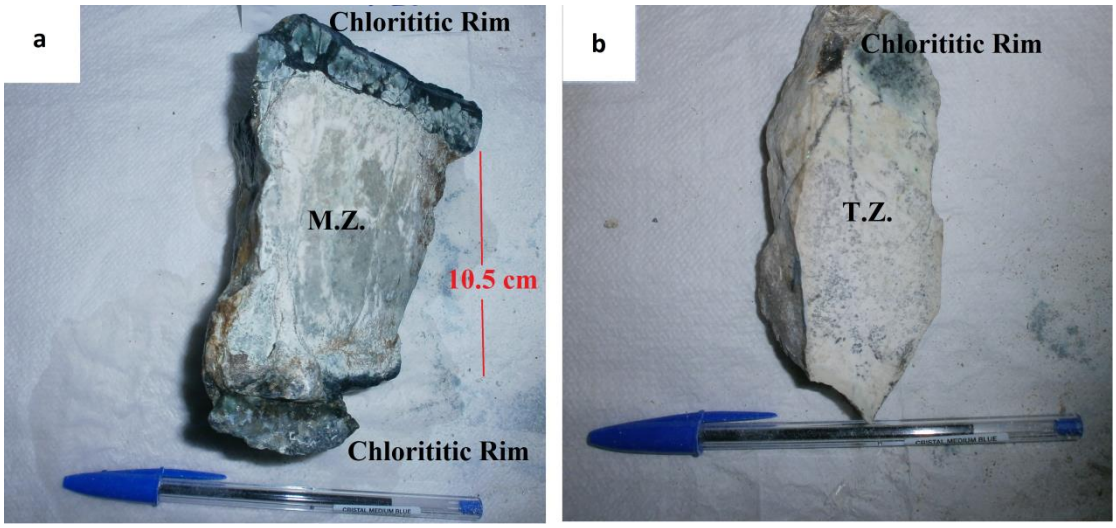

Figure 32. a. Rodingites with chlorite rich rims with garnet breccias and garnet-diopside rich cores (Sample EROD10), b. rodingite with garnet-diopside rich core and chlorite rich zone respectively (Sample EROD7).M.Z.:Marginal Zone, T.Z.: Transitional Zone.

Figure 33. Rodingite sample (EROD18) with cataclastic texture and green colored chlorite veins.

4.3 Talc Schists

Talc schists are present as big or small sized sheets in contact with highly sheared and deformed serpentinitic masses with cataclastic texture. Their thickness is ranging from 20 cm to 1m. They are white, grey (Fig. 34a,b) or green colored (Fig. 34c) and show generally E-W direction. They can be observed both in Choneftiko (Fig. 34a, b, c) and Kalimeriani areas (Fig. 34d).

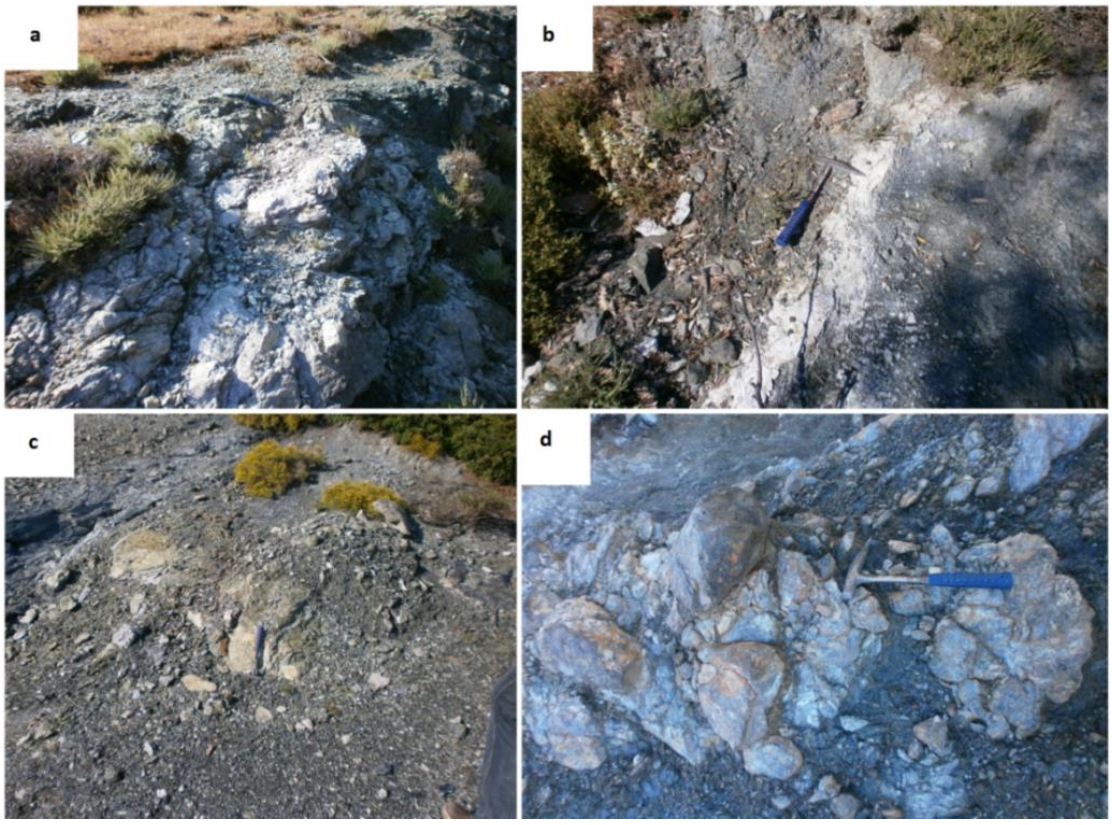

Figure 34. a Talc schist white colored vein inside highly sheared serpentinite, b., Talc schist small sized white colored vein inside serpentinite in Choneftiko area, c. Green colored talc inside serpentinite in Kalimeriani area, d. Talc body intrusion with cataclastic texture inside serpentinitic body in Kalimeriani area.

5 Analytical Methods

For our study nineteen rodingite samples, eight ultramafic samples and plenty samples from the aforementioned lithologies were collected. The rodingitic samples correspond to twelve rodingitic dykes (Table 1). The majority of them were collected from Choneftiko area, while one chloritite, two serpentinized peridotites and one rodingite samples were collected from Kalimeriani-Grammatikiani villages.

Table 1. Rodingite and Ultramafic Samples with their Sampling Sites

Rod. Dykes	Rodingite			Ultramafics			Location	Longtitude	Latitude	Sampling Site
	Core (Inner) Zone	Transitional (Mid) Zone	Marginal (Outer) Zone	Chloritite	Garnet Metasomatized Serpentinite	Serp. Peridotite				
1	EROD11						Kimi-Choneftiko	240927	386502	1
2	EROD21									
3		EROD6, EROD7			SERP6-7		Kimi-Choneftiko	240933	386457	2
4			EROD10				Kimi-Choneftiko	241013	386460	3
5		EROD12		SERPV12R, SERPV12RR			Kimi-Choneftiko	240925	386473	4
6	EROD18						Kimi-Choneftiko	240917	386470	5
7		EROD22L	EROD22M		SERP22		Kimi-Choneftiko	240938	386461	6
8	EROD23M	EROD23R			SERP25		Kimi-Choneftiko	240925	386500	7
9	EROD25, EROD25L									
10			EROD24M, EROD24R							
11	EROD26M		EROD26L				Kimi-Choneftiko	240290	386506	8
12		EROD7SC	EROD7SCC	EROD7SR		SERPEG, SERPEL	Kimi-Kalimeriani	240901	386220	9

The petrographic study was performed at the Department of Mineralogy and Petrology of National and Kapodistrian University of Athens. For the petrographic examination of the rodingite dykes twenty-six thin sections were prepared corresponding to different positions of a dyke. More specifically they correspond to marginal positions, marginal to core transitions and clearly core positions of the rodingitic dyke. On the other hand, eight thin sections from seven ultramafic rock samples were made and petrographically studied.

X-ray examination was conducted at the Department of Mineralogy and Petrology of the National and Kapodistrian University of Athens using a Siemens Model 5005 X-ray diffractometer, Cu Ka radiation at 40 kV, 40 nA, 0.020 step size and 1.0 s step time. Representative samples from the different positions of the rodingite dykes, serpentinitic samples as well as chloritites were prepared for XRD-analyses. More specifically twenty-six rodingitic and seven ultramafic samples were analyzed. The mineral phases were identified with the use of EVA® 2.2 program of the Siemens DIFFRAC and the D5005 software package.

Whole rock chemical analyses were conducted at ACME Laboratories in Canada using ICP-MS method for major, trace and rare earth elements. Their upper and lower detection limits for major elements, trace elements and REE are given in Table 2. The analyzed samples include nineteen rodingite samples and six ultramafic samples.

Mineral chemical analyses were carried out at the Department of Mineralogy and Petrography of the Institute of Geological and Mineral Exploration of Greece (IGME), using a JEOL-JSM 5600, with associated Energy Dispersive Spectroscopy analyzer (SEM-EDS). One CZ sample (EROD 11) two MZ samples (EROD24R, EROD22M) and three TZ samples (EROD23R, EROD12, EROD7SC) were analyzed using SEM.

Table 2. Upper and lower detection limits for major elements, trace elements and REE of ACME Lab ICP-MS analyses.

ELEMENT	DETECTION LIMIT	UPPER LIMIT
SiO_2	0.01 %	100 %
Al_2O_3	0.01 %	100 %
CaO	0.01 %	100 %
Cr_2O_3	0.002 %	100 %
Fe_2O_3	0.04 %	100 %
K_2O	0.01 %	100 %
MgO	0.01 %	100 %
MnO	0.01 %	100 %
Na_2O	0.01 %	100 %
P_2O_5	0.01 %	100 %
TiO_2	0.01 %	100 %
Ba	5 ppm	5 %
Nb	5 ppm	10,000 ppm
Ni	20 ppm	10,000 ppm
Sc	1 ppm	10,000 ppm
Sr	2 ppm	50,000 ppm
Y	3 ppm	50,000 ppm
Zr	5 ppm	50,000 ppm
LOI	0.1 %	100 %
Sum	0.01 %	100 %
Ce	30 ppm	50 000 ppm
Co	20 ppm	10 000 ppm
Cu	5 ppm	10 000 ppm
Zn	5 ppm	10 000 ppm
Ba	1 ppm	50,000 ppm
Be	1 ppm	10,000 ppm
Ce	0.1 ppm	50,000 ppm
Co	0.2 ppm	10,000 ppm
Cs	0.1 ppm	10,000 ppm
Dy	0.05 ppm	10,000 ppm
Er	0.03 ppm	10,000 ppm
Eu	0.02 ppm	10,000 ppm
Ga	0.5 ppm	10,000 ppm
Gd	0.05 ppm	10,000 ppm
Hf	0.1 ppm	10,000 ppm
Ho	0.02 ppm	10,000 ppm
La	0.1 ppm	50,000 ppm
Lu	0.01 ppm	10,000 ppm
Nb	0.1 ppm	10,000 ppm
Nd	0.3 ppm	10,000 ppm
Pr	0.02 ppm	10,000 ppm
Rb	0.1 ppm	10,000 ppm
Sm	0.05 ppm	10,000 ppm
Sn	1 ppm	10,000 ppm
Sr	0.5 ppm	50,000 ppm
Ta	0.1 ppm	10,000 ppm
Tb	0.01 ppm	10,000 ppm
Th	0.2 ppm	10,000 ppm
Tm	0.01 ppm	10,000 ppm
U	0.1 ppm	10,000 ppm
V	8 ppm	10,000 ppm
W	0.5 ppm	10,000 ppm
Y	0.1 ppm	50,000 ppm
Yb	0.05 ppm	10,000 ppm
Zr	0.1 ppm	50,000 ppm
Ag	0.1 ppm	100 ppm
As	0.5 ppm	10,000 ppm
Au	0.5 ppb	100,000 ppb
Bi	0.1 ppm	2,000 ppm
Cd	0.1 ppm	2,000 ppm
Cu	0.1 ppm	10,000 ppm
Hg	0.01 ppm	50 ppm
Mo	0.1 ppm	2,000 ppm
Ni	0.1 ppm	10,000 ppm
Pb	0.1 ppm	10,000 ppm
Sb	0.1 ppm	2,000 ppm
Se	0.5 ppm	100 ppm
Tl	0.1 ppm	1,000 ppm
Zn	1 ppm	10,000 ppm

Geochemical isotope analyses were conducted in calcites from six calcite samples (Table 3). Calcite was separated by hand-picking under stereoscopic microscope from two rodingite dykes (sampling sites a and b) two ophicalcite samples (sampling sites c) and two red mudstones (sampling site d), in order to examine the origin of O and C in relation with meteoric, seawater of magmatic-metamorphic derived fluids (as discussed in the next chapters), studying both the metamorphic-metasomatic and sedimentary lithologies of Kimi area.

Table 3. Rodingite, Ophicalcite and Sedimentary rocks with their calcite samples used for O-C isotope analyses and their sampling sites.

Sampling Site	Rock Type	Rock Sample	Calcite Sample	Longtitude	Latitude
a	Rodingite	EROD12	EROD12cc	240925	386473
b	Rodingite	EROD7SCC	EROD1Mcc	240901	386220
c	Ophicalcite	SOPHA	SOPHAcc	240522	383853
	Ophicalcite	ZTOPH	ZTOPHcc		
d	Red Mudstone	CARED	CAREDcc	240521	383854
	Red Mudstone	CARED 2	CARED2cc		

Our analyses were conducted in GeoZentrum Nordbayern Labs (Germany). For these analyses calcite was reacted with 100% phosphoric acid at 70°C using a Gasbench II

connected to a ThermoFisher Delta V Plus mass spectrometer. All values are reported in per mil related to V-PDB. Reproducibility and accuracy was monitored by replicate analysis of laboratory standards calibrated by assigning $\delta^{13}C$ values of +1.95‰ to NBS19 and -46.6‰ to LSVEC and $\delta^{18}O$ values of -2.20‰ to NBS19 and -23.2‰ to NBS18. Reproducibility for $\delta^{13}C$ and $\delta^{18}O$ was ±0.0x and ±0.0y respectively.

6 Petrography

6.1 Rodingites

Rodingite petrography and geochemistry (see below) were accomplished by the study of marginal, core and transitional areas of the rodingitic dykes, permitting us to detect any possible change of their mineral assemblages and fluid chemistry in a direction perpendicular to the sides of rodingite dykes. As calcite is present in some of the dykes and taking in mind its importance, because it is directly related to the nature and physicochemical conditions of the metasomatic processes (see discussion), an additional division for the studied rodingites was used. These two groups, namely Group I and Group II, correspond to non-carbonated and carbonated rodingite dykes respectively (Table 4).

Table 4. Discrimination of Kimi rodingites into Group-I and Group-II based on their main mineral assemblage. Rodingite Zone division into: Core Zone, Transitional Zone and Marginal Zone.

Sampling Site	Rod. Dyke	Sample	Group	Rodingite Zone	Main Mineral
1	1	EROD11	Group-II	Core	Ves
5	6	EROD18	Group-II	Core	Grt
1	2	EROD21	Group-I	Core	Ves
7	8	EROD23M	Group-I	Core	Grt
7	9	EROD25	Group-I	Core	Grt
7	9	EROD25L	Group-I	Core	Grt
8	11	EROD26M	Group-I	Core	Ves
6	7	EROD22M	Group-II	Marginal	Chl
7	10	EROD24M	Group-I	Marginal	Di
7	10	EROD24R	Group-I	Marginal	Di
8	11	EROD26L	Group-I	Marginal	Di
9	12	EROD7Scc	Group-II	Marginal	Di
3	4	EROD10	Group-II	Marginal	Chl
6	7	EROD22L	Group-II	Transitional	-
7	8	EROD23R	Group-I	Transitional	-
2	3	EROD6	Group-I	Transitional	-
2	3	EROD7	Group-I	Transitional	-
9	12	EROD7SC	Group-II	Transitional	Cal
4	5	EROD12	Group-II	Transitional	-

The study under polarized and electron microscopy, as well as XRD analyses, confirm the macroscopic observation of different mineral assemblages between core and margins of the rodingite dykes. Thus, samples from the CZs are enriched in vesuvianite and garnet samples from MZs are enriched in chlorite and diopside, while samples from TZs consist of all the aforementioned mineral phases in different proportions (Table 4). Samples from all three zones may or may not contain calcite.

This petrographic and macroscopic distinction of rodingite areas is also reflected into their chemistry (see Chapter 8).

6.1.1 Group-I Non-Carbonated Rodingites

This rodingite group includes samples EROD6, EROD7, EROD21, EROD23M, EROD23R, EROD24M, EROD24R, EROD25, EROD25L, EROD26M and EROD26L

6.1.1.1 Rodingite Core Zones

Samples EROD21, EROD23M, EROD25, EROD25L and EROD26M belong to this zone of Group-I rodingites. Their mineral assemblage mostly comprises garnet and vesuvianite which is also confirmed by XRD patterns of Samples EROD21 and EROD23M (Figs 36 and 37), but usually in unequal amounts. As a result the cores can usually be garnet or vesuvianite rich. Accessory minerals are found in both garnet and vesuvianite rich varieties and include chlorite, diopside, prehnite and opaque Fe-Ti oxides as well. Their texture ranges from cryptocrystalline consisting of a garnet-vesuvianite rich groundmass to fine grained consisting of idiomorphic usually zoned garnet and vesuvianite crystals of 200-250μm and 130μm size respectively (Fig. 35a,b,c). Chlorite and diopside can either occur intergranular between garnet crystals (Fig. 35d), while microcrystalline garnet veinlets of later generation with various directions crosscut the groundmass.

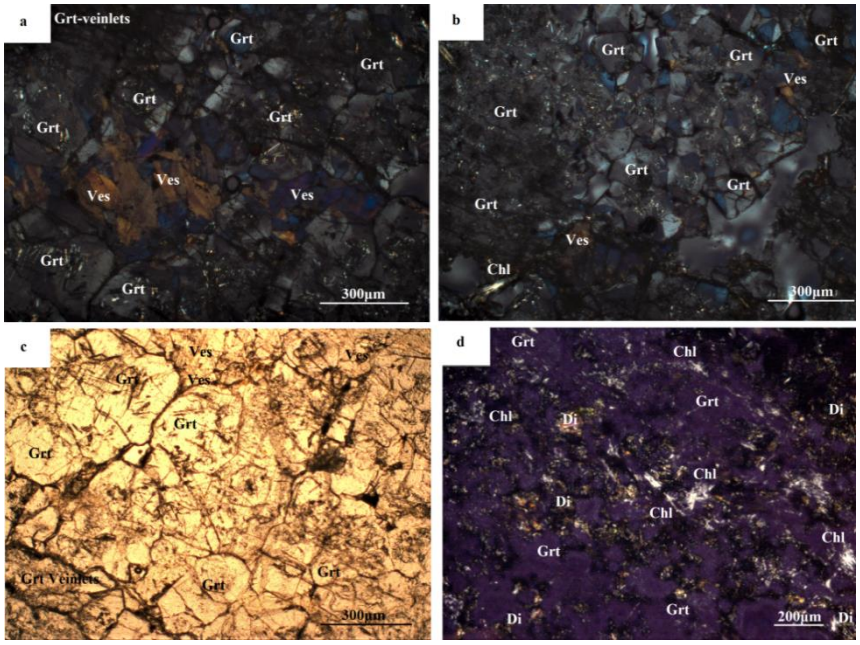

Figure 35. Group-I Core Zone photomicrographs. a.,b. XPL photomicrograph of Garnet-Vesuvianite groundmass (Sample EROD23M), c. PPL photomicrograph of Garnet rich Core Zone, d. Garnet rich groundmass. Diopside and Chlorite appear intergranular between garnets. Grt: Garnet, Ves: Vesuvianite, Chl: Chlorite, Di: Diopside.

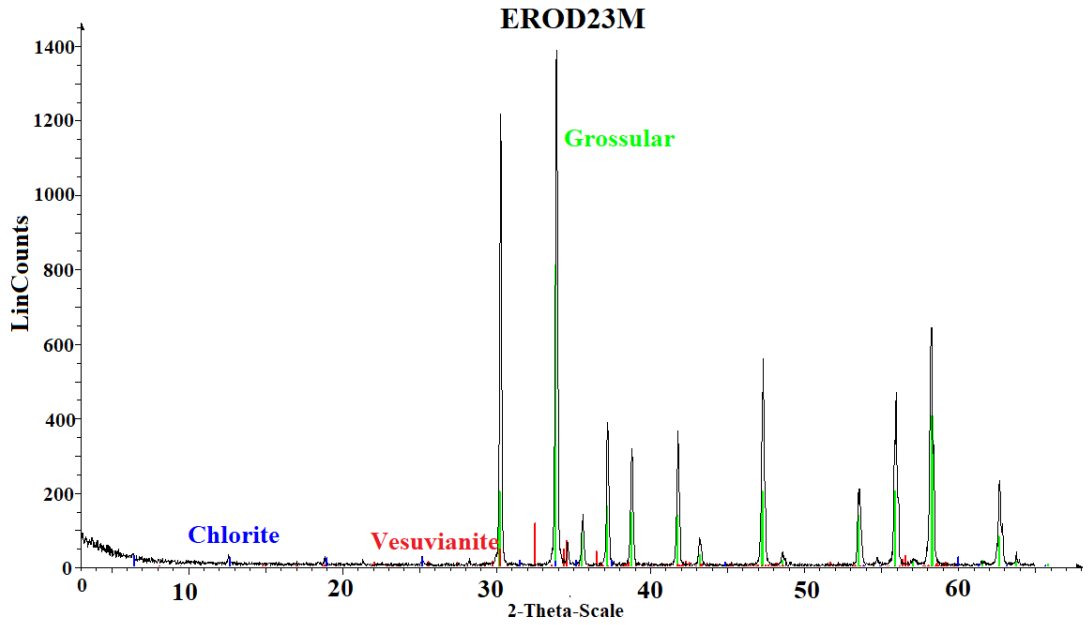

Figure 36. XRD pattern of a CZ Group-I grossular-rich sample (EROD23M). Vesuvianite and chlorite are present in lesser amounts.

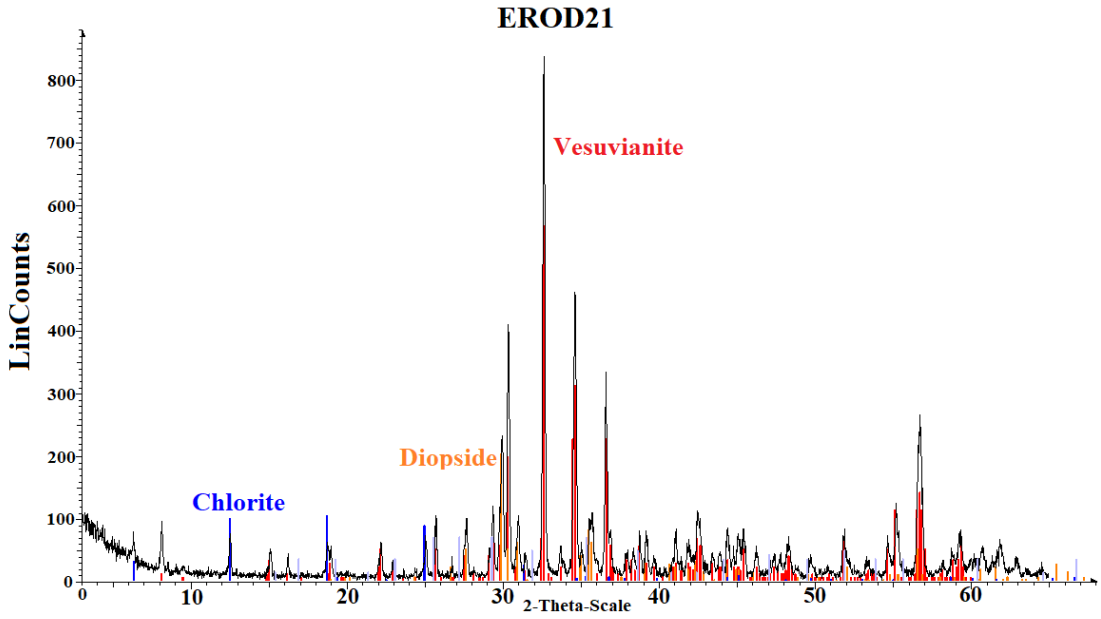

Figure 37. XRD pattern of a CZ Group-I vesuvianite-rich sample (EROD21). Diopside and chlorite are present in lesser amounts.

6.1.1.2 Rodingite Marginal Zone

Samples, EROD24M, EROD24R and EROD26L correspond to this zone. They are chlorite and/or diopside-rich also confirmed by XRD pattern of Sample EROD24M (Fig. 40), while accessory minerals include garnet, vesuvianite and Fe-Ti-opaque minerals. Their texture is microcrystalline, consisting of chlorite and diopside grains (Fig. 38a), while chlorite rich matrix (Fig. 39) is often crossed by younger fine-grained chlorite veins of 300 μm vein size (Fig. 38b). Diopside occurs along with cryptocrystalline garnet and chlorite.

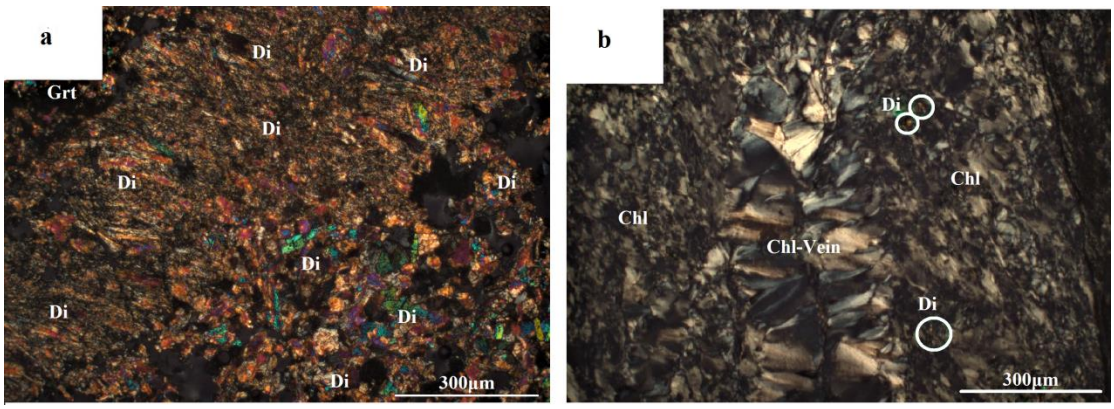

Figure 38. Group-I M.Z. rodingite photomicrograph (Sample EROD24M) consisting of diopside (Di) matrix with cryptocrystalline garnet (Grt) grains. b. Chlorite rich area in Group-I Rodingites (Sample EROD24M) with a chlorite vein (Clc) crossing the fine-grained chlorite zone. Diopside appears inside the chlorite matrix.

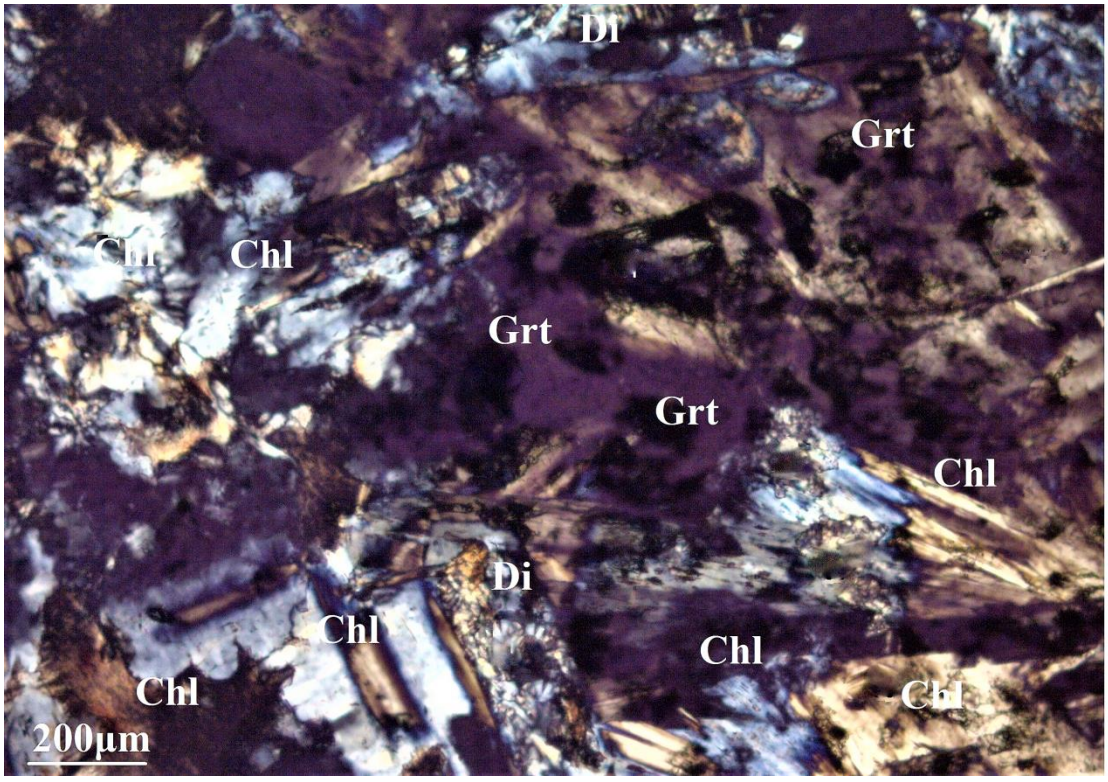

Figure 39. M.Z. Group-I rodingite photomicrograph (Sample EROD26L). It consists of Chlorite rich matrix (Chl) along garnet (Grt) and minor diopside (Di).

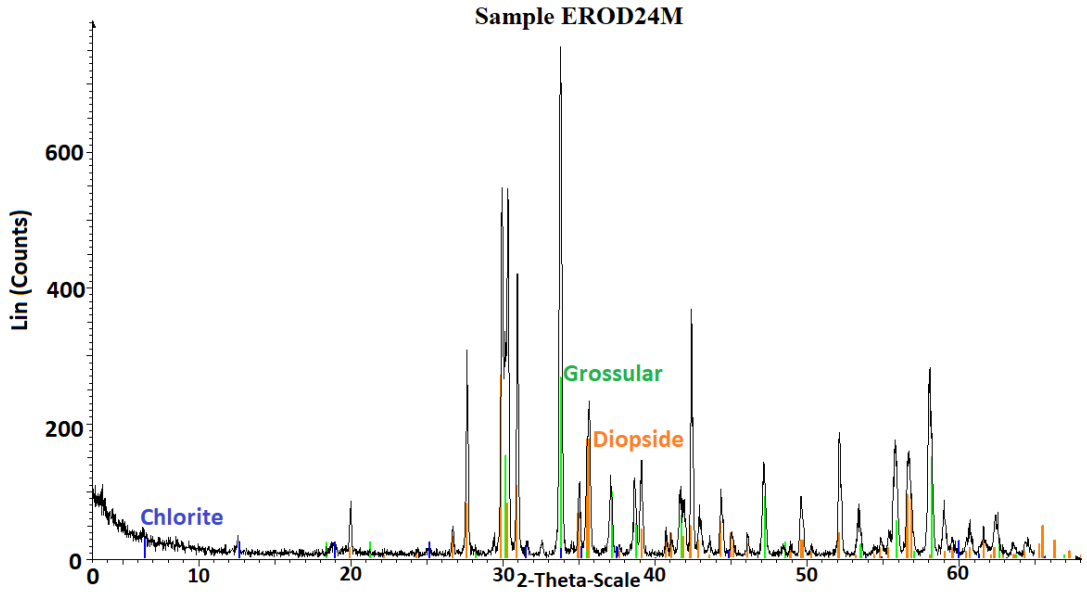

Figure 40. XRD pattern of a diopside-garnet rich sample (EROD24M) from MZ. Chlorite is also present in minor amounts.

6.1.1.3 Rodingite Transitional Zone

Samples EROD6, EROD7 and EROD23R belong to this zone. Their mineral assemblage consists of garnet, chlorite, vesuvianite and diopside in different proportions, which is also confirmed by XRD pattern of Sample EROD7 (Fig 43).

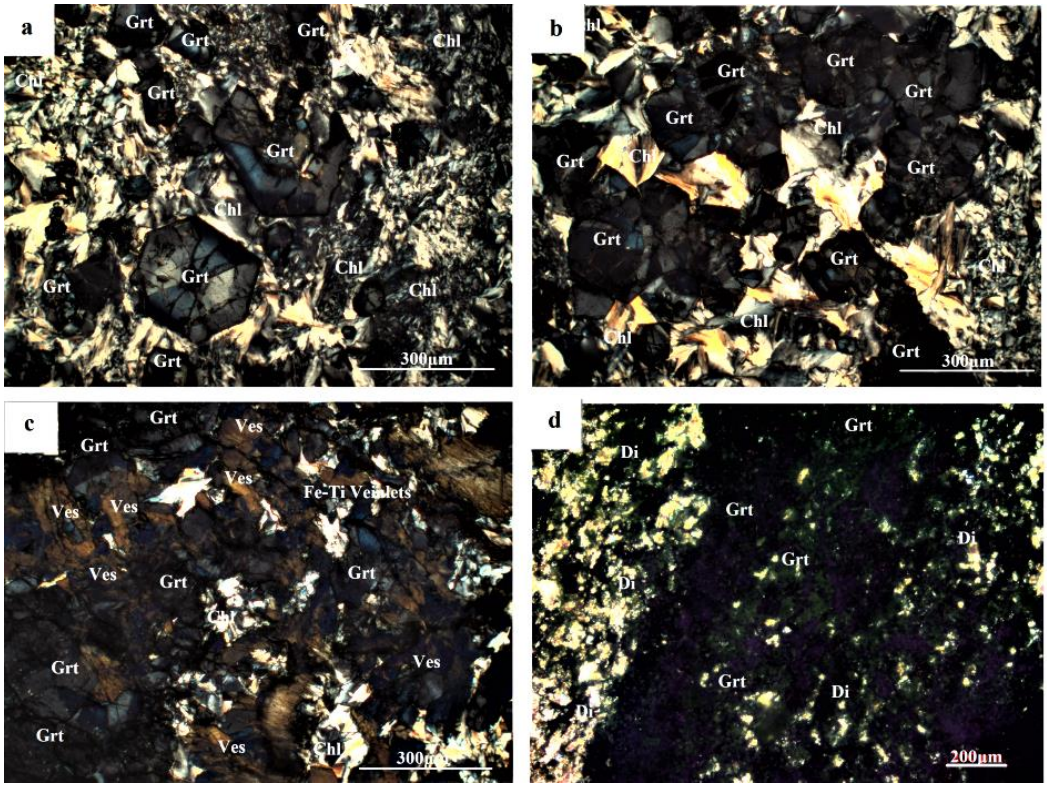

Figure 41. a.,b.,c. TZ photomicrograph of Group-I rodingites (Sample EROD23R). Garnet hourglass zoned porphyroblasts are present within a chlorite rich matrix. c. Chlorite appears intergranular between garnet and vesuvianite crystals. d. TZ photomicrograph of Group-I cryptocrystalline rodingite (Sample EROD6) consisting of garnet and vesuvianite. Grt: Garnet, Ves: Vesuvianite, Chl: Chlorite, Di: Diopside.

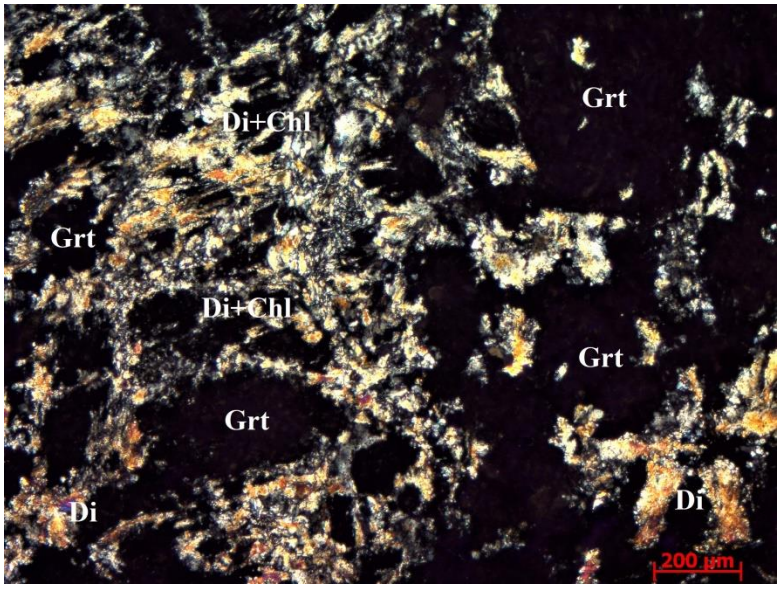

Figure 42. TZ photomicrograph (XPL) of Group-I rodingite (Sample EROD7) presenting a subophitic texture consisting of diopside (Di), chlorite (Chl) and garnet (Grt).

Their texture can either be cryptocrystalline (Fig. 41d) consisting of a garnet rich groundmass with diopside grains or it can be porphyroblastic fine-grained consisting of garnet and vesuvianite porphyroblasts within a chlorite rich groundmass. Furthermore, they usually exhibit remnants of a gabbroic subophitic texture where garnet appears surrounded by a diopside-chlorite rich mass (Fig. 42) Garnet porphyroblasts are usually broken and deformed idiomorphic 300 - 400μm size crystals presenting hourglass zoning (Fig. 41a,b). The groundmass is usually crosscutted by subparallel Fe-Ti-opaque veinlets (Fig. 41c).

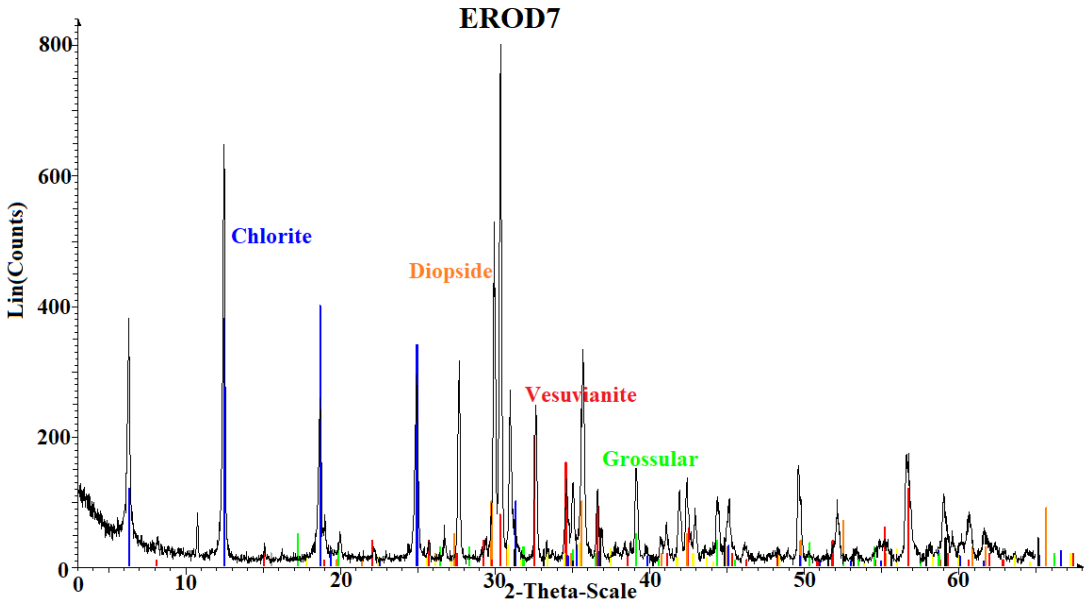

Figure 43. XRD pattern of a TZ Group-I Chlorite-rich sample (EROD23M). Vesuvianite, diopside and grossular are present in lesser amounts.

6.1.2 Group-II Calcite bearing rodingites

This group includes samples EROD11, EROD18, EROD22M, EROD7SCC, EROD10, EROD22L, EROD7SC and EROD12.

6.1.2.1 Rodingite Core Zones

Samples EROD11 and EROD18 correspond to Group-II rodingites from CZs. Their mineral assemblage mostly comprises garnet and vesuvianite in various and unequal amounts as it is confirmed by XRD patterns of Sample EROD11 (Ves-rich) and Sample EROD18 (Grt-Rich) (Figs 46 and 47). Accessory minerals include calcite, diopside, chlorite and Fe-Ti-opaque minerals. Their texture is cryptocrystalline (Fig. 44), consisting of a garnet-vesuvianite rich groundmass along with chlorite, while diopside appears intergranular between garnet and vesuvianite. Calcite and opaque minerals are usually present within small cavities in the rodingite matrix (Fig. 45). Veinlets of later generations crosscut the groundmass and consist of vesuvianite, calcite, chlorite and garnet. However, within big sized veins of about 750μm calcite is mainly concentrated towards the margins, while chlorite is concentrated towards the cores. This could be indicative of a later formed chlorite generation or it could suggest a chlorite-calcite recrystallization.

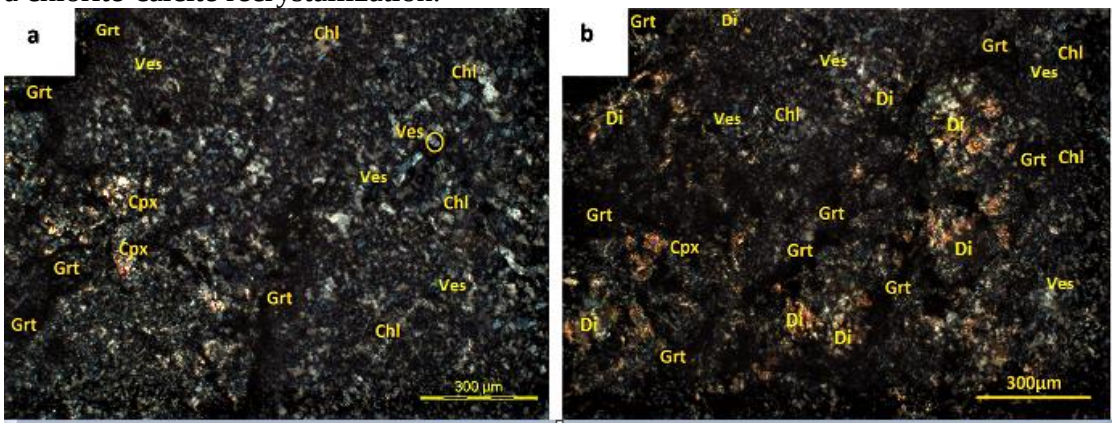

Figure 44. Group-II fine grained rodingite photomicrograph from the CZ (Sample EROD11) consisting of chlorite (Chl) garnet (Grt) and vesuvianite (Ves).

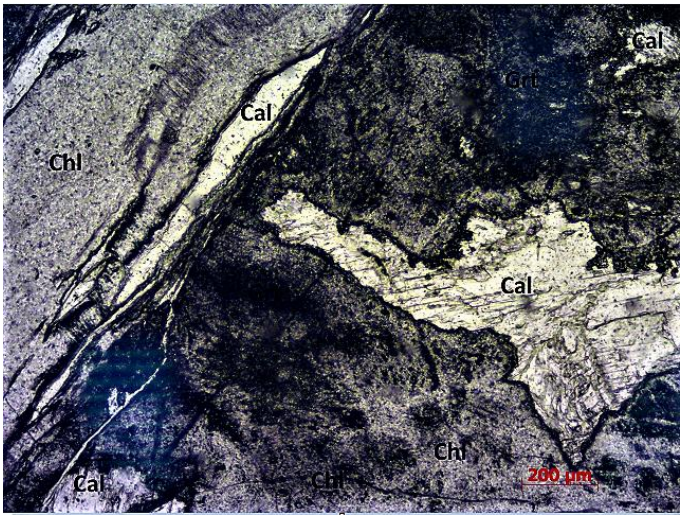

Figure 45. Group-II rodingite photomicrograph from the CZ (Sample EROD 18). Chlorite appears in the core of veins, formed after calcite, which is concentrated in the margins. The groundmass consists of chlorite (Chl) and garnet (Grt).

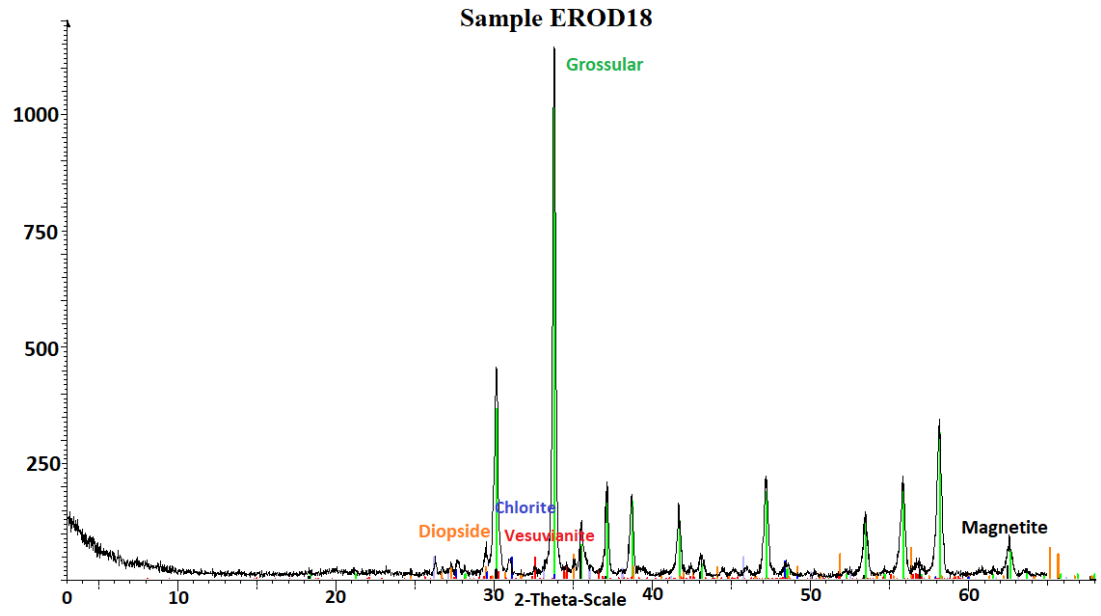

Figure 46. XRD pattern of a CZ garnet-rich Group-II sample (EROD18). Diopside, chlorite and magnetite have been also detected in lesser amounts.

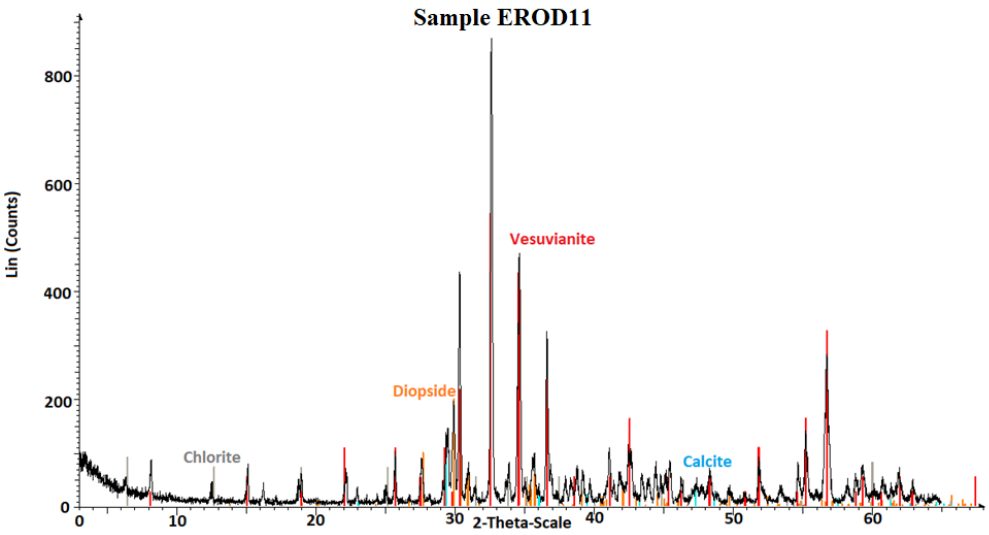

Figure 47. XRD pattern of a CZ vesuvianite-rich Group-II sample (EROD11). Grossular garnet, diopside and chlorite are present in lesser amounts.

6.1.2.2 Rodingite Marginal Zone

Samples EROD22M, EROD7SCC and EROD10 belong to this zone. They mainly consist of chlorite and/or diopside as it is also confirmed by XRD patterns of Samples EROD22M and EROD10M (Figs 50 and 51). Accessory minerals include calcite as well as garnet, vesuvianite and opaque minerals. Their texture can either be microcrystalline consisting of chlorite and diopside grains, or porphyroblastic, including idiomorphic chlorite crystals of 250-400 μm size within a cryptocrystalline

chlorite groundmass. Chlorite porphyroblasts usually occur within calcite cavities along with garnet porphyroblasts and vesuvianite as well. Diopside is mainly part of the micorcystalline matrix appearing along with garnet and chlorite whereas it can also occur within 300-350 μm sized veins which crosscut the chlorite-garnet matrix (Fig. 49). Calcite can either occur within cavities surrounding the earlier formed chlorite and garnet porphyroblasts (Fig. 48), or within veins of 300 μm size in diopside-chlorite-garnet rich matrix.

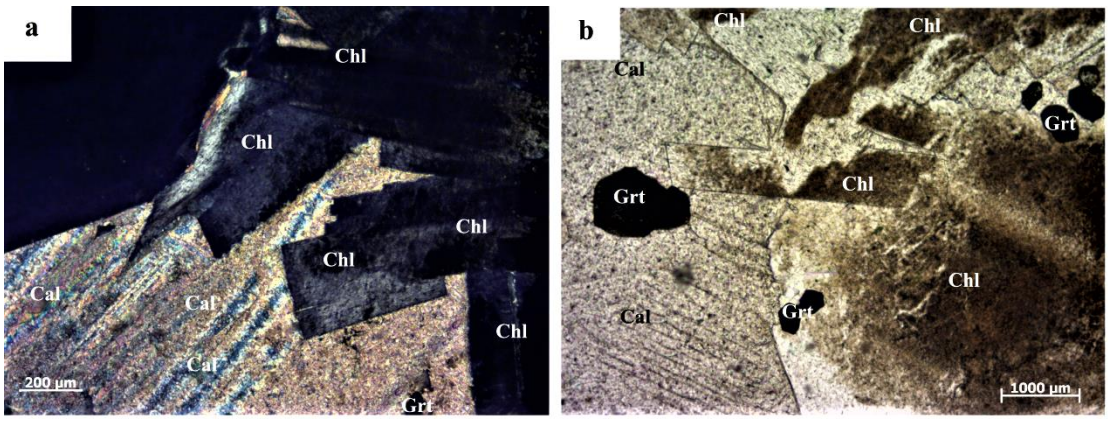

Figure 48. MZ photomicrograph of Group-II rodingite (Sample EROD10). a. (XPL) photomicrograph. Chlorite idiomorphic crystals (Chl) within calcite (Cal) cavities. b. (PPL) photomicrograph of chlorite appearing as part of the groundmass or in the form of idiomorphic crystals. Garnet (Grt) is idiomorphic and either occurs within calcite (Cal) cavities or within the chlorite matrix.

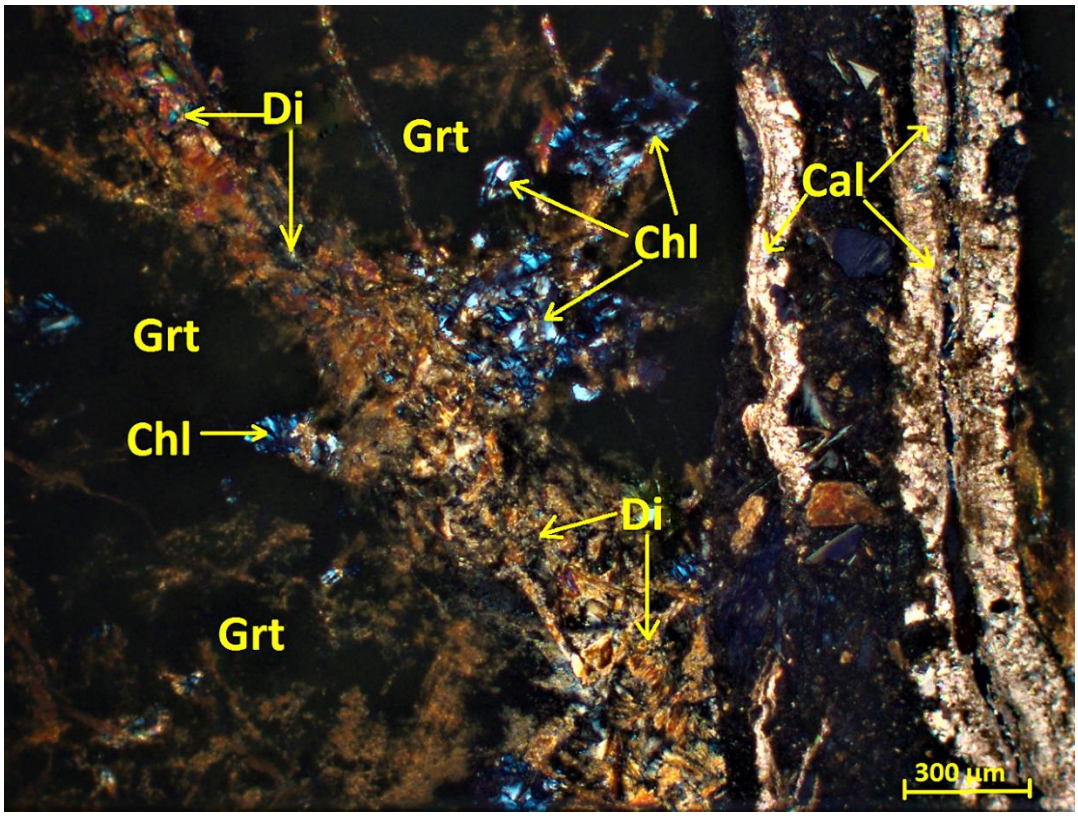

Figure 49. M.Z. photomicrograph of Group-II rodingites (Sample EROD7SCC). Diopside (Di)- Chlorite (Chl) rich veins of 300μm size crosscut the groundmass. Later formed veins of 500μm consisting of calcite (Cal) along with Chlorite (Chl) are also observed. Garnet (Grt) occurs as part of the cryptocrystalline groundmass.

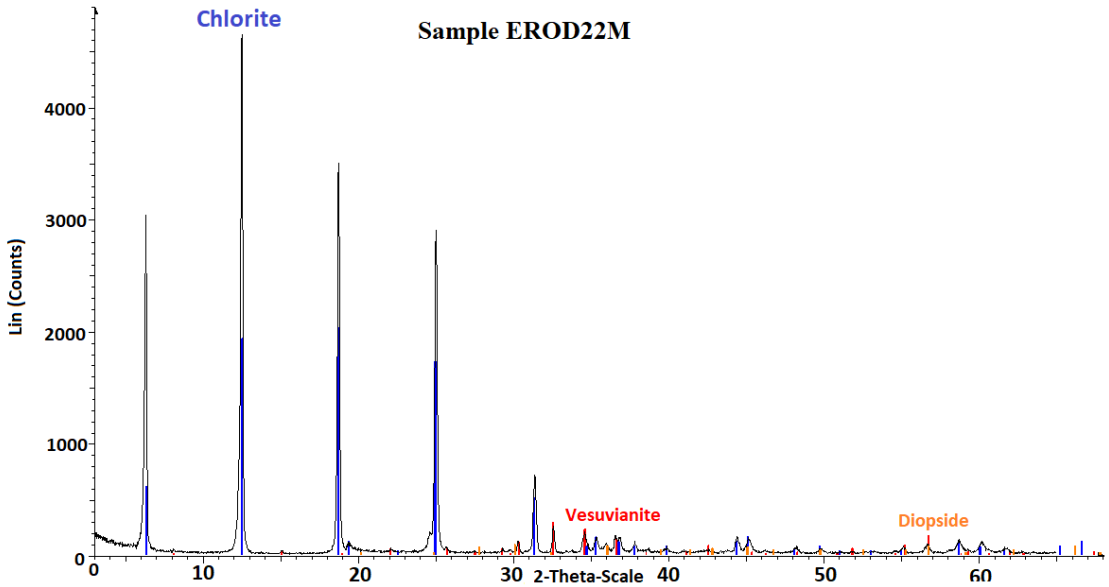

Figure 50. XRD pattern of a chlorite-rich Group-II sample from MZ (Sample EROD22M). Vesuvianite and diopside are also present in minor amounts.

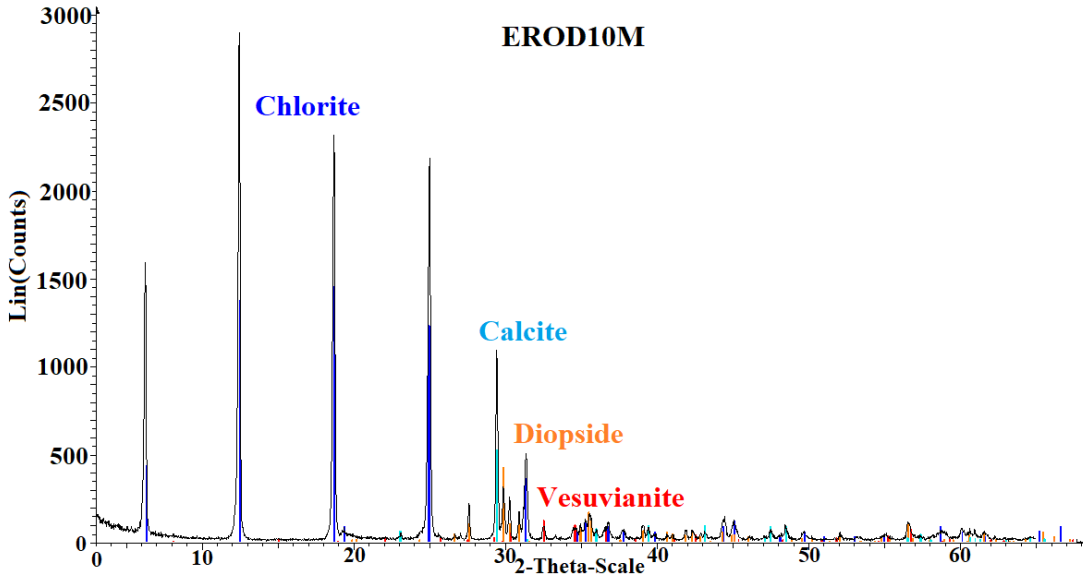

Figure 51. XRD pattern of a chlorite-diopside rich Group-II sample from MZ (Sample EROD10M). Calcite is detected, while vesuvianite is also present in minor amounts.

6.1.2.3 Rodingite Transitional Zone

Samples EROD12, EROD7SC and EROD22L belong to this zone. Their mineral assemblage consists of garnet, chlorite, vesuvianite and diopside in different proportions. Accessory minerals include calcite, prehnite, epidote, opaque Fe-Ti-minerals and relict diopside crystals. Their texture can either be microcrystalline consisting of garnet and chlorite (Fig. 52a,b), whereas fine grained textures consisting of chlorite of 300μm size, garnet of 60-100 μm size and vesuvianite of 100 μm size also occur. Remnants of subophitic textures including relict clinopyroxenes of 200 μm size are indicative of a gabbroic origin (Figs 56 and 57b). At these textures chlorite and garnet are formed at the expense of clinopyroxene, while cryptocrystalline veinlets of later formed garnet cross the clinopyroxene mass. Calcite is present within

veins of 300-150 μm thickness, or cavities of more than 1mm size (Figs 53b, 54a and 55b) as it is also confirmed by the XRD patterns of Samples EROD12 and EROD7SC (Figs 57 and 58). In these cavities fine grained garnet, vesuvianite, chlorite and microcrystalline epidote have formed earlier than calcite. Epidote has been formed at the expense of garnet and vesuvianite. The depositional sequence is garnet-vesuvianite →epidote→calcite. Chlorite can also occur within veins of 300 μm size surrounding earlier formed hypidiomorphic vesuvianite and garnet crystals (Figs 53a,b and 54a), or coexisting with calcite (Fig. 57a). Diopside is part of the groundmass appearing intergranular between garnet and chlorite, or in the form of later formed veins crossing the cryptocrystalline garnet matrix (Fig. 55b), giving the following depositional sequence: garnet→chlorite→diopside.

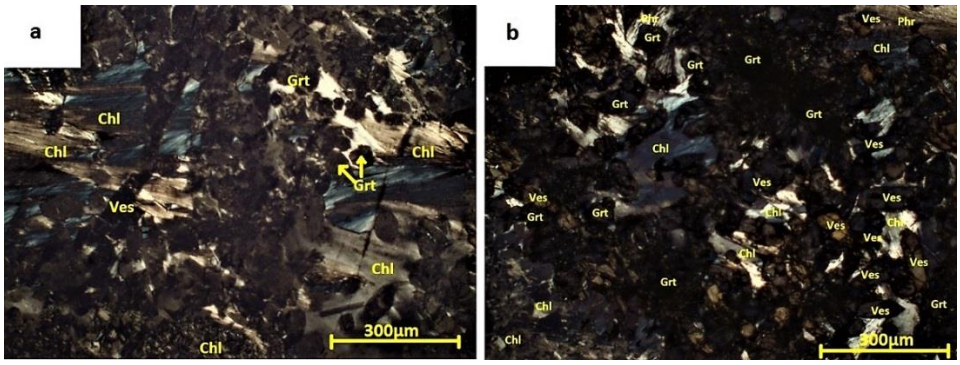

Figure 52a.,b. Group-II Choneftiko rodingite from TZ (Sample EROD12) photomicrograph (XPL) with vesuvianite (Ves) and garnet (Grt) porphyroblasts inside a chlorite (Chl) matrix.

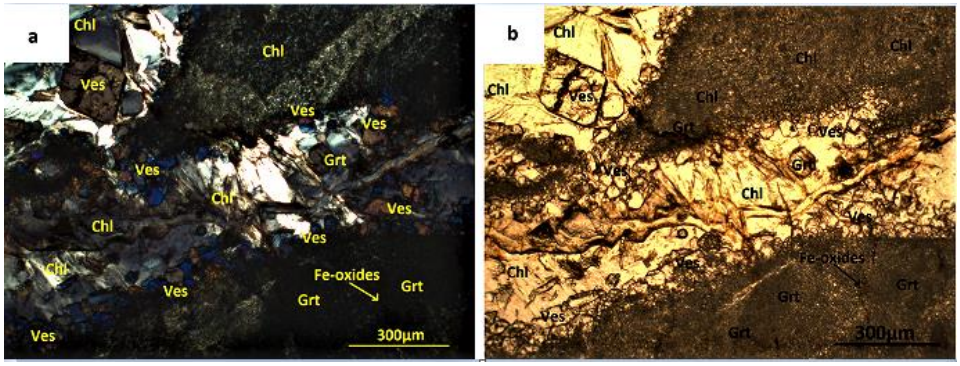

Figure 53. a. Group-II rodingite TZ photomicrograph (XPL) (Sample EROD22L) mainly consisting of clinochlore (Clc) along with garnet (Grt) and vesuvianite (Ves) idiomorphic crystals. Chlorite (Chl) and garnet are also present as parts of the fine-grained groundmass. b. PPL photomicrograph of Figure 53a.

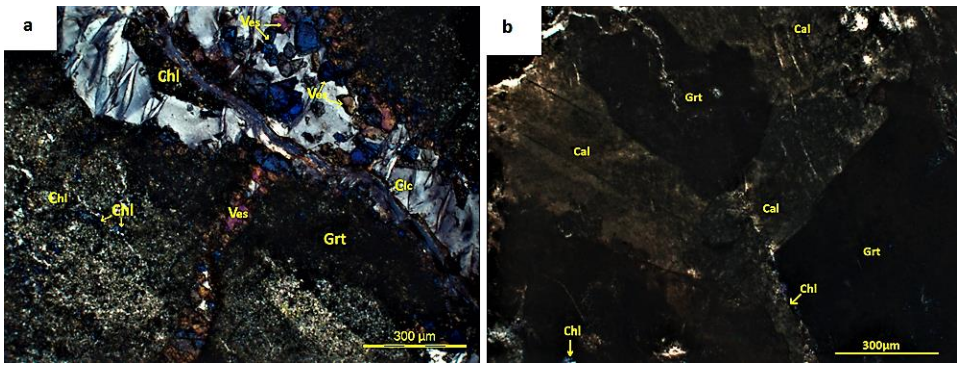

Figure 54. a. Group-II rodingite TZ photomicrograph (Sample EROD22L) with chlorite (Chl) matrix crossed by a vesuvianite (Ves) rich vein. A second vein crosses and cuts the first and consists of white and brown colored chlorite (Chl), vesuvianite (Ves) and garnet (Grt). b. Group-II TZ photomicrograph (Sample EROD22L) with a calcite grain inside a garnet (Grt) matrix. Blue colored chlorite (Chl) appears between calcite and garnet.

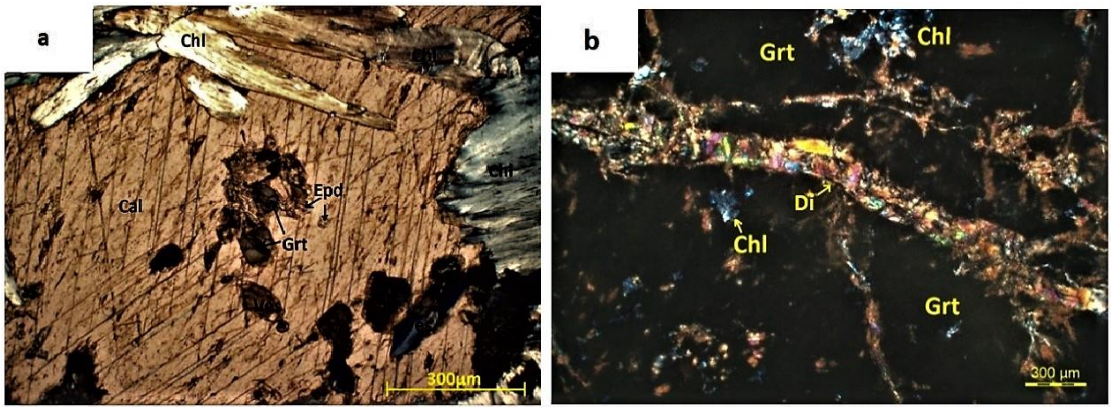

Figure 55.a. Group-II Choneftiko rodingite TZ photomicrograph (EROD12) with calcite (Cal) cavity inside a chlorite-garnet matrix. Calcite cavities include garnet (Grt) vesuvianite (Ves) and chlorite (Chl) crystals, while small sized epidote (Ep) grains appear surrounding garnet and vesuvianite. b. Group-II Kalimeriani rodingite TZ photomicrograph (Sample EROD7Sc) (XPL) with chlorite (Chl), appearing intergranular between clinopyroxene (Cpx) rims and garnet (Grt). Calcite (Cal) veins cross the matrix.

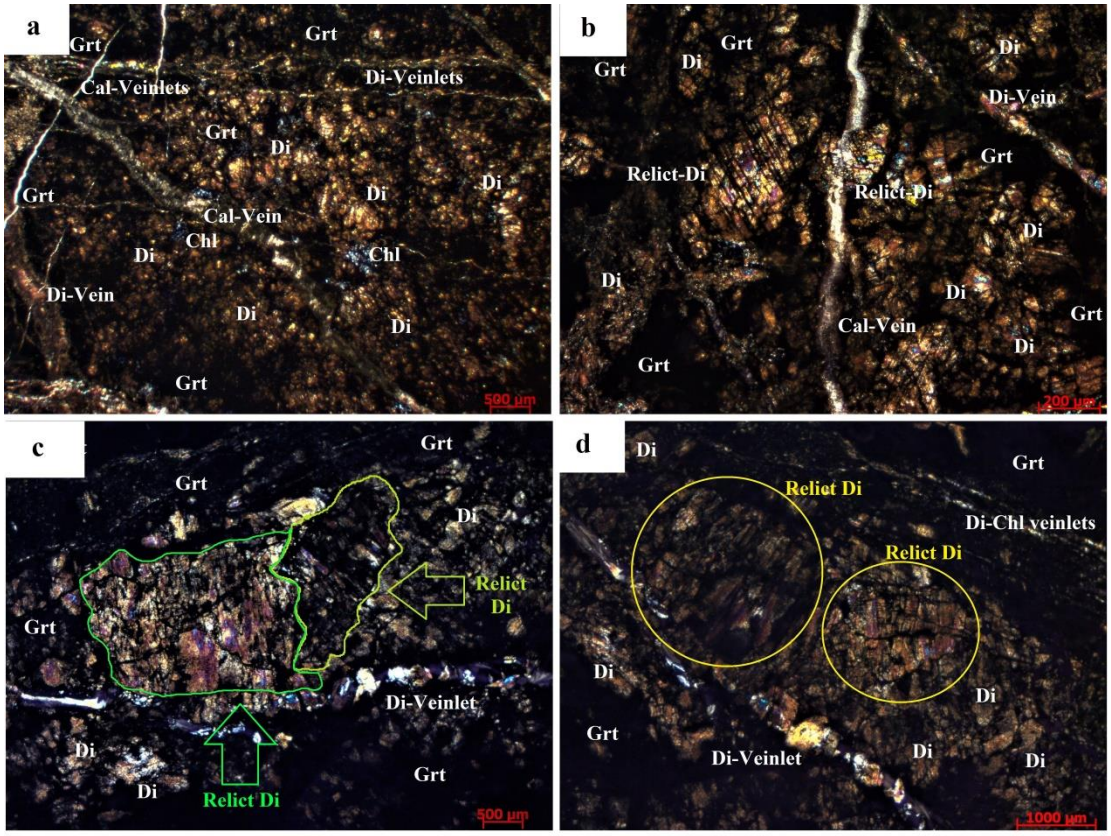

Figure 56. a,b. Group-II TZ rodingite photomicrograph (XPL) (Sample EROD7SC), consisting of a diopside-garnet (Di-Grt) rich groundmass crosscutted by garnet, chlorite (Chl), calcite (Cal) and diopside veins and veinlets. Chlorite also appears intergranular between diopside and garnet. c,d. Relict diopside grains within a diopside-garnet rich groundmass in a Group-II TZ rodingite photomicrograph (Sample EROD7SC) (XPL). Diopside and chlorite rich veins and veinlets crosscut the matrix.

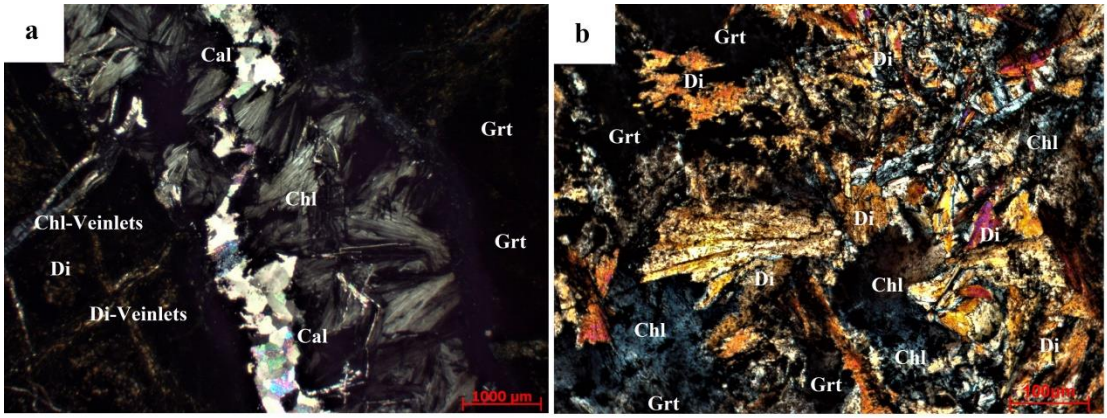

Figure 57.a. TZ photomicrograph of Group-II rodingite (Sample EROD7SC) (XPL) consisting of 1mm size chlorite-calcite rich vein (Chl-Cal) within a garnet (Grt)-Diopside (Di) groundmass. b. Group-II Kalimeriani rodingite TZ photomicrograph (Sample EROD7SC) (XPL) with garnet (Grt) matrix crossed by diopside (Di) and calcite (Cal) veins. Blue colored chlorite (Chl) appears intergranular between clinopyroxene and garnet.

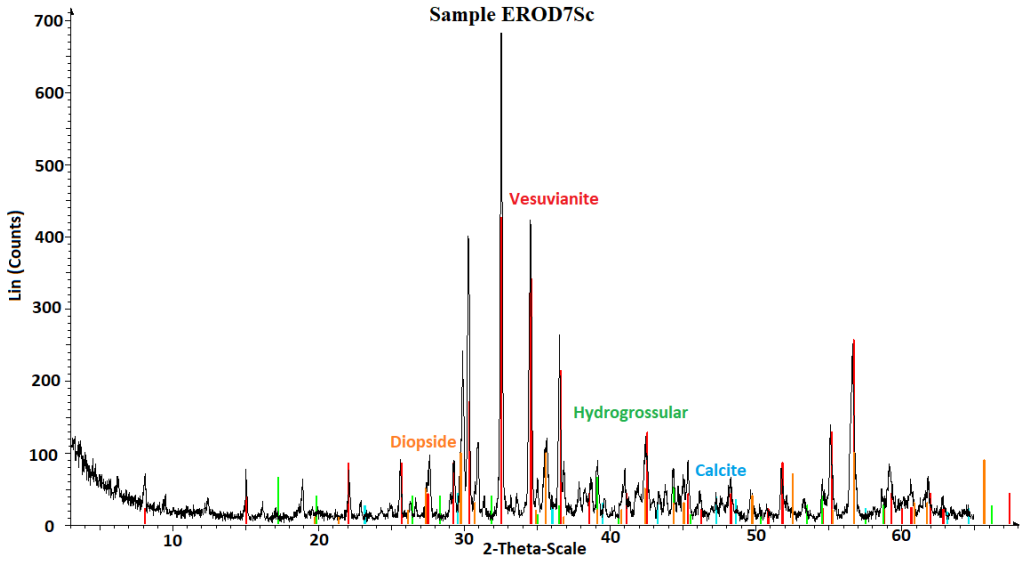

Figure 58. XRD pattern of a diopside-grossular-vesuvianite rich Group-II sample from MZ (Sample EROD10M). Calcite is also present in minor amounts

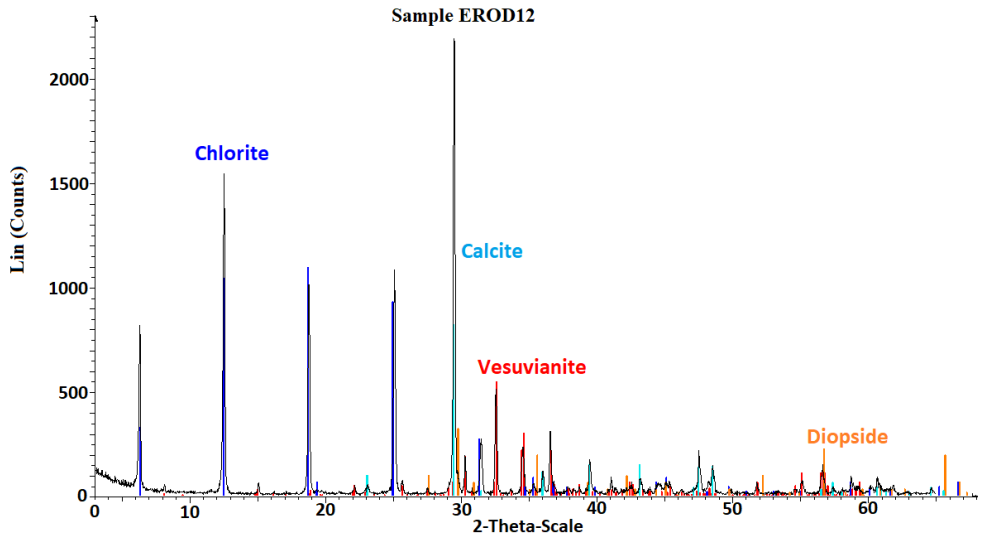

Figure 59. XRD pattern of a chlorite-vesuvianite-diopside rich Group-II sample from MZ (Sample EROD10M). Calcite is also present in high amounts.

6.2 Ultramafics

6.2.1 Serpentinized Peridotites

They include samples SERP25 from Choneftiko area and samples SERPEG and SERPEL from Kalimeriani village. They present mesh and cataclastic textures with chrysotile veins (Figs 60 and 61). Their main mineral assemblage consists of serpentine which is mainly antigorite as it is shown by the XRD patterns of Samples SERPEL and SERP25R (Figs 62 and 63), bastite grains deriving from orthopyroxene and clinopyroxene alteration (Fig. 60), as well as a few relict spinel, olivine and clinopyroxene grains (Figs 60 and 61). Orthopyroxene-bastites usually include serpentinized olivine inclusions (Fig. 60b).

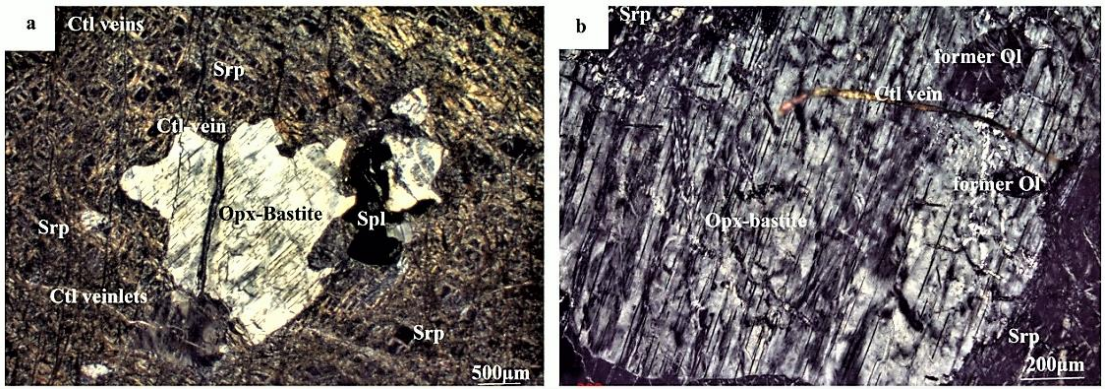

Figure 60. Serpentinized peridotite photomicrograph (Sample SERPEG) presenting mesh texture with serpentine (Srp) and pyroxene bastite grains along with relict spinel (Spl) grain and chrysotile (Ctl) vein. b. Orthopyroxene bastite crystal with brucite dissolutions in a serpentine (Srp) matrix.

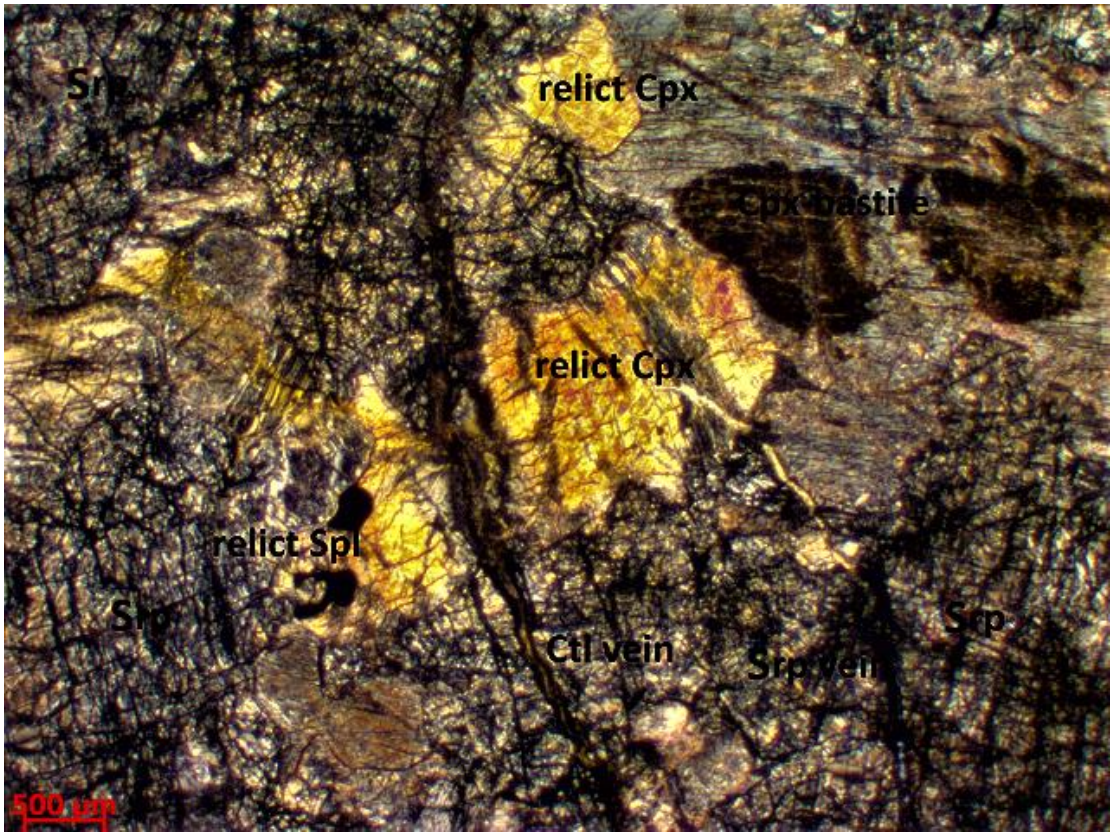

Figure 61. Serpentinized peridotite photomicrograph (Sample SERPEL) with relict clinopyroxenes (Cpx), chrysotile veins (Ctl), bastites and cataclastic texture.

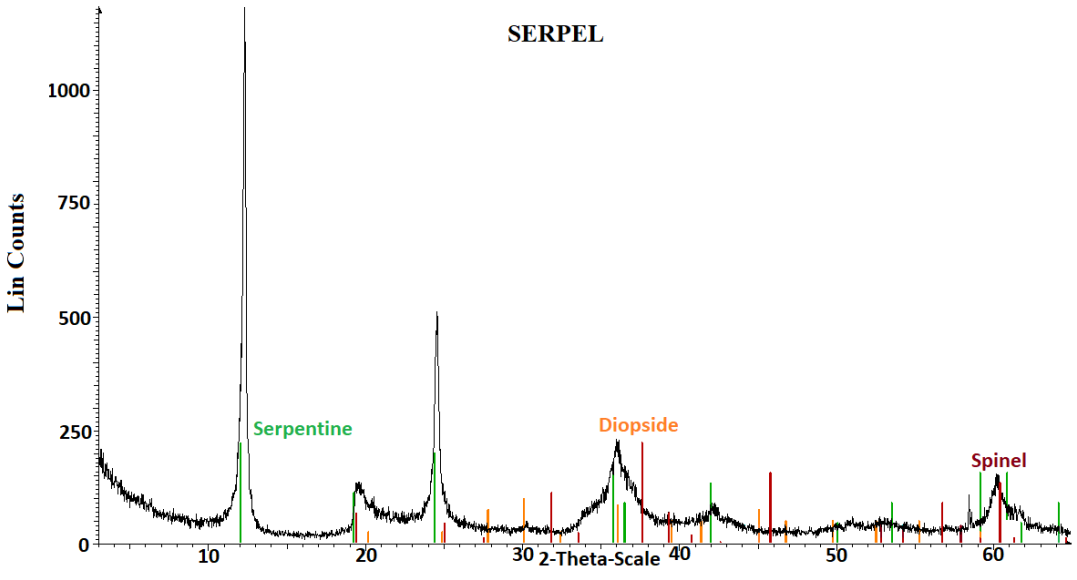

Figure 62. XRD pattern of Serpentinized peridotites (Sample SERPEL) consisting of serpentine, relict diopside and spinel.

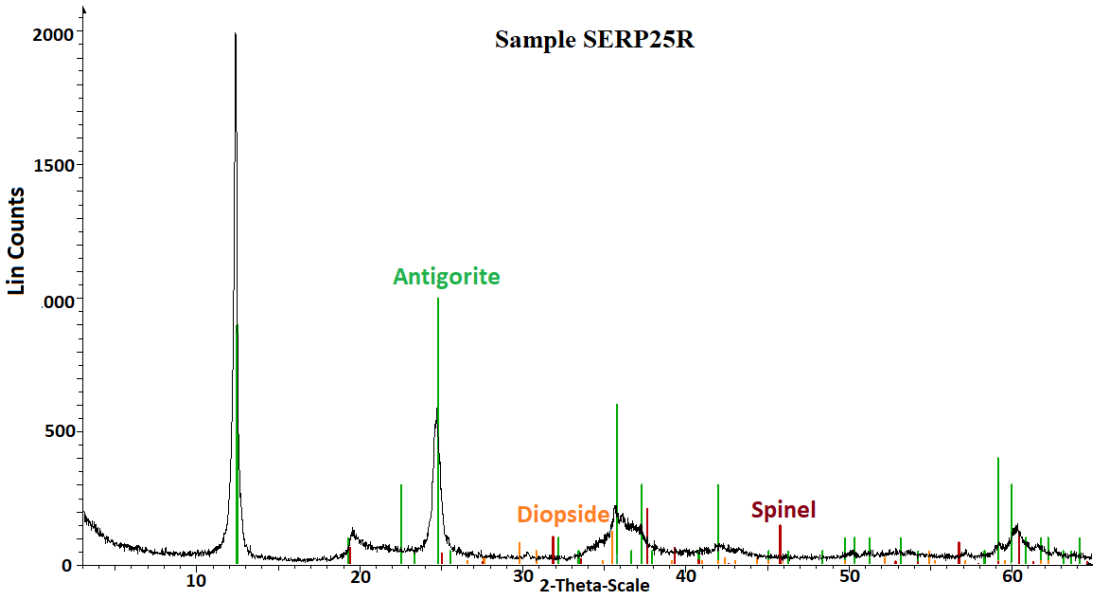

Figure 63. XRD pattern Serpentinized Peridotites (Sample SERP25R). Serpentine, spinel, diopside and a few enstatite crystals are also present in lesser extent.

6.2.2 Metasomatized Serpentinites

They include samples SERP6-7, SERP22 and SERP25. Their texture is meshed with chrysotile veins. Their mineral assemblage mostly includes serpentine, garnet crystals and bastites. Relict spinel as well as relict diopside grains also occurs (Figs 64a and 65d). Chlorite is present as accessory mineral, while serpentine occur as green to yellowish grains in crossed polars, which plausibly indicates the existence of two serpentine generations. Idiomorphic garnet crystals occur as inclusions within serpentine and relict diopside grains (Figs 64 and 65).

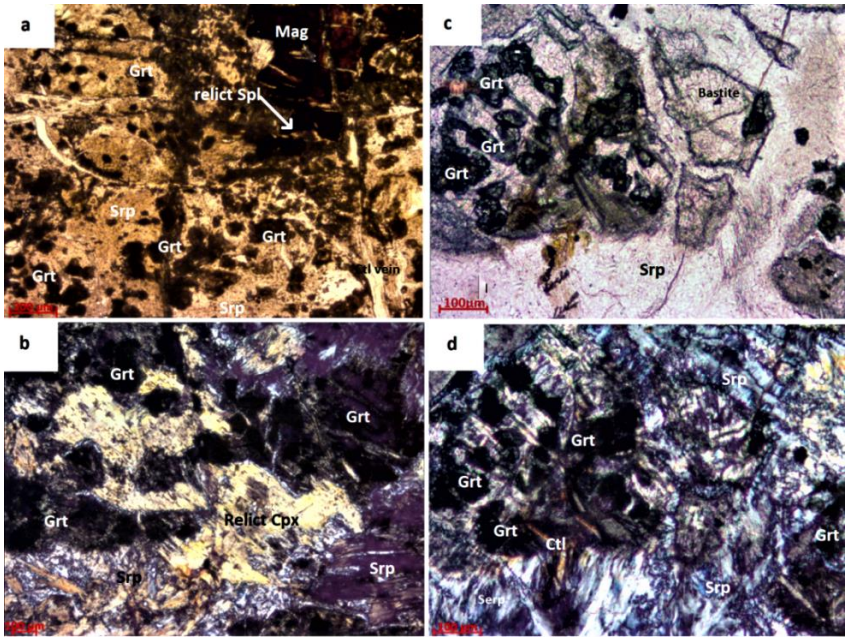

Figure 64. Metasomatized Serpentinites microphotographs. a. Sample SERP 6-7(PPL) Serpentinites present mesh texture with serpentine (Srp) metasomatic garnets (Grt), relict spinel (Spl) and magnetite (Mag) grains b. Sample SERP6-7 (XPL) relict clinopyroxenes (Cpx) and metasomatic garnets (Grt) in a serpentine mass. c. Sample SERP22(PPL) metasomatic garnets (Grt), chrysotile (Ctl) veins and bastites. d. Sample SERP 22 (XPL) image.

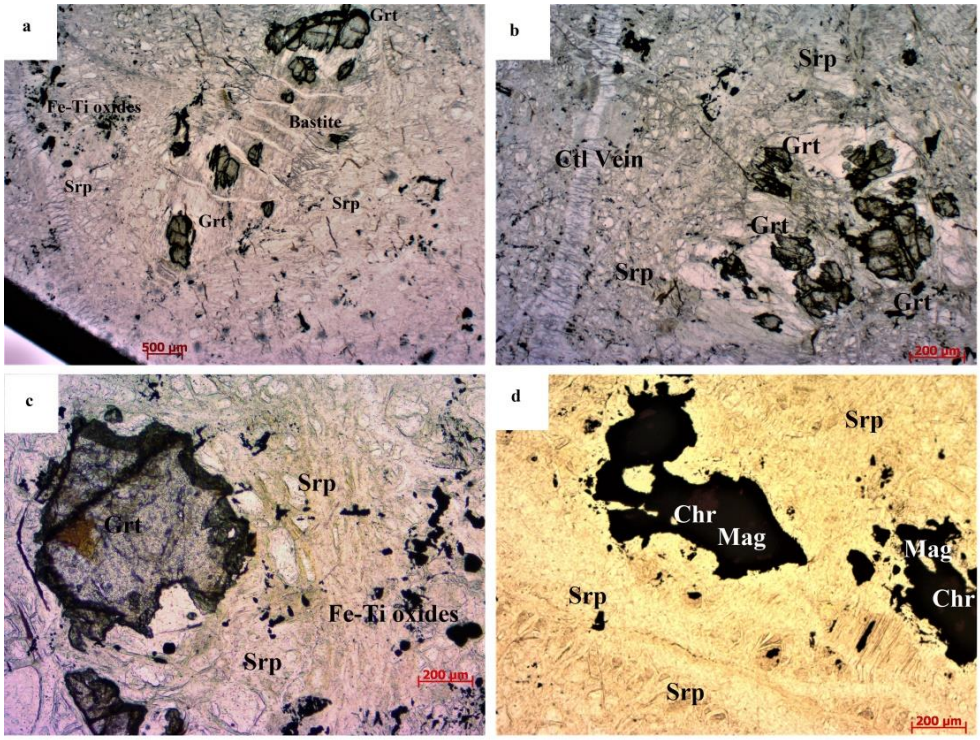

Figure 65. Garnet metasomatized serpentinite photomicrograph (PPL) (Sample SERP25) consisting of a serpentine (Srp) rich matrix along with Fe-Ti opaque minerals and chrysotile (Ctl) veins. Garnet (Grt) is hypidiomorphic and appears as porphyroblasts within the matrix. d. Garnet metasomatized photomicrograph (Sample SERP25) consisting of chromite patches (Chr) within relict magnetite grains (Mag).

6.2.3 Chloritites

Chloritites include samples EROD7Sr and SERPV12RR, from Kalimeriani and Choneftiko areas respectively. They are fine grained chlorite rich with cataclastic texture, also including a few relict serpentine and spinel grains (Fig. 66b). Bastite as well as chrysotile veins (Fig. 66a) also occur. In veins of 200-300μm size calcite is concentrated towards the margins, coexisting with chlorite which is concentrated towards the cores (Fig. 67). XRD pattern of sample SERPV12RR (Fig. 68) also confirms the presence of chlorite as well as minor calcite and serpentine.

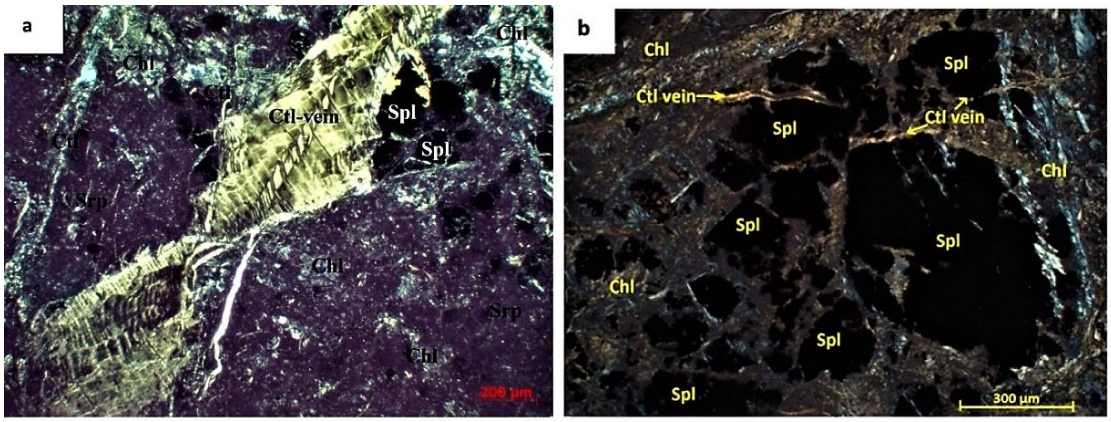

Figure 66a. Chloritite photomicrograph (XPL) (Sample SERPV12RR) with chlorite (Chl), serpentine (Srp), chrysotile veins (Ctl) and relict spinel grains (Spl) b. (XPL) Chloritite photomicrograph (Sample SERPV12RR) with spinel (Spl) grains inside a chlorite (Chl) matrix. Spinels are usually crossed by chrysotile veinlets.

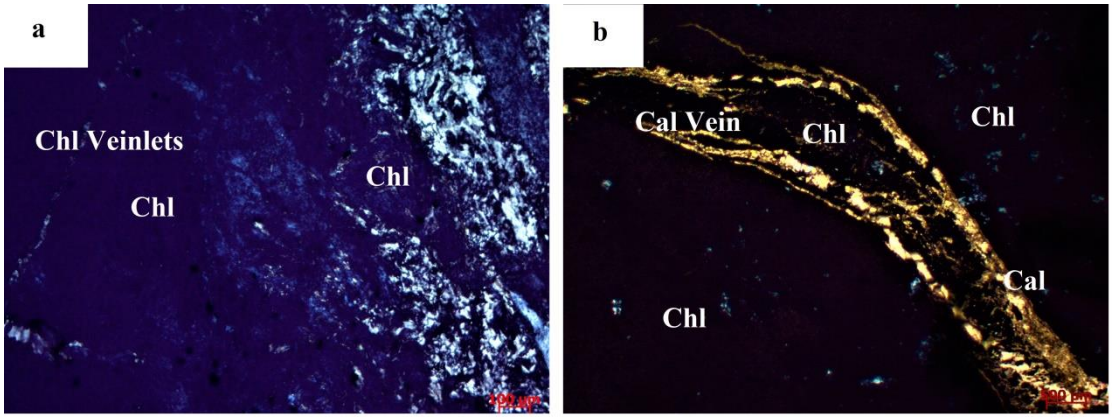

Figure 67. a. Chloritite photomicrograph (XPL) (Sample SERPV12RR) consisting of a chlorite (Chl) groundmass and chlorite-rich veinlets, b. Chloritite photomicrograph (XPL) (Sample EROD7SR) consisting of a chlorite (Chl) groundmass and a calcite-chlorite rich (Cal, Chl) vein.

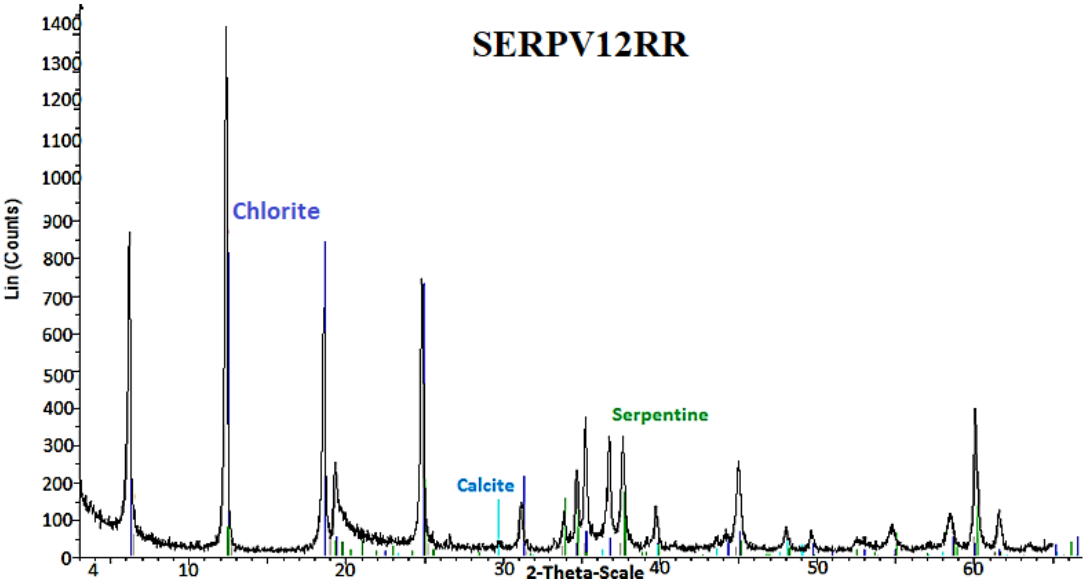

Figure 68. XRD analyses of Kimi chloritites from Chloritite ultramafics (Sample SERPV12RR), consisting of chlorite, serpentine and calcite.

7 Mineral Chemistry

Mineral analyses indicate that Kimi rodingites mostly include garnet, vesuvianite, diopside, chlorite and calcite, while minor amphibole, dolomite and quartz crystals were also detected. Accessory minerals include spinel grains, apatite and allanite. On the other hand, chloritic rims mainly include chlorite, serpentine and a few relict spinel grains. Mineral analyses as well as their chemical features are described in the following Tables.

7.1 Vesuvianite

Vesuvianite chemical formula is $X_{19}Y_{13}Z_{18}T_{0\text{-}5}O_{68}W_{10}$, where x = Ca, Na, Ln^{3+}, Pb^{2+}, Sb^{3+}, y = Al, Mg, Fe^{3+}, Fe^{2+}, Ti^{+4}, Mn, Cu, Zn, Z = Si, T = B, W = (OH,F,O) (Groat et al., 1992a) and its recalculation (Table 5) is based on 73 oxygens.

Table 5. Representative chemical analyses of Group-II Rodingite vesuvianites (Ves).

Group	**II**	**II**	**II**
Sample	**EROD22M**	**EROD12**	**EROD12**
Analyses	**F14S2**	**F16S1**	**F8S1**
Mineral	**Ves**	**Ves**	**Ves**
Area	**MZ**	**TZ**	**TZ**
Location	**Choneftiko**	**Choneftiko**	**Choneftiko**
SiO_2	35.16	33.84	37.91
TiO_2	0.13	0.00	0.00
Al_2O_3	15.70	14.63	15.43
FeO	1.12	3.97	3.80
MnO	0.38	0.00	0.18
MgO	3.28	2.93	2.31
CaO	34.25	34.57	36.88
Na_2O	0.28	0.00	0.36
K_2O	0.00	0.31	0.00
Cr_2O_3	0.00	0.04	0.00
NiO	0.36	0.30	0.00
Total	90.65	90.58	96.87
Si	18.12	17.81	18.48
Al	9.53	9.07	8.87
Ti	0.05	0.00	0.00
Fe	0.48	1.75	1.55
Mn	0.17	0.00	0.08
Mg	2.52	2.30	1.68
Ca	18.91	19.49	19.26
Na	0.28	0.00	0.34
K	0.00	0.20	0.00
Cr	0.00	0.01	0.00
Ni	0.15	0.13	0.00
Total	50.21	50.75	50.25

Vesuvianite is detected in both rodingite groups. Their FeOt contents range from quite low to quite high (1.12-3.97 wt%), while MgO values range from 2.31 to 3.28 wt%.

On the other hand, vesuvianite from MZs of Group-II rodingites is richer in SiO_2 and CaO contents compared to those of TZs. Total alkalies values ($NaO+K_2O$) are very low (0.28-0.36 wt%). MgO is increased from MZs to TZs, while Fet and Ca contents remain almost constant moving from MZs to TZs (Fig. 71a,b).

Vesuvianite of TZs (Figs 69 and 70), is part of the fine grained matrix. Its size ranges from 125 to 220 μm, while bigger crystals range from 500μm to 1mm size. On the other hand, vesuvianite from MZs has smaller size compared to those of TZs and appears as part of the microcrystalline groundmass. As a result it usually presents CaO and SiO_2 enrichment and cannot be easily distinguished from garnet. Furthermore, it can also occur within calcite-filled cavities along with garnet, apatite and chlorite.

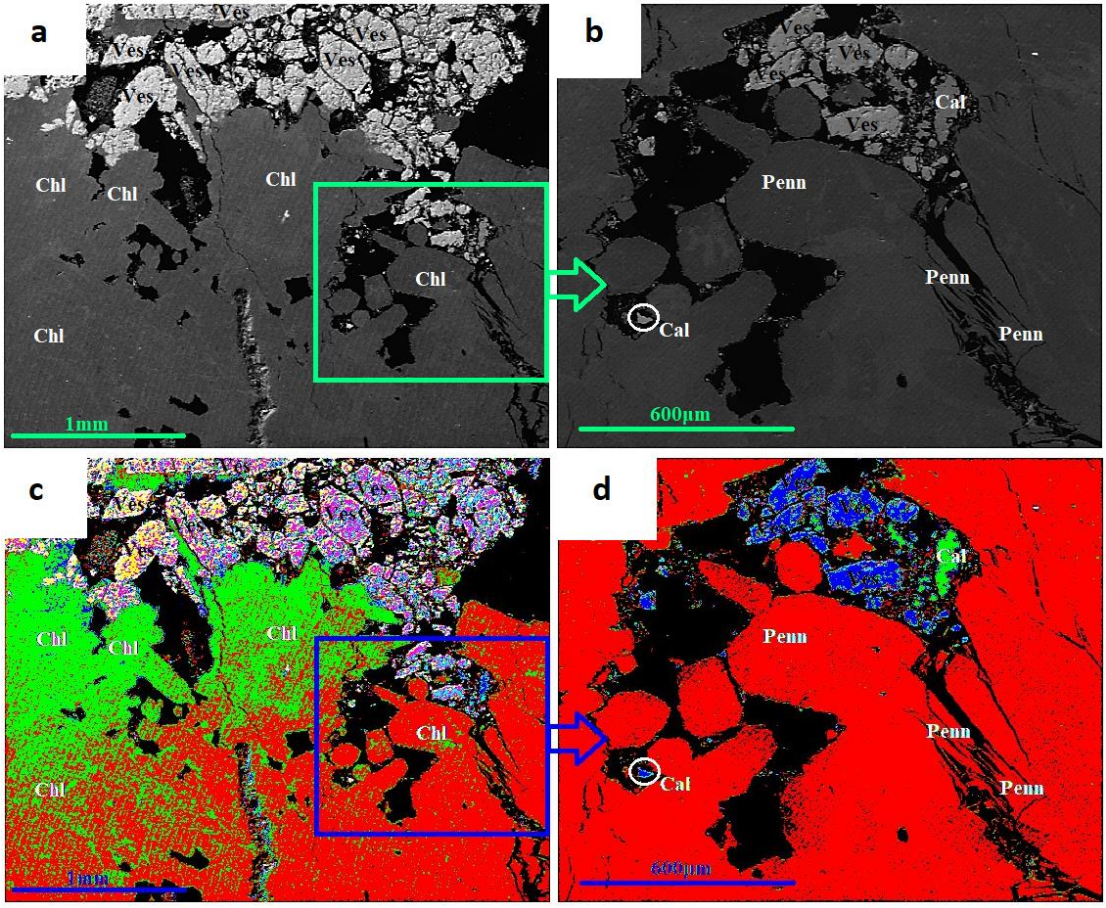

Figure 69. a.,b. Group-II rodingite BES SEM-EDS image of Sample EROD12 from TZ. Vesuvianite (Ves) is idiomorphic, while chlorite (Chl) appears light and dark patches respectively. c. Colored BES SEM-EDS image of the aforementioned figure. Green chlorite patches are Fe rich compared to the red ones. Red chlorite patches are mainly classified as penninites (Penn). d. Cavities in the penninites matrix filled with calcite (Cal) and vesuvianite (Ves) crystals.

According to Groat et al. (1992a), a possible substitution in vesuvianite sample without Na^+ and extremely low Al and very high Ti content, is $Ln^{3+} + Na^+ \rightarrow 2Ca^{+2}$ and $Na^+ + Ti^{4+} + Ca^{+2} \rightarrow Al$ or $Ln^{3+} + Mg^{+2} \rightarrow Ca + Al$ and $Mg + Ti \rightarrow 2Al$, while O^{-2} could also substitute for OH^-.

Fitzgerald et al. (1992), conducted microprobe analyses to 44 vesuvianites in order to examine their chemical variation, dividing them into 4 types according to the percentage of Mg, Ti, Si, Mn, Cu, the presence and variability of Fe^{3+} and Fe^{2+}.

Following these discriminations Kimi vesuvianites can be distributed in the following types. TZs of Group-II rodingites consist of vesuvianites which belong to Type-1 and Type-2 respectively (Mg~2, Ti< 0.25 for Type-1 and with Mg> 2.5 and Ti<0.5 for Type-2). On the other hand, vesuvianite crystals from MZs of Group-II rodingites most probably display Type-1 affinities with (Mg: 1.68 and Ti:0).

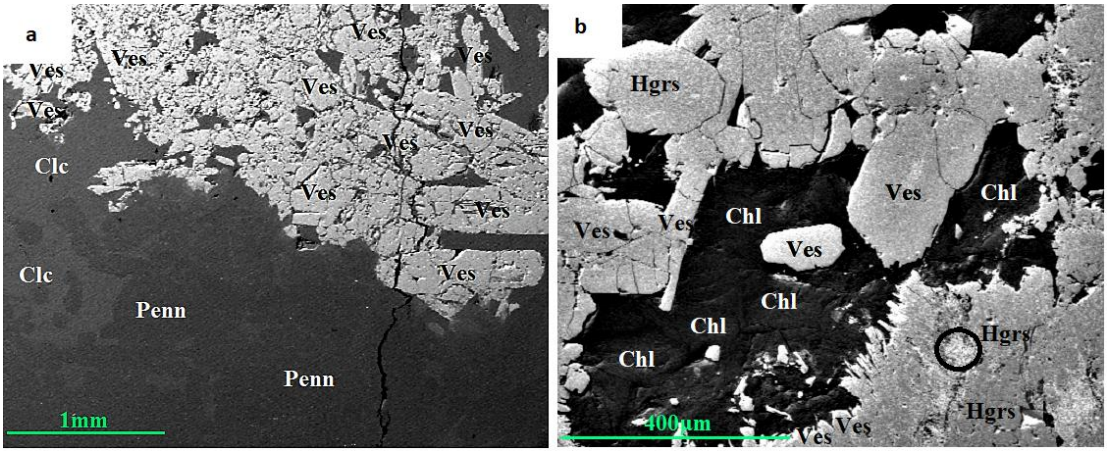

Figure 70. Group-II rodingite BES SEM-EDS image of Sample EROD12 from the TZ, consisting of vesuvianite (Ves) porphyroblasts within a chlorite matrix. Light chlorite patches are classified as clinochlore (Clc), while dark patches are classified as penninite (Penn). b. TZ Group-I rodingite BES SEM-EDS image of Sample EROD23R consisting of chlorite (Chl), vesuvianite porphyroblasts (Ves) and hydrogrossular (Hgrs).

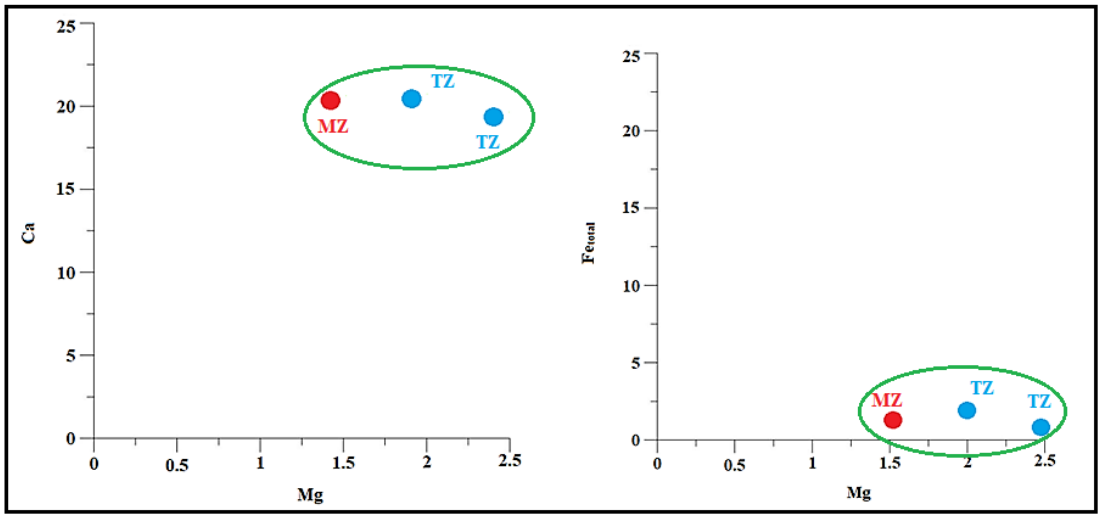

Figure 71. Ca-Mg and Fe_{total}-Mg Diagram for vesuvianites of Group-II rodingites from Transitional (TZ) and Marginal Zones (MZ).

7.2 Garnet and Hydrogarnet

Garnet chemical formula is $X_3Y_2(ZO_4)_{3-P}(H_4O_A)_P$, X:Ca,Mn,$Fe^{2+}$,Mg, Y:$Al^{vi}$, Fe^{3+}, Cr and Z:Si,Al^{iv}. Its division depends on the presence of water or not. Garnet crystals which contain water are called hydrogarnet (0<p<3) (Meagher, 1980), while the anhydrous phases are called garnet (p=0). The recalculation of anhydrous garnets is based on 12 oxygens. According to their mineral chemistry garnets are divided into two groups, the andradite group with $Ca^{2+}>Fe^{2+}+Mn+Mg^{2+}$ and the almandine group with $Ca^{2+}<Fe^{2+}+Mn+Mg^{2+}$. Andradite group includes grossular, uvarovite and andradite, whereas the almandine group includes almandine and spessartine. Their

chemistry depends on the P-T conditions (e.g. Banno et al., 1986). In high T conditions Fe, Mg is increased, while Ca and Mn are depleted. Garnets usually present a chemical zoning, which according to Spear (1995), can be divided into two types: the growth zoning and the diffusion zoning, while most times the garnet crystals present both zoning types. Zoning growth is characterized by a Fe, Mg rim to core enrichment and a decrease in Fe/(Fe+Mg) ratio respectively. At T>650 ^{o}C zoning growth cannot be observed due to the chemical homogeneity of garnet crystals (Tracy, 1976; Woodsworth, 1977; Graessner and Schenk, 1999).

Table 6. Representative garnet/hydrogarnet (Grt-Hgrt) analyses for Group-I and Group-II rodingites, Hgrt: Hydrogarnet, Grt: Garnet.

Group	I	I	I	I	I	II
Sample	EROD24R	EROD24R	EROD24R	EROD24R	EROD24R	EROD12
Analyses	F4S2	F8S1	F8S2	F16S8	F16S1	F12S1
Mineral	Hgrt	Hgrt	Grt	Grt	Grt	Hgrt
Area	MZ	MZ	MZ	MZ	MZ	TZ
Location	Choneftiko	Choneftiko	Choneftiko	Choneftiko	Choneftiko	Choneftiko
SiO_2	37.94	36.05	38.57	41.82	38.30	38.03
TiO_2	0.56	0.00	0.06	0.11	0.23	0.00
Al_2O_3	20.26	14.24	15.15	17.08	18.04	17.06
FeO	1.50	6.90	7.38	3.78	4.07	2.94
MnO	0.26	0.00	0.21	0.00	0.00	0.00
MgO	0.00	0.00	0.00	3.32	2.71	3.26
CaO	33.27	33.98	39.28	38.11	38.43	36.44
Na_2O	0.41	0.00	0.52	0.22	0.41	0.00
K_2O	0.00	0.00	0.10	0.00	0.02	0.00
Cr_2O_3	0.38	0.90	0.22	0.00	0.00	0.14
NiO	0.00	0.00	0.16	0.00	0.00	0.40
Total	94.59	92.07	101.66	104.45	102.21	98.28
Si	3.03	3.02	2.97	3.05	2.89	2.96
Ti	0.03	0.00	0.00	0.01	0.01	0.00
Al iv	0.00	0.00	0.03	0.00	0.11	0.04
Al vi	1.91	1.43	1.37	1.48	1.51	1.53
Cr	0.02	0.06	0.01	0.00	0.00	0.01
Fe3+	0.00	0.42	0.47	0.23	0.26	0.19
Fe2+	0.10	0.06	0.00	0.00	0.00	0.00
Mn	0.02	0.00	0.01	0.00	0.00	0.00
Mg	0.00	0.00	0.00	0.36	0.30	0.38
Ni	0.00	0.00	0.01	0.00	0.00	0.03
Ca	2.85	3.05	3.24	2.98	3.10	3.04
Total	7.97	8.06	8.12	8.11	8.19	8.17
Almandine	1.11	0.00	0.00	0.00	0.00	0.00
Andradite	0.04	22.26	25.49	13.58	13.79	10.85
Grossular	97.01	74.57	73.28	72.27	75.28	74.37
Pyrope	0.00	0.00	0.00	14.15	10.93	14.30
Spessartin	0.62	0.00	0.50	0.00	0.00	0.00
Uvarovite	1.23	3.17	0.73	0.00	0.00	0.48

Garnet crystals of TZs from Group-II rodingites are idiomorphic porphyroblasts of 220μm size (Fig. 72a), while they usually are part of the matrix coexisting with chlorite and vesuvianite. They usually occur within calcite cavities along with vesuvianite and chlorite (Fig. 72b). On the other hand, garnet and hydrogarnet of MZs

from Group-II rodingites appears as porous prorphyroblast (Fig. 77) within a chlorite rich matrix or in the form of 50μm size allotriomorphic impure crystals with micro inclusions of cacl-silicate minerals in a diopside rich matrix. Cr-bearing grossular and Cr-uvarovite neoblasts are usually formed at the expense of spinel (Fig. 79).

The chemical changes in such crystals are the result of secondary diffusional processes and the reaction between garnet and other mineral phases. Kimi garnets analyses of Group-I and Group-II rodingite are shown in Table 6.

Most garnets are classified as grossulars/hydrogrossulars (Grs: 72.27-97.01), with high andradite or pyrope contents (Adr: 0.04-25.49; Prp: 0.00-14.30 respectively) (Fig 69a), while many hydroandradite crystals also occur (Figs 77 and 78). On the other hand minor uvarovite crystals have been also detected as well. Garnets can be further divided according to their Fe_{total} and Mg contents (Fig. 73b) into Mg or Fe rich types respectively. Garnet of MZs from Group-I rodingites contains both types, while hydrogarnet analysis of TZs from Group-II rodingite corresponds to Mg-rich type. On the other hand, F4S2-hydrogarnet analysis of MZ (Sample EROD24R), presents low Mg and Fe_{total} contents as well. Hydrogarnet crystals of Group-I MZ rodingites present low total values (92.07-94.59 wt%) while hydrogarnet of Group-II TZ rodingites (Sample EROD12) presents higher total values (98.28 wt%).

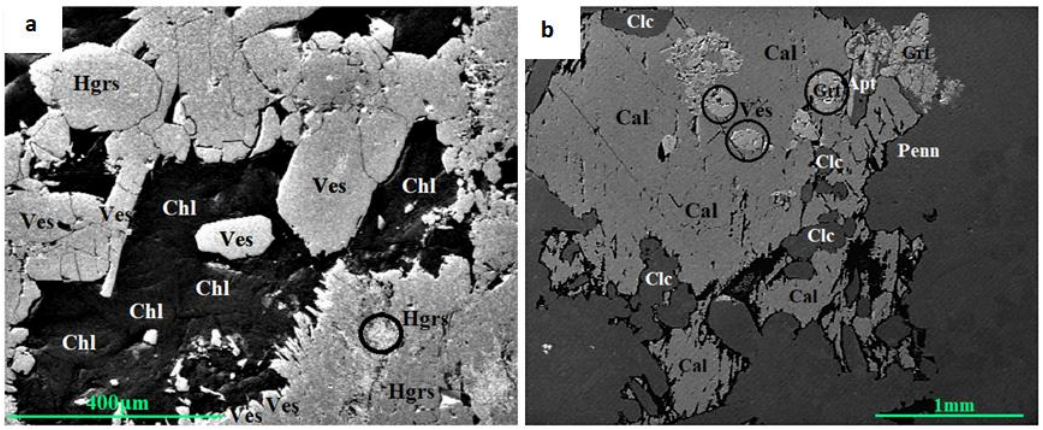

Figure 72. a. Group-II rodingite (Sample EROD12) from the TZ, BES SEM-EDS image consisting of vesuvianite (Ves) and hydrogrossular (Hgrs) porphyroblasts within a chlorite matrix (Chl)., b. Cavity within a clinochlore (Clc) - penninite (Penn) matrix filled with calcite (Cal), vesuvianite (Ves), garnet (Grt) and apatite (Apt) (Group-II TZ rodingites-Sample EROD12)

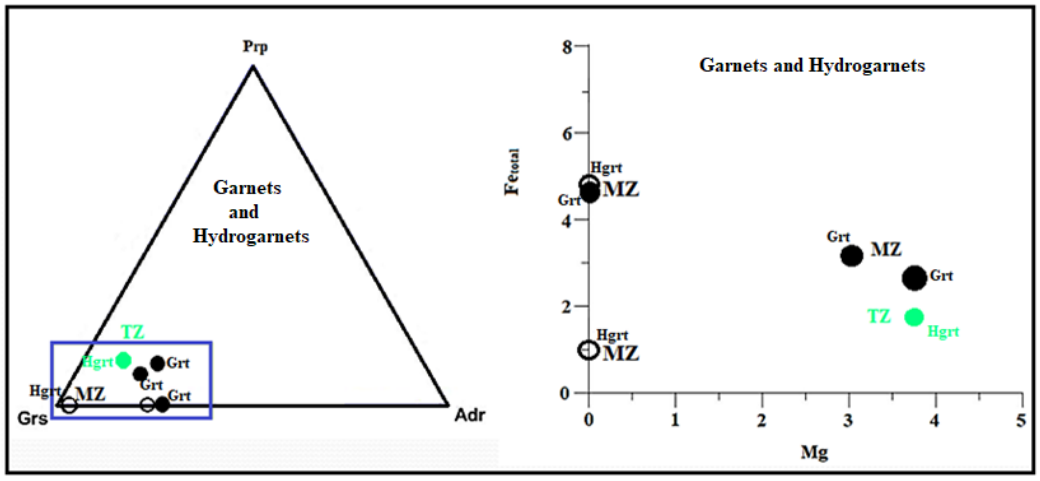

Figure 73. Garnet and Fe-Mg classification Diagram for MZs, TZs garnets and hydrogarnets.

7.3 Clinopyroxene and Amphibole

Pyroxene chemical analyses were conducted to Kimi rodingites. The chemical formula of pyroxenes is XYZ_2O_6 with $Z_{tetrahedral}$:Si,Al,Fe, $Y_{octahedral}$:Fe^{2+},Fe^{3+},Mg,Al,Cr,Ti,Mn^{2+} and $X_{octahedral}$:Na,Ca,Fe^{2+},Mg. They are divided into monoclinic (clinopyroxene) and orthorhombic (orthopyroxene) groups, while their discrimination is based on Morimoto et al. (1988), in which pyroxenes are divided into four groups: trapezoid pyroxenes, Calcium-Sodium pyroxenes, Sodium pyroxenes and other pyroxenes. Their recalculation (Table 7) was based on 6 oxygens.

In MZs diopside appears as fine grained crystals of 100-200 μm size, being the main mineral of the rodingitic matrix and coexisting with garnet (Fig. 70a). On the other hand, TZs consist of diopside grains of 500 μm size within a chlorite matrix or veinlets. Diopside usually forms radial aggregates around FeO rich cores (Fig. 75b).

Table 7. Representative mineral chemistry analyses for clinopyroxenes (Cpx) of Group-I rodingites.

Group	**I**	**I**
Sample	**EROD24R**	**EROD24R**
Analyses	**F5S2**	**F16S2**
Mineral	**Cpx**	**Cpx**
Area	**MZ**	**MZ**
Location	**Choneftiko**	**Choneftiko**
SiO_2	53.79	55.82
TiO_2	0.37	0.27
FeO	4.74	2.78
MnO	0.31	0.14
MgO	14.77	17.48
CaO	24.77	25.88
Na_2O	0.00	0.15
Total	98.75	102.52
Si	2.01	1.98
Ti	0.01	0.01
Fe^{+3}	0.00	0.03
Fe^{+2}	0.15	0.05
Mn	0.01	0.00
Mg	0.82	0.93
Ca	0.99	0.99
Na	0.00	0.01
Wo	50.53	50.15
En	41.91	47.13
Fs	7.56	2.72

Pure clinopyroxene analyses from MZs of Group-I rodingites are classified as diopside (Fig. 74) presenting high FeO contents (FeO: 2.78-4.74 wt%).

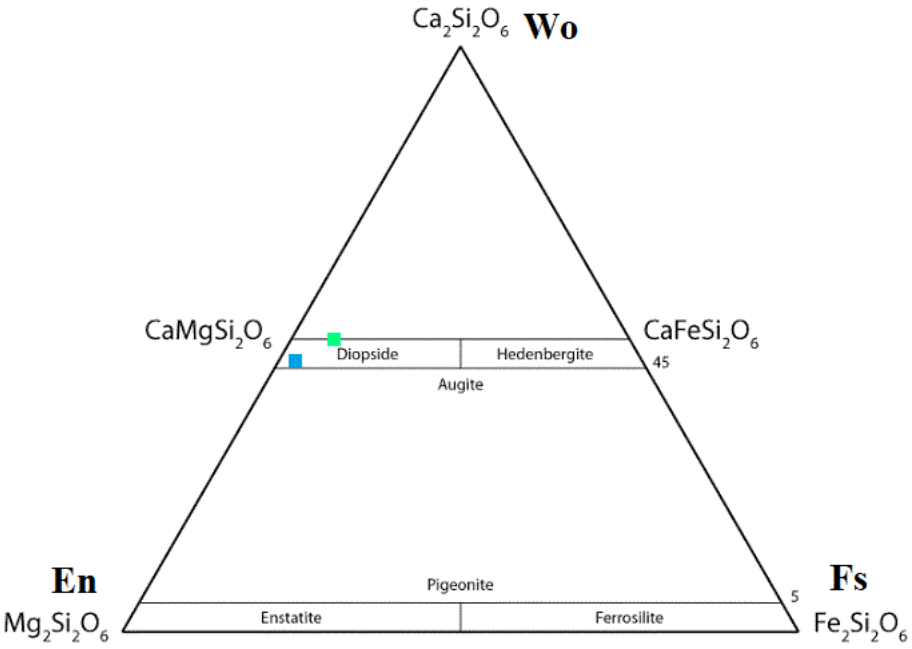

Figure 74. Clinopyroxene classification Diagram Wo-En-Fs (Morimoto et al., 1988) MZ: Marginal Zone.

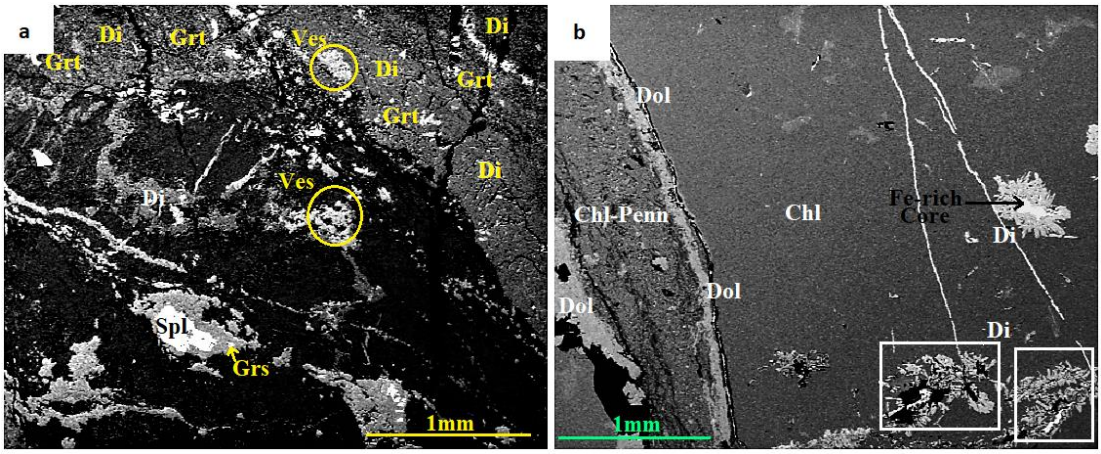

Figure 75. Group-I rodingite BES SEM-EDS image of Sample EROD24R from MZ. Diopside crystals (Di) coexist with garnet (Grt) and vesuvianite allotriomorphic grains. Later formed grossular grains (Grs) have replaced spinel cores (Spl) within a chlorite matrix. b. Group-II rodingite BES SEM-EDS image of Sample EROD7SC from TZ, consisting of a chlorite (Chl) rich matrix and diopside crystals (Di). Diopside forms radial aggregates with FeO rich cores, while it also appears within veinlets that cross the chlorite rich matrix. Veins of 750 μm size consisting of dolomite rich rims and later formed penninititc chlorite (Chl-Penn) cross the chlorite matrix as well.

On the other hand, the general chemical formula for amphiboles is $A_{0-1}B_2C_5T_8O_{22}(OH)_2$,where Tetrahedral: Si,Al,C octahedral: Al,Ti,Cr,Fe^{2+},Fe^{3+},Mg,Mn, B:Ca,Na,Mn,Fe^{2+},Mg , A:Na,K. The OH^- anions can also be replaced by Cl, F and O. Their recalculation is based on 23 O. Amphiboles are distinguished according to the cations that fill the B sites into the following four groups: Fe-Mn-amphiboles, Na-amphiboles, Ca-amphiboles and Ca-Na-amphiboles. Amphiboles are enriched in Ti, Al, Na and K with the increase of metamorphism grade, while in Ca-amphiboles the Mg/Mg+Fe ratio is also increased (Koutsovitis, 2009). On the other hand, Si and the sum of Fe+Mn+Mg+Ca are decreased with the increase of the metamorphism grade (Ernst and Liu, 1998). Al^{iv} and Al_t values depend on the T and P of metamorphism

respectively (Hammarston and Zen, 1986). Ti increases with the increase of $T_{metamorphsim}$(Spear and Gilbert, 1984), while Hynes (1982), claims that Ti and Na+K in amphiboles are related with Pmetamorphism and Tmetamorphism respectively. F5S7 amphibole analysis of TZ Group-II rodingites (Sample EROD7SC) (Table 8), shows high Mg contents (MgO: 39.28 wt%).

Table 8. Representative mineral chemical analyses for Group-I Kalimeriani-Grammatikiani rodingites amphibole (Amph).

Group	**II**
Sample	**EROD7SC**
Analyses	**F5S7**
Mineral	**Amph**
Area	**TZ**
Location	**Choneftiko**
SiO_2	43.51
TiO_2	0.04
Al_2O_3	8.81
FeO	2.82
MnO	0.59
MgO	39.28
Cr_2O_3	0.32
NiO	0.21
Si	6.04
Ti	0.00
Al iv	1.44
Al vi	0.00
Fe^{3+}	0.33
Fe^{2+}	0.00
Mn	0.07
Mg	8.12
Cr	0.04
Ni	0.02
OH*	2.00
Total	18.06

7.4 Chlorite

Chlorite chemical formula is $(Mg, Al^{iv}, Fe^{2+}, Fe^{3+})_{12}(Si,Al^{iv})_8O_{20}(OH)_{16}$. Its chemistry depends on the whole rock chemistry of the protolith and the metamorphic conditions.

Chlorites from Kimi belong either to rodingite matrix or appear in their serpentinitic host rock rims as the main mineral assemblage.

In TZs, chlorite has almost 130μm size, coexisting with idiomorphic garnet and vesuvianite porphyroblasts, while it mainly occurs as part of a microcrystalline matrix, including light or dark chlorite patches (Figs 69 and 70). The dark chlorite areas of the matrix are usually FeO richer compared to the light ones. On the other hand, chlorite can also occur within cryptocrystalline veins or within calcite cavities as well. Chlorite of MZs can either be part of the microcrystalline matrix, whereas it usually appears as part of the fine grained matrix along with idiomorphic hydroandradite neoblasts.

Kimi chlorite (Table 9), is Mg-rich (MgO: 25.36-35.52%), while the Cr_2O_3, NiO, K_2O, NaO values as well as Fe# are very low. Their recalculation is based on 28 O. Kimi chlorites have been classified according to their Si and Mg# contents (Fig. 76). In TZs two analyses are plotted within the sheridianite field (analyses F1S7 and F2S6 of Sample EROD23R). The vast majority of TZ chlorite crystals including all the analyses of sample EROD7SC and four analyses from sample EROD12 (Group-II rodingites) rodingites are classified as penninites. All the chlorite analyses from MZs of Group-II rodingites are classified as penninites, while one analysis (F6S2, Sample EROD22M) is classified as clinochlore. Moreover, one analysis from chloritic rim of Sample EROD7SR is classified as penninite as well.

Finally, based on their FeO and MgO contents chlorites can be divided into Fe and Mg rich respectively (Table 9 and Table 10). In Mg-rich chlorites MgO ranges from 35.52 to 30.94 wt%, while FeO ranges from 1.16 to 7.64 wt% respectively.

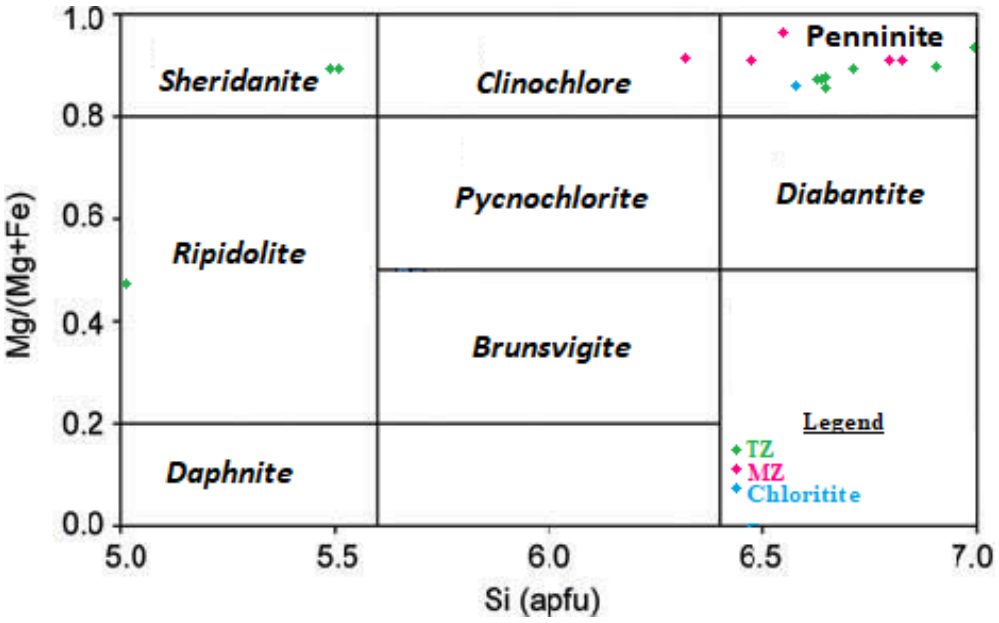

Figure 76. Chlorite discrimination diagram for Kimi Group-I and Group-II rodingites, TZ: Transitional Zone, MZ: Marginal Zone.

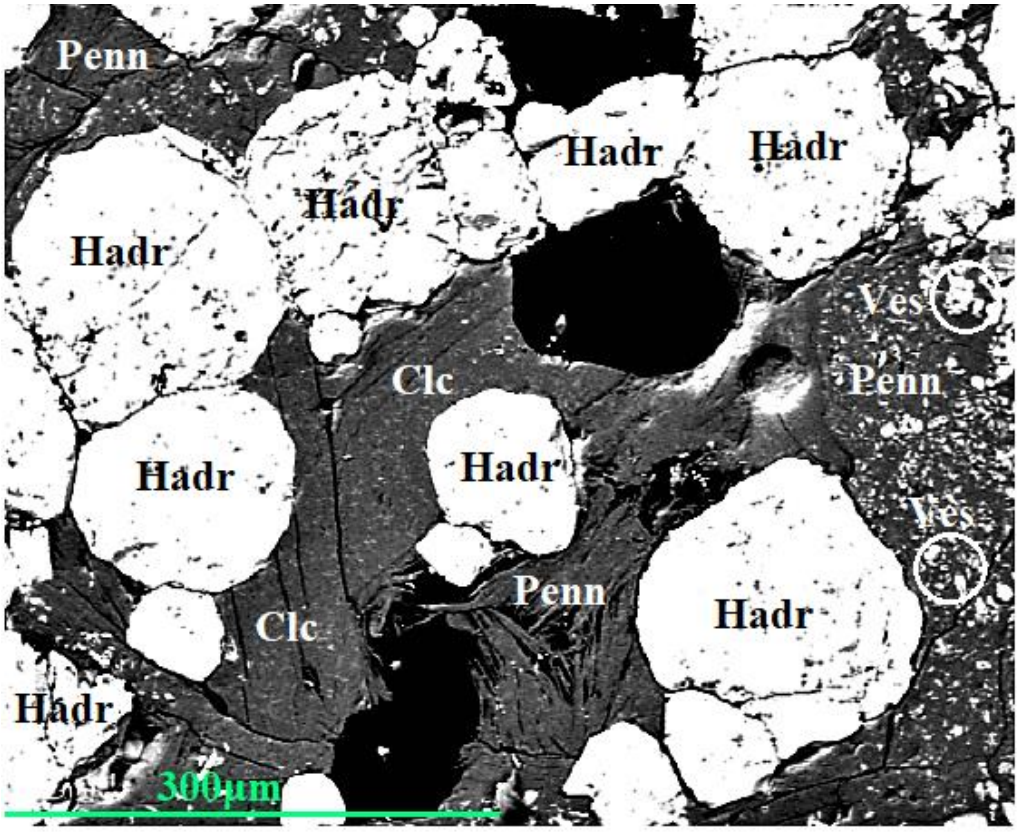

Figure 77. MZ Group-II rodingite BES SEM-EDS image of Sample EROD22M. Hydroandradite porphyroblasts are present within a chlorite (Chl) groundmass. Chlorite is classified as clinochlore (Clc) and penninites (Penn) as well. Microcrystalline vesuvianite inclusions are present within fine grained chlorite.

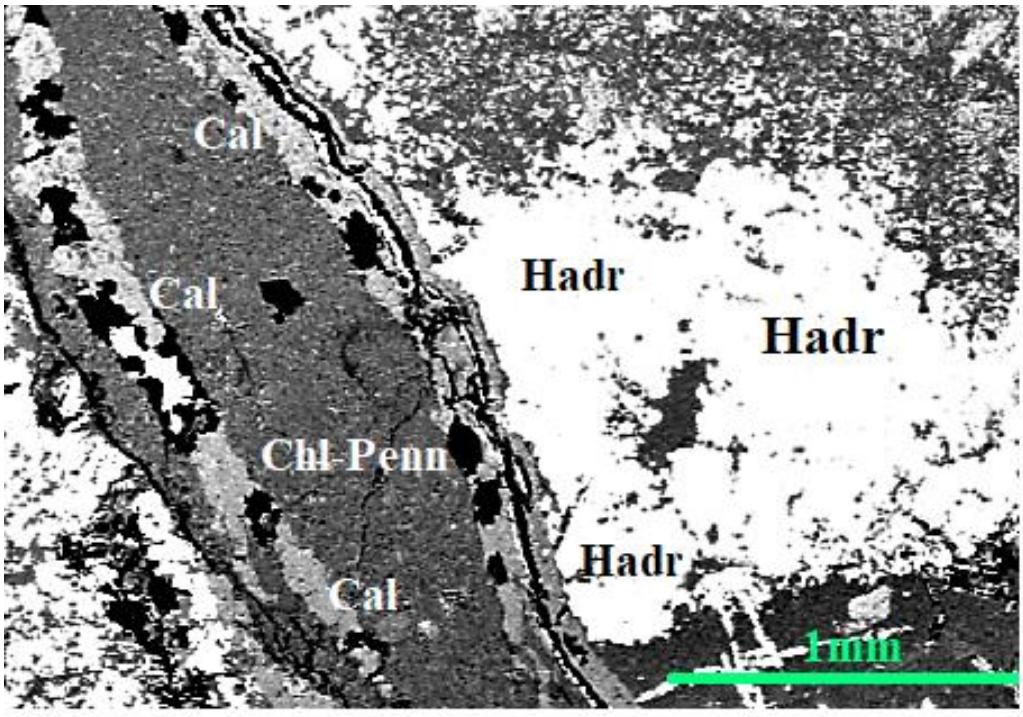

Figure 78. Group-II TZ rodingite BES SEM-EDS image of Sample EROD7SC consisting of Hydroandradite (Hadr) porphyroblast. Later chlorite-penninite (Penn)- calcite (Cal) rich veins also occur.

Table 9. Representative chemical chlorite (Chl) analyses for Group-I and Group-II rodingites (continued).

Group	II	II	II	II	I	I	II
Sample	EROD12	EROD12	EROD12	EROD12	EROD23R	EROD23R	EROD7SC
Analyses	F7S1	F7S2	F8S4	F15S2	F7S1	F2S6	F15S6
Mineral	Chlorite	Chlorite	Chlorite	Chlorite	Chlorite	Chlorite	Chlorite
Area	TZ	TZ	TZ	TZ	TZ	TZ	TZ
Location	Choneftiko	Choneftiko	Choneftiko	Choneftiko	Choneftiko	Choneftiko	Kalimeriani
SiO_2	35.42	36.07	33.89	34.49	27.80	27.84	37.07
TiO_2	0.01	0.00	0.00	0.07	0.37	0.21	0.20
Al_2O_3	13.07	10.48	12.06	13.89	18.20	19.74	12.25
FeO	4.60	2.73	3.82	3.42	2.50	2.39	3.21
MnO	0.22	0.07	0.00	0.34	0.56	0.02	0.41
MgO	32.32	35.89	31.48	32.10	32.82	32.32	31.85
CaO	0.00	0.31	0.09	0.00	0.24	0.44	0.85
Na_2O	0.00	0.00	0.00	0.28	0.00	0.00	0.00
K_2O	0.00	0.27	0.00	0.44	0.00	0.00	0.00
Cr_2O_3	0.04	0.05	0.29	0.00	0.00	0.48	0.85
NiO	0.00	0.00	0.00	0.00	0.00	0.00	0.00
Total	85.69	85.87	81.62	85.02	82.51	83.43	86.70
H_2O*	12.53	12.60	11.96	12.44	12.00	12.17	12.72
Si	6.75	6.86	6.77	6.61	5.51	5.45	6.93
Ti	0.00	0.00	0.00	0.01	0.06	0.03	0.03
Al^{iv}	1.25	1.14	1.23	1.39	2.49	2.55	1.07
Al^{vi}	1.70	1.21	1.61	1.77	1.80	2.04	1.66
Fe^{3+}	0.26	0.01	0.24	0.13	0.00	0.00	0.44
Fe^{2+}	0.47	0.42	0.40	0.41	0.66	0.55	0.07
Mn	0.04	0.01	0.00	0.05	0.09	0.00	0.07
Mg	9.18	10.17	9.37	9.17	9.69	9.44	8.88
Ca	0.00	0.06	0.02	0.00	0.05	0.09	0.17
Na	0.00	0.00	0.00	0.21	0.00	0.00	0.00
K	0.00	0.13	0.00	0.22	0.00	0.00	0.00
Cr	0.01	0.01	0.05	0.00	0.00	0.07	0.13
Ni	0.00	0.00	0.00	0.00	0.00	0.00	0.00
OH*	16.00	16.00	16.00	16.00	16.00	16.00	16.00
Fe#	0.07	0.04	0.06	0.06	0.06	0.05	0.05
Mg#	0.93	0.96	0.94	0.94	0.94	0.95	0.95
Total	35.66	36.03	35.69	35.97	36.35	36.22	35.43

Table 10.Representative chemical chlorite (Chl) analyses for Group-I rodingites and Chloritite

Group	II	II	Chloritite	II	II	II	II	II
Sample	EROD7SC	EROD7SC		EROD22M	EROD22M	EROD22M	EROD22M	EROD22M
Analyses	F16S1	F16S5	F7S2	F6S2	F8S2	F11S2	F12S4	F13S7
Mineral	Chlorite	Chlorite	Chlorite	Chlorite	Chlorite	Chlorite	Chlorite	Chlorite
Area	TZ	TZ	CL-Z	MZ	MZ	MZ	MZ	MZ
Location	Kalimeriani	Kalimeriani	Kalimeriani	Choneftiko	Choneftiko	Choneftiko	Choneftiko	Choneftiko
SiO_2	35.45	36.66	35.23	33.00	34.73	36.75	34.49	36.22
TiO_2	0.33	0.00	0.53	0.21	0.02	0.00	0.00	0.17
Al_2O_3	12.91	11.12	13.16	15.68	15.50	14.38	10.56	15.70
FeO	5.73	3.29	7.68	2.12	2.44	2.36	2.29	1.17
MnO	0.46	0.15	0.00	0.47	0.05	0.28	0.35	0.01
MgO	30.67	31.85	32.52	25.75	33.96	32.37	34.22	35.29
CaO	0.59	0.03	0.49	8.51	0.06	0.00	0.39	0.39
Na_2O	0.37	0.22	0.00	0.00	0.00	0.00	0.00	0.00
K_2O	0.00	0.00	0.00	0.22	0.00	0.00	0.18	0.00
Cr_2O_3	0.00	0.13	0.04	0.18	0.00	0.03	0.00	0.06
NiO	0.00	0.00	0.19	0.00	0.58	0.00	0.50	0.00
Total	86.51	83.46	89.85	86.14	87.33	86.16	82.97	89.01
H_2O*	12.52	12.31	12.86	12.34	12.86	12.80	12.15	13.24
Si	6.75	7.08	6.56	6.38	6.46	6.84	6.80	6.54
Ti	0.05	0.00	0.07	0.03	0.00	0.00	0.00	0.02
Al^{iv}	1.25	0.92	1.44	1.62	1.54	1.16	1.20	1.46
Al^{vi}	1.66	1.63	1.45	1.97	1.86	2.02	1.26	1.89
Fe^{3+}	0.23	0.38	0.09	0.23	0.18	0.37	0.02	0.18
Fe^{2+}	0.68	0.15	1.10	0.12	0.20	0.00	0.36	0.00
Mn	0.07	0.02	0.00	0.08	0.01	0.04	0.06	0.00
Mg	8.70	9.17	9.02	7.42	9.41	8.98	10.06	9.50
Ca	0.12	0.01	0.10	1.76	0.01	0.00	0.08	0.08
Na	0.27	0.17	0.00	0.00	0.00	0.00	0.00	0.00
K	0.00	0.00	0.00	0.11	0.00	0.00	0.09	0.00
Cr	0.00	0.02	0.01	0.03	0.00	0.00	0.00	0.01
Ni	0.00	0.00	0.03	0.00	0.09	0.00	0.08	0.00
OH*	16.00	16.00	16.00	16.00	16.00	16.00	16.00	16.00
Fe#	0.09	0.05	0.12	0.04	0.04	0.04	0.04	0.02
Mg#	0.91	0.95	0.88	0.96	0.96	0.96	0.96	0.98
Total	35.80	35.56	35.88	35.75	35.76	35.42	36.01	35.68

7.5 Serpentine

Serpentine is a product of olivine and pyroxene serpentinization (bastites). Its chemical formula is $X_{2-3}Si_2O_5(OH)_4$, where X = Mg, Fe^{2+}, Fe^{3+}, Ni , Al, Zn, or Mn. Serpentine minerals include antigorite, lizardite and chrysotile.

The chlorititic rims of Kimi chloritites were highly altered and only a few grains were preserved (Fig. 81). Serpentine is MgO rich, while FeO values are very low (0.00-3.92%). TiO_2 is almost absent, except for one analysis (TiO_2: 1.05%) (Table 11). Their recalculation is based on 7 O.

Table 11. Representative serpentine (Srp) analyses for chloritites.

	Chloritites		
Sample	**SERPV12R**	**SERPV12R**	**SERPV12R**
Analyses	**F6S4**	**F8S3**	**F9S4**
Mineral	**Srp**	**Srp**	**Srp**
Location	**Choneftiko**	**Choneftiko**	**Choneftiko**
SiO_2	38.35	41.37	39.40
TiO_2	0.42	1.05	0.00
Al_2O_3	0.00	5.18	9.30
FeO	3.92	0.73	0.00
MnO	0.00	0.00	0.07
MgO	38.16	36.81	35.31
CaO	0.00	0.04	0.00
K_2O	0.20	0.12	0.00
Cr_2O_3	0.11	0.00	0.30
NiO	0.88	0.19	0.44
Total	82.04	85.50	84.81
Si	1.94	1.94	1.86
Al	0.00	0.29	0.52
Ti	0.02	0.04	0.00
Fe	0.17	0.03	0.00
Mn	0.00	0.00	0.00
Mg	2.88	2.57	2.48
Ca	0.00	0.00	0.00
Na	0.00	0.00	0.00
K	0.01	0.01	0.00
Cr	0.00	0.00	0.01
Ni	0.04	0.01	0.02
Total	5.05	4.88	4.88

7.6 Spinel Group Minerals

The general chemical formula for spinel group minerals is XY_2O_4, with X: Mg, Fe^{2+}, Mn, Zn, Ni, and Y: Al, Fe^{3+},Cr. Spinels were detected in the serpentinite rims of Group-II TZ rodingites (Table 12).

In chloritic rims, minor magnetite grains (Fig. 81) and one spinel were detected, while in TZ of Group-I rodingites no magnetite was detected. Kimi spinels are Cr rich (38.02-43.58%). Their recalculation is based on 32 oxygens.

Table 12. Representative spinel analyses of Chloritites and Group-I Rodingites.

Choneftiko Spinel Analyses				
Rock Type	**Chloritite**	**Rodingite**	**Rodingite**	**Rodingite**
Group		**I**	**I**	**I**
Sample	**SERPV12R**	**EROD23R**	**EROD23R**	**EROD23R**
Area	**Rim**	**TZ**	**TZ**	**TZ**
Location	**Choneftiko**	**Choneftiko**	**Choneftiko**	**Choneftiko**
TiO_2	0.16	0.00	0.00	0.00
Al_2O_3	27.20	24.26	24.08	24.79
FeO^t	19.50	18.96	17.17	17.54
MgO	11.50	13.41	13.75	12.04
Cr_2O_3	40.70	42.78	41.58	43.25
Total	99.06	99.41	96.58	97.62
Cr	0.98	1.03	1.01	1.06
Ti	0.00	0.00	0.00	0.01
Al	0.98	0.87	0.87	0.91
Fe^{3+}	0.03	0.09	0.12	0.02
Fe^{2+}	0.47	0.39	0.32	0.43
Mg	0.52	0.61	0.63	0.56
Total cat	2.99	3.00	2.95	2.98
Mg#	0.53	0.61	0.66	0.56
Cr#	0.50	0.54	0.54	0.54
Fe^{2+}/Fe^{3+}	16.82	4.15	2.68	19.68

Based on their Mg# and Cr# spinel grains have been classified into spinel, magnesiochromite, hercynite and chromite (Fig. 80). Spinel grains from Group-I rodingites are classified as Mg-chromites, while spinel analysis from chloritic rim is plotted in the border line between spinel and Mg-chromite fields.

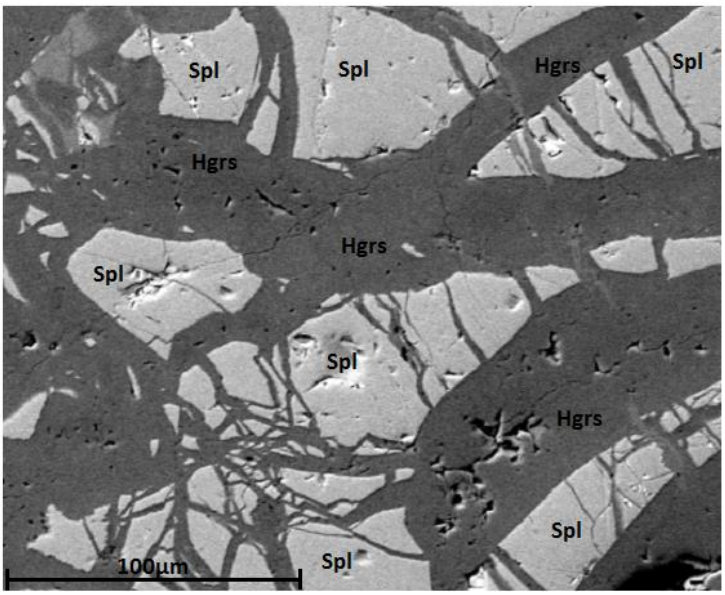

Figure 79. Group-I rodingite photomicrograph of Sample EROD23R including spinel grains. Cr-Hydrogrossular is formed at the expense of spinel.

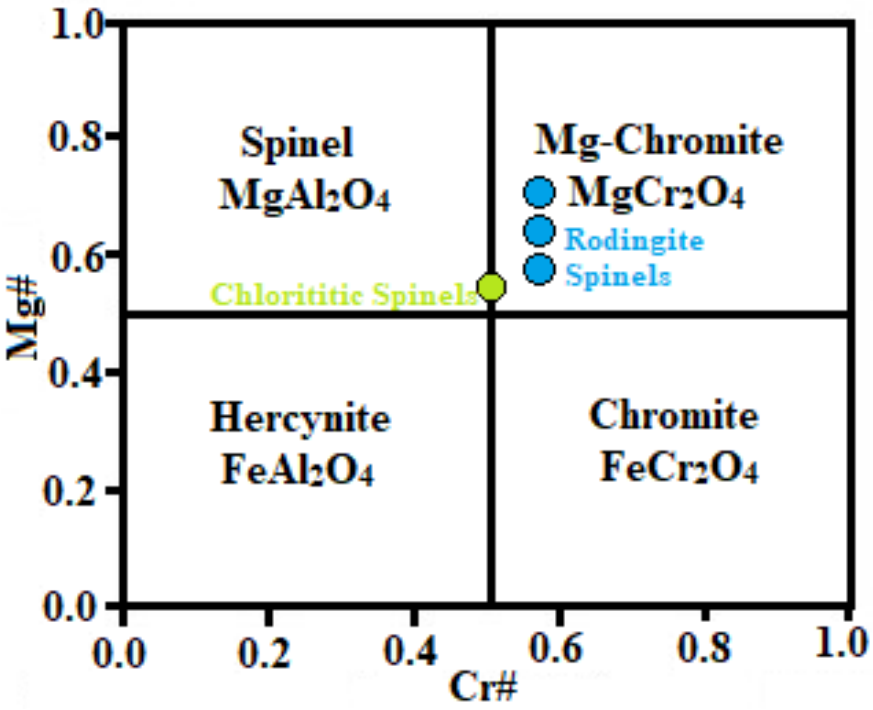

Figure 80. Chemical plot for spinel group minerals of Kimi chloritites (green symbols) and TZ of Group-I rodingites (Sample EROD23R, blue symbols.) Mg#-Cr# (Dick&Bullen,1984).

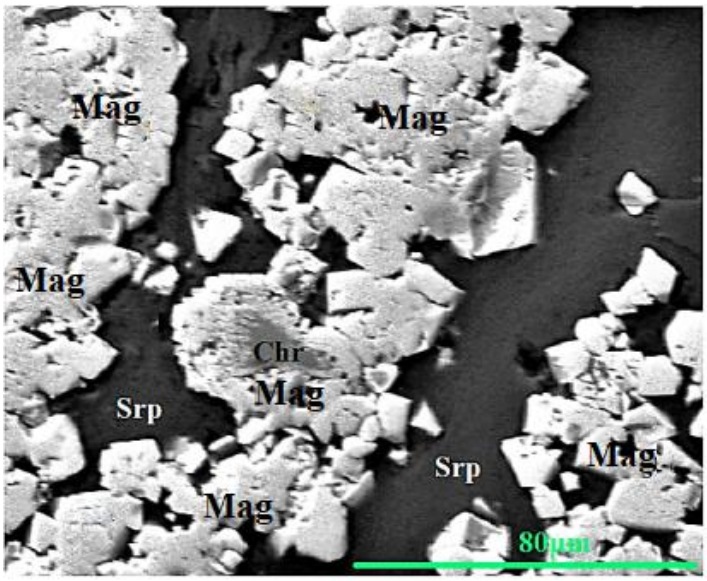

Figure 81. Chlorititic BES SEM-EDS image (Sample EROD7SR). It includes a few relict serpentine (Srp) grains along with magnetite grains (Mag). Relict chromite cores (Chr) altered to magnetite also occurs.

7.7 Calcite

Calcite was mainly detected within veins or cavitis in the rodingite groundmass (Figs 78, 72b and 69b) surrounding earlier formed minerals such as garnet, vesuvianite, apatite and chlorite. In some cases minor dolomite was detected as well. Calcite substitutes Mg^{2+} for Ca^{2+}, creating magnesian calcites with a range of Mg^{2+} contents. Kimi calcite (Table 13) present minor MgO contents (MgO: 0.05-0.51%) and low FeO values (0.00-0.10%).

Table 13. Representative calcite (Cal) analyses for Group-II TZ rodingites.

Group	II	II
Sample	EROD12	EROD7SC
Analyses	F16S2	F11S1
Mineral	Cal	Cal
Area	TZ	TZ
Location	Choneftiko	Kalimeriani
Na_2O	0.00	0.00
MgO	0.05	0.51
K_2O	0.04	0.00
CaO	52.57	60.32
TiO2	0.41	0.08
Cr_2O_3	0.17	0.00
MnO	0.00	0.04
FeO	0.00	0.10
NiO	0.00	0.01
Total	53.24	61.07

7.8 Quartz

Quartz has been detected in the Transitional and Marginal Zones of Choneftiko rodingites and their recalculation is based on 2 oxygens. In Marginal Zones it appears as grains within a chlorite-hydroandradite rich matrix.

7.9 Apatite

Apatite is a phosphate mineral with the following general formula: $Ca_{10}(PO_4)_6X_2$ where X can be F (fluorapatite), OH^- (hydroxyapatite), or Cl^- (chlorapatite). There are many possible substitutions such as Ca^{2+} replacement by Sr, Ba, Pb, Na^+ and PO_4^{-3} replacement by AsO_4, VO_4, SiO_4 or CO_3^{-2} (Elliot et.a al, 2002). They are mainly present as accessory minerals in igneous rocks and in small amounts in metamorphic rocks too. Apatite was detected in Group-II rodingites (Table 14). Their recalculation is based on 25 oxygens.

Apatite is usually enriched in REE and other elements such as S and Si. Group-II rodingites include apatite crystals which are enriched in LREE including high Y_2O_3 and Ce_2O_3 contents (7.53 wt% and 2.16 wt% respectively), while La_2O_3 value is 0.19 wt%. Apatite analyses seem to be SiO_2 rich. This is probably caused by the presence of other minerals surrounding apatite, which affect the analysis or by the presence of cryptocrystalline inclusions within the apatite crystal. Apatite from MZ Group-II rodingites (Choneftiko) exhibits quite high SiO_2 values (1.01 wt%), while no REE are present. Due to its total oxide (Total: 98.94 wt%) it is classified as hydroxyl-apatite, while it also contains low ClO_2 values (0.29 wt%). Apatite appears as patches of 10 μm size within the chlorite matrix of MZ and TZ or within diopside crystals respectively (Fig. 82).

Table 14. Apatite (Apt) analyses for TZ and MZ of Group-II Kalimeriani and Choneftiko Rodingites.

Group	**II**	**II**
Sample	**EROD7SC**	**EROD22M**
Analyses	**A9**	**A23**
Mineral	**Apt**	**Apt**
Area	**TZ**	**MZ**
Location	**Kalimeriani**	**Choneftiko**
CaO	56.22	61.53
P_2O_5	28.66	36.11
MgO	1.57	0
SiO_2	6.38	1.01
Cl_2O	0.11	0.29
Y_2O_3	7.53	0
La_2O_3	0.19	0
Ce_2O_3	2.16	0
Total	102.82	98.94

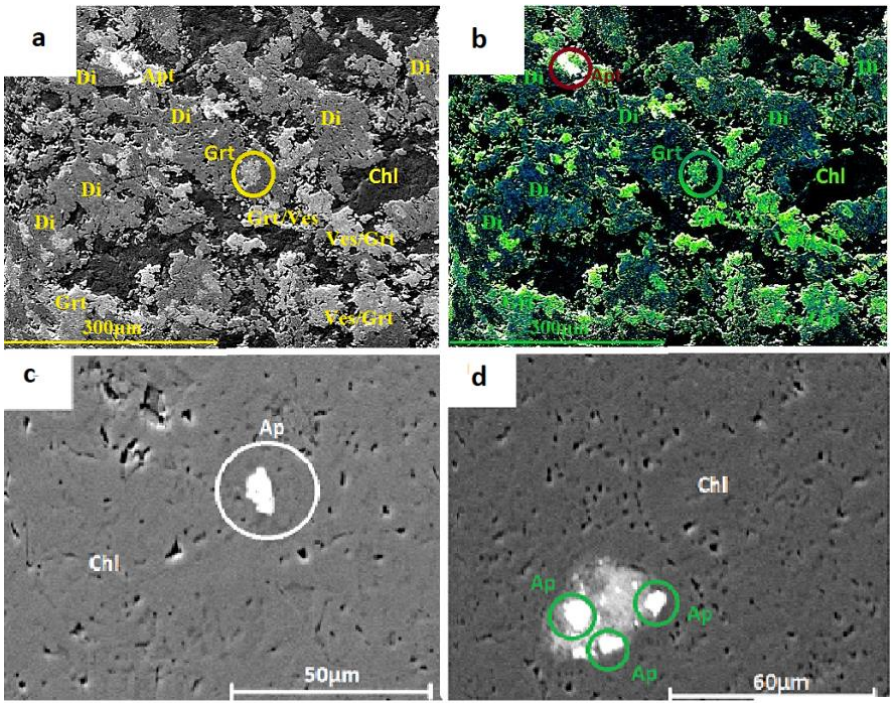

Figure 82. a.b. Group-I MZ rodingite BES SEM-EDS image (Sample EROD22M) including fine grained diopside (Di) grains and allotriomorphic microcrystalline garnet (Grt) and vesuvianite (Ves). Apatite patches are observed intergranular between diopside and garnet or vesuvianite. Diopside is porous with microinclusions b. Pseudo-colored BES SEM-EDS image of Fig. 76a. c,d. Group-II rodingite of Sample EROD7SC from the Transitional Zone including apatite patches in a chlorite (Chl) matrix.

7.10 Allanite

It occurs with clinopyroxenes, calcic amphiboles, garnets and other minerals, being the result of the replacement of Ca^{2+} and Fe^{3+} (in epidote) from REE and Fe^{2+} respectively. Allanite appears as patches within a diopside-garnet rich microcrystalline matrix of Group-I rodingites (Fig. 83). In Kimi one allanite was analyzed and shows a clear enrichment in Ce_2O_3 (LREE), while it is also enriched in CaO (CaO: 14.82 wt%) (Table 15).

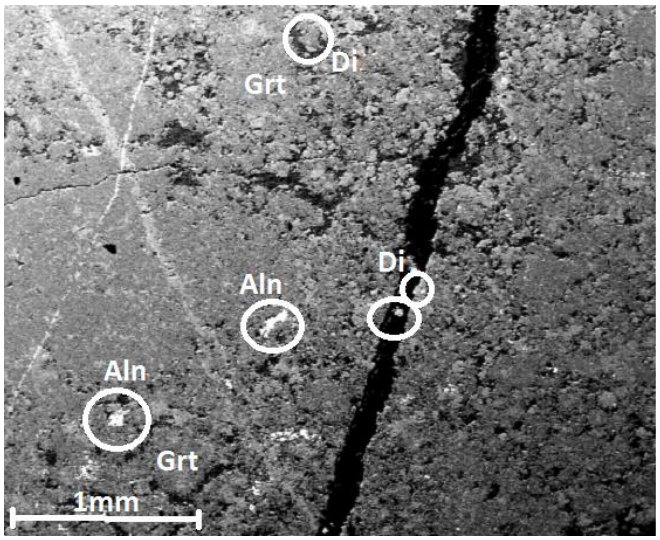

Figure 83. BES SEM-EDS image of MZ from Group-I rodingite (Sample EROD24R) with allanite (Aln) patches appearing in a diopside (Di) garnet (Grt) rich matrix

The CNMMN formal approved the name allanite-(Ce) (Nickel & Mandarino, 1987). Cerium is the dominant REE in most “allanite (Armbruster et al., 2006). Many names have been suggested for REE-bearing allanites. In our case the most probable name is Ferriallanite-(Ce). Its formula is $CaCeFe^{3+}AlFe^{2+}[Si_2O_7][SiO_4]O(OH)$, and is the analogue of allanite-(Ce) with Fe^{3+} dominant in the octahedral M1 site, while it presents a metasomatic origin (Kartashov et al., 2002).

Table 15. Allanite (Aln) analyses form MZ of Group-I Rodingite.

Group	**I**
Sample	**EROD24R**
Analyses	**F12S8**
Mineral	**Aln**
Area	**MZ**
Location	**Choneftiko**
SiO_2	36.09
Al_2O_3	17.93
FeO	12.81
MgO	0.53
CaO	14.82
NiO	1.15
Ce_2O_3	16.67
Total	100.00

8 Geochemistry

Whole rock chemical analyses for both Kimi rodingites and ultramafic rocks are presented in the following Table (Table 16).

Table 16. Whole rock chemistry analyses for major, trace elements and REE of 20 rodingite and 5 serpentinite samples wt% for major elements and ppm for trace elements and REE.

Sample	SERPV12RR	SERPV12R	EROD12	SERP22	EROD22L	EROD22M	EROD7	EROD6	SERP6-7	EROD7SR	EROD7SC	EROD7SCC
Rock Type	Ultramafic	Rodingite	Rodingite	Serpentin	Rodingite	Rodingite	Rodingite	Rodingite	Ultramafic	Ultramafic	Rodinigte	Rodingite
SiO_2	35.57	35.59	35.06	39.37	36.8	35.12	43.56	41.51	39.3	33.38	38.14	39.44
Al_2O_3	6.44	10.28	17.17	2.29	17.76	13.11	11.34	13.02	2.92	13.3	14.02	11.33
Fe_2O_3	8.35	3.25	2.67	7.85	1.21	4.32	1.34	1.83	7.6	3.36	0.39	1.62
MgO	36.11	35.95	10.89	32.76	7.53	23.87	9.02	7.85	32.84	33.99	12.36	16.42
CaO	0.06	1.59	27.28	5.73	31.73	12.64	31.93	32.44	5.01	2.57	26.75	22.81
Na_2O	<0.01	<0.01	0.01	<0.01	<0.01	<0.01	0.07	0.03	<0.01	<0.01	<0.01	<0.01
K_2O	<0.01	0.02	<0.01	<0.01	<0.01	<0.01	<0.01	<0.01	<0.01	<0.01	<0.01	<0.01
TiO_2	<0.01	0.02	0.02	<0.01	0.02	0.05	0.02	0.02	<0.01	<0.01	<0.01	<0.01
P_2O_5	0.01	0.01	0.04	0.01	0.04	0.08	0.04	0.08	<0.01	<0.01	<0.01	<0.01
MnO	0.11	0.18	0.47	0.12	0.29	0.19	0.08	0.12	0.12	0.11	0.07	0.17
LOI	12.8	12.8	6.1	11.2	4.5	10.4	2.5	3	11.6	13.2	8.2	8.1
Sum	99.95	99.93	99.8	99.94	99.89	99.82	99.94	99.92	99.94	99.91	99.92	99.91
Be	<1	<1	5	<1	<1	<1	2	3	<1	<1	4	6
Co	96.1	74.4	18.3	82.7	15.6	59.7	10.1	13.4	73.7	25.2	1.9	8.7
Cs	<0,1	0.1	<0.1	<0.1	<0.1	<0.1	<0.1	<0.1	0.1	0.5	<0.1	0.1
Ga	3.6	4.5	3.5	1.8	6.5	2.4	8	8.5	1.4	5.4	10.4	4.5
Hf	0.1	1.7	9.6	0.2	2.2	12.9	2.7	3	0.2	6.6	5	7.8
Nb	2.9	16.5	89	4.6	14.8	32.6	45.9	112.9	4	90.2	80.2	101.6
Rb	0.3	1.3	0.6	0.4	0.1	0.4	0.2	<0.1	0.4	0.5	<0,1	0.2
Sn	<1	<1	<1	<1	<1	<1	3	3	<1	<1	<1	<1
Sr	1.5	6.9	97.3	2	21.6	12.9	47.9	50.4	8.3	7.4	24.8	19.2
Ta	0.2	2.9	8.3	0.2	0.8	1.6	3	17.6	0.3	6.6	6.1	6.1
Th	<0.2	13.4	30.2	<0,2	27.8	45.1	7.9	9.4	<0,2	10.4	8	8.2
U	0.2	1.1	4.5	<0.1	0.5	1.1	7.5	12.9	0.6	6.1	6.1	4.2
V	36	37	11	36	<8	13	<8	<8	34	<8	<8	<8
W	<0.5	<0.5	3.7	0.7	0.7	<0.5	0.8	<0.5	0.7	<0.5	<0.5	<0.5
Zr	2.2	57.8	241.5	8.8	72.7	391.3	36.4	37.8	6.1	101.7	86.1	107.1
Y	3.1	10.1	74	1	12.6	19.5	11.3	15	0.5	71.7	35	52.9
La	1.6	6.7	126.3	2.8	110.9	156.6	2.4	4.8	2	8.7	6	11.1
Ce	4.2	20	305.6	7	214.4	290.2	6.9	12.1	5.1	26.2	17.7	28.6
Pr	0.5	2.41	32.14	0.81	21.12	27.92	0.86	1.25	0.53	3.38	2.32	3.46
Nd	1.9	9.4	107.4	2.5	68.6	87.4	2.9	4.1	1.6	11.9	8.7	11.1
Sm	0.47	2.74	21.46	0.31	10.36	11.48	1.4	1.62	0.08	5.13	3.49	4.54
Eu	<0,02	0.07	1.34	0.12	2.47	2.61	0.07	0.08	0.05	<0.02	0.04	0.1
Gd	0.54	2.64	17.18	0.18	7.68	8.04	1.24	1.71	0.06	7.56	4.49	5.78
Tb	0.09	0.41	2.37	0.03	0.79	0.91	0.29	0.39	<0.01	1.57	1.09	1.31
Dy	0.51	2.29	13.81	0.16	3.66	4.55	2.18	2.73	0.06	11.2	7.77	9.44
Ho	0.12	0.43	2.58	0.03	0.44	0.69	0.35	0.49	<0,02	2.29	1.46	1.93
Er	0.37	1.16	7.73	0.07	0.97	1.74	1.07	1.6	0.04	6.61	4.79	6.11
Tm	0.06	0.18	1.18	0.02	0.13	0.25	0.23	0.28	<0.01	1.02	0.84	0.95
Yb	0.4	1.09	7.56	0.11	0.78	1.73	1.84	2.11	0.06	6.58	5.63	6.7
Lu	0.06	0.2	1.07	0.01	0.11	0.29	0.26	0.31	0.01	0.9	0.8	0.94
TOT/C	0.19	0.05	0.17	0.06	<0.02	0.85	0.04	0.05	0.04	0.36	1.01	0.65
TOT/S	<0.02	<0.02	<0.02	<0.02	<0.02	<0.02	<0.02	<0.02	<0.02	<0.02	<0.02	<0.02
Mo	<0.1	<0.1	<0.1	<0.1	<0.1	<0.1	<0.1	<0.1	<0.1	<0.1	<0.1	<0.1
Cu	7.4	12.2	110.6	9.1	<0,1	1.3	1	1.2	6.6	0.2	0.7	0.3
Pb	1.2	1.1	1.3	1.7	0.9	4.5	2	3.1	0.7	2.8	2.8	2.7
Zn	20	29	30	18	34	17	9	15	19	17	12	32
Ni	1900	764.8	90.7	1982.9	24.2	201.6	154.4	93.6	1926.5	61	9.2	30.8
As	1.1	<0.5	<0.5	1.7	<0.5	<0.5	2.8	3	11.7	<0.5	<0.5	<0.5
Cd	<0.1	<0.1	<0.1	<0.1	<0.1	<0.1	<0.1	<0.1	<0.1	<0.1	<0.1	<0.1
Sb	<0.1	<0.1	<0.1	<0.1	<0.1	<0.1	0.3	0.2	<0.1	<0.1	<0.1	<0.1
Bi	<0.1	<0.1	<0.1	<0.1	<0.1	<0.1	<0,1	<0,1	<0.1	<0.1	<0.1	<0.1
Ag	<0.1	<0.1	<0.1	<0.1	<0.1	<0.1	<0,1	<0,1	<0.1	<0.1	<0.1	<0.1
Hg	<0.01	<0.01	<0.01	<0.01	0.01	0.05	<0.01	0.04	<0.01	<0.01	<0.01	<0.01
Tl	<0.1	<0.1	<0.1	<0.1	<0.1	<0.1	<0.1	<0.1	<0.1	<0.1	<0.1	<0.1
Se	<0.5	<0.5	<0.5	<0.5	<0.5	<0.5	<0.5	<0.5	<0.5	<0.5	<0.5	<0.5
Ba	0.282	0.133	0.007	0.314	0.002	0.037	0.016	0.016	0.313	<0.002	<0.002	<0.002
Sc	2	1	4	3	2	3	4	4	2	4	18	12
Au	8	10	2	10	<1	3	2	3	9	1	<1	<1
Cr	0.0007	0.0006	<0.0005	0.0017	<0.0005	<0.0005	<0.0005	<0.0005	0.0009	<0.0005	<0.0005	<0.0005

Sample	EROD26M	EROD26L	EROD23M	EROD23R	EROD24R	EROD24M	EROD11	EROD21	EROD10	EROD18	SERP25R	EROD25	EROD25L
Rock Type	Rodingite	Rodingite	Rodingite	Rodingite	Rodingite	Rodingite	Rodingite	Rodingite	Rodingite	Rodingite	Ultramafic	Rodingite	Rodingite
SiO_2	37.36	39.95	38.33	37.38	43.46	42.96	38.03	39.26	33.47	34.05	40.00	36.44	37.45
Al_2O_3	16.63	11.12	22.15	20.97	9.24	9.68	17.85	15.85	13.25	16.52	0.66	19.08	18.57
Fe_2O_3	2.55	3.80	0.63	2.08	6.40	4.70	0.20	0.29	3.79	0.22	7.98	0.85	1.18
MgO	4.75	18.04	0.82	6.51	17.87	16.85	4.02	5.91	34.70	1.67	35.14	2.74	2.83
CaO	34.47	20.56	35.96	29.55	17.78	19.81	36.23	35.08	1.71	38.14	2.58	37.61	36.68
Na_2O	<0.01	<0.01	0.03	0.03	0.03	0.02	<0.01	<0.01	<0.01	0.05	<0.01	<0.01	<0.01
K_2O	<0.01	<0.01	<0.01	<0.01	<0.01	<0.01	<0.01	<0.01	0.02	<0,01	<0.01	<0.01	<0.01
TiO_2	0.03	0.03	0.04	0.05	0.08	0.07	0.02	0.03	0.03	0.02	<0.01	0.03	0.02
P_2O_5	0.01	0.02	0.01	0.02	0.02	0.03	<0.01	0.01	0.04	0.02	0.01	<0.01	<0.01
MnO	0.23	0.23	0.04	0.07	0.15	0.12	0.05	0.06	0.16	<0.01	0.10	0.22	0.18
LOI	3.70	6.10	1.90	3.00	4.70	5.50	3.50	3.40	12.70	9.20	12.80	2.90	2.90
Sum	99.79	99.88	99.91	99.82	99.84	99.88	99.92	99.92	99.94	99.91	99.94	99.85	99.89
Be	10.00	3.00	<1	8.00	4.00	5.00	7.00	5.00	<1	<1	<1	17.00	9.00
Co	13.20	39.90	2.20	18.50	55.30	35.50	0.80	1.10	22.00	1.20	94.20	5.50	10.50
Cs	<0.01	<0.10	<0.1	<0.1	0.40	0.20	<0.1	<0,1	0.90	0.10	<0,1	<0.1	<0.1
Ga	1.20	1.00	6.70	7.70	10.90	7.20	7.70	7.40	5.50	15.10	2.30	5.60	5.00
Hf	8.80	5.80	3.70	12.10	9.20	6.40	3.00	2.60	2.60	2.90	<0.1	8.10	6.00
Nb	493.00	126.90	152.90	274.90	164.40	113.20	86.30	79.10	29.50	15.70	0.50	154.30	81.70
Rb	0.30	<0.1	0.10	0.20	0.80	0.20	<0.1	<0.1	3.40	0.30	0.30	<0,1	0.20
Sn	<1	<1	9.00	8.00	3.00	1.00	3.00	1.00	<1	<1	<1	7.00	8.00
Sr	43.70	26.10	17.20	32.50	14.80	12.10	32.90	24.00	5.00	117.80	3.00	37.20	38.30
Ta	55.90	16.70	26.70	41.90	46.50	23.70	6.80	9.70	2.20	1.90	0.10	22.70	10.30
Th	20.50	21.30	8.90	27.80	22.80	21.90	10.20	11.10	15.00	22.70	<0,2	27.00	17.30
U	9.30	11.90	5.40	17.90	11.00	8.40	8.40	9.90	1.20	1.90	0.20	13.00	6.60
V	<8	11.00	<8	16.00	24.00	48.00	<8	<8	<8	<8	40.00	<8	<8
W	3.50	0.80	<0.5	0.80	1.00	<0.5	0.70	2.20	<0.5	<0.5	1.00	0.70	<0.5
Zr	184.70	135.70	71.20	250.90	178.00	146.20	68.30	46.60	62.30	83.10	1.70	159.80	128.60
Y	148.90	72.60	54.50	145.90	109.50	70.60	57.90	49.50	19.50	22.10	0.40	171.90	73.90
La	55.50	16.80	13.10	38.90	55.80	16.00	10.00	11.40	11.80	56.30	0.30	27.40	27.50
Ce	137.40	45.00	35.10	93.80	147.90	39.80	27.10	30.50	28.20	103.30	0.20	70.20	65.00
Pr	14.43	5.23	4.04	10.58	16.08	4.86	3.04	3.50	3.16	10.31	0.03	8.13	7.02
Nd	45.80	19.30	14.00	36.50	48.80	18.90	11.90	13.50	13.50	35.50	<0.3	30.60	22.30
Sm	11.93	6.12	4.48	10.86	10.12	6.00	4.36	4.78	3.09	6.50	<0.05	11.22	5.63
Eu	0.43	0.16	0.14	0.36	0.44	0.18	0.17	0.22	0.28	1.28	<0.02	0.59	0.20
Gd	14.41	7.38	5.18	13.01	10.04	7.49	6.39	6.16	3.16	5.42	0.08	15.74	6.93
Tb	3.08	1.57	1.02	2.83	1.90	1.51	1.30	1.18	0.50	0.75	0.01	3.55	1.40
Dy	23.03	11.12	7.42	20.82	14.19	10.79	9.85	8.56	3.24	4.25	0.07	26.80	10.30
Ho	4.67	2.35	1.44	4.37	2.85	2.34	2.08	1.68	0.67	0.73	<0.02	5.77	2.30
Er	14.47	7.49	5.14	14.24	9.47	7.55	6.28	5.29	1.98	2.13	0.05	18.40	7.29
Tm	2.24	1.24	0.83	2.36	1.62	1.18	0.93	0.75	0.31	0.30	<0,01	2.76	1.21
Yb	15.08	8.47	5.88	15.67	10.83	7.79	5.77	4.85	2.17	1.81	0.06	16.49	8.16
Lu	2.03	1.20	0.82	2.25	1.51	1.12	0.82	0.69	0.33	0.30	<0.01	2.20	1.14
TOT/C	0.06	0.03	0.83	0.03	0.20	0.97	0.18	0.25	0.06	2.29	0.04	<0.02	0.03
TOT/S	<0.02	<0.02	<0.02	<0.02	<0.02	<0.02	<0.02	<0.02	<0.02	<0.02	<0.02	<0.02	<0.02
Mo	<0.1	<0.1	<0,1	<0.1	<0.1	<0.1	<0.1	<0.1	<0.1	0.20	<0.1	<0.1	<0.1
Cu	0.60	12.60	2.90	1.20	2.10	2.00	15.10	0.40	2.60	4.10	33.70	0.20	1.60
Pb	20.00	32.80	2.70	4.40	10.10	476.40	4.10	31.30	41.30	5.30	12.10	0.50	16.40
Zn	17.00	15.00	1.00	6.00	52.00	27.00	5.00	5.00	25.00	<1	22.00	20.00	18.00
Ni	39.80	231.50	9.30	209.60	512.30	328.00	1.80	2.10	240.00	19.70	2,311.50	4.00	84.60
As	<0.5	<0.5	<0.5	0.60	<0.5	<0.5	<0.5	<0.5	<0.5	<0.5	<0.5	<0.5	2.00
Cd	<0.1	<0.01	<0.1	<0.1	<0.1	<0.1	<0.1	<0.1	<0.1	<0.1	<0.1	<0.1	<0.1
Sb	<0.1	<0.01	<0.1	0.30	<0.1	<0.1	<0.1	<0.1	<0.1	<0.1	<0.1	<0.1	<0.1
Bi	<0.1	<0.01	0.10	0.30	<0.1	<0.1	<0.1	<0.1	<0.1	<0.1	<0.1	<0.1	0.10
Ag	<0.1	<0.01	<0.1	<0.1	<0.1	<0.1	<0.1	<0.1	<0.1	<0.1	<0.1	<0.1	<0.1
Hg	0.09	0.01	<0.01	<0.01	<0.01	0.02	<0.01	<0.01	<0.01	<0.01	<0.01	<0.01	<0.01
Tl	<0.1	<0.1	<0.1	<0.1	<0.1	<0.1	<0.1	<0.1	<0.1	<0.1	<0.1	<0.1	<0.1
Se	<0.5	<0.5	<0.5	<0.5	<0.5	<0.5	<0.5	<0.5	<0.5	<0.5	<0.5	<0.5	<0.5
Ba	<0.002	0.01	<0.002	0.12	0.07	0.10	<0.002	<0.002	0.02	<0.002	0.37	<0.002	0.01
Sc	2.00	4.00	2.00	3.00	3.00	2.00	1.00	2.00	3.00	25.00	3.00	1.00	1.00
Au	3.00	4.00	2.00	8.00	13.00	18.00	1.00	2.00	2.00	<1	10.00	3.00	3.00
Cr	0.00	<0.0005	<0.0005	0.00	0.00	0.00	<0.0005	<0.0005	0.00	0.00	<0.0005	<0.0005	0.00

8.1 Rodingite Chemistry

Samples were analyzed for major elements (wt %) trace elements (ppm) and REE (ppm). Based on their petrographic and macroscopic features, three distinct zones have been distinguished in each rodingite sample. This division is in accordance with

their whole rock chemistry as it is shown by the following cluster analysis dendogram (Fig. 84), which is based on their CaO, MgO, FeO, Al_2O_3 SiO_2 and TOT/C contents. Samples EROD11, EROD18, EROD21, EROD23M, EROD25, EROD25L and EROD26M correspond to the CZ. Samples EROD22M, EROD24M, EROD24R, EROD26L and EROD7SCC correspond to the MZ, whereas Samples EROD6, EROD7, EROD7SC, EROD12, EROD22L and EROD23R, belong to the TZ respectively. The choice of the aforementioned chemical elements was based to their different concentration between the samples of each rodingite groups. On the other hand, REE and trace elements do not show significant differences from one group to another.

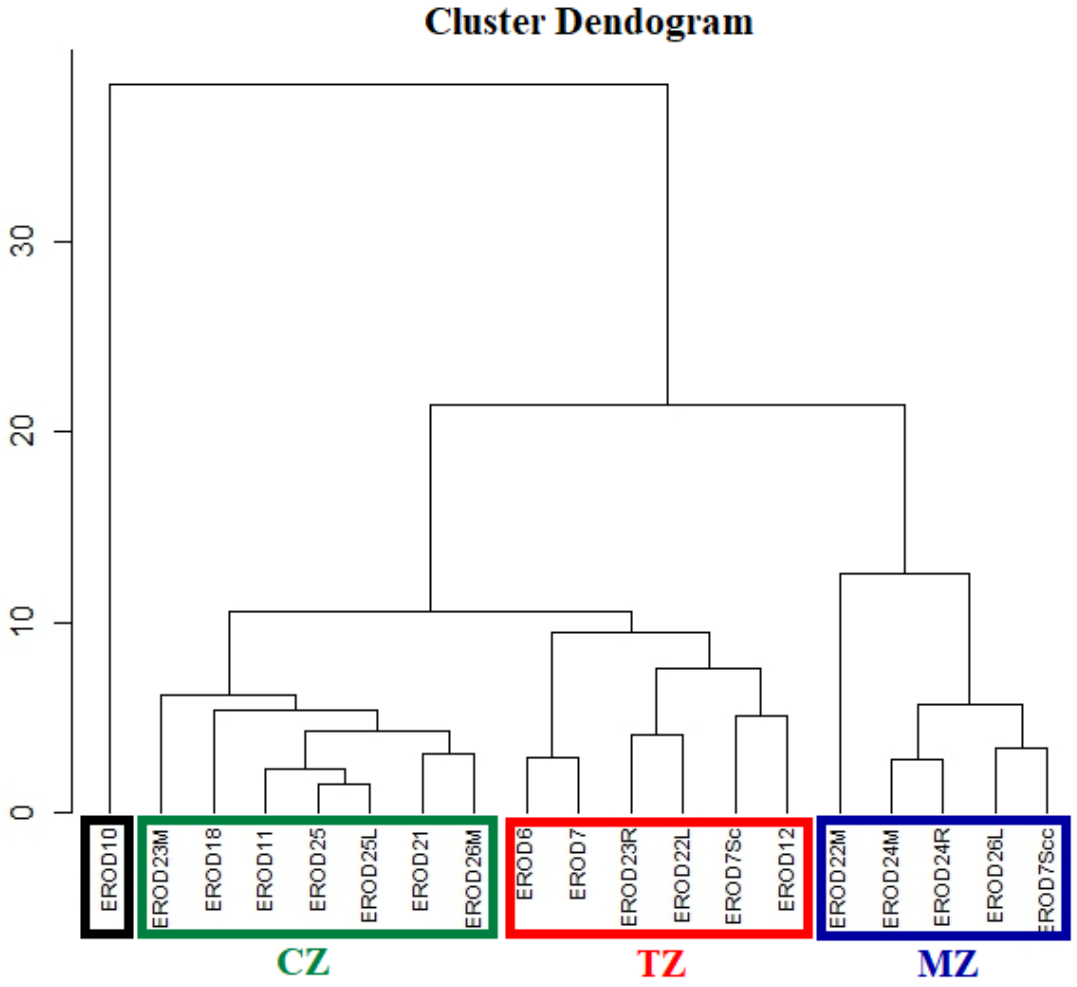

Figure 84. Cluster analyses dendogram based on CaO, MgO, FeO, SiO_2 Al_2O_3 and TOT/C values for Kimi rodingites.

As we mentioned above our chemical cluster is in accordance with our initial petrographic and macroscopic discrimination, with a notable exception of Sample EROD10. Sample EROD10 belongs to the MZ of Group-II rodingites. It is part of a very thin rodingitic dyke of almost 15 cm thickness. Its mineral assemblage mainly includes fine grained idiomorphic crystals, while the other two zones of the rodingitic dyke (core zone and transitional zone) are absent. Consequently it presents a chemistry which is differentiated from all three rodingite groups, being similar with that of an ultramafic rock. However, based on the mineralogical data of this sample, it is classified in marginal samples.

Table 17. Whole rock chemical analyses of Group-I rodingites for major elements (wt%), trace elements (ppm) and REE (ppm).

Sample	EROD21	EROD23M	EROD25	EROD25L	EROD26M	EROD24M	EROD24R	EROD26L	EROD23R	EROD6	EROD7
Area	CR-VE	CR-GT	CR-GT	CR-GT	CR	RM-DI	RM-DI	RM-DI	TR	TR	TR
Type	G-I	G-I	G-I	G-I	G-I	G-I	G-I	G-I	G-I	G-I	G-I
Rock Type	CZ	CZ	CZ	CZ	CZ	MZ	MZ	MZ	TZ	TZ	TZ
SiO_2	39.26	38.33	36.44	37.45	37.36	42.96	43.46	39.95	37.38	41.51	43.56
Al_2O_3	15.85	22.15	19.08	18.57	16.63	9.68	9.24	11.12	20.97	13.02	11.34
Fe_2O_3	0.29	0.63	0.85	1.18	2.55	4.70	6.40	3.80	2.08	1.83	1.34
MgO	5.91	0.82	2.74	2.83	4.75	16.85	17.87	18.04	6.51	7.85	9.02
CaO	35.08	35.96	37.61	36.68	34.47	19.81	17.78	20.56	29.55	32.44	31.93
Na_2O	<0.01	0.03	<0.01	<0.01	<0.01	0.02	0.03	<0.01	0.03	0.03	0.07
K_2O	<0.01	<0.01	<0.01	<0.01	<0.01	<0.01	<0.01	<0.01	<0.01	<0.01	<0.01
TiO_2	0.03	0.04	0.03	0.02	0.03	0.07	0.08	0.03	0.05	0.02	0.02
P_2O_5	0.01	0.01	<0.01	<0.01	0.01	0.03	0.02	0.02	0.02	0.08	0.04
MnO	0.06	0.04	0.22	0.18	0.23	0.12	0.15	0.23	0.07	0.12	0.08
LOI	3.40	1.90	2.90	2.90	3.70	5.50	4.70	6.10	3.00	3.00	2.50
Sum	99.92	99.91	99.85	99.89	99.79	99.88	99.84	99.88	99.82	99.92	99.94
Be	5.00	<1	17.00	9.00	10.00	5.00	4.00	3.00	8.00	3.00	2.00
Co	1.10	2.20	5.50	10.50	13.20	35.50	55.30	39.90	18.50	13.40	10.10
Cs	<0.1	<0.1	<0.1	<0.1	<0.1	0.20	0.40	<0.1	<0.1	<0.1	<0.1
Ga	7.40	6.70	5.60	5.00	1.20	7.20	10.90	1.00	7.70	8.50	8.00
Hf	2.60	3.70	8.10	6.00	8.80	6.40	9.20	5.80	12.10	3.00	2.70
Nb	79.10	152.90	154.30	81.70	493.00	113.20	164.40	126.90	274.90	112.90	45.90
Rb	<0.1	0.10	<0.1	0.20	0.30	0.20	0.80	<0.1	0.20	<0.1	0.20
Sn	1.00	9.00	7.00	8.00	<1	1.00	3.00	<1	8.00	3.00	3.00
Sr	24.00	17.20	37.20	38.30	43.70	12.10	14.80	26.10	32.50	50.40	47.90
Ta	9.70	26.70	22.70	10.30	55.90	23.70	46.50	16.70	41.90	17.60	3.00
Th	11.10	8.90	27.00	17.30	20.50	21.90	22.80	21.30	27.80	9.40	7.90
U	9.90	5.40	13.00	6.60	9.30	8.40	11.00	11.90	17.90	12.90	7.50
V	<8	<8	<8	<8	<8	48.00	24.00	11.00	16.00	<8	<8
W	2.20	<0.5	0.70	<0.5	3.50	<0.5	1.00	0.80	0.80	<0.5	0.80
Zr	46.60	71.20	159.80	128.60	184.70	146.20	178.00	135.70	250.90	37.80	36.40
Y	49.50	54.50	171.90	73.90	148.90	70.60	109.50	72.60	145.90	15.00	11.30
La	11.40	13.10	27.40	27.50	55.50	16.00	55.80	16.80	38.90	4.80	2.40
Ce	30.50	35.10	70.20	65.00	137.40	39.80	147.90	45.00	93.80	12.10	6.90
Pr	3.50	4.04	8.13	7.02	14.43	4.86	16.08	5.23	10.58	1.25	0.86
Nd	13.50	14.00	30.60	22.30	45.80	18.90	48.80	19.30	36.50	4.10	2.90
Sm	4.78	4.48	11.22	5.63	11.93	6.00	10.12	6.12	10.86	1.62	1.40
Eu	0.22	0.14	0.59	0.20	0.43	0.18	0.44	0.16	0.36	0.08	0.07
Gd	6.16	5.18	15.74	6.93	14.41	7.49	10.04	7.38	13.01	1.71	1.24
Tb	1.18	1.02	3.55	1.40	3.08	1.51	1.90	1.57	2.83	0.39	0.29
Dy	8.56	7.42	26.80	10.30	23.03	10.79	14.19	11.12	20.82	2.73	2.18
Ho	1.68	1.44	5.77	2.30	4.67	2.34	2.85	2.35	4.37	0.49	0.35
Er	5.29	5.14	18.40	7.29	14.47	7.55	9.47	7.49	14.24	1.60	1.07
Tm	0.75	0.83	2.76	1.21	2.24	1.18	1.62	1.24	2.36	0.28	0.23
Yb	4.85	5.88	16.49	8.16	15.08	7.79	10.83	8.47	15.67	2.11	1.84
Lu	0.69	0.82	2.20	1.14	2.03	1.12	1.51	1.20	2.25	0.31	0.26
TOT/C	0.25	0.83	<0.02	0.03	0.06	0.97	0.20	0.03	0.03	0.05	0.04
TOT/S	<0.02	<0.02	<0.02	<0.02	<0.02	<0.02	<0.02	<0.02	<0.02	<0.02	<0.02
Mo	<0.1	<0.1	<0.1	<0.1	<0.1	<0.1	<0.1	<0.1	<0.1	<0.1	<0.1
Cu	0.40	2.90	0.20	1.60	0.60	2.00	2.10	12.60	1.20	1.20	1.00
Pb	31.30	2.70	0.50	16.40	20.00	476.40	10.10	32.80	4.40	3.10	2.00
Zn	5.00	1.00	20.00	18.00	17.00	27.00	52.00	15.00	6.00	15.00	9.00
Ni	2.10	9.30	4.00	84.60	39.80	328.00	512.30	231.50	209.60	93.60	154.40
As	<0.5	<0.5	<0.5	2.00	<0.5	<0.5	<0.5	<0.5	0.60	3.00	2.80
Cd	<0.1	<0.1	<0.1	<0.1	<0.1	<0.1	<0.1	<0.1	<0.1	<0.1	<0.1
Sb	<0.1	<0.1	<0.1	<0.1	<0.1	<0.1	<0.1	<0.1	0.30	0.20	0.30
Bi	<0.1	0.10	<0.1	0.10	<0.1	<0.1	<0.1	<0.1	0.30	<0.1	<0.1
Ag	<0.1	<0.1	<0.1	<0.1	<0.1	<0.1	<0.1	<0.1	<0.1	<0.1	<0.1
Hg	<0.01	<0.01	<0.01	<0.01	0.09	0.02	<0.01	0.01	<0.01	0.04	<0.01
Tl	<0.1	<0.1	<0.1	<0.1	<0.1	<0.1	<0.1	<0.1	<0.1	<0.1	<0.1
Se	<0.5	<0.5	<0.5	<0.5	<0.5	<0.5	<0.5	<0.5	<0.5	<0.5	<0.5
Cr	<13.7	<13.7	<13.7	<13.7	<13.7	656.84	458.42	41.05	800.53	109.47	109.47
Ba	2.00	2.00	1.00	1.00	2.00	2.00	3.00	4.00	3.00	4.00	4.00
Sc	2.00	2.00	3.00	3.00	3.00	18.00	13.00	4.00	8.00	3.00	2.00
Au	<0.0005	<0.0005	<0.0005	0.00	0.00	0.00	0.00	<0.0005	0.00	<0.0005	<0.0005

Group-I non-carbonated and Group-II carbonated rich rodingites have been geochemically studied for major, trace elements and REE as well (Table 17 and Table 18).

The MZs present high SiO_2 and low Al_2O_3 contents (SiO_2: 39.95 to 43.46 wt%, Al_2O_3: 9.24 TO 11.12 wt%). Fe_2O_3 and MgO are quite high ranging from 3.80 to 6.40 wt% and 16.85 to 18.04 wt% respectively. On the other hand CaO is very low 17.78 to 20.51 wt%. Total alkalies, MnO, P_2O_5 and TiO_2 are very low, whereas LOI is quite high ranging from 4.70 to 6.10 wt%. Zr, Y and Nb are quite high (Zr: 135.70 to 178.00 ppm, Y: 70.60 to 109.50 ppm and Nb: 113.20 to 164.40 ppm). Ni and Cr are high ranging from 231.50 to 512.30 ppm and 41.05 to 656.84 ppm respectively. ΣREE range from 125.51 to 331.55 ppm, while EROD24R presents high Ce content (Ce: 147.90 ppm).

In TZs SiO_2 values range from 37.38 to 43.56 wt%, while Al_2O_3 ranges from 11.34 to 20.97 wt%. Fe_2O_3 and MgO range from 1.34 to 2.08 wt% and 6.51 to 9.02 wt% respectively. CaO ranges from 29.55 to 32.44 wt%, while total alkalis, MnO, TiO_2 and P_2O_5 are very low. LOI ranges from 2.50 to 3.00 wt%. Zr, Y and Nb also present various values ranging from 36.40 to 250.90 ppm, 11.30 to 145.90 ppm and 45.90 to 274.90 ppm respectively. Their ΣREE values range from 21.99 to 266.55 ppm, while Ni and Cr exhibit high contents ranging from 93.60 to 209.60 ppm and 109.47 to 800.50 ppm respectively.

In CZs SiO_2 and CaO values range from 36.45 to 39.26 wt% and 34.47 37.61 wt% respectively. Their Al_2O_3 contents are quite high for rodingite rocks, ranging from 15.85 to 22.15 wt%. Fe_2O_3 and MgO range from 0.29 to 2.55 wt% and 0.82 to 5.91 as well. Total alkalies as well as MnO, TiO_2 and P_2O_5 values are very low and near the direction limits. LOI ranges from 1.90 to 3.70 wt%. Zr, Y and Nb present various contents ranging from 46.6 to 184.7 ppm, 49.50 to 171.50 ppm and 79.1 to 493.00 ppm respectively. ΣREE range from 93.06 to 344.50 ppm, while Ce content of sample EROD26M is very high (Ce: 137.40 ppm).

MZs whole rock chemical analyses of Group-II carbonated rich rodingites present quite low SiO_2 and CaO values ranging from 33.47 to 39.44 wt% and 1.71 to 22.81 wt% respectively. Al_2O_3 ranges from 11.33 to 13.25 wt% and Fe_2O_3 ranges from 1.62 to 4.32 wt% respectively. MgO is very high ranging from 16.42 to 34.70 wt%, while total alkalies, MnO TiO_2 and P_2O_5 are very low. LOI is very high ranging from 8.10 to 12.70 wt%. Sample EROD7SCC presents high Nb value (Nb: 101.60 ppm), while Zr values are very high (Zr: 62.30 to 391.30 ppm). Ni is quite high ranging from 240.00 to 38.80 ppm, whereas Cr ranges from values below detection limit to 253.16 ppm. Sample EROD22M presents high LREE contents and more specifically high La and Ce values (La: 156.60 ppm and Ce: 290.20 ppm). ΣREE values range from 72.39 to 594.41 ppm.

The TZs of Group-II rodingites exhibit SiO_2 values ranging from 35.06 to 38.14 wt%, while CaO ranges from 26.75 to 31.73 wt%. Al_2O_3 ranges from 14.02 17.76 wt%, while Fe_2O_3 ranges from 0.39 to 2.67 wt% and MgO presents high contents ranging from 7.53 to 12.36 wt%. Total alkalies, TiO_2, MnO and P_2O_5 are very low, whereas LOI ranges from 4.50 to 8.20 wt%.

Table 18. Whole rock chemical analyses of Group-II rodingites for major elements (wt%), trace elements (ppm) and REE (ppm).

Sample	EROD11	EROD18	EROD22M	EROD7Scc	EROD10	EROD22L	EROD7Sc	EROD12
Area	CR-VE	CR-GT	RM-CHL	RM-DI	RM-CHL	TR	TR-CC	TR
Type	G-II	G-II	G-II	G-II	G-II	G-II	G-II	G-II
Rock Type	CZ	CZ	MZ	MZ	MZ	TZ	TZ	TZ
SiO_2	38.03	34.05	35.12	39.44	33.47	36.80	38.14	35.06
Al_2O_3	17.85	16.52	13.11	11.33	13.25	17.76	14.02	17.17
Fe_2O_3	0.20	0.22	4.32	1.62	3.79	1.21	0.39	2.67
MgO	4.02	1.67	23.87	16.42	34.70	7.53	12.36	10.89
CaO	36.23	38.14	12.64	22.81	1.71	31.73	26.75	27.28
Na_2O	<0.01	0.05	<0.01	<0.01	<0.01	<0.01	<0.01	0.01
K_2O	<0.01	<0.01	<0.01	<0.01	0.02	<0.01	<0.01	<0.01
TiO_2	0.02	0.02	0.05	<0.01	0.03	0.02	<0.01	0.02
P_2O_5	<0.01	0.02	0.08	<0.01	0.04	0.04	0.01	0.04
MnO	0.05	<0.01	0.19	0.17	0.16	0.29	0.07	0.47
LOI	3.50	9.20	10.40	8.10	12.70	4.50	8.20	6.10
Sum	99.92	99.91	99.82	99.91	99.94	99.89	99.92	99.80
Be	7.00	<1	<1	6.00	<1	<1	4.00	5.00
Co	0.80	1.20	59.70	8.70	22.00	15.60	1.90	18.30
Cs	<0.1	0.10	<0.1	0.10	0.90	<0.1	<0.1	<0.1
Ga	7.70	15.10	2.40	4.50	5.50	6.50	10.40	3.50
Hf	3.00	2.90	12.90	7.80	2.60	2.20	5.00	9.60
Nb	86.30	15.70	32.60	101.60	29.50	14.80	80.20	89.00
Rb	<0.1	0.30	0.40	0.20	3.40	0.10	<0.1	0.60
Sn	3.00	<1	<1	<1	<1	<1	<1	<1
Sr	32.90	117.80	12.90	19.20	5.00	21.60	24.80	97.30
Ta	6.80	1.90	1.60	6.10	2.20	0.80	6.10	8.30
Th	10.20	22.70	45.10	8.20	15.00	27.80	8.00	30.20
U	8.40	1.90	1.10	4.20	1.20	0.50	6.10	4.50
V	<8	<8	13.00	<8	<8	<8	<8	11.00
W	0.70	<0.5	<0.5	<0.5	<0.5	0.70	<0.5	3.70
Zr	68.30	83.10	391.30	107.10	62.30	72.70	86.10	241.50
Y	57.90	22.10	19.50	52.90	19.50	12.60	35.00	74.00
La	10.00	56.30	156.60	11.10	11.80	110.90	6.00	126.30
Ce	27.10	103.30	290.20	28.60	28.20	214.40	17.70	305.60
Pr	3.04	10.31	27.92	3.46	3.16	21.12	2.32	32.14
Nd	11.90	35.50	87.40	11.10	13.50	68.60	8.70	107.40
Sm	4.36	6.50	11.48	4.54	3.09	10.36	3.49	21.46
Eu	0.17	1.28	2.61	0.10	0.28	2.47	0.04	1.34
Gd	6.39	5.42	8.04	5.78	3.16	7.68	4.49	17.18
Tb	1.30	0.75	0.91	1.31	0.50	0.79	1.09	2.37
Dy	9.85	4.25	4.55	9.44	3.24	3.66	7.77	13.81
Ho	2.08	0.73	0.69	1.93	0.67	0.44	1.46	2.58
Er	6.28	2.13	1.74	6.11	1.98	0.97	4.79	7.73
Tm	0.93	0.30	0.25	0.95	0.31	0.13	0.84	1.18
Yb	5.77	1.81	1.73	6.70	2.17	0.78	5.63	7.56
Lu	0.82	0.30	0.29	0.94	0.33	0.11	0.80	1.07
TOT/C	0.18	2.29	0.85	0.65	0.06	<0.02	1.01	0.17
TOT/S	<0.02	<0.02	<0.02	<0.02	<0.02	<0.02	<0.02	<0.02
Mo	<0.1	0.20	<0.1	<0.1	<0.1	<0.1	<0.1	<0.1
Cu	15.10	4.10	1.30	0.30	2.60	<0.1	0.70	110.60
Pb	4.10	5.30	4.50	2.70	41.30	0.90	2.80	1.30
Zn	5.00	<1	17.00	32.00	25.00	34.00	12.00	30.00
Ni	1.80	19.70	201.60	30.80	240.00	24.20	9.20	90.70
As	<0.5	<0.5	<0.5	<0.5	<0.5	<0.5	<0.5	<0.5
Cd	<0.1	<0.1	<0.1	<0.1	<0.1	<0.1	<0.1	0.10
Sb	<0.1	<0.1	<0.1	<0.1	<0.1	<0.1	<0.1	<0.1
Bi	<0.1	<0.1	<0.1	<0.1	<0.1	<0.1	<0.1	<0.1
Ag	<0.1	<0.1	<0.1	<0.1	<0.1	<0.1	<0.1	<0.1
Hg	<0.01	<0.01	0.05	<0.01	<0.01	0.01	<0.01	<0.01
Tl	<0.1	<0.1	<0.1	<0.1	<0.1	<0.1	<0.1	<0.1
Se	<0.5	<0.5	<0.5	<0.5	<0.5	<0.5	<0.5	<0.5
Cr	<13.7	<13.7	253.16	<13.7	143.68	13.68	<13.7	47.89
Ba	1.00	25.00	3.00	12.00	3.00	2.00	18.00	4.00
Sc	1.00	<1	3.00	<1	2.00	<1	<1	2.00
Au	<0.0005	0.00	<0.0005	<0.0005	0.00	<0.0005	<0.0005	<0.0005

Zr and Nb content are quite high (Zr: 72.70 to 241.50 ppm, Nb: 14.80 to 89 ppm), while Ni, Cr are quite low. ΣREE ranges from 65.12 to 647.72 ppm. More specifically La, Ce and Nd values are quite (La: 110.90 and 126.30 ppm respectively, Ce: 214.40 and 305.60 for Sample EROD22 and Sample EROD12 respectively, Nd: 107.40 for Sample EROD12).

CZs present SiO_2 and Al_2O_3 contents ranging from 34.05 to 38.03 wt% and 16.52 to 17.85 wt% respectively. Fe_2O_3 and MgO are quite low (MgO: 1.67 to 4.02 wt%), while CaO is very high ranging from 36,23 to 38.14 wt%. Total alkalies, TiO_2 MnO and P_2O_5 are very low, while LOI ranges from 3.50 to 9.20 wt%. Sample EROD18 is Sr rich (Sr: 117.80 ppm) and also presents high Ce and TOT/C contents (Ce: 103.30 ppm TOT/C: 2.29). ΣREE contents range from 89.99 to 228.88 ppm.

8.2 Rodingite Chemical Mobility

Major and trace element binary diagrams for MZs, TZs and Czs were made in order to examine the element mobility through the evolution of the metasomatic processes. Our aim is to make a comparison concerning the element mobility between the different areas of each group and the same areas of the two different Groups as well.

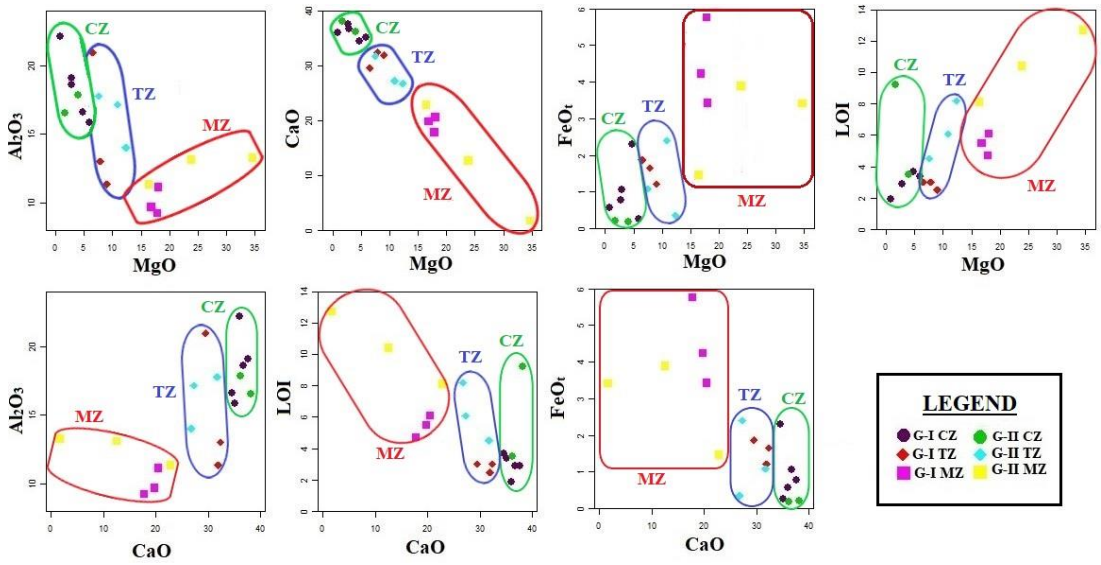

Figure 85. Whole rock chemical plot of MZs,TZs,CZs of Group-I and Group-II in MgO vs Al_2O_3, CaO, FeOt, LOI diagrams and CaO vs Al_2O_3, FeOt, LOI diagrams.

MgO and CaO exhibit a strong negative correlation (r: 0.99). In both groups CaO is increased from MZ to CZ, while MgO is depleted (Fig. 85). MZ samples of Group-II rodingites present a wide range of MgO and CaO contents, whereas MZ samples of Group-I rodingites almost have the same CaO and MgO values (Fig. 85). MgO also presents a negative correlation with Al_2O_3 (r: 0.71) which is mostly concentrated towards the CZ and TZ. On the other hand, MgO exhibits a positive correlation with FeOt (r: 0.71) and LOI (r: 0.73). CaO presents negative correlation with FeOt (r: 0.76) and LOI (r: 0.73) and positive correlation with Al_2O_3 (r: 0.61).

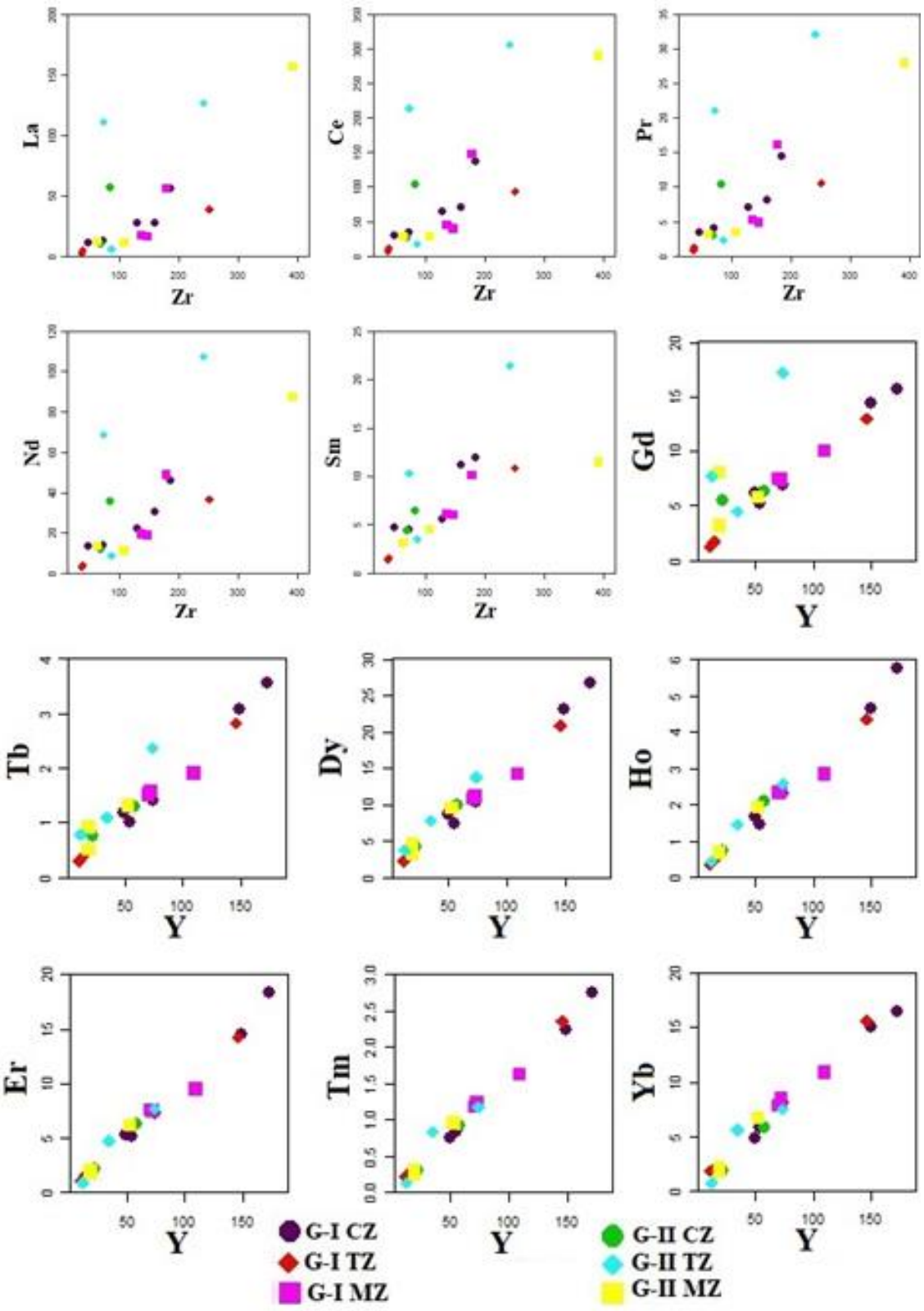

Figure 86. Whole rock chemical plot of MZ,TZ,CZ rodingites of Group-I and Group-II in Zr vs LREE and Y vs HREE diagrams.

Zr is mainly regarded as an immobile element, whereas it usually behaves as a mobile under specific physicochemical conditions that will be discussed in Chapter 9. It presents a positive correlation with all the LREE (r ranges from 0.71 to 0.74)

especially in Group-I, while many samples from each zone of Group-II exhibit a wide spreading (Fig. 86). Furthermore, Y presents a strong positive correlation with HREE (r ranges from 0.80 to 0.99), while the LREE are positively correlated with each other and usually with Eu (Figs 86 and 87).

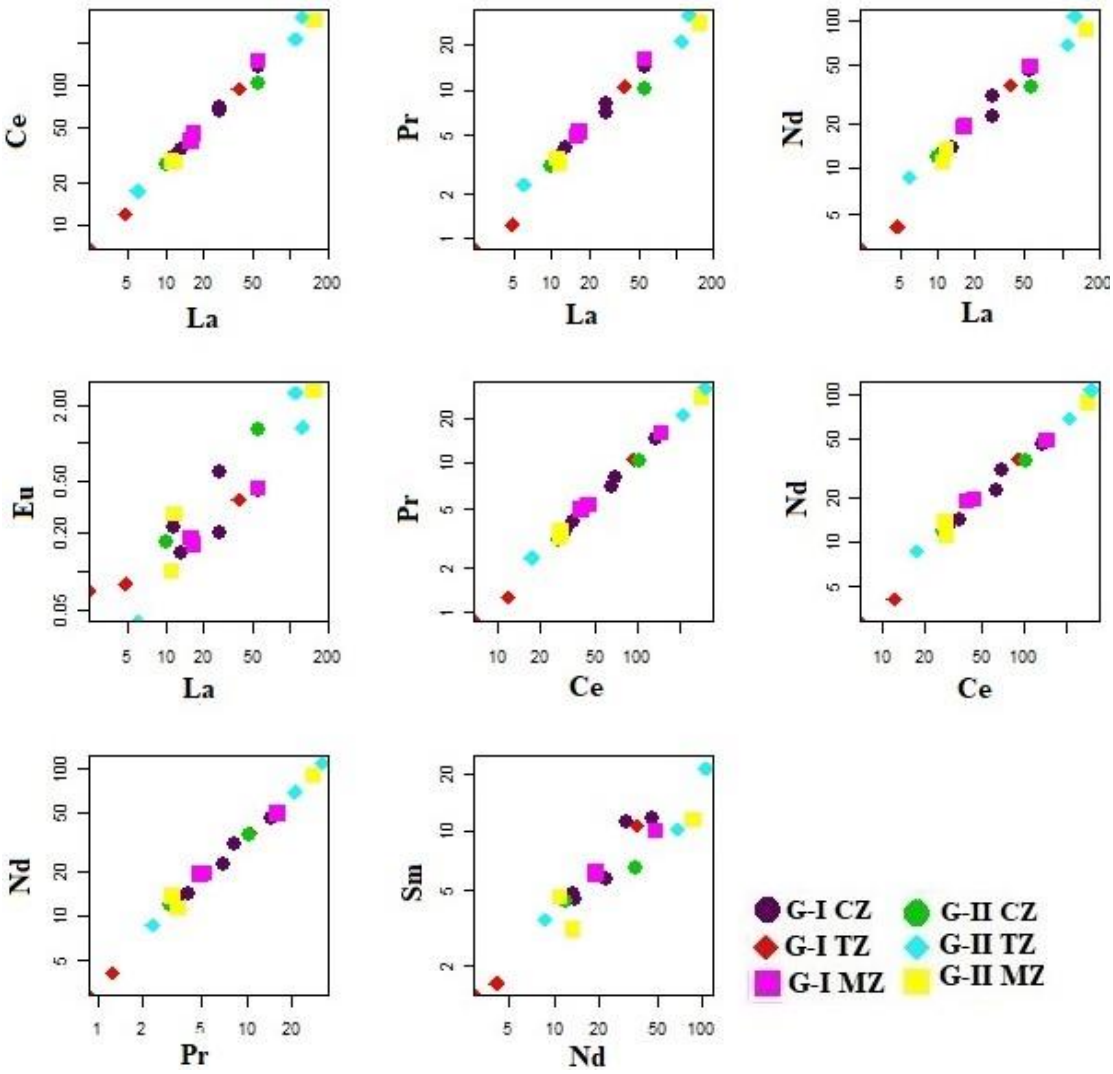

Figure 87. Whole rock chemical plots of MZ,TZ,CZ rodingites of Group-I and Group-II in La vs LREE-Eu, Ce vs Pr, Ce vs Nd, Pr vs Nd and Nd vs Sm diagrams.

Rodingite plots in ACF diagram (A: Al_2O_3-Na_2O-K_2O, C: CaO, F: FeOt+MgO+MnO) (Fig. 88) exhibit a clear discrimination between MZs, TZs and CZs of each group. Moving from MZ to CZ in each rodingite group, rodingites are plotted closer to C and A top respectively. As a result MZs are richer in MgO, MnO, and FeOt and poorer in CaO, Al_2O_3 compared to those of TZs and CZs. On the other hand CZs present slightly higher or equal CaO and Al_2O_3 contents compared to those of TZs. Furthermore, the fields of the common zones (MZ-MZ, TZ-TZ and CZ-CZ) between the two different groups tend to overlap each other moving closer to the CaO top.

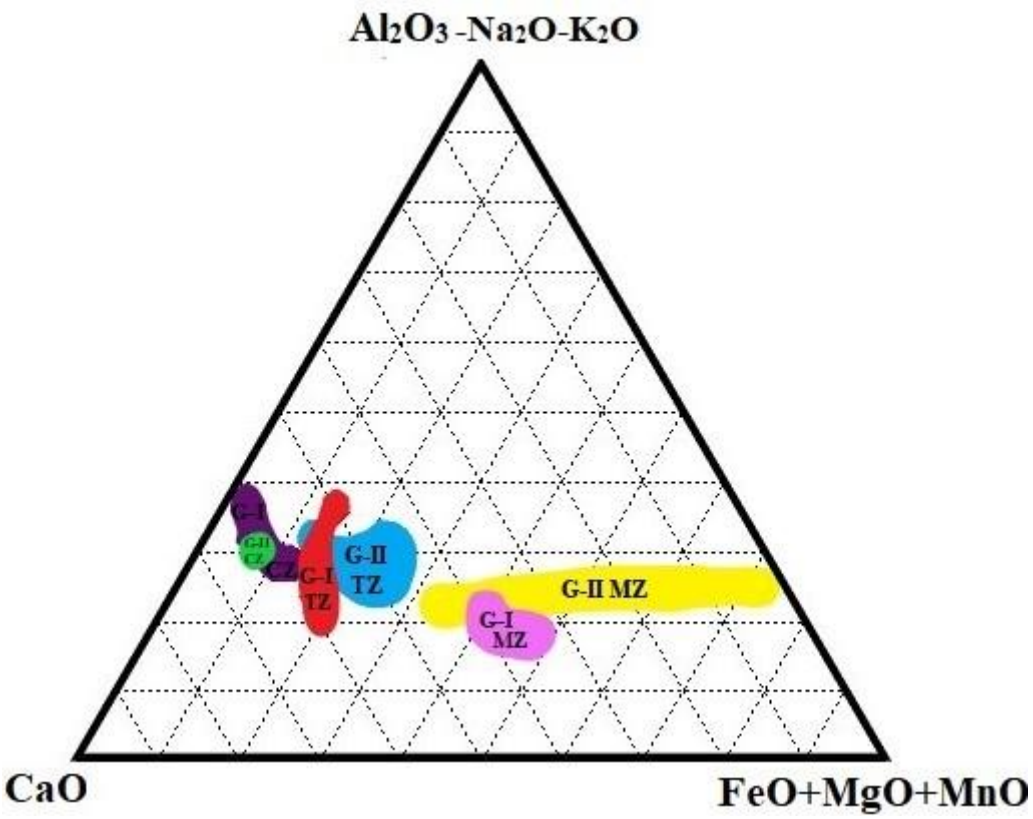

Figure 88. Whole rock chemical plot of MZ, TZ and CZ of Group-I and Group-II rodingites in ACF ternary diagram (A: Al_2O_3-Na_2O-K_2O, C: CaO, F: FeOt+MgO+MnO).

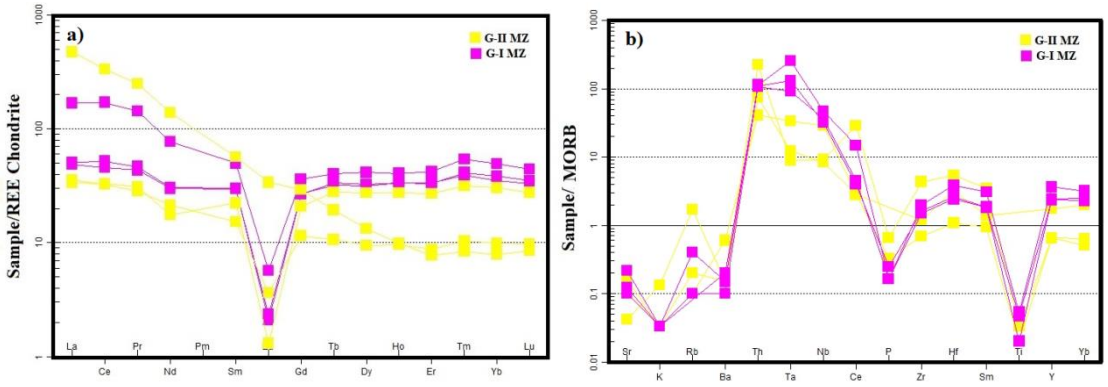

Figure 89. a. REE-Chondrite normalized patterns for MZ of Group-I and Group-II rodingites (Normalization after Nakamura, 1974), b. MORB normalized Multitrace patterns for MZ of Group-I and Group-II rodingites (Normalization after Pearce, 1983).

Chondrite normalized REE patterns for MZs of Group-I and Group-II rodingites (Fig. 89a) are subparallel apart from Sample EROD22M of Group-II. They present a slight fractionation between LREE and HREE and strong negative Eu anomalies. On the other hand Sample EROD22M does not present any Eu anomaly, whereas it exhibits a strong LREE enrichment and strong fractionation between LREE and HREE. $(La/Sm)_N$ values range from 1.64 to 3.39 and 1.5 to 8.39 for Group-I and Group-II rodingites respectively. $(La/Yb)_N$ values range from 1.32 to 3.43 and 1.1 to 60.35 for Group-I and Group-II rodingites, while (Eu_N /Eu*) ranges from 0.07 to 0.13 and 0.06 to 0.84 for Group-I and Group-II rodingites respectively. Multitrace element MORB

normalized patterns of MZ from Group-I and Group-II rodingites (Fig. 89b) are subparallel, presenting strong negative K, Ba, Ti and P as well as positive Rb, Th, Ta and Hf anomalies.

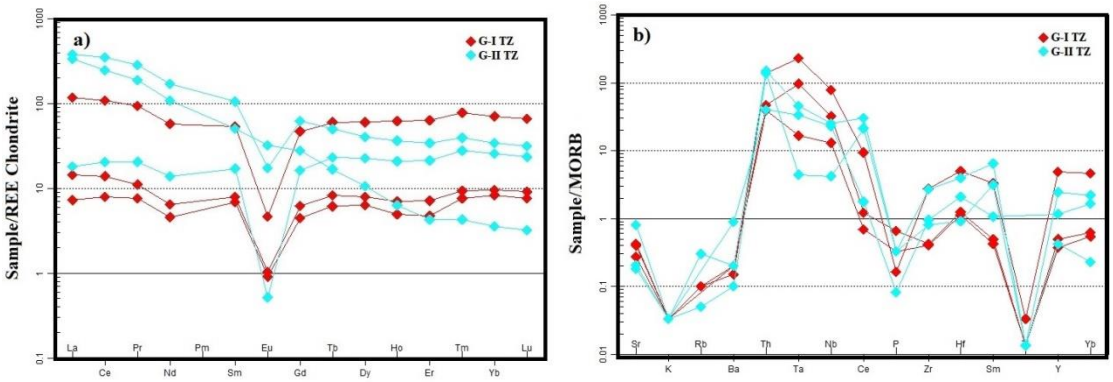

Figure 90. a. REE-Chondrite normalized patterns for TZ of Group-I and Group-II rodingites (Normalization after Nakamura, 1974), b. MORB normalized Multitrace patterns for TZ of Group-I and Group-II rodingites (Normalization after Pearce, 1983).

TZs of Group-I and Group-II rodingites present subparallel Chondrite normalized REE patterns (Fig. 90a), except for Sample EROD22L which presents a similar behavior with Sample EROD22M of MZ rodingites. They exhibit strong negative Eu anomalies (EuN/Eu*: 0.09 to 0.16 and 0.03 to 0.85 for Group-I and Group-II rodingites respectively) except for Sample EROD22L. Furthermore, they present slight or no fractionation between LREE and HREE, apart from Samples EROD22L and EROD12 of Group-II which exhibit strong LREE-HREE fractionation ((La/Sm)N ranges from 1.05 to 2.2 and 1.06 to 6.58 for Group-I and Group-II rodingites respectively, while (La/Yb)N ranges from 0.87 to 1.65 and 0.71 to 94.79 for Group-I and Group-II respectively). MORB normalized multitrace element patterns (Fig. 90b) are also subparallel presenting strong negative K, P, Ti and positive Rb, Th, Ta and Hf anomalies.

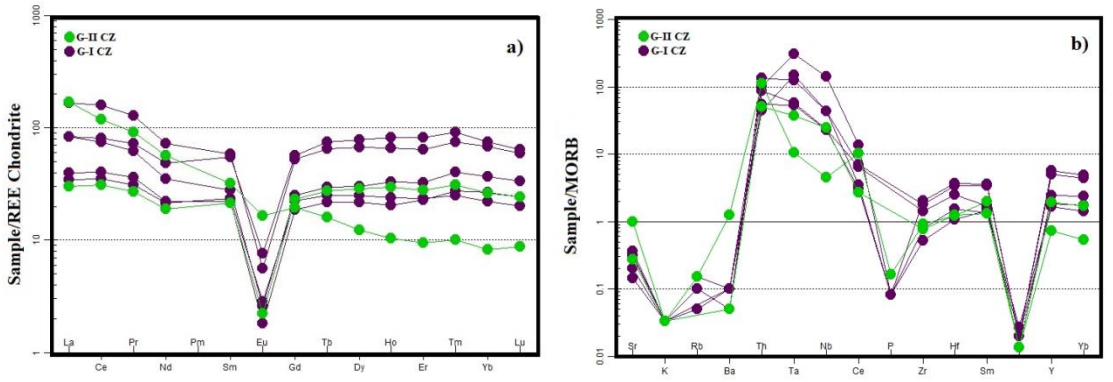

Figure 91. a. REE-Chondrite normalized patterns for CZ of Group-I and Group-II rodingites (Normalization after Nakamura, 1974), b. MORB normalized Multitrace patterns for CZ of Group-I and Group-II rodingites (Normalization after Pearce, 1983).

TZs of Group-I and Group-I rodingites present subparallel Chondrite normalized REE patterns (Fig. 91a) apart from Sample EROD18 of Group-II rodingites. They exhibit strong negative Eu anomalies, while Sample EROD18 presents slightly negative Eu

anomaly (Eu_N/Eu^* ranges from 0.09 to 0.14 for Group-I and 0.1 to 0.66 for Group-II rodingites). The vast majority presents no fractionation between LREE and HREE, except for Sample EROD18 which is LREE enriched ($(La/Sm)_N$ ranges from 1.47 to 3 and 1.41 to 5.33 for Group-I and Group-II rodingites, while $(La/Yb)_N$ ranges from 1.11 to 2.45 for Group-I and 1.16 to 20.14 for Group-II rodingites respectively). Multitrace element MORB normalized patterns present negative K, Nb, P, Zr and Ti anomalies as well as positive Rb, Th, Ta and slightly positive Hf anomalies (Fig. 91b).

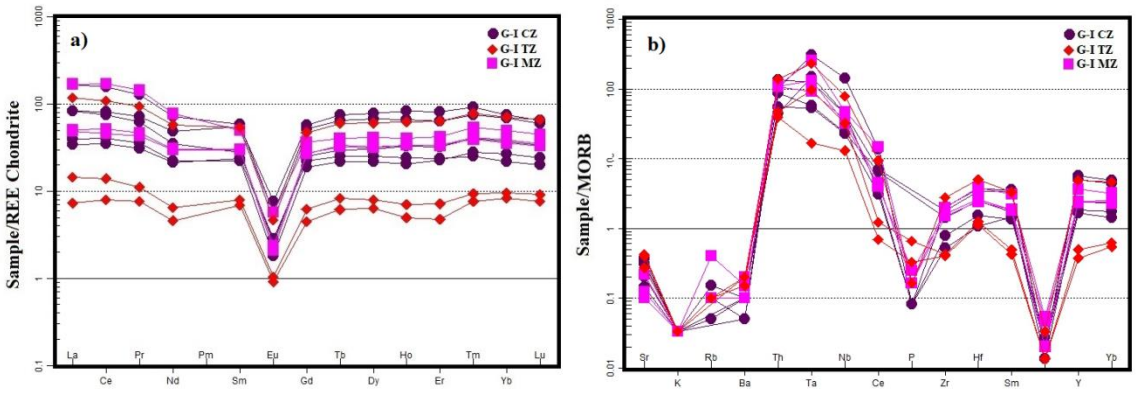

Figure 92. a. REE-Chondrite normalized patterns for Group-I rodingites (Normalization after Nakamura, 1974), b. MORB normalized Multitrace patterns for Group-I rodingites (Normalization after Pearce, 1983).

Chondrite normalized REE patterns for Group-I rodingites (Fig. 92a) present subparallel patterns. They exhibit strong negative Eu anomalies (EuN/Eu*: 0.07-0.16) and no or slight fractionation between LREE and HREE. $(La/Sm)_N$ ranges from 1.05 to 3.00, while $(La/Yb)_N$ ranges from 0.87 to 3.43. Multitrace MORB normalized patterns exhibit strong negative K, P, Ti, Zr and strong positive Rb, Ta and Hf anomalies (Fig. 92b).

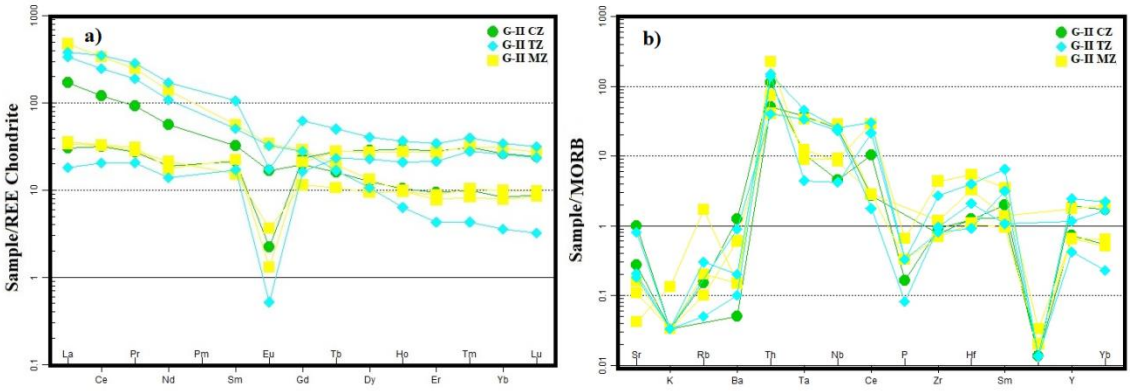

Figure 93. a. REE-Chondrite normalized patterns for Group-II rodingites (Normalization after Nakamura, 1974), b. MORB normalized Multitrace patterns for Group-II rodingites (Normalization after Pearce, 1983).

Chondrite normalized REE patterns for Group-II rodingites (Fig. 93a) present subparallel patterns. However Samples EROD18 (CZ), EROD22M (MZ) and EROD22L (TZ) exhibit patterns that differ from the vast majority as we mentioned in detailed above. They display high fractionation between LREE and HREE and no Eu anomalies. On the other hand the other samples of Group-II rodingites present no

fractionation between LREE and HREE and strong negative Eu anomalies, except for Sample EROD12 which exhibits LREE enrichment. EuN/Eu* values range from 0.06 to 0.85, $(La/Sm)_N$ ranges from 1.41 to 8.39, while $(La/Yb)_N$ ranges from 0.71 to 94.79. Multitrace MORB normalized patterns exhibit strong negative K, P, Ti and strong positive Th, Ce, Rb and Hf anomalies (Fig. 93b).

8.3 Ultramafics Chemistry

Samples were analyzed for major elements (wt %) trace elements (ppm) and REE (ppm). Ultramafic rock chemical division is in accordance with petrographic discrimination as it is shown by the following cluster analysis dendogram which is based on their CaO, MgO, FeO, Al_2O_3 and SiO_2 contents (Fig. 94). Whole rock chemical analyses were conducted to garnet metasomatized serpentinites and chloritites as well.

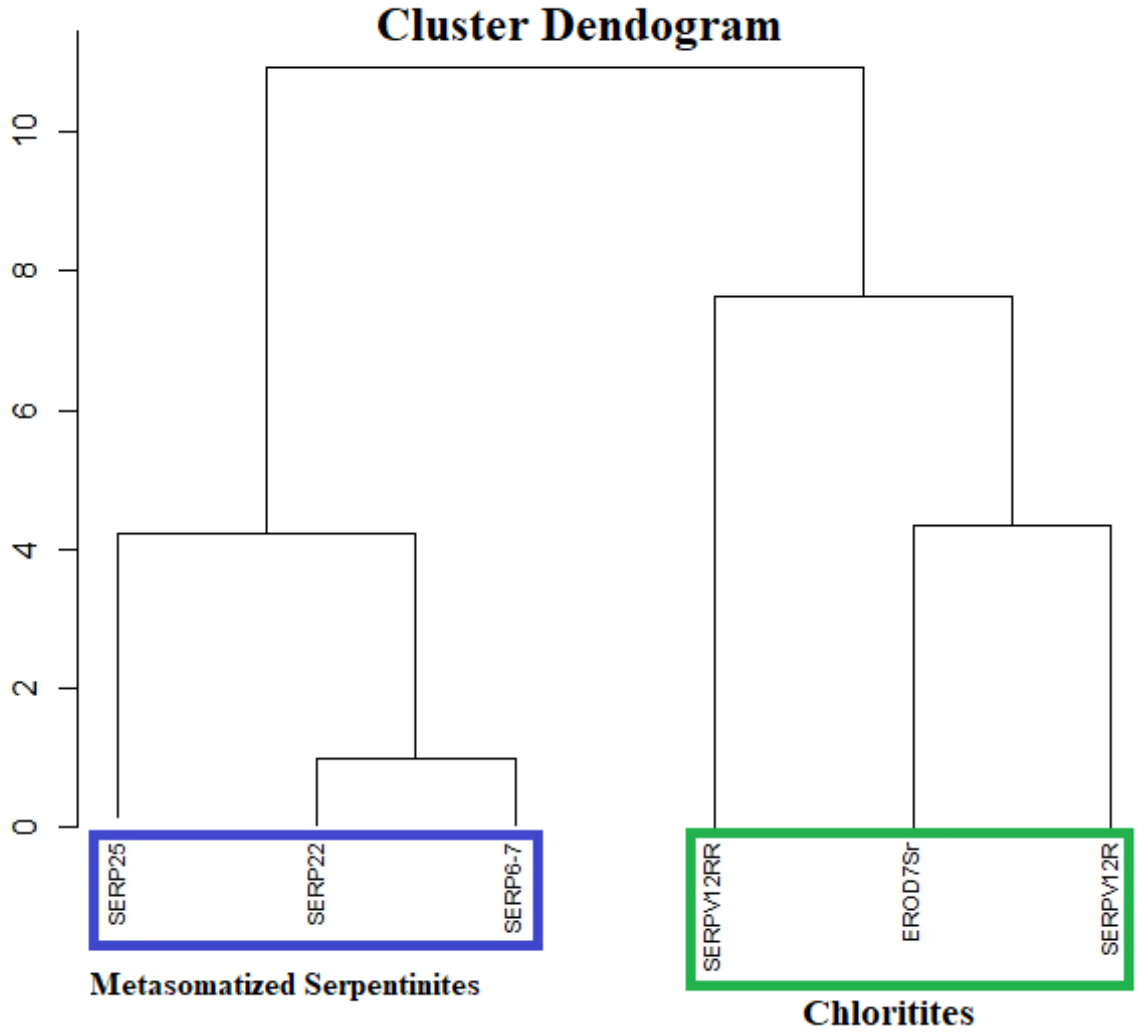

Figure 94. Cluster analyses dendogram based on CaO, MgO, FeO, SiO_2 and Al_2O_3 values for Kimi ultramafic rocks.

Table 19. Whole rock chemical analyses of ultramafic rocks.

Sample	SERP22	SERP6-7	SERP25	SERPV12RR	EROD7SR	SERPV12R
Area	Rim	Rim	Rim	Rim	Rim	Rim
Rock Type	Met. Serpentinite	Met. Serpentinite	Met. Serpentinite	Chroritite	Chroritite	Chloritite
SiO_2	39.37	39.30	40.00	35.57	33.38	35.59
Al_2O_3	2.29	2.92	0.66	6.44	13.30	10.28
Fe_2O_3	7.85	7.60	7.98	8.35	3.36	3.25
MgO	32.76	32.84	35.14	36.11	33.99	35.95
CaO	5.73	5.01	2.58	0.06	2.57	1.59
Na_2O	<0.01	<0.01	<0.01	<0.01	<0.01	<0.01
K_2O	<0.01	<0.01	<0.01	<0.01	<0.01	0.02
TiO_2	<0.01	<0.01	<0.01	<0.01	<0.01	0.02
P_2O_5	0.01	<0.01	0.01	0.01	<0.01	0.01
MnO	0.12	0.12	0.10	0.11	0.11	0.18
LOI	11.20	11.60	12.80	12.80	13.20	12.80
Sum	99.94	99.94	99.94	99.95	99.91	99.93
Be	<1.00	<1.00	<1.00	<1.00	<1.00	<1.00
Co	82.70	73.70	94.20	96.10	25.20	74.40
Cs	<0.10	0.10	<0.10	<0.10	0.50	0.10
Ga	1.80	1.40	2.30	3.60	5.40	4.50
Hf	0.20	0.20	<0.10	0.10	6.60	1.70
Nb	4.60	4.00	0.50	2.90	90.20	16.50
Rb	0.40	0.40	0.30	0.30	0.50	1.30
Sn	<1.00	<1.00	<1.00	<1.00	<1.00	<1.00
Sr	2.00	8.30	3.00	1.50	7.40	6.90
Ta	0.20	0.30	0.10	0.20	6.60	2.90
Th	<0.20	<0.20	<0.20	<0.20	10.40	13.40
U	<0.1	0.60	0.20	0.20	6.10	1.10
V	36.00	34.00	40.00	36.00	<8.00	37.00
W	0.70	0.70	1.00	<0.50	<0.50	<0.50
Zr	8.80	6.10	1.70	2.20	101.70	57.80
Y	1.00	0.50	0.40	3.10	71.70	10.10
La	2.80	2.00	0.30	1.60	8.70	6.70
Ce	7.00	5.10	0.20	4.20	26.20	20.00
Pr	0.81	0.53	0.03	0.50	3.38	2.41
Nd	2.50	1.60	<0.3	1.90	11.90	9.40
Sm	0.31	0.08	<0.05	0.47	5.13	2.74
Eu	0.12	0.05	<0.02	<0.02	<0.02	0.07
Gd	0.18	0.06	0.08	0.54	7.56	2.64
Tb	0.03	<0.01	0.01	0.09	1.57	0.41
Dy	0.16	0.06	0.07	0.51	11.20	2.29
Ho	0.03	<0.02	<0.02	0.12	2.29	0.43
Er	0.07	0.04	0.05	0.37	6.61	1.16
Tm	0.02	<0.01	<0.01	0.06	1.02	0.18
Yb	0.11	0.06	0.06	0.40	6.58	1.09
Lu	0.01	0.01	<0.01	0.06	0.90	0.20
TOT/C	0.06	0.04	0.04	0.19	0.36	0.05
TOT/S	<0.02	<0.02	<0.02	<0.02	<0.02	<0.02
Mo	<0.1	<0.1	<0.1	<0.1	<0.1	<0.1
Cu	9.10	6.60	33.70	7.40	0.20	12.20
Pb	1.70	0.70	12.10	1.20	2.80	1.10
Zn	18.00	19.00	22.00	20.00	17.00	29.00
Ni	1,982.90	1,926.50	2,311.50	1,900.00	61.00	764.80
As	1.70	11.70	<0.5	1.10	<0.5	<0.5
Cd	<0.10	<0.10	<0.10	<0.10	<0.10	<0.10
Sb	<0.10	<0.10	<0.10	<0.10	<0.10	<0.10
Bi	<0.10	<0.10	<0.10	<0.10	<0.10	<0.10
Ag	<0.10	<0.10	<0.10	<0.10	<0.10	<0.10
Hg	<0.01	<0.01	<0.01	<0.01	<0.01	<0.01
Tl	<0.10	<0.10	<0.10	<0.10	<0.10	<0.10
Se	<0.50	<0.50	<0.50	<0.50	<0.50	<0.50
Ba	3.00	2.00	3.00	2.00	4.00	1.00
Sc	10.00	9.00	10.00	8.00	1.00	10.00
Au	0.00	0.00	<0.0005	0.00	<0.0005	0.00
Cr	2,148.42	2,141.58	2,538.42	1,929.47	<13.7	910.00

Metasomatized serpentinites include samples SERP25, SERP22 and SERP6-7 of metasomatized serpentinites (Table 19). They display low SiO_2 which range from

40.00 to 39.30 wt%, while their Al_2O_3 values range from 0.66 to 2.92 wt% respectively. MgO ranges from 32.76-35.64. Their CaO contents are relatively high for a serpentinitic rock, ranging from 2.58 to 5.73 wt%. Ni is very high and ranging from 1926.5 to 2311.5 ppm. Cr is very high ranging from 2148.42 to 2538.42ppm. Their LOI values are high ranging from 11.2 to 12.8, while they do not present REE enrichment.

Chloritites (Samples EROD7SR, SERPV12R, SERPV12RR). MgO ranges from 33.99 to 36.11 wt%. They present the lowest SiO_2 contents compared to those of other groups (SiO_2: 33.38-35.57 wt%), while they are Al_2O_3 rich (6.44 – 13.3 wt%). FeO is quite high ranging from 3.25-8.35 wt%, whereas Ni ranges from 1900 and 61 ppm. Zr ranges from 2.2 101.7, while they also present the highest Y contents compared to those of the other ultramafic groups (3.1-71.7 ppm). Their LOI values are high ranging from 12.8 to 13.2 wt%. Their Cr values range from very low (below detection limit of 13.7 ppm) to very high (Cr: 1929.47 ppm).

Table 20 CIPW normed recalculated mineral assemblages for Chloritites (Samples SERPV12RR, SERPV12R and EROD7SR), and Metasomatized Serpentinites (Samples SERP25, SERP22 and SERP6-7). Ol: olivine, Opx: orthopyroxene and Cpx: Clinopyroxene.

Rock Type	Met. Ser.	Met. Ser.	Met. Ser.	Chloritite	Chloritite	Chloritite
Sample	SERP22	SERP6-7	SERP25	SERPV12RR	EROD7SR	SERPV12R
Cpx	23.34	18.24	11.16	0.00	0.00	0.00
Opx	22.82	27.24	41.23	39.73	13.53	26.06
Ol	53.84	54.52	47.62	60.27	86.48	73.93
Sum	99.99	100.00	100.01	100.01	100.00	100.00

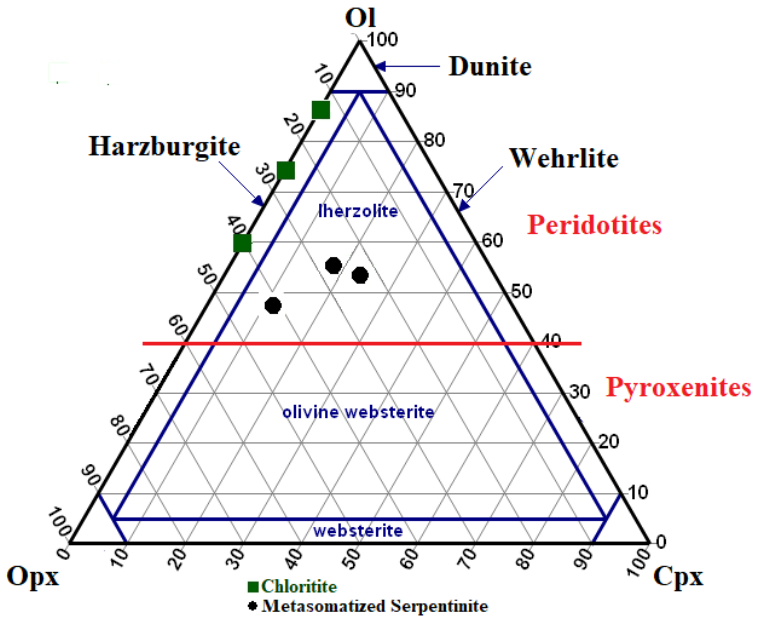

Figure 95. Ultramafic rock discrimination diagram for Chloritites (Samples SERPV12RR, SERPV12R and EROD7SR) and Metasomatized Serpentinites (Samples SERP25, SERP22 and SERP6-7) (Streckeisen, 1976).

CIPW norm has been used for whole rock chemical analyses of Kimi ultramafic rocks (Table 20). Their mineral assemblage has been recalculated in 100% total for Cpx

(clinopyroxene), Opx (orthopyroxene) and Ol (olivine). The results are plotted in a Ternary discrimination diagram for ultramafic rocks (Fig. 95). We assume serpentinization as an isochemical process and taking into consideration the preservation of some minerals such as relict clinopyroxenes, we try to conclude about their ultramafic protolith. All samples are plotted in the ‘’Peridotites” field having olivine contents > 40% (Ol ranges from 47.62 to 86.48). Chloritites seem to exhibit a harzburgitic origin, while metasomatized serpentinites could possibly have a lherzolitic origin as well.

8.4 Chemical Mobility of Ultramafic Rocks

Based upon their whole rock chemical analyses, ultramafic rocks have been plotted in correlation diagrams concerning their major, trace elements and REE. Furthermore, normalized REE and multi-trace element patterns are also presented.

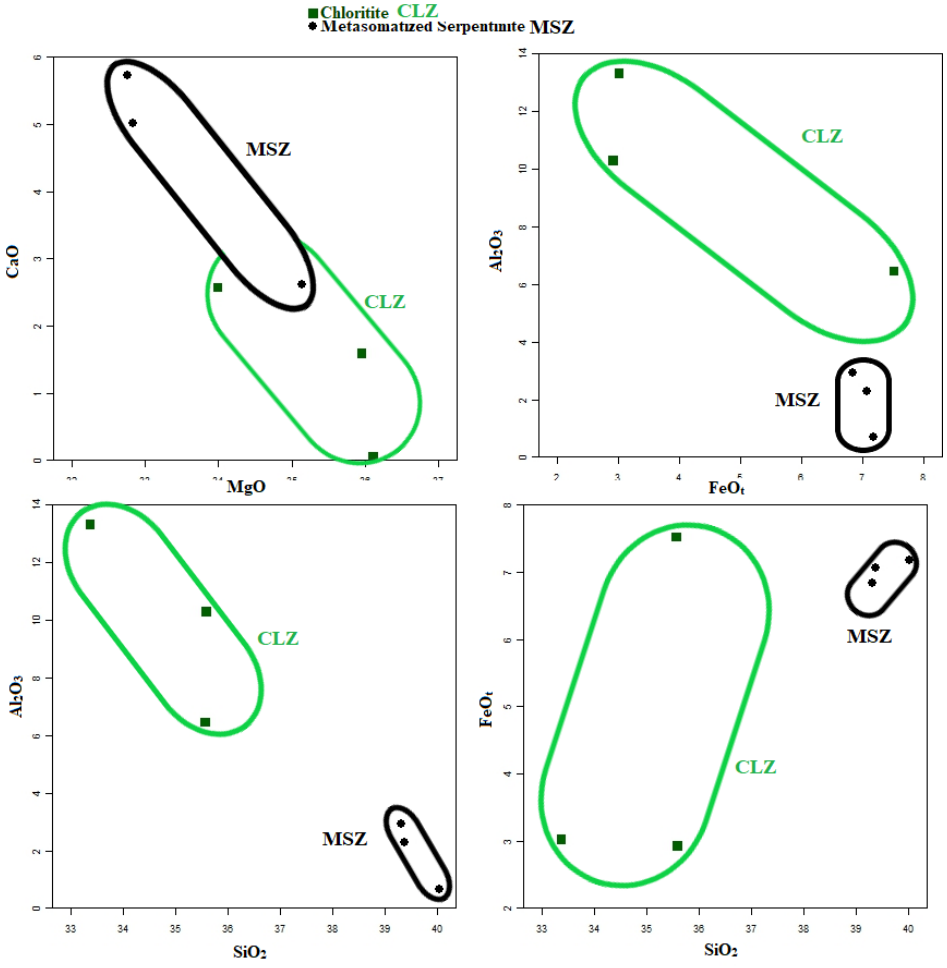

Figure 96. Correlation diagrams, Ca vs Mg, FeO_t vs Al_2O_3, SiO_2 vs Al_2O_3 and SiO_2 vs FeO_t for Chloritites (Samples SERPV12RR, SERPV12R and EROD7SR) and Metasomatized Serpentinites (Samples SERP25, SERP22 and SERP6-7).

Based on binary major element diagrams (Fig. 96), CaO and MgO are negative correlated (r: 0.94), while Al_2O_3 is negative correlated with SiO_2 and FeO_t as well (r:

0.96 and r: 0.87 respectively). On the other hand, a relatively positive correlation is present between FeOt and SiO_2 (r: 0.72). Chloritites present the highest Al_2O_3 contents, while metasomatized serpentinites present the highest CaO contents. The highest SiO_2 values correspond to metasomatized serpentinites, while sample SERPV12RR from chloritites present the highest FeO_t contents.

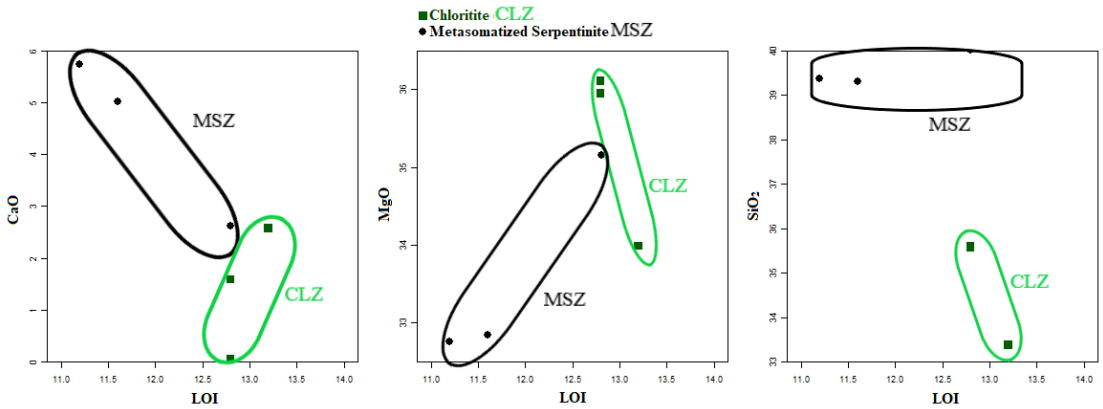

Figure 97. LOI vs CaO, MgO and SiO_2 diagram for Chloritites (Samples SERPV12RR, SERPV12R and EROD7SR) and Metasomatized Serpentinites (Samples SERP25, SERP22 and SERP6-7)

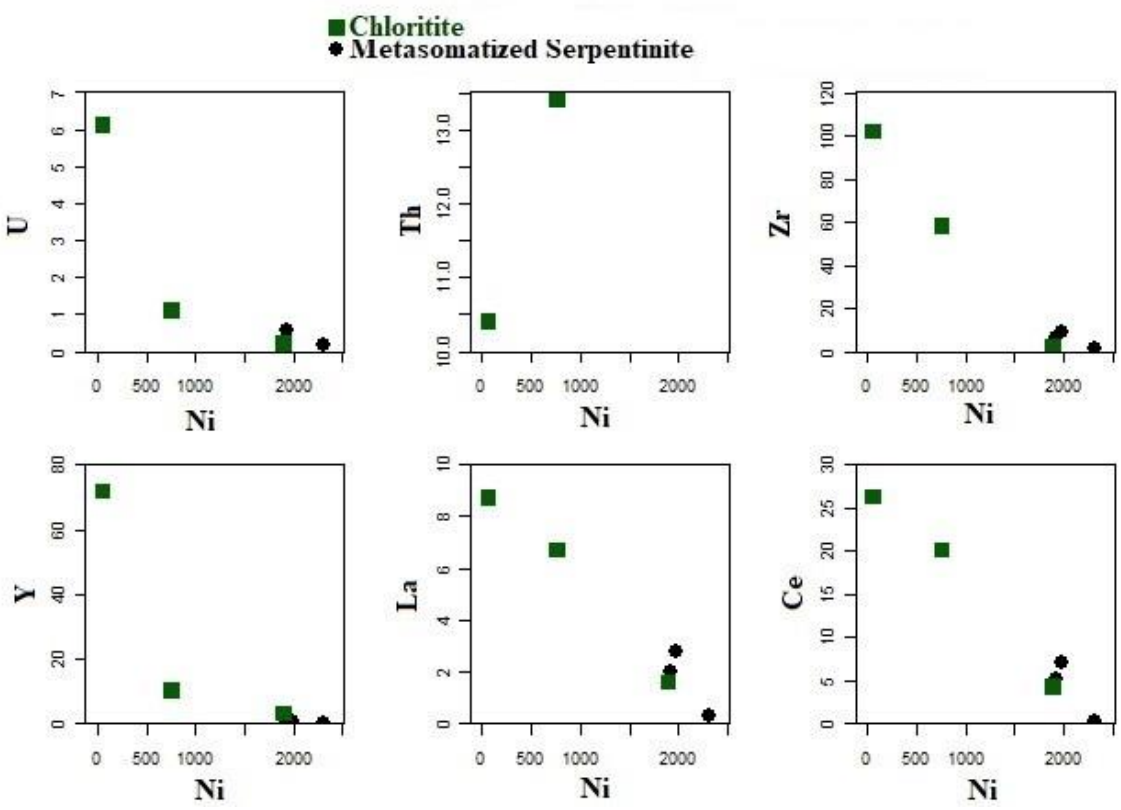

Figure 98. Ni vs U, Th, Zr, Y, La and Ce diagrams, for Chloritites (Samples SERPV12RR, SERPV12R and EROD7SR) and Metasomatized Serpentinites (Samples SERP25, SERP22 and SERP6-7).

Binary diagrams of LOI values compared to those of CaO, MgO and SiO_2 are presented in Figure 97. LOI exhibits a negative correlation with Ca (r: 0.84) and SiO_2

(r: 0.69). On the other hand, LOI is positive correlated with MgO. The highest LOI values correspond to Chloritites and SERP25 metasomatized serpentinite. In Figure 97, Ni contents are correlated with U, Th, Zr, Y, La and Ce. Ni presents a strong negative correlation with La-Ce and Zr-Y, while it is negative correlated with U and Th respectively. The highest LREE, Zr, Y, Th and U values correspond to chloritites (Fig. 98).

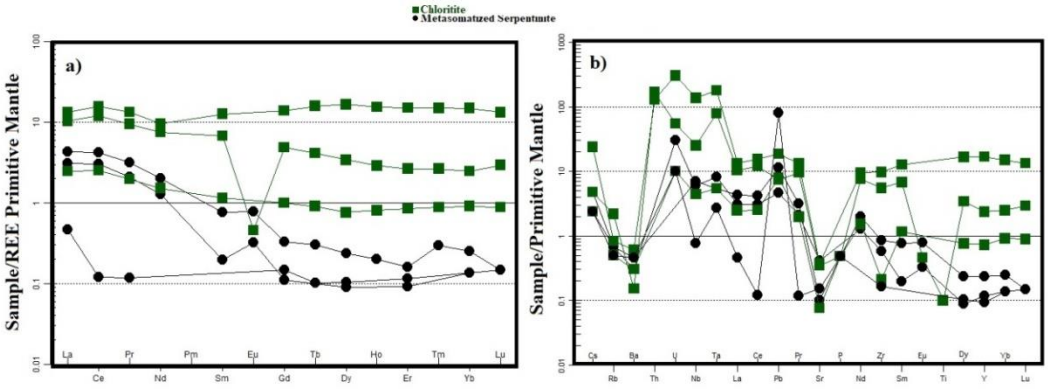

Figure 99. Primitive mantle REE normalized patterns for Kimi ultramafic rocks (Normalization after McDonough & Sun, 1995), b. Multitrace element Primitive mantle normalized patterns (Normalization after McDonough & Sun, 1995).

Primitive mantle normalized patterns are almost subparallel for every ultramafic rock, except for Sample SERP15 which presents very low LREE contents compared to those of SERP22 and SERP6-7 (Fig. 99a). They exhibit a high fractionation between LREE and HREE with LREE enrichment. Samples SERP22 and SERP6-7 exhibit strong positive Eu anomalies ((Eu_N/Eu^*)=1.55-2.2), while sample SERP25 present Eu value below detection limit. $(La/Yb)_N$ ratio ranges from 3.4 to 22.69. On the other hand, samples SERP6-7 and SERP22 $(La/Sm)_N$ ratio ranges from 5.66 to 15.66. Sample SERP6-7 presents negative Sm, Tb, Ho and Tm anomalies and positive Dy, Er and Yb anomalies as well, whereas Sample SERP22 exhibits negative Er anomaly. LREE patterns of metasomatized serpentinites SERP6-7 and SERP22 seem to be subparallel with those of chloritic sample SERPV12RR chloritites.

Chloritites present subparallel REE-Primitive mantle normalized patterns. They exhibit relatively high LREE and HREE contents and strong negative Eu anomalies (Eu_N/Eu^*:0-0.08). Sample EROD7SR does not present a fractionation between LREE and HREE, while samples SERPV12RR and SERPV12R present a slight fractionation. Their $(La/Sm)_N$ ratio ranges from 1.06 to 2.13, while their $(La/Yb)_N$ ratio ranges from 0.9 to 4.18. Multitrace element Primitive mantle normalized patterns (Fig. 99b) of SERP25 metasomatized serpentinite sample exhibits positive U, Ta, Pb and P anomalies and strong negative Nb, Ce and Ti anomalies. On the other hand, sample SERP22 of metasomatized serpentinites exhibits positive U (except for Sample SERP6-7), Ta, Pb, Nd and Eu (except for Sample SERP6-7) anomalies and negative Sm, Ti and Ba anomalies as well. Metasomatized serpentinite SERP6-7 sample presents positive Pb, Nd and negative Ti and Ba anomalies respectively.

Chloritites present positive Th Ta, Pb and Sm anomalies, while Sample EROD7SR also presents a strong U anomaly. On the other hand, Ba, Nb, Sr, Zr and Ti exhibit strong negative anomalies.

8.5 Chemical mobilization from ultramafic host rock to rodingite dyke

In Kimi both rodingites and ultramafic host rocks present distinct zones. The ultramafic host rocks are serpentinized peridotites which turn to garnet-bearing metasomatized serpentinites and then to chloritic rims near the contact with the rodingitic dyke. On the other hand rodingite dykes also present clear zoning which begins with marginal zone areas near the contact with the ultramafic host rock, which are chlorite-diopside rich, then they turn to the transitional zone areas which consist of chlorite, diopside, garnet and vesuvianite. The core zones follow the transitional ones and they are garnet and vesuvianite rich.

Based on the aforementioned zoning we present average chemical analyses of major elements, REE and Zr, Y, Ni from each rodingitic zone, as well as from the metasomatized serpentinites and chloritic rims in logarithmic diagrams, similar with those created by Coleman, (1967). Values below the detection limits are not plotted (Fig. 100).

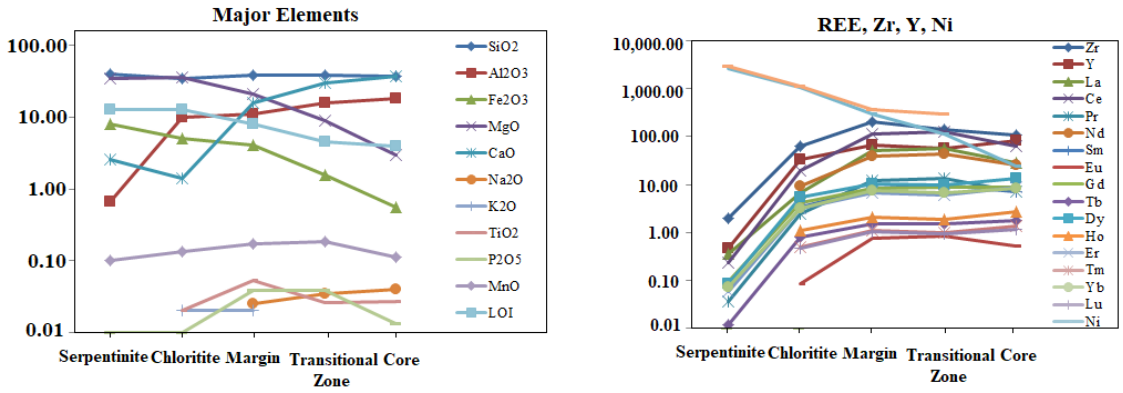

Figure 100. Semi-logarithmic diagrams for Major elements, REE, Zr, Y and Ni mobilization from the Serpentinitic host rock to the rodingite core via the chloritic rims.

From metasomatized serpentinite to rodingite core SiO_2 remains almost constant. Al_2O_3 is highly increased from metasomatized serpentinite to chloritic rim, while afterwards it presents a slight enrichment. MgO remains constant within the ultramafic lithologies, whereas it is strongly depleted moving to CZs (Total MgO mobility: -97.7 %). Fe_2O_3 is also depleted from metasomatized serpentinite to CZs with a strong depletion from MZ to CZs (Total Fe_2O_3 mobility: -22.87%). CaO is strong depleted from metasomatized serpentinite to chloritite, while afterwards it is gradually increased within the different zones of the rodingite dyke (Total CaO mobility: +23.30 %). LOI is continuously decreased from metasomatized serpentinite to TZs, while from TZs to CZs it remains almost constant. MnO is slightly enriched from metasomatized serpentinite to MZs and slightly decreased from TZs to CZs.

P_2O_5 remains constant within the ultramafic host rocks, while it is increased from chloritite to MZs. From MZs to TZs it remains constant and it rapidly decreased towards the CZs.

LREE are increased from metasomatized serpentinites to chloritite and rapidly increased from chlorititic rim towards the MZs. From MZs to TZs they almost remain constant and they are decreased from TZs to CZs (Total Mobility: +235 ppm for ΣLREE και 76ppm Zr). On the other hand, HREE and Y present a similar behavior with LREE up to the TZ, while afterwards they are slightly increased moving from TZs to CZs (Total Mobility 37ppm for HREE and for Y: 70ppm). Eu presents a rapid decreasing from metasomatized serpentinite to chlorititic margins, whereas it is rapidly increased towards the MZ and rapidly decreased towards the CZs after being constant from TZs to CZs. Cr and Ni exhibit similar behavior from metasomatized serpentinites to MZ being decreased, whereas Cr remains constant moving to TZs and decreased towards the CZs (-6828 ppm for Cr). On the other hand, Ni is continuously decreased moving to the CZs (-6200ppm for Ni). Zr is rapidly increased from metasomatized serpentinite to MZs and rapidly decreased moving to CZs.

8.6 Isotope Geochemistry

8.6.1 Introduction to isotope geochemistry theories

Isotopes are variants of a particular chemical element which differ in neutron number. All isotopes of a given element have the same number of protons (atomic number Z) and different number of nucleus (mass number A) in each atom.

Isotopes are subdivided into radiogenic and stable. The first group includes those isotopes which spontaneously decay because of their radioactivity and those which are the final products of the decay, including the parent-daughter element pairs such as Rb-Sr, Sm-Nd, U-Pb, Th-Pb and K-AR. Isotopes can be expressed as ratios. For example Sr is expressed as 87Sr/86Sr (Rollinson, 1993). On the other hand, they can also be expressed with a standard correlation. Radiogenic isotope ratios are not modified during partial melting and magma fractionation and they are used as indicators of the source region of magmas, while they are also applied in geochronology (e.g. Rb-Sr, Sm-Nd, Lu-Hf) (Rollinson, 1993).

On the other hand, stable isotope studies in geology correspond to light elements and mainly include H, O, C and S, which may be fractionated on the basis of mass differences between the isotopes of the element, while their contribution concerns the understanding of fluid and volatile species in geology. They are expressed as ratios relative to a standard using the δ-notation (Rollinson, 1993) and applied in the investigation of post-depositional processes. O and H are used for the investigation of different water-types related to diagenetic fluids, while O can also be used to geothermal gradients calculations (Rollinson, 1993).

Stable isotope ratios are measured relative to a standard and are expressed in parts per thousand (parts per mil (‰)). The δ value for oxygen is expressed by the following equation (Rollinson, 1993; White, 2013):

$$\delta^{18}O‰ = [(^{18}O/^{16}O_{(sample)} - {}^{18}O/^{16}O_{(standard)})/ (^{18}O / {}^{16}O_{(standard)})] * 1000$$

Stable isotope study aims to the investigation of the natural processes which separate isotopes on the basis of their mass rather than their chemistry, known as isotopic fractionation, being describing by the following three processes (Rollinson, 1993):

- Isotopic exchange reaction. For example oxygen is exchanged between quartz and magnetite, controlled by bond-strength and following the general rule that the lighter isotope forms a weaker bond than the heavier isotope.
- Kinetic processes, which reflect the ability of a particular isotope to react.
- Physico-chemical processes such as melting-crystallization and diffusion.

8.6.2 Oxygen isotopes

There are the three stable O isotopes: ^{16}O = 99.763%, ^{17}O = 0.0375 % and ^{18}O = 0.1995%. For oxygen isotopic calculations two standards are used. Low temperature geothermometry measurements are conducted using PDB, which is a belemnite from the Cretaceous Peedee formation of South Carolina and is also used as a standard for carbon isotopes, while for all the other measurements all other measurements the Standard Mean Ocean Water (SMOW) is used (Rollinson, 1993). The relation of these two standards is described as the following (Rollinson, 1993; White, 2013):

$$\delta^{18}OPDB = 1.03086\delta^{18}O_{SMOW} + 30.86$$

Oxygen isotope ratios are used in igneous rocks to determine whether they have assimilated crustal material, as crust generally has different O isotope ratios than does the mantle (White, 2013).

8.6.3 Carbon isotopes

Carbon has two stable isotopes with the following abundances: ^{12}C = 98.89% and ^{13}C= 1.11% and their measurements are measured as CO_2 gas and relative to PDB (Rollinson, 1993; White, 2013).

Combination of oxygen and carbon isotopes (δ18 O-δ13C) is widely applied in order to distinguish carbonates of different origins. These isotope applications will be further discussed in the Discussion chapter later.

8.6.4 O-C isotope analyses in Kimi calcites

For our study geochemical isotope analyses were conducted in six carbonated-rich samples, which include calcite powders extracted from two rodingite samples (EROD1Mc and EROD12cc calcite samples) two ophicalcite samples (ZTOPHcc and SOPHAcc calcite samples) and two red mudstones (CAREDcc and CARED2cc calcite samples), in order to examine the origin of O and C in relation with meteoric, seawater of magmatic-metamorphic derived fluids (discussed in the following chapter), studying both the metamorphic-metasomatic and sedimentary lithologies of Kimi area. All values are reported in per mil related to V-PDB.

Table 21. Isotope geochemical $\delta^{13}C$-$\delta^{18}O$ analyses for Kimi Group-II Choneftiko and Kalimeriani rodingites (SERPV12cc, EROD1Mc), ophicalcites (SOPHAcc, ZTOPHcc) and mudstones (CAREDcc and CARED2cc).

Rodingite Groups	Rock Type	Sample	δ13C ‰ VPDB	δ18O ‰ VPDB
Group-II Choneftiko	Rodingite	EROD 12cc	3.63	-13.32
Group-II Kalimeriani	Rodingite	EROD 1Mc	-14.4	-7.9
x	Ophicalcite	SOPHA cc	0.29	-12.24
x	Ophicalcite	ZTOPH cc	0.27	-6.76
x	Mudstone	CARED 2cc	2.16	-7.84
x	Mudstone	CARED cc	2.18	-6.88

From the analyses above (Table 21), δ13C ranges from 3.63 to 14.40 for rodingitic calcites of Choneftiko and Kalimeriani areas respectively, while their δ18O ranges from -7.0 to -13.32. As far as the ophicalcites concern, both ZTOPHcc and SOPHAcc calcite samples have been collected from Choneftiko area and their δ13C notation range from 0.27-0.29, while δ18C ranges from -6.76 to -12.24. Finally, calcite samples from red mudstones present δ13C values that range from 2.16-2.18, whereas δ18 O ranges from -6.88 to -7.84.

8.7 Geochemical Comparison between Kimi and Skyros Rodingites

In this chapter a whole rock chemical comparison between Kimi rodingites and ophiolitic rocks of Skyros, (North Sporades island -Greece). Based on their geochemical data (Karkalis et al., 2016) we try to compare the two areas. Kimi rodingites cores present subparallel patterns compared to those of Skyros (Fig. 100a). They mainly present a high fractionation between LREE and HREE and LREE enrichment as well. Eu usually presents negative anomalies ($Eu_N/Eu^*_{average}$= 0.22), while $(La/Sm)_N$ and $(La/Yb)_N$ values are 2.77 and 11.19 respectively. On the other hand, based upon the multitrace element diagram (Fig. 101), both Skyros and Kimi rodingites present similar patterns, which are mainly characterized by negative K, P,Ti anomalies and positive Th anomalies.

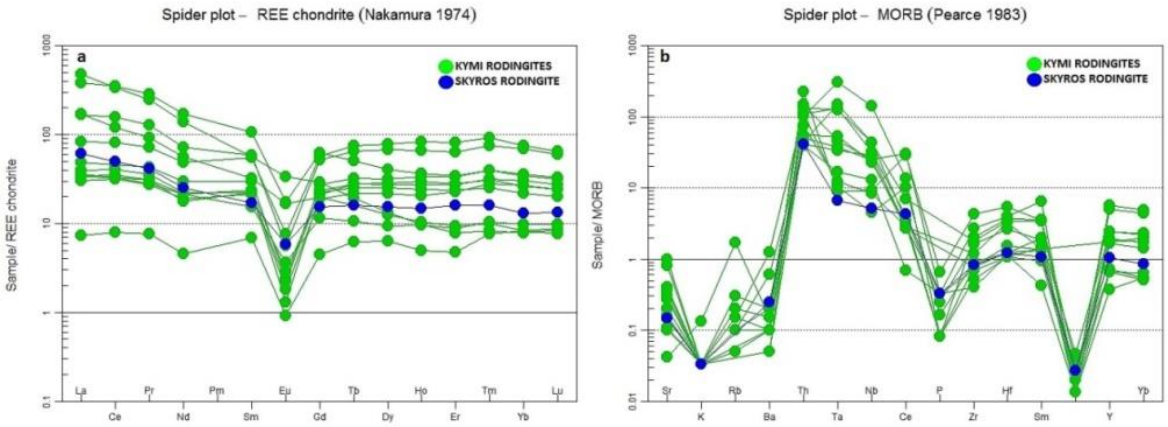

Figure 101. . REE-Chondrite normalized patterns for Skyros (Karkalis et al., 2016) and Kimi rodingites (Normalization after Nakamura, 1974). b. Multitrace element diagram for Kimi-Skyros rodingites (Normalization after Pearce, 1983).

9 Discussion

9.1 Kimi Flysch

Kimi is located in central Evia, the second biggest greek island. It includes rocks from the Pelagonian Zone, while its stratigraphic sequence ends up with the Cretaceous-Paleocene flysch. In Kimi and nearby locations, the Late Cretaceous meso-autochthonous platform passes up into hemipelagic limestones which could possibly be indicative of a rifting event inside Vardar Ocean. The main flyschoid lithologies include shales, cherts and sandstones, while it is also characterized by the presence of serpentinized peridotitic bodies, ophicalcites, pillow lavas (Robertson, 1990), Upper Cretaceous limestone intercalations overlying the peridotitic bodies, chert formations and the chaotic relations between many different lithologies such as ophicalcites and red colored mudstones. The presence of Upper Cretaceous limestones above the peridotitic bodies is possibly indicative of an earlier formation age of the peridotites.

Many similarities between Kimi and Beotian flysch can be observed. Kimi flysch is characterized by the occurrences of ultramafic bodies which are fully or partly serpentinized and chloritized and limestone intercalations as well. The presence of marly limestones underlying the flysch formation, as well as the radiolarite occurrences and the presence of reddish sedimentary material, is also an indicative similarity between the two flyschs. However, their main difference concerns the age of flysch formation, which for the Beotian flysch is Lower Cretaceous (Nirta et al., 2015), while Kimi flysch has an Upper Cretaceous to Paleocene age (Katsikatsos et al., 1970).

Although, the similarities between Kimi and Beotian flysch cannot be genetically correlated, since they have formed in different periods, the stratigraphic and chronological similarities of Kimi flysch with those of Bornova flysch (Turkey) can be indicative of a possible genetic correlation. The Cretaceous-Paleocene Bornova flysch includes blocks of Mesozoic limestones radiolarites and ophiolitic bodies. The ophiolites consist of serpentinized peridotites, gabbros and diabases as well (Okay et al., 2012). Based on their geochemical data and stratigraphic features, the Bornova flysch was probably formed in a Tethyan oceanic basin, while the chert ages suggest that the İzmir–Ankara ocean was active during Cretaceous (Okay et al, 2012).

Geochemical data of pillow basalts analyzed by Robertson (1990), exhibit MORB-affinities, corresponding to a Late Cretaceous oceanic fracture zone which was thrusted over a continental margin during the closure of Vardar Ocean.

The stratigraphic and chronological similarities of Kimi and Bornova flysch, further supported by geochemical data (Robertson, 1990), possibly indicate that these ophiolitic fragments correspond to Neotethyan oceanic basins inside the Vardar strand which remain active during the Upper Cretaceous.

9.2 Geotectonic Setting

According to Pe-Piper and Piper (2002), the convergence of Apulia and Eurasia seems to continue during Middle to Late Cretaceous, while at this time seafloor spreading and SSZ ophiolite formation take part in Greece. The flysch emplacement over Pelagonian zone was extending from Thessaly through Evia and Argolis to the Cyclades, probably belonging to the Vardar Ocean.

Robertson (1990), based on the deposition of deep-water carbonated rocks of Cretaceous age suggests a rifting of an oceanic basin inside the Vardar oceanic strand during Cretaceous to Early Tertiary. According to his model a small ocean basin is developed inside Vardar Ocean during the Late Cretaceous. At the beginning of Tertiary this basin started to close and as a result a subduction accretion complex developed giving rise to trench-type turbidities. Subsequently a foreland basin was developed on the Pelagonian passive margin. Finally, during the collision stage, the Pelagonian zone was overthrusted by the entire complex, which was towards northwest.

Maestrichtian pelagic limestones which overlie the ultramafic slices were also observed in our field study, but no volcanic rocks were detected. Moreover, the ophicalcite presence, indicate an OCT- environment (ocean continent transition), where ophicalcites were formed along transform faults or rifted spreading, plausibly suggesting the existence of an oceanic basin in Vardar ocean (Robertson, 1990). The coexistence of ophiolitic bodies within sedimentary (trench-type siliclastic) sequences is explained by the formation of a subduction –accretion complex which developed at this period, following the collision of the whole sequence into the passive Pelagonian margin, forming a foreland basin, consisting of ophiolitic slices, limestone olistholiths and debris flows (Robertson, 1990). The suturing of Vardar Ocean resulted in the westward thrust of the accretionary complex, leading to a final stage of deformation, which created folds and thrusts (Robertson, 1990).

We present mineral chemical and geochemical data, concerning the geotectonic setting of formation of Kimi rodingites and ultramafic lithologies.

9.2.1 Mineral Chemistry Data

Spinel discrimination diagram (Fig. 102a) is based on TiO_2 and Al_2O_3 contents. Chlorititic spinel is plotted within the common field of MORB (Middle Ocean) peridotites and SSZ (Supra Subduction Zone) peridotites. Its chemical fingerprints possibly indicate a Supra Subduction Zone origin. Spinel Cr# number (%) ranges from 50.05 to 54.5, while Fe# and Mg# range from 1.6 to 7.7 and 52.9 to 68.6 respectively.

Cr presents almost no mobility and it could be used as an indicator of the tectonic setting under which rodingite parent rocks were formed. Cr# relatively high values along with TiO_2 and Al_2O_3 contents are indicative of supra-subduction processes, possibly resembling a back arc basin.

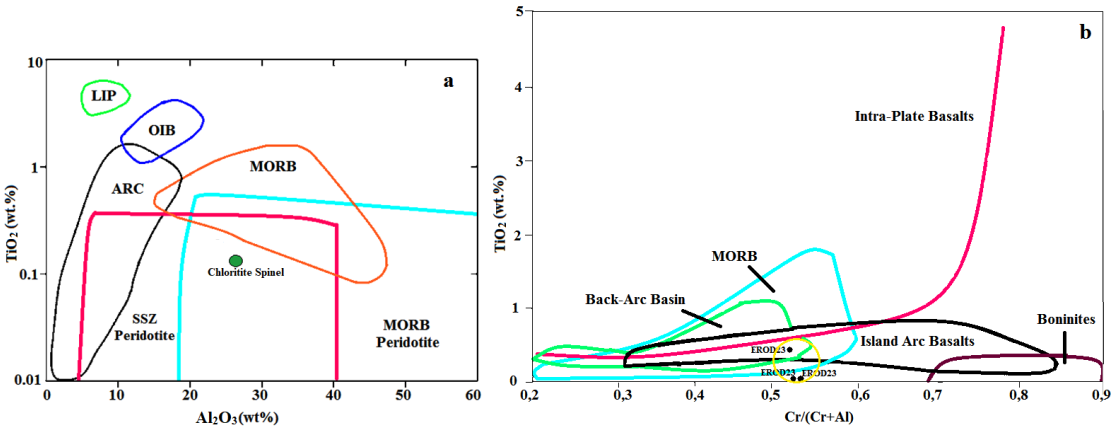

Figure 102.a. Al_2O_3-TiO_2 compositional relationship in spinel from Group-I MZ rodingite (Sample EROD23) and Chloritic (SERPV12rr sample) (after Kamenetsky, 2001).. b. TiO_2 versus Cr/(Cr+Al) after Arai (1992)

In Figure 102b, one sample is plotted within in the intersection of the back arc basin and island arc field, while the other two samples are plotted very close to MORB field. Furthermore a geotectonic discrimination of Kimi Mg-chromites as well as a comparison between Kimi chromites and spinels from other areas of Central Greece is shown below. Based on Cr# vs Mg# discrimination spinel diagram of Pomonis and Magganas (2017), Kimi Mg-chromites are either plotted within the field of Fore-Arc peridotites or within the common fields of N-MORBs and Fore-Arc peridotites (Fig. 103a). Moreover Mg-chromite plots are close with those of other parts from Central Greece such as Megaplatanos (Fig. 103a), Pindos-Vourinos-Kallindromon and Koziakas areas (Fig. 103b).

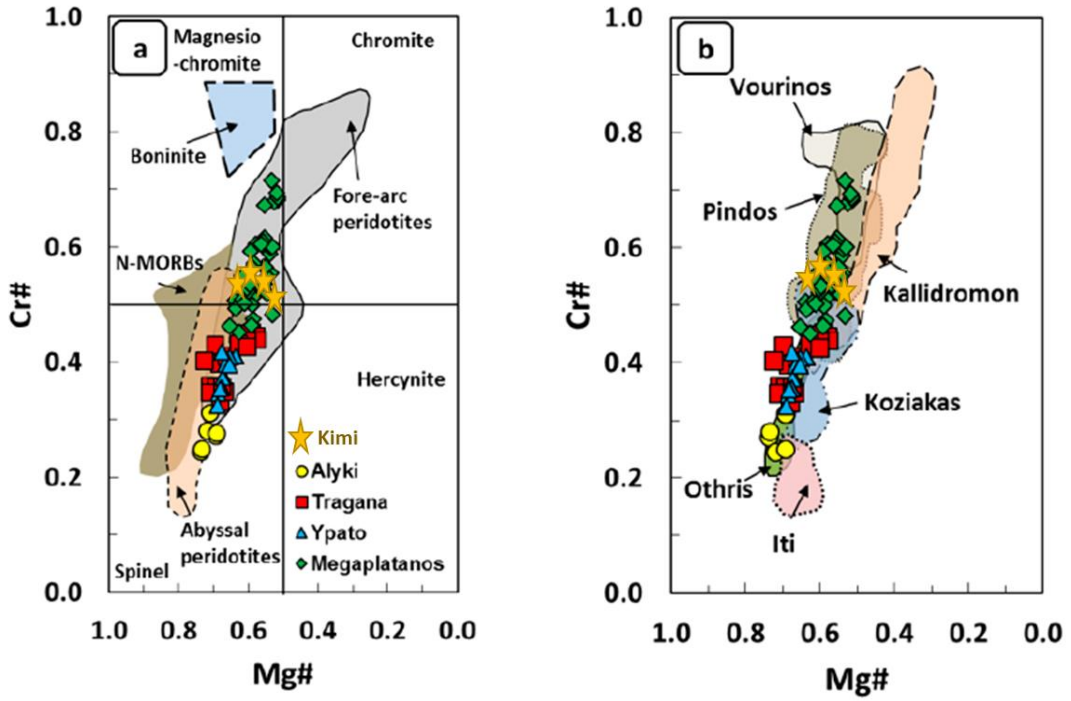

Figure 103. a,b. Cr # vs Mg# geotectonic discrimination diagrams for Kimi Mg-chromites and spinel plots from other parts of Central Greece (after Pomonis and Magganas, 2017).

Based on their TiO_2 and Al_2O_3 values Kimi Mg-chromites are plotted within the common field of IAV and MORB (Fig. 104a), while their Fe^{+2}/Fe^{+3} ratio vs their Al_2O_3 present SSZ affinities (Fig. 104b). Furthermore, chemical similarities between Kimi chromites and spinels from Eretria Ol-websterites, as well as Kimi chromites and spinels from Vrinena Ol-websterites and Eretria-Pelasgia serpentinitic rocks are also observed (Magganas and Koutsovitis, 2015).

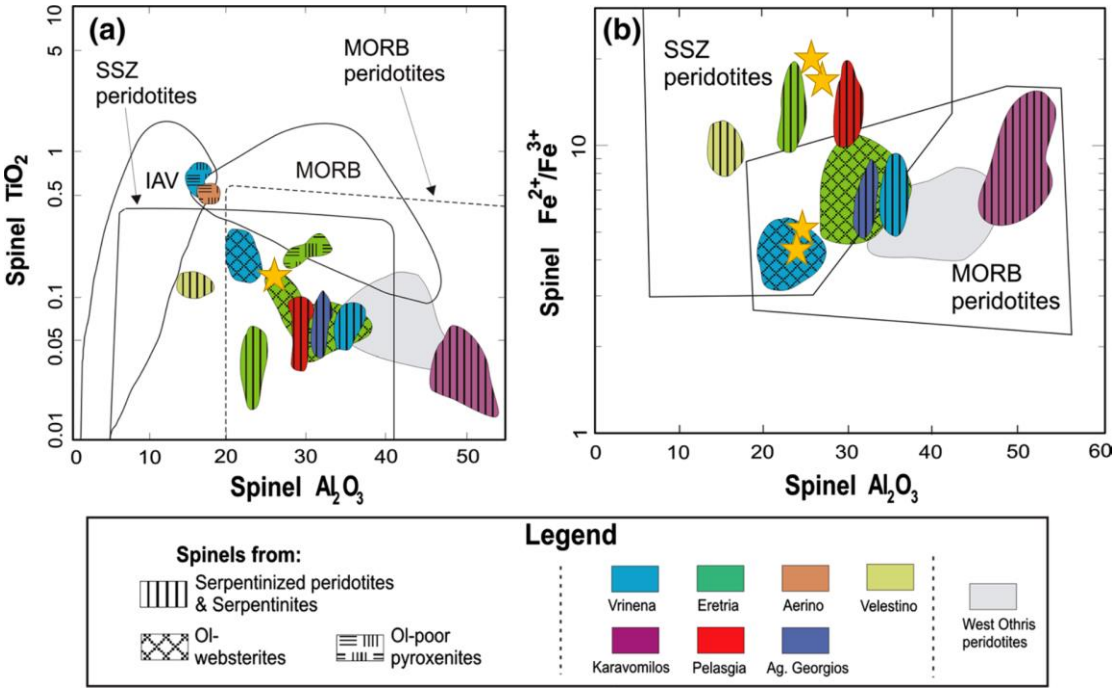

Figure 104. a,b. Spinel geotectonic discrimination diagrams for Kimi Mg-chromites compared to those of other parts of Central Greece (after Magganas and Koutsovitis, 2015).

The aforementioned features are indicative of processes affected by a SSZ environment. Furthermore, the types of hydrogarnets and vesuvianite crystals are also highly indicative for the involvement of subduction related fluids during the formation of rodingites (Koutsovitis et al, 2013). In addition the Cr# spinel value of SERPV12R chloritic sample is indicative of subduction related processes (Cr#> 0.4 on average Dick and Bullen, 1984; Ozawa, 1994; Parkinson and Arculus, 1999).

9.2.2 Geochemical Data

Rodingites have been affected by metasomatic processes characterized by strong major and trace element mobilization. Their chemical fingerprints can be probably the result of these processes, while many relatively constant elements such as Nb, Ta, Ti, could possibly be used for geotectonic setting conclusions. MORB-normalized patterns of Kimi Th rodingitic values are higher than those of Nb and Ta. This is indicative of subduction related processes. Furthermore, rodingite cores present negative Ti anomalies, which further support subduction. Moreover, negative P, K and positive Rb anomalies are attributed to subduction related fluids as well. LILE/HFSE ratio is quite high, while in REE Chondrite normalized patterns there is a strong LREE enrichment.

Experimental studies on seawater–peridotites interactions have shown that hydrothermal fluids and serpentinites after harzburgite are enriched in LREE (Allen and Seyfried, 2005; Menzies et al., 1993), while the REE still reflect the geochemical signature of the original protoliths, distinguishing their protoliths, at least for abyssal and mantle wedge serpentinites (Deschamps et al., 2013).

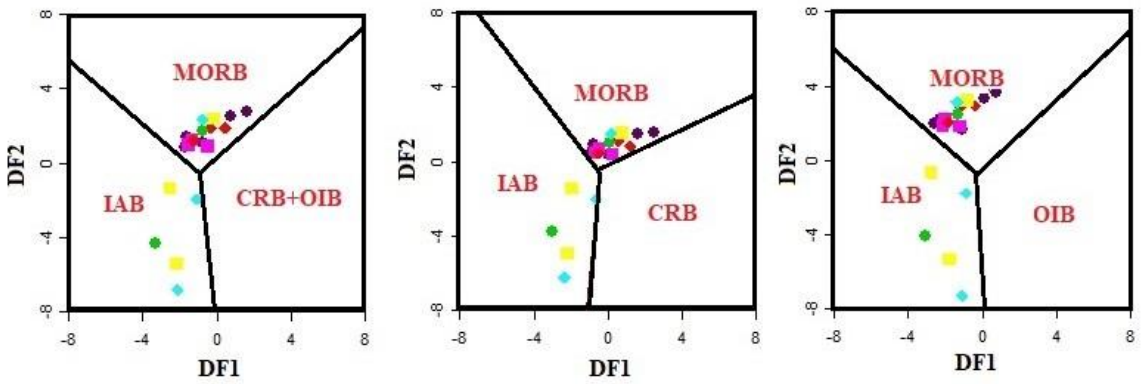

Figure 105. Discrimination plots proposed by Agrawal et al. (2008) for (ultra-) basic rocks (SiO2 < 52 wt. %), for island arc, continental rift, ocean-island and mid-ocean ridge basic rocks. DF1 and DF2, are mathematically designed to maximize the separation between the groups and account for 100 percent of the variance in the data.

The presence of high U values in serpentinite multi-trace element diagrams, compared to those of Ta and Nb, as well as the negative Nb and Zr anomalies also indicate subduction processes. Since rodingites have been affected by intensive metasomatism, there is a lack of a range of geotectonic setting diagrams for their discrimination.

In Figure 105, such a diagram is presented, proposed by Agrawal et al. (2008). It is based on linear discriminant analysis applied to log-transformed concentration ratios of five trace elements (La, Sm, Yb, Nb, and Th), using four ratios ln(La/Th), ln(Sm/Th), ln(Yb/Th), and ln(Nb/Th) and it is applicable for both basic and ultrabasic altered rocks. It is use for plots of samples with SiO_2 < 52 wt.%. On the diagram above, both Kimi rodingites can be divided into two types, where the first concerns these ones which were formed in a Middle Ocean Ridge environment, while the second type includes island arc basic rocks, implying subduction related processes. These features could further support the scenario of a SSZ (Supra Subduction Zone) environment.

On the other hand, Skyros rodingites seem to display island arc affinities, proposing a protolith that formed in a subduction related environment, also displaying further similarities with Kimi rodingites.

Moreover, according to REE Chondrite normalized patterns, Kimi and Skyros rodingites display subparallel patterns, with similar Eu anomalies and LREE-HREE fractionation. Skyros rodingitic patterns are near MORB, which is also detected in the most Kimi rodingite rocks, whereas some of them show patterns similar to island arc settings. Multitrace element pattern also show similarities which favor subduction, including Ti, Zr and Nb negative anomalies. Ti, P and K negative anomalies and Th positive anomalies can be attributed to the sediments of the subducted slab. These similar geochemical subduction affinities are also observed in multitrace element

diagram between Kimi rodingite and Skyros basalt and gabbro, including negative K anomalies and high Th values compared to those of Nb.

Skyros rodingite protoliths have been formed in a subduction related environment, as it is supported by their very low Nb/Th ratios (0.5-0.75), their slightly enriched Th/Yb ratios and their high MORB-normalized Th and U values compared to those of Nb for the gabbro and basalt samples respectively (Karkalis et al., 2016).

Kimi metasomatized serpentinitic rocks exhibit LOI values of both abyssal (LOI: 12.8 for Sample SERP25R) and subduction related environments (L.O.I.: 11.2 and 11.6 wt.% for metasomatized serpentinites) (average LOI for subduction environments: 11.15 wt.% and LOI for abyssal environments: 12.38 wt.%).

Cs, U enrichment and high Ta values are evident of subduction processes. Furthermore, LREE enrichment is also indicative of such processes as well, with possible interpretation their enrichment due to supra-subduction related fluids-interaction (Deschamps, 2013).

In addition, spinels from Kimi possibly reflect back-arc affinities, similar to those of Skyros high Mg and Al chromitites whose petrological and geochemical features indicate a supra-subduction zone (SSZ)/back arc basin environment (Economou et al., 1999). Similar geochemical similarities of Kimi rodingites with those of Skyros could possibly indicate that they were formed under the same SSZ system. They could also reinforce the assumption of an elongated ophiolitic zone of Vardar ocean, which hosts dispersed ophiolitic complexes.

The geochemical similarities between Kimi and Skyros rodingites (Fig. 100), are possibly indicative of a common origin, formed under the same geotectonic setting of Vardar Ocean. Furthermore, the geochemical similarities of Skyros ophiolitic rocks with those from other parts of the Eohellenic Nappe such as North Sporades islands and East Thessaly (Migiros, 1986; Pe-Piper and Piper, 2002; Karkalis et al. 2016) could further support the formation of Kimi ophiolitic rocks under the same subduction related environment inside Vardar oceanic strand, which hosts despressed ophiolitic thrusts/slices of an elongated ophiolitic zone of Vardar ocean (Karkalis et al., 2016). This elongated zone could also be associated with the northward extension of the North Cycladic Detachment System (Karkalis et al., 2016), but this scenario would require an extensive geochemical, petrological and structural study to be confirmed.

9.3 Metasomatic processes and Chemical transformation

Based on the SCMR definition, rodingitization is a metasomatic process in which basic rocks within serpentinized ultramafic bodies are replaced by grossular-andradite garnet and calcic pyroxene-rich rocks, called rodingites. Other accessory minerals include vesuvianite, epidote, scapolite and iron ores. Rodingites original protoliths are mainly basic dykes or inclusions, while they sometimes originate from other basic rocks such as volcanic rocks and amphibolites. Rodingites are metasomatic rocks enriched in CaO (increase in CaO) and depleted in silica and Na_2O (Pirajno, 2013), while they usually present Mg^{2+} enrichment (Coleman, 1977).

Rodingitization takes place at T between 250 ^{o}C and 450 ^{o}C (Schandl and Mittwede, 2001), while the rodingite formation depends on the P-T conditions of serpentinitic fluids. Rodingites are usually related with serpentinization processes. A number of metasomatic reactions release a high amount of mobile elements. Ca^{2+} derives from dissolution of the clinopyroxene of the ultramafics during serpentinization (Coleman, 1977), while silica and alkalies release is the result of anorthite breakdown during the reaction of mafic dykes with serpentinization fluids (Frost et al., 2008). Furthermore, the olivine breakdown releases Mg^{2+} leading to Mg enrichment in the metasomatized protoliths (Tsikouras et al., 2009).

Kimi rodingites Rodingite appear as in situ dykes or smaller veins in serpentinitic bodies presenting NNE-SSW or almost horizontal E-W directions. They are coarse-grained (usually containing miarolitic cavities) to aphanitic (mostly), zoned or patched in different colors. They consist mainly of garnet, vesuvianite, chlorite, diopside and occasionally calcite. In the most thicked dykes garnet and vesuvianite are mainly concentrated towards cores, while their margins are mostly chlorite and diopside rich. An intermediate or transitional zone between cores and margins which comprises all the aforementioned minerals in various proportions can be distinguished. Rodingites are found as massive-hard rocks, brecciated, sheared or heavily cataclastic. The last three types of rodingite indicate deformation of dykes in a brittle environment following the metasomatic event. On the other hand, the massive dykes seem to be rich in vesuvianite and calcite, while the cataclastically fractured ones vesuvianite and calcite are very low amount or completely absent.

9.3.1 Petrography and Mineral Chemistry

Rodingites have been divided into two groups according to the presence of calcite or not. These two groups, namely Group I and Group II, correspond to non-carbonated and carbonated rodingite dykes respectively. Furthermore, based on our microscopic and geochemical studies the rodingite dykes present three distinct zones which are characterized by the predominance of specific mineral phases. Marginal Zones (MZs) mainly include chlorite or/and diopside, while Core Zone (CZs) mainly consist of garnet and/or vesuvianite. Transitional Zones (TZs), which lie between MZs and CZs, include all the aforementioned minerals in various proportions. This ideal complete zoning is not present in every rodingite dyke and usually only one or two zones from the total three have been evolved. Moreover it often seems that the dyke thickness plays an important role concerning the development of the three distinct zones. In small rodingite dykes of some cm thick the MZs and CZs are usually absent, while some chlorite rich rodingite dykes o a few cm thickness present only MZs. Kimi rodingites sometimes exhibit features which are indicative of their gabbroic origin, such as relict diopside grains and subophitic textures which mainly consist of diopside and minor chlorite crystals. Their texture ranges from cryptocrystalline-microcrystalline indicating a doleritic origin to fine grained which indicates a typical gabbroic origin. The main rodingite minerals include garnet, vesuvianite, chlorite, diopside and calcite as well.

Garnet is either part of the microcrystalline to cryptocrystalline groundmass or it usually appears in the form of 200-300μm size porphyroblasts within a chlorite rich

matrix. Based on their mineral chemical data garnet porphyroblasts are mainly classified as hydrogrossulars, while many hydroandradite crystals have also been detected. In many cases idiomorphic garnet crystals exhibit hourglass zoning which is attributed to element preference 0on the various growing faces which surround a crystal (e.g. Van Hinsberg et al., 2006).

Vesuvianite either occurs as idiomorphic crystals of 200-300μm size or as part of the microcrystalline matrix. In the first case it mainly appears the classic blue-purple vesuvianite colors in crossed polars, while usually macroprismatic brown-yellow colored crystals in crossed polars also occur. In the second case vesuvianite is mainly grey colored in crossed polars. Furthermore, vesuvianite crystals from the TZs tend to be Mg richer compared to those from the MZs. This could be possibly related with vesuvianite formation under Mg-rich conditions in the final rodingitization stages (Li et. al, 2007) as the metasomatic fluids move from the MZs to the CZs.

Diopside crystals can be divided into relict and metasomatic ones. MZ diopside appears in the form of grains of 100-200 μm size whereas TZ diopside occurs as crystals of 500 μm size within a chlorite matrix or within veinlets. It usually forms radial aggregates with FeO rich cores and FeO poor rims.

Chlorite is present both in the chloritic rims of the ultramafic host rocks and in the MZs and TZs of the rodingite dyke. Chlorite appears as part of the microcrystalline matrix or within later formed veins mostly as big crystals of ca 300μm size. Chlorite crystals from the CZs and MZs of Group-I rodingites present similar XRD patterns while TZs chlorite of Group-I rodingites seems to differ from that of MZs and CZs since its patterns are similar to those of clinochlore (Fig. 106).

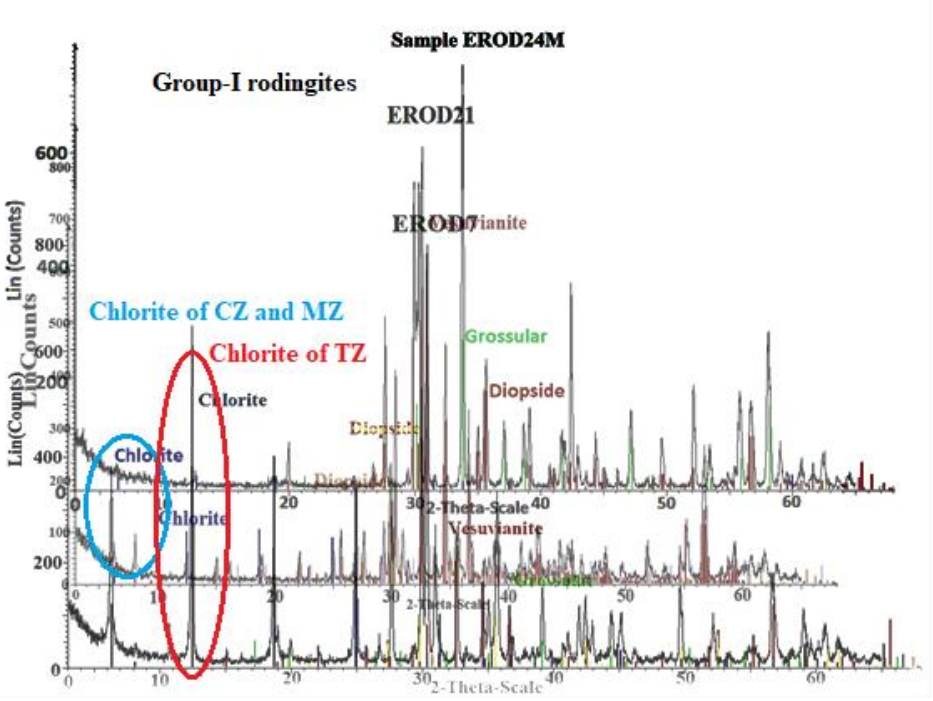

Figure 106. XRD patterns of Group-I rodingites presenting the two different chlorite types.

In Group-II rodingites chlorite of MZs and TZs present XRD patterns which seem closer to clinochlore while CZs chlorite presents different patterns which are similar with those of MZ and TZ of Group-I rodingites (Fig. 107). Consequently CZs and TZs of both rodingite groups present similar chlorite patterns, but they differ in the MZ. Furthermore XRD patterns of chloritites are similar with those of MZs, TZs Group-II rodingites and MZs Group-I rodingites. From the above XRD features it seems possible that specific chlorite species are concentrated towards the margins and the rims of the rodingite dykes, while others prefer the CZs. Based on their chemical discrimination and more specifically on their Mg# and Si values chlorites are mostly discriminated as penninites. Chlorites from the TZs are classified as penninites. On the other hand, chlorite crystals from MZs are mainly penninites with a few clinochlore crystals, while one chlorite analysis from chloritic sample SERPV12RR is plotted within the penninites field. Based on both the XRD patterns, the mineral chemical analyses as well as the petrographic study we conclude that chlorite mostly appears in the form of penninite and secondly in the form of clinochlore crystals, with the first being mostly concentrated towards the CZs, while the second is mostly concentrated towards the TZs and MZs. Our results coincide with those of Marakis (1972), concerning the presence of clinochlore.

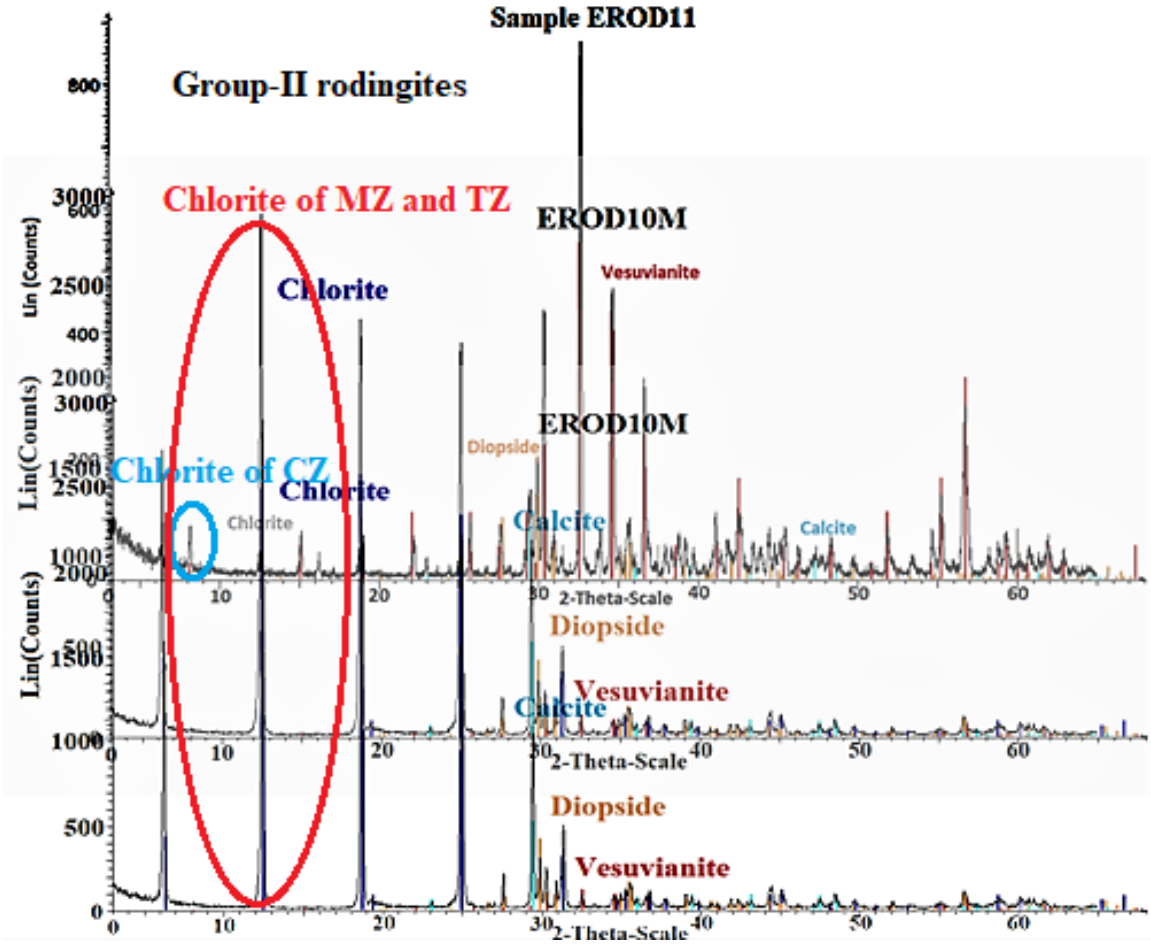

Figure 107. XRD patterns of Group-II rodingites presenting the two different chlorite types.

9.3.2 Geochemical Interpretation

9.3.2.1 Whole Rock Chemical Data

Rodingite different zones mostly differ from each other concerning their major elements and more specifically, CaO, MgO, FeOt and LOI contents. Based upon the binary major element and ternary ACF diagrams we see that MZ are richer in MgO and FeOt compared to the other zones. This is justified by the presence of Mg-Fe silicate minerals in these zones such as chlorite and diopside. On the other hand, CZ present higher CaO contents compared to those of the other two zones, which is explained by the predominance of garnet and vesuvianite. TZs present intermediate CaO, MgO and FeOt contents due to the participation of every mineral in various contents. LOI exhibits higher amounts in MZ areas and it is gradually decreased moving to the CZ. This is attributed to the presence of chlorite which is more hydrous compared to garnet and vesuvianite respectively. The high LOI amount of Sample EROD18 from CZ is attributed to the high hydrogarnets participation and the relatively higher chlorite amounts compared to the other CZ samples.

Ca enrichment is equivalent with the metasomatism degree. As rodingitization is increased rodingites are also enriched in CaO. In the different samples of same groups and same zone areas we see a negative correlation between CaO and MgO which indicates Mg depletion as metasomatism degree is increased. To examine the different metasomatism degrees we compare the CaO contents of each group in the same zones. CZs of both groups present similar CaO contents, with Group-II rodingites presenting quite higher CaO values. This could not be attributed to higher metasomatism degrees but it could be the result of calcite presence in Group-II. MZs and TZs of both Groups present similar CaO behavior with CZs. However Sample EROD10 from MZs of Group-II rodingites presents very low CaO contents and its chemical analyses is close to an ultramafic rock. This is attributed to its high chlorite amounts and the minor presence of calc-silicate minerals.

The discrimination of different zones is reflected both in the mineralogy and the whole rock chemistry of each zone. It is the result of the gradual metasomatic fluid entrance from the margin to the core of the mafic dyke (O'Hanley et. al, 1996; Li et al., 2004; Li et al., 2007). Furthermore, taking into consideration the presence of relict diopside grains within the TZs and MZs, as well as the higher CaO and lower MgO contents towards the CZs, we could possibly conclude that CZ have experienced greater rodingitization degrees compared to those of MZs and TZs.

REE enrichment in Group-II carbonated bearing rodingites coupled with their higher TOT/C contents could be indicative of the presence of carbonic-LREE complexes in the metasomatic fluids as we will discuss below. Furthermore, Eu anomalies are attributed to plagioclase breakdown during metasomatism which leads to Eu release, while it could be also attributed in changes of the oxidation state of Eu which is related with the physicochemical conditions (Tsikouras et al., 2009). Group-I rodingites present strong negative Eu anomalies. The vast majority of Group-II

rodingites presents the same negative Eu anomalies as well. However samples EROD18, EROD22L and EROD22M of Group-II rodingites do not display any Eu anomaly at all. This could be attributed to different oxidation states in some rodingite dykes. Another scenario could support that sample EROD18 experienced low metasomatism and as a result plagioclase dissolution took place in lower degrees. This could also justify the presence of plagioclase pseudomorphic crystals of sample EROD18. However, this scenario is less likely for samples EROD22M and EROD22L since their high vesuvianite contents (vesuvianite is formed in late rodingitization stages) indicate that they have experienced all the metasomatic stages. Ti negative anomalies, coupled with the high TOT/C contents and the calcite presence indicate that rodingitization in a subduction setting was definitely affected by sediment derived CO_2 rich fluids.

The high CaO contents of metasomatized serpentinites are attributed to the presence of metasomatic garnet crystals, while the presence of relict diopside grains could also contribute to the high Ca contents. On the other hand, the high CaO contents in chlorititic samples SERPV12RR and EROD7SR is the result of calcite rich veins which crosscut the chloritite matrix. Chloritites present higher MgO contents and lower Fe_2O_3 contents compared to those of metasomatized serpentinites. This could be attributed to the presence of Mg rich chlorites in the chlorititic rims, whereas the higher Fe_2O_3 contents of metasomatized serpentinites could also result from Fe participation in relict diopside grains. CIPW classification in serpentinized rocks and especially in metasomatized serpentinites is not reliable but it could give a sense of the ultramafic protoliths which according to the chemical and petrographical features are peridotites.

9.3.2.2 Isocon Plots

Isocon diagrams are simple means of quantitative changes in mass and volume or concentrations in mass transfer. The equation is rearranged into a linear relationship between the concentration of a component in the altered and the original rock respectively (Grant, 2005). Simultaneous solution of such equations for all components that show no relative gain or loss of mass defines an "isocon, with the slope of the isocon defining the mass change in the alteration (Grant, 1986, 2005).

Since no magmatic protoliths were found in our field study, we chemically compare Kimi rodingites with unaltered magmatic protoliths from other ophiolitic parts of the Vardar Ocean, such as Skyros Island and East Othris. As we mentioned above Kimi rodingites present features, such as relict diopside grains, which are indicative of gabbroic origin. On the other hand their textures range from fine grained to microcrystalline to cryptocrystalline. The fine grained samples seem to derive from a gabbroic protolith, while the microcrystalline ones more likely present a doleritic origin. Taking into consideration the aforementioned conclusions we use three rodingite samples from each rodingite Zone compared with two magmatic protoliths which correspond to a gabbro and a dolerite protolith respectively.

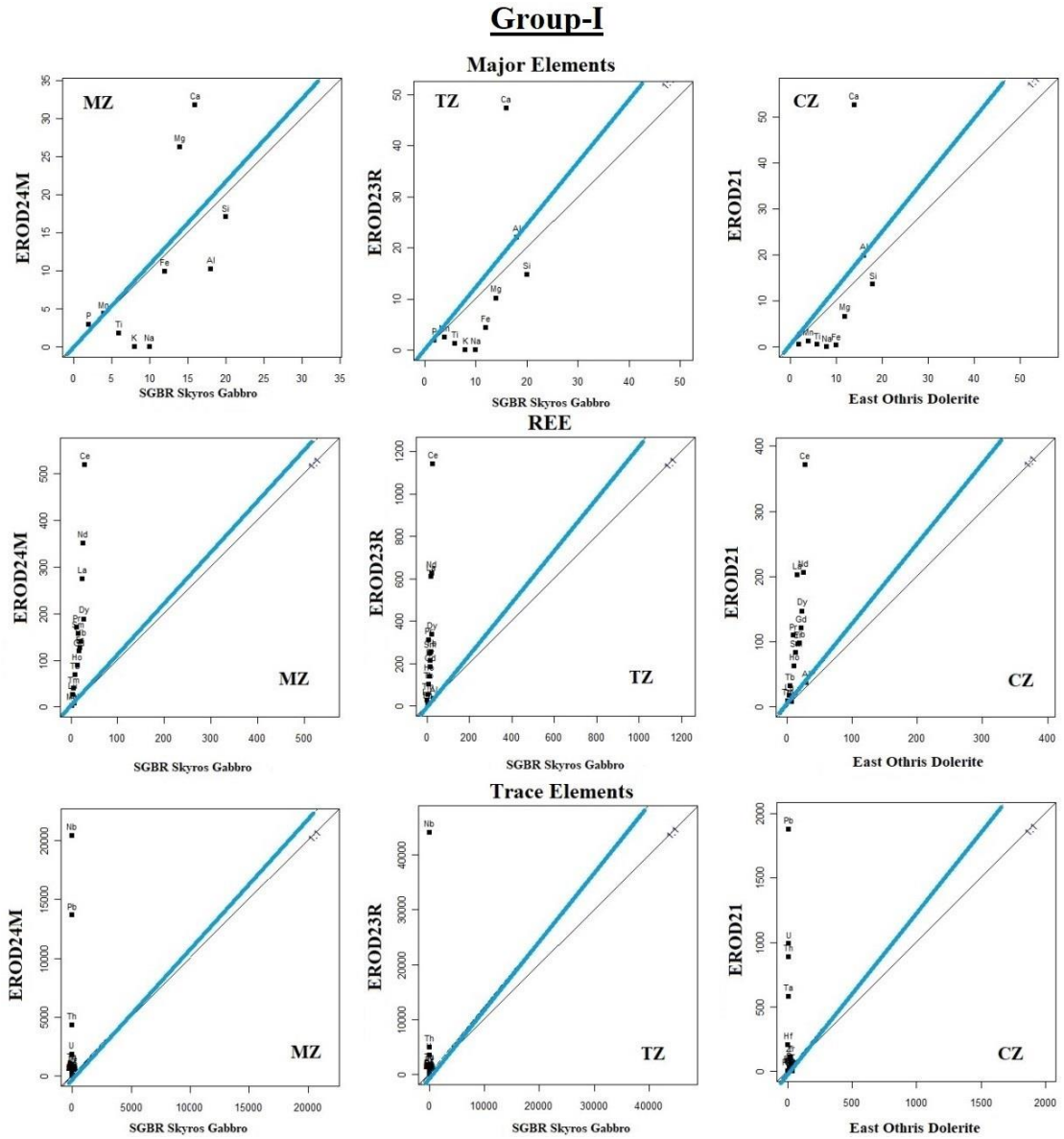

Figure 108. Isocon plots for Major, REE and Trace elements of Kimi Group-I rodingites from MZ (Sample EROD24M), TZ (Sample EROD23R) and CZ (Sample EROD21). Sample SGBR from Skyros (Karkalis et al., 2016) and 272 AER from E. Othris(Koutsovitis et al., 2013) were used as gabbroic and doleritic protoliths.

CZ sample EROD21 from Group-I rodingites is very microcrystalline to cryptocrystalline possibly reflecting a doleritic origin and it is matched with East Othris doleritic sample 272 AER (Koutsovitis et al., 2013). Furthermore, samples EROD24M and EROD23R from MZ and TZ respectively are compared with Skyros gabbroic sample SGBR (Karkalis et al., 2016).

For ISOCON plots (Fig. 108), we use Al as constant since no Al mobility is excluded from the mineral assemblages that occur in rodingitic samples. Al for chlorite formation and other calc-silicate minerals, most probably derives from the feldspars of the gabbroic protoliths (Tsikouras et al., 2009). Assuming Al remaining constant Ca is enriched, whereas Si and alkalies are depleted. This further reinforces our choice of Al as an immobile element. On the other hand for isocon plot of sample EROD24M of MZ Group-I rodingites, assuming Al or Ti as constant elements, Si is enriched which is not concomitant with rodingitization. The ISOCON slope of

samples EROD24M-SGBR is 1.09, EROD23R-SGBR 1.23 and for samples EROD21-AER is 1.24 These slope values correspond to total mass losses of -8.26 for MZs, -18.70 for TZs and -19.35 for CZs.

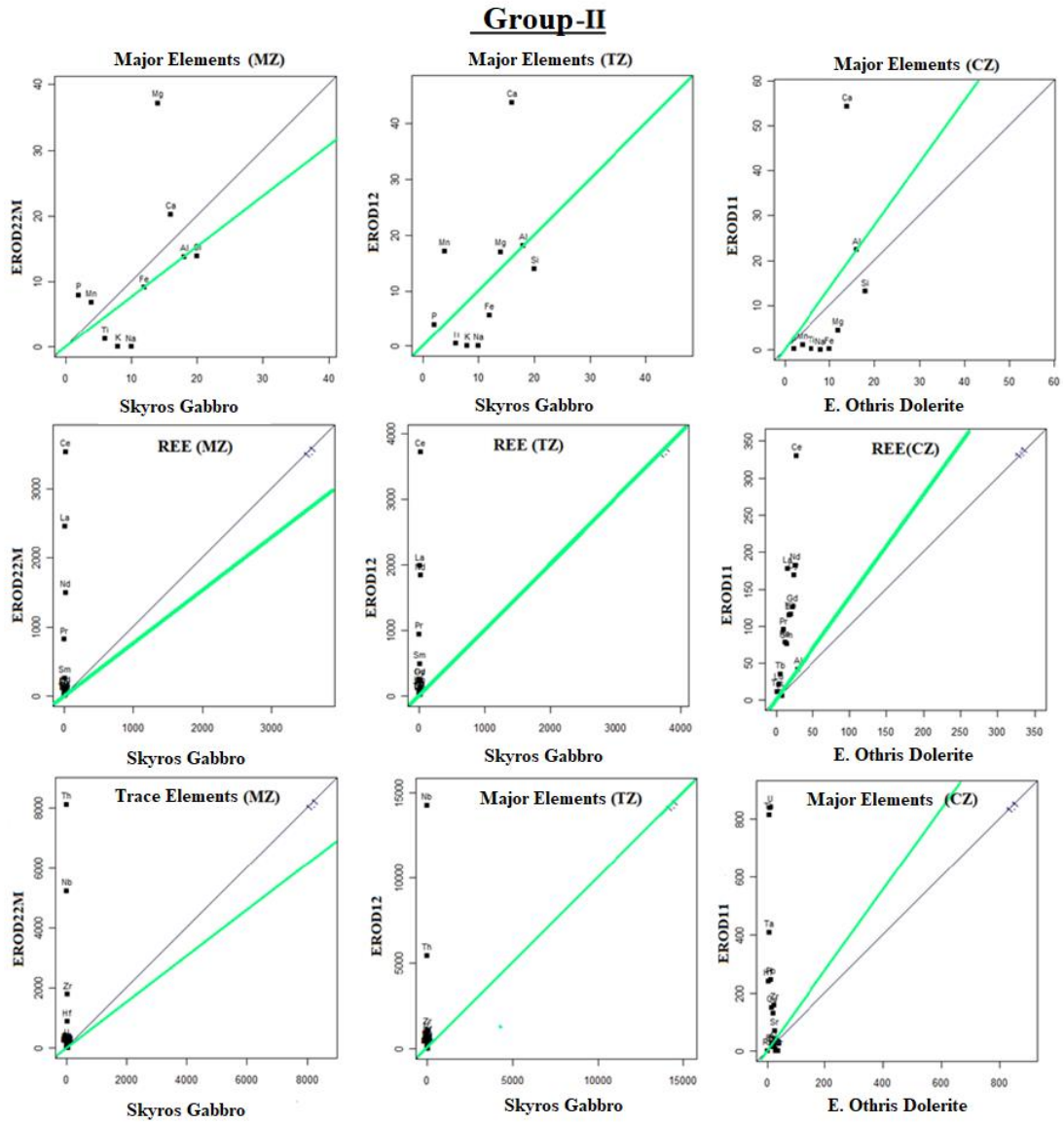

Figure 109. Isocon plots for Major, REE and Trace elements of Kimi Group-II rodingites from MZ (Sample EROD22M), TZ (Sample EROD12) and CZ (Sample EROD11). Sample SGBR from Skyros (Karkalis et al., 2016) and 272 AER from E. Othris (Koutsovitis et al., 2013) were used as gabbroic and doleritic protoliths

CZ sample (EROD11) of Group-II rodingites presents a doleritic microcrystalline texture and it is compared with East Othris doleritic sample 272 AER (Koutsovitis et al., 2013) for ISOCON plots. On the other hand, samples EROD22M and EROD12 are matched with Skyros gabbro sample SGBR (Karkalis et al., 2016).

For ISOCON plots (Fig. 109), Al is used as constant. Assuming Al as immobile Ca is enriched, whereas Si and alkalies are depleted. The ISOCON slope of samples EROD12-SGBR is 1.01, EROD22M-SGBR 0.77 and for samples EROD11-AER is 1.4. These slope values correspond to total mass gains for MZs (29.87), almost constant mass contents for TZs (-0.99) and mass losses for CZs (-28.57).

Table 22. Losses and Gains of Major Elements, Trace Elements and REE for MZ, TZ and CZ rodingite samples.

Losses and Gains						
Protolith	**Skyros Gabbro**	**Skyros Gabbro**	**E. Othris Dolerite**	**Skyros Gabbro**	**Skyros Gabbro**	**E. Othris Dolerite**
Rodingite	**EROD24M**	**EROD23R**	**EROD21**	**EROD22M**	**EROD12**	**EROD11**
Group	**Group-I**	**Group-I**	**Group-I**	**Group-II**	**Group-II**	**Group-II**
Area	**MZ**	**TZ**	**CZ**	**MZ**	**TZ**	**CZ**
Major Elements (wt%)						
Si	-5.14	-9.33	-9.56	-2.18	-7.26	-11.63
Al	-4.33	0.00	0.00	0.00	0.00	0.00
Fe	-0.95	-2.78	-8.18	-0.03	-2.11	-6.26
Mg	3.89	-2.23	-3.63	13.30	1.10	-4.77
Ca	5.85	10.05	13.50	4.62	12.24	11.83
Na	-2.06	-2.06	-2.47	-2.07	-2.07	-2.48
K	-0.67	-0.67	0.00	-0.67	-0.67	0.00
Ti	-0.10	-0.11	0.00	-0.10	-0.13	-0.20
P	-0.10	-0.11	0.00	0.04	0.01	-0.01
Mn	0.00	-0.04	0.00	0.11	0.28	-0.11
REE (ppm)						
La	13.27	30.25	8.28	202.38	124.09	6.25
Ce	34.18	74.01	22.25	375.34	301.34	17.07
Pr	4.12	8.27	2.50	35.99	31.59	1.85
Nd	15.92	28.29	9.17	112.33	105.31	6.81
Sm	4.89	8.23	3.05	14.33	20.71	2.32
Eu	-0.04	0.08	-0.06	3.19	1.12	-0.12
Gd	5.74	9.45	3.84	9.33	15.94	3.45
Tb	1.16	2.08	0.73	0.96	2.13	0.71
Dy	8.28	15.33	5.49	4.31	12.11	5.64
Ho	1.77	3.19	1.03	0.53	2.19	1.17
Er	5.72	10.38	3.28	1.06	6.48	3.51
Tm	0.90	1.74	0.44	0.15	0.99	0.50
Yb	5.92	11.53	2.91	1.03	6.29	3.13
Lu	86.00	1.66	0.40	0.21	0.89	0.43
Trace Elements (ppm)						
Ba	-32.17	-31.56	0.71	-30.10	-30.03	-0.19
Sr	-181.91	-166.56	7.12	-176.21	-96.32	11.32
Rb	-10.82	-10.84	-0.01	-10.48	-10.40	-0.01
Nb	103.67	223.54	0.00	42.32	88.33	0.00
Ta	21.86	34.04	7.71	2.03	8.20	4.76
U	7.60	14.46	7.87	1.33	4.37	5.90
Th	19.97	22.52	8.84	58.59	29.91	7.19
Pb	435.30	2.18	25.00	4.46	-0.11	2.73
Cu	-13.37	-14.22	-1.28	-13.51	94.69	9.19
Zn	17.75	-2.12	0.00	15.12	22.81	-16.43
Ni	189.57	59.42	-107.31	151.24	-20.98	-107.71
Cr	82.07	131.26	-544.49	-190.57	-472.42	-545.10
Co	1.84	6.01	0.00	46.99	-12.52	-41.53
Zr	122.62	108.70	27.12	497.80	228.55	38.42
Y	54.72	192.72	30.95	15.38	63.53	32.49
V	133.00	-163.98	-251.78	-160.08	-166.07	-252.14
Sc	-24.50	-34.49	-42.39	-37.10	-39.01	-43.29

Based on their ISOCON plots and their mass losses and gains both Group-I and Group-II rodingites present similar element mobilities. However they seem to differ a lot concerning their REE extent of mobilization (Table 25).

Major Elements

Major elements present similar behaviour in both rodingite groups. Their mobility is in agreement with the nature of rodingitization characterized by Ca enrichment and Alkalies-Si loss. More specifically in both rodingite Groups Ca is strongly enriched presenting strong gains moving from MZs towards the CZs, while Si and total alkalies are strongly depleted. Fe is depleted in every rodingite zone but the strongest depletion is observed moving towards the CZs. On the other hand Mg is strongly enriched in MZs and depleted in CZs of each rodingite group. Ti, P and Mn are either depleted or they almost remain constant.

REEs

In both rodingite groups REEs and more specifically the LREEs (La, Ce and Nd) are enriched. However Group-II rodingites present a strong enrichment and higher values compared to those of Group-I. This could be associated with LREE transportation in metasomatic fluids mainly via carbonic ligands as it will be discussed below. In both groups REEs tend to be concentrated towards the MZs and TZs rather than in CZs.

Trace Elements

The majority of trace elements are mobilized through metasomatic processes. However, their mobility seems to depend mainly on the zone area and secondly on the presence of carbonated minerals or not.

In both rodingite groups Ba and Sr are strongly depleted from the MZs, while moving to the CZs Ba is tend to be added. Nb is enriched in MZs and TZs, whereas it remains constant in CZs. However it presents a stronger enrichment in Group-I rodingites compared to Group-II ones. Pb does not exhibit a strong mobility apart from Group-I MZs where Pb is strongly enriched (Pb: + 435.30 ppm). In Group-I rodingites Ni and Cr are strongly enriched towards the MZs and TZs, while they are strongly depleted from CZs. On the other hand in Group-II rodingites Cr is strongly and continuously depleted moving from the MZs to CZs, while Ni is added in MZs and depleted from TZs and CZs respectively. Zr and Y are strongly mobilized enriching every rodingite zone in both groups.

9.3.2.3 Chemical Composition of Metasomatic fluids and Element Mobilization

The isocon slopes for CZs, MZs and TZs rodingites are 1.4, 0.77 and 1.01 respectively. Based on the method proposed by Grand (1986), which is based on the repricosal ratios, these slopes correspond to total mass transfers of 29.8% for marginal zones, -0.6% for transitional zones and -28.5% for core zones. We observe a quite high mass gain for rodingite margins, which is decreased in rodingite transitional zones exhibiting a very low mass loss, which is continued moving to rodingite core presenting a quite high value. These results differ from the majority of total mass modifications in Central Greece which are relatively low (Koutsovitis et al., 2013). The metasomatic fluids moving from the ultramafic protoliths to the rodingitic rim

could have possibly enriched the rodingitic dykes in mobile elements, while afterwards they gradually started to deplete the dykes from mobile elements moving from the transitional to the core zone. This could be further supported by the decreasing of many trace elements values such as La and Ce moving from the marginal to the core zone in semi-logarithmic diagrams. From the aforementioned chemical results it is clear that metasomatic processes in Kimi possibly took places under various pH and oxidation conditions. This is also indicative of the rodingitization evolution through several stages of different pH, oxidation and temperature conditions.

In accordance to rodingite literature Kimi rodingites present Ca enrichment and silica-alkalies depletion. Although in some cases some magmatic minerals such as, relict diopside grains have been preserved, the majority of Kimi rodingites have been highly affected by metasomatic processes, which is also confirmed by the presence of vesuvianite, which is regarded as late stage mineral in rodingitization processes (Li et al., 2007; Normand and Williams-Jones,2007; Koutsovitis et al., 2013). These are consistent with serpentinization as an alkaline (pH=8–12), Ca rich, hydrous process (Barnes and O'Neil, 1969; Neal and Stanger, 1985), where Ca enrichment possibly derives from clinopyroxene breakdown of the surrounding harzburgite (e.g. Coleman 1977; O'Hanley 1996). In some cases, Na and K constant values could be indicative of alkaline conditions as well.

Most of them seem to have a gabbroic origin, attributing their desilification, alkalies, Rb and Ba feldspar-plagioclase dissolution and clinopyroxene breakdown, resulting in garnet formation (e.g. Coleman, 1977; Li et al., 2004, 2008; O'Hanley et al., 1992). During serpentinization clinopyroxene of the ultramafic rocks, breaks and Ca^{+2} is released in the form of $CaOH^{+}$ (e.g. Bach and Klein, 2009; Coleman, 1977).

Frost et al (2008), gives another explanation for Ca enrichment. Ca enrichment is the result of silica loos from the mafic protoliths, caused by the interaction with the ultramafic derived fluids, which caused the Si depletion from anorthite, while Ca concentration was increased. Lack of alkalies is attributed to the absence of feldspars, while the very high MgO values (MgO: 0.2 -34.7 wt%) are mainly the result of chlorite formation. The presence of diopside and impure diopside crystals can also contribute to MgO contents. High LOI contents result from the hydrous mineral phases such as chlorite, hydrogarnet, vesuvianite, prehnite.

In Kimi Ca enrichment is probably the result of clinopyroxene dissolution of ultramafic protoliths as it is further confirmed by the presence of totally or serpentinized peridotites which arise from the field study and the CIPW norm based discrimination of ultramafic rocks.

As we mentioned above samples of the same Zones within the same groups, as well as samples of the same zones between the two different groups, present similar CaO contents. This possibly indicates that the same zones have been affected by similar metasomatic grades between the two groups. However, the presence of some relict diopside crystals in TZ areas of Kalimeriani rodingite sample EROD7SC possibly

implies that Kalimeriani rodingites have been affected by different metasomatic grades.

The presence of distinct rodingite zones within the same dykes could be indicative of a gradual fluid infiltration through the rodingite dyke where water/rock ratio is gradually increased from MZs to CZs as it is supported by the high amounts of vesuvianite crystals in the second. Moreover, this could also imply that CZs have been affected by higher metasomatic grades, since vesuvianite is formed at late rodingitization stages

9.3.2.3.1 REE and Y

Kimi rodingites exhibit REE enrichment especially in La and Ce (LREE). More specifically CZs average ΣREE value is 180.18 ppm. In MZs rodingite areas ΣREE value is 224.89 ppm, while for TZs rodingite areas the ΣREE is 246.23 ppm. REE mobilization depends on the fluid-rock interaction and composition. More specifically the water/rock ratio and the ligands presence are two major factors concerning the REE mobility (Tsikouras et al., 2009). In water/rock ratios greater than 100 REE are immobile. REE mobilization can either occur at low or high pH values (Price et al., 1991; Valsami and Cann, 1992; Verma, 1992).

REE mobility in Kimi rodingites can probably result from primary plagioclase breakdown in gabbro or pyroxene dissolution from the surrounding peridotites (Tsikouras et al., 2009). High REE contents can be attributed to their mineral assemblage. According to the semi-logarithmic diagrams LREE La, Ce, Pr are slightly increased from MZs to TZs and slightly decreased CZs. Nd, Sm and Eu remain almost constant moving from the marginal to the transitional zone and slightly decreased moving to the core. HREE apart from Dy remain almost constant from the rodingitic margin to the core, while Dy remains constant from the marginal to the transitional zone and they present an enrichment moving to the core zone.

From the aforementioned chemical data it is understood that REE are mainly concentrated in the TZs and MZs, while the CZs are poorer. REE mobility concerns mainly LREE, while HREE values are similar for every rodingite zone. This is explained by the mineral assemblages of each zone. LREE are mainly hosted within apatite and allanite which tend to be concentrated towards the MZs and TZs as it is shown by their petrographic and mineral chemical features of Cerium bearing apatite and allanite crystals.

Rodingitization is a process which evolves hydrous environments. This is also reinforced by Zr mobility which occurs as complexes with OH^- in the form of $Zr(OH)_4$ at low temperature aqueous environments (Rubin et al., 1993; Aja et al., 1995; Veyland et al., 2000). This further confirms the assumption of REE ligands with OH^-. On the other hand, the presence of calcite and the high Cr and Ni mobility are highly indicative of CO_3^{-2} existence. REE-carbonate ligands are formed at low pH values. However, calcite formation leads to a αCO_3^{-2} decreasing which gives rise to REE-carbonate ligands dissolution (Caruso and Simmons, 1985). CO_3^{-2}, OH^-,F^-, Cl^-,

PO_4^{-3} are the main REE ligands for REE in metasomatic fluids. Metasomatic fluids are enriched in the aforementioned ligands after the interaction between fluids and minerals which host REE. In our case the REE sources mainly are the pyroxene breakdown from the ultramafic rocks (Bizimis et al., 2000; Barth et al., 2003), the plagioclase breakdown from doleritic and gabbroic protoliths (Bau, 1991) and amphibole dissolution as well (Koutsovitis et al., 2013).

At low pH CO_2 and F^- rich fluids REE mobilization is promoted fluid phases rich in CO_2 (Price et al., 1991; Valsami and Cann, 1992; Verma, 1992), while very important is the presence of REE ligands such as CO_3^{-2}, OH-, PO_4^{-3} in the metasomatic fluids (Tsikouras et al., 2009 and references therein). Moreover, REE enrichment in MZs is related with high f_{O2} values, while the REE decreasing from MZs to CZs rodingites could possibly indicate a f_{O2} depletion (Koutsovitis et al. 2013 and references therein).

REE can be strongly mobilized by carbonic fluids leading to the formation of carbonate–REE complexes and especially with LREE (e.g. Wendlandt and Harrison, 1979; Gimeno-Serrano et al., 2000) resulting in soluble (LREE)CO_3 complexes. This is further confirmed by the fact that Group-In non-carbonated rodingites present lower REE values compared to those of Group-II carbonated rich rodingites. Formation of calcite decreases the activity of CO_3^{2-} ions, causing the breakdown of REE-carbonate complexes (Caruso and Simmons, 1985). As a result, the amount of REE is decreased in the fluid, because REE complexes display higher solubility compared to uncomplexed REE species (Bau, 1991). These REE complexes are promoted at higher pH (Wendlandt & Harrison, 1979).

Subsequently, the main ligands of REE, are the CO_3^{2-} ions, as well as, the OH^- ions, which form complexes with HREE (Haas et al., 1995). Additionally, the presence of apatite is indicative of PO_4^{3-} -REE complexes and deposition of REE during the late metasomatic stage. Apatite formation is further facilitated by alkalic CO_2-rich fluids (Ayers and Watson, 1991).

Furthermore, the presence of REE-bearing apatite, as well as the P_2O_5 increasing in semi-logarithmic diagrams is clearly connected with the existence of REE-PO_4^{-3} complexes. These complexes are more likely to have formed under high Temperature, alkaline (high pH) values and low CO_2 conditions (Ayers and Watson, 1991). Apatite formation in the late stages of the metasomatic processes is also supported by the increase of P_2O_5 as serpentinization fluids move from ultramafic rims to rodingite core zone as it is shown in the logarithmic diagrams. Apatite formation is further confirmed by the P_2O_5 increasing in logarithmic diagrams from chloritic and serpentinitic rim to the marginal zone. Apatites are usually REE and Y rich. Kimi apatite presents high Ce_2O_3, Y_2O_3 and SiO_2 contents. The distribution of REE in apatite has been described by many authors. Comodi et al., 1999 studied the Si, S and REE rich apatite from Abbruzzi in Italia, suggesting the following substitution for REE: $REE^{+3}+Si^{4+} \rightarrow Ca^{2+} + P^{+5}$. This chemical substitution could also explain the REE and Si enrichment for apatite bearing rodingites. On the other hand, another

substitution suggested for REE apatite involves Na^{+2}enrichment according to the following substitution: $2Ca^{+2} + Na^{+} \rightarrow REE^{+3}$ (e.g. Roeder et al., 1987; Ronsbo, 1989) but such a scenario is rejected since no Na_2O contents have been detected. Y enrichment is possibly explained by its similar behavior with REE.

Allanite REE deposition can be explained by late hydrothermal alteration stages (e.g. Excley, 1980), where REE are remobilized and concentrated in allanites. Ce is always present in greater amounts compared to those of La with La/Ce ratio ranging between 0.3 and 0.5 (Frondel, 1964). Allanite is characterized by heterovalent substitutions where $(REE)^{3+}$ replaces Ca^{2+} on the A2 site (Dollase, 1971), balanced by Fe^{2+} occupation of the octahedral M 3site according to the following chemical substitution

$$REE^{+3} + Fe^{+2} \rightarrow Ca^{+2} + Fe^{+3}$$

As metasomatism evolves, REE remain relatively constant due to their deposition in minerals which are indicative of late metasomatic stages such as vesuvianite (Li et al., 2007). During vesuvianite formation the vesuvianite influx was very high, and fluids were low CO_2. In a later stage carbonic rich fluids transferred REE as ligands and form the interaction of vesuvianite with fluids vesuvianite was REE enriched. In these late stages PO_4^{-3} ions formed complexes with REE and reacting with Ca^{2+} rich metasomatic fluids of serpentinisation, deposition of REE-apatite took place. REE concentration in vesuvianite is described by Groat et al (1992a). They suggest three possible substitutions involving the incorporation of REE at the X sites for San Benito County vesuvianite samples: Ln^{3+} Na$\rightarrow$ + 2Ca and Na + $Ti^{4+}\rightarrow$ Ca + Al, while for very high Ti contents Ln^{3+} + Mg $\rightarrow$ Ca + Al and Mg + Ti $\rightarrow$ 2Al are suggested. The other possible mechanism involves substitution of O^{2-} for OH^{-}Fitzgerald et al. (1987), stated that the REE substitute for Ca, Ti substitutes for Al , OH is an oxygen atom rather than a hydroxyl, and Mg substitutes for Al. However this scenario can only be hypothetic since no chemical analyses of REE-bearing vesuvianite were detected in Kimi rodingites.

LREE and LILE enrichment of Kimi rodingites is attributed to their interaction with hydrothermal rich fluids possibly deriving from sediments of subducted slab. Kimi chloritites and garnet metasomatized serpentinites present LREE enrichment and present Eu anomalies, possibly reflecting hydrothermal fluid interaction which have previously reacted with plagioclase-bearing rocks, such as oceanic gabbros (e.g. Douville et al., 2002) and/or changes in the fluid chlorinity and local redox conditions (e.g. Allen and Seyfried, 2005; Deschamps et al., 2013).

9.3.2.3.2 Zr

Zr is a generally immobile element, remaining quite constant in metasomatic processes, but in alkaline hydrothermal conditions of high pH, it is commonly mobile. In such conditions Zr makes complexes with OH^{-} as $Zr(OH)_4$ in low temperatures and aqueous environments (Rubin et al., 1993; Aja et al., 1995; Veyland et al., 2000). This scenario seems consistent with the Ca rich alkaline metasomatic fluids deriving from serpentinisation. On the other hand, Zr can also be mobile in environments with pH

values less than 4, forming complexes with F^-. Such a scenario cannot be very possible, because our rocks do not present high bulk rock F^- contents, but the presence of apatites in many samples could suggest such a scenario although the alkaline conditions seem to be more possible, since Y also behaves as mobile.

9.3.2.3.3 Cr and Ni

Cr and Ni are generally immobile elements and they are mainly concentrated in olivine and spinels of ultramafic protoliths (Tsikouras et al., 2009). However in Kimi rodingites Cr and Ni exhibit a strong mobilization, mainly leading to Cr and Ni depletion, while in sample EROD22M of marginal rodingites Ni strongly enters the system. At the very initial metasomatic stages the CO_2 rich conditions lower the pH, causing the mobilization of Cr and Ni (Aiuppa et al., 2000). This could explain the Ni enrichment in some rodingites. However, rodingitization is generally thought to be an alkaline process and Cr-Ni mobility should be explained under such high pH values.

Cr has two oxidation stages of Cr^{+3} and Cr^{+6}. The trivalent Cr is present within minerals such as spinels and olivine and it is strongly immobile, while the Cr^{+6} is very soluble compared to Cr^{+3} (Aiuppa et al., 2000, Izbicki et al., 2008, Tsikouras et al., 2009). Cr^{+3} remains stability mainly occurs at reducing conditions, while at oxidizing conditions Cr^{+3} is converted to Cr^{+6}. However, Rai et al. (2007), suggest tha under alkaline conditions the presence of CO_2 reinforces Cr mobility via CO_3^{-2} ligands. This could explain the Cr leaching from rodingite minerals. Furthermore, according to Aiuppa et al. (2000), Ni can be mobilized in alkaline environments under aquatic CO_2-rich conditions, forming Ni-carbonate complexes. Consequently under alkaline conditions Ni can be possibly leached from the ultramafic protoliths and entering the rodingitic marginal zone via carbonate ligands, while under the same conditions Cr is leached from the minerals of the mafic protoliths

9.3.3 O-C Isotope Geochemical Data

According to Rollinson (1993), $\delta^{13}C$ mean mantle value is about -6 ‰. MORB has a mean value of $\delta^{13}C$ = -6.6 ‰ (Exley *et al.*, 1986), while seawater has by $\delta^{13}C$ value of close to 0 ‰ and marine carbonate has a narrow range of values between -1 and + 2 ‰.

Samples CARED2cc and CAREDcc are red mudstone calcite crystals and present a range in $\delta^{13}C$ VPDB of 0.02‰ and 0.96‰ for $\delta^{18}O$ VPDB. The results arising from red mudstones show a small range of carbon and oxygen isotope values indicating their homogeneity.

Keith and Weber (1964), give the following equation for the discrimination between marine and fresh water limestones assuming that they were not recrystallized: $Z = 2.048 (\delta^{13}C + 50) + 0.498 (\delta^{18}O + 50)$, where $\delta^{13}C$ and $\delta^{18}O$ are expressed as ‰ PDB. Limestones with Z values above 120 are classified as marine, while those with Z below 120 are as fresh-water ones. CARED2cc and CARED Z values are 127.83 and 128.35 respectively, which is indicative of a marine origin. Furthermore, according to Rollinson (1993), the $\delta^{13}C$ values are close to those of marine carbonates.

SOPHAcc and ZTOPHcc calcite from Kimi ophicalcites present a reange in $\delta^{13}C$ and $\delta^{18}O$ values of 0.02 ‰ and 5.48 ‰ respectively. $\delta^{13}C$ are very close to seawater which is approximately 0 ‰. Mudstone calcite $\delta^{18}O$ isotope values are heavier compared to those of ophicalcite calcite (-7.36‰ for mudstones and -9.5‰ for ophicalcites). This could probably indicate that the depleted oxygen isotope values of the calcite in the ophicalcites are likely related to higher precipitation temperatures relative to the marine calcites of red mudstones (Melfos et al., 2009).

The $\delta^{13}C$ values for Kimi ophicalcites are 0.29 ‰ and 0.27‰ respectively, which could be indicative of seawater participation because their values lie close to 0 ‰. Taking into consideration that red mudstones usually occur as lenses within ophicalcites we plot these samples into a δ^{18} O PDB and $\delta^{13}C$ PDB diagram in order to determine their origin and possible mixture processes of different water types.

According to Figure 110, ophicalcite calcites (ZTOPHcc and SOPHAcc) are plotted within the Limestones and Marbles field, while both samples are near with the border line of Limestone/Marble field for sedimentary carbonates, with hydrothermal fields. ZTOPHcc calcite is plotted near Middle Ocean Ridge field, showing a combination of mantle derived carbon and seawater carbon (Stakes and O'neill, 1982), while SOPHAcc calcite is plotted near Mississippi Valley Hydrothermal field (Richardson et al., 1988). This probably implies that calcite veins from ophicalcites could have a mixed origin of marine water and hydrothermal fluids deriving from metasomatic processes, which generate from the mixing. More specifically, they originate from a combination of chemical hydrothermal processes, with resedimentary processes such as sediment gravity flows and debris flows. Z values range from 121.8 to 124.5 probably indicating that their sedimentary carbonated part derives from marine carbon.

On the other hand, red mudstones (samples CAREDcc and CARED2cc), are plotted in the field of Limestones/Marbles, possibly indicating their sedimentary origin. These features probably suggest that both ophicalcite sedimentary calcite and the calcite veins from red mudstones have the same origin, but they present isotopic differences due to the possible hydrothermal contribution to the calcite of the first.

Group-II Kalimeriani rodingites consist of calcite with quite negative $\delta^{13}C$ (PDB) (-14.40 ‰) values which are indicative of hydrothermal calcite, consisting of mantle dirived C. In isotopic plots of Figure 110, Kimi Kalimeriani rodingite calcite is plotted within the common field of Missisipi Valey hydrothermal carbonates and Middle Ocean Ridge carbonates. This suggests their formation in a rock dominated environment with low water/rock ratio and high temperatures (Rollinson, 1993). The very negative $\delta^{13}C$ values may also reflect the presence of light carbon propably diriving from the oxidation of methane released during serpentinization process mixed with seawater and manlte dirived carbon (De Felipe et al., 2012).

Furthermore, EROD12cc rodingite calcite from Kimi-Choneftiko presents quite negative $\delta^{18}O$ (PDB) values (-13.32 ‰) and is plotted within the Limestone 2 Ga field, close to that of Middle Ocean Ridge hydrothermal carbonates. This could be indicative of a mixed origin from both mantle derived and marine water carbon. The $\delta^{13}C$ value is 3.63‰ which is similar to those of marine carbonates (Rollinson, 1993 and refernces therein) and hydrothermal calcites veins from mantle rock in the Lost City and MARK areas (δ13CPDBb+4.5‰, Alt and Shanks, 2003; Früh-Green et al., 2003; Bach etr al., 2011).

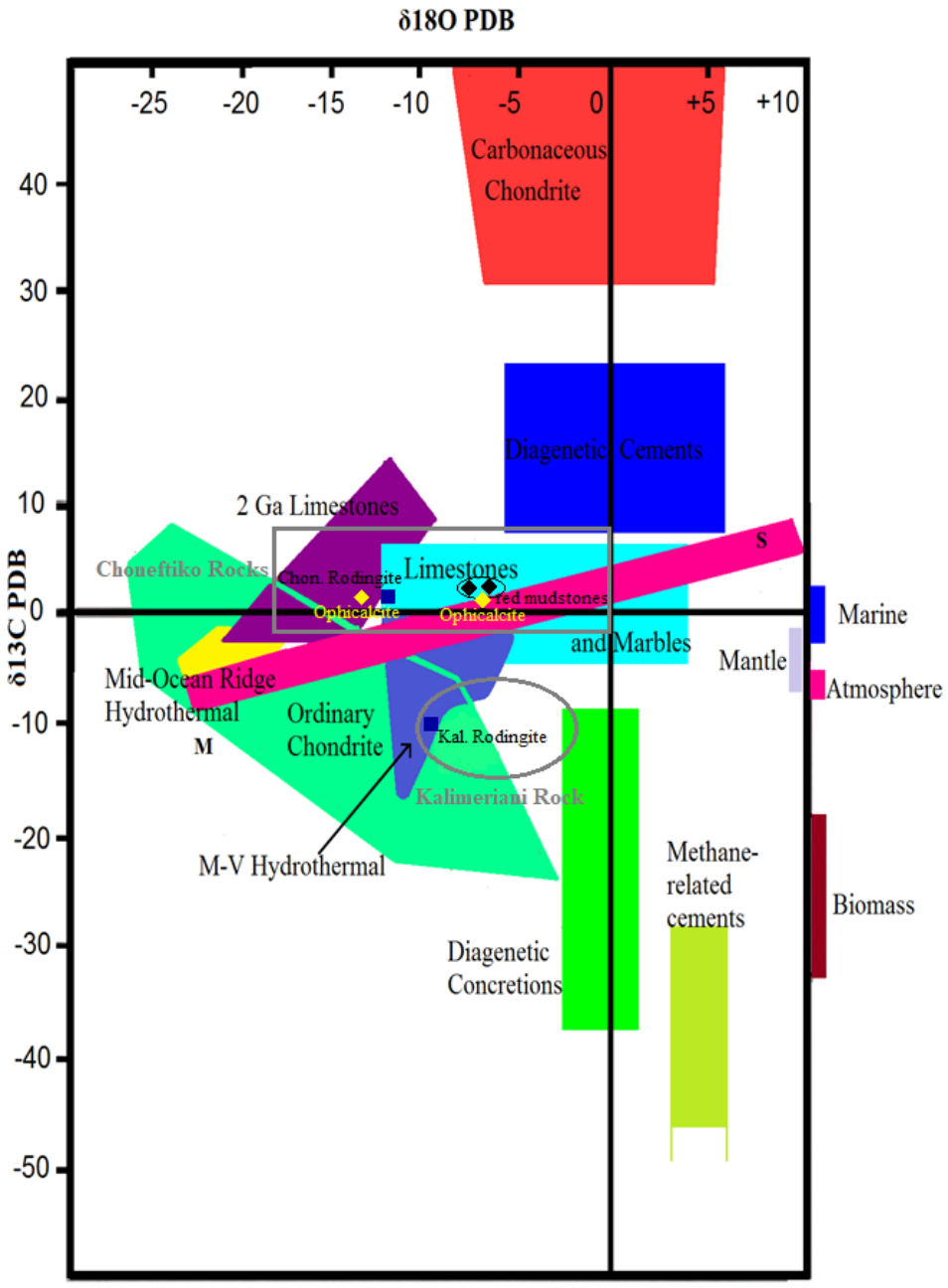

Figure 110. Modified δ^{18} O vs δ^{13}C plot showing the composition of carbonates from a variety of environments. (Rollinson, 1993 and references therein)

Taking into consideration all the isotope geochemical data we conclude that:

- Choneftiko rocks present a small range in δ13C values, while their δ18O contents is indicative of a marine isotopic source.

- Red mudstone calcite veins propably derive from marine environments as it is indicated by their Z values (Z: 127.83 and 128.35), which is further supported by the C-O isotope plots, according to Hudson (1977) and Rollinson (1993) diagrams.

- Ophicalcites probably present a mixed origin consisting of hydrothermal derived carbon (a mixing of mantle derived carbon and marine seawater carbon), as it is suggested by Z values.

- Calcite from Kalimeriani rodingite displays isotope signatures which indicate a formation from hydrothermal fluids with a possible contribution of mantle C, formed by methane oxidation during serpentinization.

- On the other hand, calcite from Choneftiko rodingite possibly exhibit a hydrothermal origin from subduction related fluids and seawater participation as well.

Hydrothermal calcite in Choneftiko derives from hydrothermal subduction related fluids with seawater participation, while in Kalimeriani area calcite presents mantle derived isotopic affinities. These fluids circulate through lithospheric mantle, causing the rodingitization of mafic protoliths in more than one stages and crystallized calcite within cavities, which cross both the rodingitic rock and the ultramafic rims. This process probably takes place at the same time with ophicalcite formation under brittle conditions during the exhumation stage.

9.3.4 Physicochemical Conditions

9.3.4.1.1 Serpentinization Chemical Reactions

Serpentinization processes in oceanic peridotites have an upper stability field of almost 450 ^{o}C, where the fluids are rich in H_2O (Früh-Green et al., 2004).

Serpentinization processes were triggered by orthopyroxene breakdown of mantle harzburgites as it confirmed by the presence of serpentinized harzburgitic protoliths. The chemical reaction of serpentinization for olivine and pyroxene respectively are the following (Klein, 2009):

$2Mg_2SiO_4 + 3H_2O \rightarrow 3Si_2O_5(OH)_4 + Mg(OH)_2$ (1)

(Forsterite) (Chrysotile) (Brucite)

$3MgSiO_3 + 2H_2O \rightarrow 3Si_2O_5(OH)_4 + SiO_2(aq)$ (2)

(Enstatite) (Chrysotile)

Magnetite is the result of reducing conditions (e.g. Mc Collom and Bach, 2009), in which many changes occur, such as the oxidation of Fe^{2+} in olivine and pyroxene to Fe^{3+}. The last process releases H^{+} as described from the reactions below, resulting to an increase of pH values:

$3Fe_2SiO_4 + 2H_2O \rightarrow Fe_3O_4 + 3SiO_2(aq) + 2H_2(aq)$ (3)

(Fayalite) (Magnetite)

and

$3FeSiO_3 + H_2O \rightarrow Fe_3O_4 + 3SiO_2(aq) + H_2(aq)$ (4)

(Ferrrosilite) (Magnetite)

These reducing serpentinization conditions occur at temperatures between 425 and 375 ^{o}C in more pervasive serpentinisation commences, while the brucite formation

correspond to temperatures near 350 ^{o}C and highly reducing conditions (Früh-Green et al., 2004).

Clinopyroxene breakdown also occurs, resulting to the formation of cpx-bastites and releasing Ca with diffusive mass transfer of $CaOH^{+}$ species (e.g. Coleman, 1977; O'Hanley, 1996; Bach and Klein, 2009). According to Thayer (1966), pyroxene (especially Ca pyroxene) are the last of the ultramafic phases to serpentinized.

Magnesite results from the CO_2-metasomatic processes that are associated with serpentinisation. At 200 ^{o}C and 100 MPa a serpentine-brucite protoliths, with progressive CO_2 metasomatism will create magnesite talc and quartz, whereas in partly serpentinsed rocks the relict olivine and pyroxenes will be replaces by magnesite and serpentine or magnesite and talc (Klein and Garrido, 2011).

Garnet formation in serpentinites is not very usual and it is related with metasomatic fluids that interact with the ultramafic rock, possibly deriving from rodingitization. Possibly a metasomatic-rodingitization fluid percolated through the serpentinitic rocks and relict orthopyroxene were affected by reactions, which formed the pseudomorphic garnet crystals. In such conditions the growing garnet will be depleted in HREE and LREE (O' Reilly and Griffin, 2013). The garnet presence i these rocks is also confirmed by the relatively high CaO contents in SERP 6-7 and SERP 22 garnet-bearing serpentinites.

The creation of chlorite rich zones in the ultramafic side could possibly be described by the following chemical reaction which is described by Menzies (1974):

$$2\ Lz + Al_2Mg_{-1}Si_{-1} \rightarrow Chl \quad (5)$$

Chemical reaction 5 shows the formation of chlorite from lizarditic part consumption of serpentine reacting with $Al_2Mg_{-1}Si_{-1}$ which mainly derives from chlorite breakdown and the aluminum molecule of serpentine, rather than diopside.

9.3.4.1.2 Rodingitization Chemical Reactions

Based on physicochemical data from the rodingite literature and our mineralogical, petrographical and chemical data we try to conclude about the physicochemical conditions under which rodingitization occurred. Kimi rodingites have been divided into two Groups according to the presence of carbonated minerals or not and more specifically calcite. Based on this discrimination and taking into consideration that calcite crosscut the chloritic rims to the rodingite cores in form of veins and cavities we assume that in Kimi rodingites two main metasomatic events occurred. The first event corresponds to the beginning of rodingitization and consists of metasomatic fluids which are CO_2 poor, while the second event concerns the entrance of CO_2 rich fluids which lead to calcite formation.

Furthermore Kimi rodingites exhibit a distinct zoning from the marginal to the core area within the dyke. This possibly indicates that metasomatic fluids gradually moved from MZ to CZ with a continuously increased water/rock ratio. We will try to describe the main chemical reactions and the physicochemical conditions in each metasomatic stage of the two main events as the fluids move from rodingite MZ to CZ.

The first metasomatic events include three main rodingitization stages which coincide with the formation of the three distinct zones from the rodingite margin to the rodingite core. Rodingitization takes place at T between 250 ^{o}C and 450 ^{o}C (Schandl and Mittwede, 2001). Taking it for granted the first metasomatic event occurred at T of 400-450^{o}C and low CO_2 conditions (XCO_2<0.02) (Likhoidov and Plyusnina, 1992; Plyusnina et al.,1993; Koutsovitis et al., 2013; Murzin et al., 2018). The Marginal Zone is characterized by the presence of chlorite and diopside crystals. Their formation can be explained by chemical reaction 1 as it is proposed by Li et al. (2008), where Cm symbolizes Ca, Si and Na mobile elements.

$$Pl + Cpx + H_2O \rightarrow (Hgrs–Hadr) + Chl + Di \pm Cm \quad (1)$$

As the metasomatic fluids move from the MZ to the CZ the temperature decreases and metasomatic fluids are gradually enriched in water. In this second rodingitization stage occurs at T of ca 300-350^{o}C and lower CO_2 conditions at P: 2-4 Kbar (Murzin et al., 2018). The main chemical reactions in this metasomatic stage are the following proposed by Coleman (1967):

$$CaAl_2Si_2O_8 + 2Ca^{2+} + 3H_2O + 0.5SiO_2 \leftrightarrow Ca_3Al_2Si_{2.5}O_{10}(OH)_2 + 4H^{+} \quad (2)$$

(Anorthite) (hydrogrossular)

while the presence of a different chlorite type in the TZ of Group-I and Group-II rodingites, as well as its presence at the expense of relict magmatic diopside crystals could also indicate another chemical reaction which produces chlorite from diopside and garnet and it is proposed by Buse et al. (2010) for low temperatures:

$$Hgrs + Di + H_2O \pm Cm \rightarrow Hadr + Chl \quad (3)$$

This reaction could also justify the presence of hydroandradite crystals within chlorite rich groundmass in samples of EROD22M Group-II rodingites.

The third rodingitization stage coincides with fluid movements towards the core zone and vesuvianite formation. Vesuvianite was most likely formed under very low CO_2 conditions with water rich fluids (high w/r ratio), at ca 300 ^{o}C (Li et al., 2004; Hatzipanagiotou et al., 2003; Li et al., 2008; Koutsovitis et al., 2013) in the max Ca^{+2} influx (Li et al., 2007). The main mineral reactions which produce vesuvianite could be the following according to Li et al. (2004, 2008) and taking into consideration that vesuvianite mainly occurs along with garnet and chlorite.

$$Hgrs + Chl + H_2O \rightarrow Ves + \text{mobile elements} \quad (4)$$

$$Hgrs + Chl + Ca^{2+} \rightarrow Ves + H_2O \quad (5)$$

The second metasomatic event occurred at lower T of about 250^{o}C (Schandl and Mittwede, 2001) and CO_2 rich conditions (XCO_2>0.1) (Murzin et al.,2018). This is further confirmed by the presence of calcite veins and cavities which crosscut the rodingite groundmass indicating their formation after the rodingite zones. Calcite is present when large quantities of aqueous fluid exist and the physicochemical conditions are the appropriate so that Ca^{2+} can react with HCO_3^{-} to form calcite both

in peridotites and rodingite. This is also consistent with the presence of rich in REE-rich samples, where HCO_3^- behaves as ligands. The formation of calcite from diopside reaction could also be possible since it could also explain the calcite and chlorite syncrystallization within veins. Both dolomite and chlorite demand MgO enrichment in the system. This could derive from calcite formation from diopside according to the following mineral reaction:

$$Di + CO_2 \rightarrow Cal + MgO_{(aq)} + 2SiO_{2(aq)} \quad (6)$$

In such conditions when the removal of Mg^{2+} occurs dolomite can be formed.

The presence of apatite in the mineral assemblage suggests that PO_4^{-3} ions were involved in the fluids, which is evident for the entrance of seawater in the metasomatic system (Tsikouras et al., 2009).

9.3.4.1.3 T-CO_2 paths

Based on the winTWQ 2.3 software (Berman, 2007), we investigated the equilibria among the minerals of MZs and CZs suggesting their main T–X_{CO2} paths (Fig. 111). Rodingitization was mainly evolved into two main metasomatic stages. However several chemical reactions have occurred. We try to present the main mineral reactions which correspond to the basic mineral assemblages in every zone during the chemical transformation of the gabbroic protolith. However, metasomatic processes are very complicated and it is possible several reactions to have interacted with each other. Chemical reaction 7 mainly corresponds to the MZs, while chemical reaction 8 mainly corresponds to the CZs. However both reactions can also explain TZ mineralogy consisting of relict diopside, chlorite and vesuvianite as well.

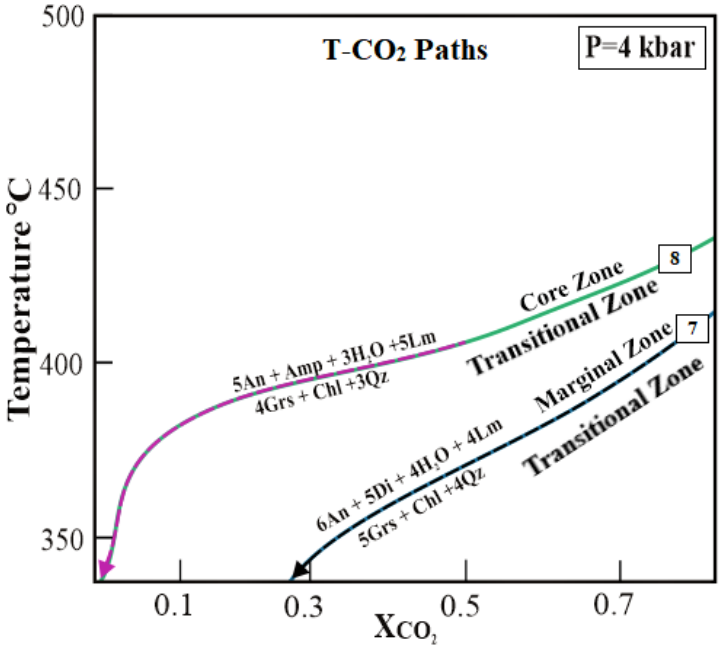

Figure 111. T–XCO_2 diagram for CZ and MZ areas.: An: anorthite, Qz: quartz, Amp: amphibole, Grs: grossular, Di: diopside, Chl: chlorite, Lm: lime.

Taking into consideration the main mineral assemblages within the three different zones, we can conclude that MZ was diopside richer compared to CZ, while CZ was amphibole rich. Amphibole rich gabbroic areas can be correlated with vesuvianite formation since CZ paths correspond to lower CO_2 contents compared to those of MZ. These paths are ideal for vesuvianite formation which is formed at ca 300 ^oC (Li et al., 2004; Hatzipanagiotou et al., 2003; Li et al., 2008; Koutsovitis et al., 2013). It can also explain vesuvianite concentration towards the CZs.

In MZs diopside is mainly reacting with anorthite in hydrous and Ca rich fluids forming grossular chlorite and quartz according to the following reaction:

$$6An + 5Di + 4H_2O + 4Lm \rightarrow 5\ Grs + Chl + 4Qz \quad (7)$$

Quartz is totally disolved and this can possibly explain the absence of high amounts of quartz crystals. However MZs are chlorite-diopside rich, while grossular is only present in minor amounts. This could possibly suggest grossular substitution by chlorite during derodingitization processes. These processes are more intene close to the chlorititic rims, while moving towards the cores via the TZs the phenomenon is reduced. This scenario is further supported by the presence of many chlorite generations.

Relict diopside is abundant in the MZs and TZs coexisting with chlorite garnet and vesuvianite. Moving towards the CZs diopside is totally reduced, while amphibole has almost totally dissolved producing chlorite and grossular according to the following reaction.

$$5An + Amph + 3H_2O + 5Lm \rightarrow 4\ Grs + Chl + 3Qz \quad (8)$$

As CO_2 is reduced vesuvianite is formed at ca 300^oC following reaction 4 and reaction 5 which also explains the absence of chlorite rich CZs. Furthermore the metasomatic fluid moving towards the CZs becomes CO_2 poorer, further confirming the scenario of a gradual fluid infiltration with CO_2 depletion moving from MZs to CZs.

10 Conclusions

In Kimi Evia the Upper Cretaceous-Paleocene flysch includes shales, sandstones, chert formations, Upper Cretaceous limestone intercalations, ophicalcites and peridotitic olistostromes. It shares many common features with Bornova flysch, possibly indicating that these ophiolitic fragments correspond to Neotethyan oceanic basins within the Vardar strand which remained active during the Upper Cretaceous. Furthermore, the geochemical similarities between Kimi rodingites and the ophiolitic parts from Skyros, possibly suggest the existence of an elongated ophiolitic zone which could be the north extension of the hanging wall of the North Cycladic Detachment System.

In Kimi rodingites occur as dykes within the serpentinized peridotites presenting either a NNE-SSW or an almost horizontal E-W direction. Their formation is strongly related with serpentinization processes and they have been divided into two Groups, according to the presence of calcite or not. Furthermore they present a distinct zoning characterized by the predominance of significant mineral assemblages. Core Zone areas (CZs) mainly include garnet-vesuvianite, while marginal zones (MZs) consist of diopside and chlorite, while Transitional Zones (TZs), and include all the aforementioned minerals in various proportions. On the other hand, ultramafic rocks include typical serpentinitic serpentinized peridotites, garnet metasomatized serpentinites and chloritites, where the last correspond to the rims of the rodingitic dykes.

Serpentinization has been possibly evolved into several stages. It has occurred in a subduction related environment, where fluids of the subducted slab triggered partial melting of mantle wedge above the subducted slab. These melts circulated and penetrated the mantle wedge in the form of mafic gabbroic and doleritite dykes. Afterwards serpentinization fluids reacted with mafic protoliths causing an extensive rodingitization. Stable O-C isotope data from calcite veins of rodingite and ophicalcite rocks clearly indicate that the metasomatic fluids exhibit a mixed sedimentary and hydrothermal origin characterized by the presence of mantle derived C.

Rodingitization begins at T: 450^{o}C and has been evolved at two main events. The first metasomatic event is CO_2 poor and has evolved in three main stages which correspond to marginal-core zoning of the rodingite dyke. These stages have evolved under generally alkaline conditions of high pH values as it is further confirmed by Zr and Cr mobility. During the initial rodingitization stages chlorite diopside and hydrogarnet were formed, while vesuvianite was formed at later stages under very low CO_2 water rich conditions with large Ca influx. In a second metasomatic event CO_2 rich fluids penetrated the rodingite dykes through cracks and calcite was crystallized within cavities and veins surrounding vesuvianite and grossular crystals. Apatite was most probably formed during the late metasomatic stages with seawater participation.

Serpentinization was continued and possibly was affected by seawater hydrothermal fluids, derived from a middle ocean ridge. These metasomatic fluids (from the subducted slab sediments and seawater hydrothermal fluids) reacted with mantle wedge ultramafic rocks and mafic dykes several times, causing the serpentinisation and rodingitization in a SSZ environment. An initial serpentinisation process could also occur in the lithospheric mantle of the subducted slab releasing metasomatic C-mantle isotopic rich fluids. This initial process could also cause the spinel olivine breakdown and Ni release from the ultramafic rocks under low pH and CO_2 rich

environments. However the final metasomatic fluids were CO_2 rich as it is indicated by the presence of calcite miarolitic cavities, where calcite surrounds garnet and vesuvianite crystals.

ISOCON diagrams present a high total mass gain in rodingite marginal zones, while afterwards moving to core zones high total mass losses occur. This is a characteristic which differs from other rodingite occurrences in Central Greece.

Semi-logarithmic and ISOCON diagrams clearly exhibit LREE enrichment for Kimi rodingites. LREEs are mainly concentrated into the marginal zone rodingites. LREE transfer was accomplished by CO_3^{-2}, OH^- and PO_4^{-3} ligands, resulting to REE deposition in apatite and allanite as well. REE entrance in allanite is described by the following substitution: $REE^{+3} + Fe^{+2} \rightarrow Ca^{+2} + Fe^{+3}$, while in apatite the REE+3 entrance is balanced by the following substitution: $REE^{+3} + Si^{4+} \rightarrow Ca^{2+} + P^{+5}$. The presence of CO_3^{-2}, OH^- and PO_4^{-3} complexes is supported by the presence of calcite, REE-apatite and Zr mobility respectively.

During the exhumation at T between 200-150^oC near the ocean continent transitional zone, fluids were enriched in hydrothermal seawater and mantle derived C as it is indicated by calcite formation, isotopic data and apatite formation as well, possibly deriving from normal faults or a rifted ocean. At this time CO_2/H_2O ratios were increased. The second metasomatic event coincides with ophicalcite formation under brittle deformation conditions where carbonic rich water fluids circulate through cracks, depositing calcite with sedimentary and mantle isotopic signatures.

11 References

Abu-Jaber, N.S., Kimberley, M.M., 1992. Origin of ultramafic-hosted vein magnesite deposits. *Ore Geology Reviews,*7,(3), 155-191.

Agrawal, S., Guevara, M., Verma, S., 2008. Tectonic discrimination of basic and ultrabasic volcanic rocks through log-transformed ratios of immobile trace elements. *Inernationa. Geoogy. Review*, 50, 1057-1079.

Aiuppa, A., Allard, P., D'Alessandro, W., Michel, A., Parello, F., Treuil, M., Valenza, M., 2000. Mobility and fluxes of major, minor and trace metals during basalt weathering and groundwater transport at Mt. Etna volcano (Sicily).*Geochimica et CosmochimicaActa,* 64, 1827–1841.

Aja, S.U.,Wood, S.A., Williams-Jones, A.E., 1995. The aqueous geochemistry and the solubility of some Zr-bearing minerals. *Applied Geochemistry*, 10, 603–620.

Aldanmaz, E., Yalınız, M.K., Güçtekin, A., Göncüoğlu, M.C., 2008. Geochemical characteristics of mafic lavas from the Neotethyan ophiolites in western Turkey: implications for heterogeneous source contribution during variable stages of ocean crust generation. *Geological Magazine*, 145, 37–54.

Allen, D.E., Seyfried Jr.,E., 2005. REE controls in ultramafic-hosted MOR hydrothermal systems: an experimental study at elevated temperature and pressure. *Geochimica et Cosmochimica Acta*, 69, 675–683.

Alt, J.C., Shanks, W.C., 2003. Serpentinization of abyssal peridotites from the MARK area, mid-Atlantic Ridge, sulfur geochemistry and reaction modeling. *Geochimica et Cosmochimica Acta*, 67, 641–653.

Anastopoulos, I., 1962. Geological Map of Greece. Kymi Sheet. *Institute of Geology and Mineral Exploration, Greece* (IGME).

Anders, B., 2005. "The Pre-Alpine Evolution of the Basement of the Pelagonian Zone and the Vardar Zone, Greece." PhD Thesis, Johannes Gutenberg-Universität, Mainz, pp. 1-153.

Andreani, M., Mével, C., Boullier, A.-M., Escartin, J., 2007. Dynamic control on serpentine crystallization in veins: constraints on hydration processes in oceanic peridotites. Geochemistry, *Geophysics, Geosystems*, 8, (2). DOI: 10.1029/2006GC001373

Andreani, M., Luquot, L., Gouze, P., Godard, M., Hoise, E., Gibert B., 2009. Experimental study of carbon sequestration reactions controlled by the percolation of CO_2-rich brine through peridotites. *Enviromenta. Science. Technoogy*., 43, (4), 1226–1231.

Arai, J., 1992. Chemistry of chromian spinel in volcanic rocks as a potential guide to magama chemistry. *Mineralogical Magazine*, 56, 173-184.

Armbruster, T., Gnos, E., Dixon, R., Gutzmer, J., Hejny, C., Döbelin, N., Medenbach, O., 2002. Manganvesuvianite and tweddillite, two new Mn3+ minerals from the Kalahari manganese fields, South Africa. *Mineralogical Magazine*, 66, 137-150.

Ashley, P.M., 1973. Petrogenesis of sulfide – bearing reaction zones in the Coolac ultramafic belt. New South Wales, Australia. *Mineralium Deposita*, 8, 370 -378.

Aubouin, J., 1959. Contribution a l' etude geologique de la Grece septentrionale: les confins de l' Epire et de la Thessalie. *Annales Géologiques des Pays Hélléniques*, 10, 1-483.

Aubouin, J., Bonneau, M.,, Celet, P., 1970. Contribution a la geologie des Hellenides: le Gavrovo, le Pinde et la Zone Ophiolitique Subpelagonian. *Annales de la Societe Geologique du Nord*, 90, 277-306.

Avigad, D., Garfunkel, Z., 1989. low-angle faults above and below a blueschist belt-Tinos Island, Cyclades, Greece. *Terra Nova*, 1, 182-187.

Avigad, D., Garfunkel, Z., Jolivet, L., Azanon, J. M., 1997. Back-arc extension and denudation of Mediterranean eclogites. *Tectonics*, 16, 924–41.

Ayers, J.C., Watson, E.B., 1991. Solubility of apatite, monazite, zircon, and rutile in supercritical aqueous fluids with implications for subduction zone geochemistry. *Philosophical Transactions of the Royal Society A*, 335, 365–375.

Bach, W., Bach, Jons, N., Klein, F., 2013. Metasomatism Within the Ocean Crust. From book Metasomatism and the Chemical Transformation of Rock. pp. 253-288.

Bach, W., Klein, F., 2009. The petrology of seafloor rodingites: insights from geochemical reaction path modelling. *Lithos*, 112, 103–117.

Bach, W., Rosner, M., Jöns, N., Rausch, S., Robinson, L.F., Paulick, H., Erzinger, J., 2011. Carbonate veins trace seawater circulation during exhumation and uplift of mantle rock: results from ODP Leg 209. *Earth and Planetary Science Letters*, 311, 242–252.

Banno, S., Sakai, C., Higashino, T., 1986. Pressure-temperature trajectory of the Snbagawa metamorphism deduced from garnet zoning. *Lithos*, 19, 51-63.

Barnes I, Lamarche V.C., Himmelberg G., 1967. Geochemical evidence of present-day serpentinization. *Science*, 156,830–832.

Barnes, I., O'Neill, J.R., 1969. The relationship between fluids in some fresh alpine-type ultramafics and possible modern serpentinisation, western United States. *Geological Society of America Bulletin*, 80, 1947-1960.

Barnes, I., Rap, J.B., O'Nerr., J.R., 1972. Metamorphic assemblages and the direction of flow of metamorphic fluids in four instances of serpentinization. *Contributions to Mineralogy and Petrology* , 35, 263-276.

Barth, M.G., Mason, P.R.D., Davies, G.R., Dijkstra, A.H., Drury, M.R., 2003. Geochemistry of the Othris ophiolite, Greece: evidence for refertilization? *Journal of Petrology*, 44,1759–1785.

Bau, M., 1991. Rare-earth element mobility during hydrothermal and metamorphic fluid-rock interaction and the significance of the oxidation state of europium. *Chemical Geology*, 93, 219–230.

Baziotis, I.P., 2008. Petrology and geochemistry of metamorphic rocks from Attica. Phd Thesis, National Technical University of Athens. 410p.

Berman, R.G., 2007. winTWQ (version 2.3): A Software Package for Performing Internally-consistent Thermobarometric Calculations. Geological Survey of Canada (Open File 5462, ed. 2.32).

Bernoulli, D., Laubscher H.,1972. The Palinspastic Problem of the Hellenides. *Eclogae Geologicae Helvetiae*, 65, (1), 107-118.

Bernoulli, D., Manatschal, G., Desmurs, L., Müntener, O., Dilek, Y., Newcomb, S., 2003. Where did Gustav Steinmann see the trinity? Back to the roots of an Alpine ophiolite concept, Ophiolite Concept and the Evolution of Geological Thought. *Geological Society of America, Special Papers*, 373, 93-110.

Bernoulli, D., Jenkyns, H. C., 2009. Ophiolites in ocean-continent transitions: From the Steinmann Trinity to sea-floor spreading. *Comptes Rendus Geoscience*, 341, (5), 363-381.

Bizimis, M., Salters, V.J.M., Bonatti, E., 2000. Trace and REE content of clinopyroxenes from supra-subduction zone peridotites. Implications for melting and enrichment processes in island arcs. *Chemical Geology*, 165 (1-2), 67-85.

Bradley, D., 2005, The kinematic history of the Coaldale Fault, Walker Lane Belt, Nevada *M.Sc. Thesis*, Lawrence, University of Kansas, 96 p.

Bröcker, M., 1990. Blueschist-to-Greenschist transition in metabasties from Tinos Island, Cyclades. Greece: Compositional control or fluid infiltration? *Lithos*, 25, 25-39.

Bröcker, M., Kreuzer, H., Matthews, A., Okrusch, M.(1993) : 40Ar/39Ar and oxygen isotope studies of polymetamor- phism from Tinos Island. Cycladic blueschist belt. - *Journal of Metamorphic Geology*, 11, 223-240.

Brownlow, H., A., 1995. *Geochemistry* (2nd Edition).

Buse, B., Schumacher, J., Sparks, R., Field, M., 2010. Growth of bultfonteinite and hydrogarnet in metasomatized basalt xenoliths in the B/K9 kimberlite, Damtshaa,Botswana: insights into hydrothermal metamorphism in kimberlite pipes. *Contributions to Mineralogy and Petrology*, 160, 533–550.

Capedri, S., Rossi, A. 1973. Conditions governing the formation of ophicalcites and listwanites (Central Evia, Greece). *Bulletin of the Geological Society of Greece*, 10, (2), 278-297.

Caruso, L., Simmons, G.,1985. Uranium and microcracks in a 1000-meter core, Redstone, New Hampshire. *Contributions to Mineralogy and Petrology*, 90, 1–17.

Chenevart, C., Katsikastos, G., 1967. Carte géologique de l'Eubée. *Institut de Géologie d'Athènes*.

Christidis, G.E., Economou-Eliopoulos, M., Marcopoulos, T., Laskou, M., 1998. An unusual assemblage of high-Ti oxides and ferroan clinochlore along zones of brittle deformation in the Vourinos (Rodiani) ophiolite complex, Greece. *The Canadian Mineralogist*, 36, (5), 1327-1338.

Clerc, C., Boulvais, P., Lagabrielle, Y., de Saint Blanquat, M., 2014. Ophicalcites from the Northern Pyrenean Belt: A field, petrographic and stable isotope study, *International Journal of Earth Sciences*, 103, 141–163.

Coleman, R.G., 1967. Low-temperature reaction zones and alpine ultramafic rocks of California, Oregon and Washington. U.S. *Geological Survey Bulletin*, 1247, 1–49.

Coleman, R. G., Keith, T. E., 1971, A chemical study of serpentinization; Burro Mountain, California: *Journal of Petrology*, 12, (2), 311–328.

Coleman, R.G., 1977. Ophiolites. Ancient Oceanic Lithosphere? *Springer*, Berlin-Heidelberg-New York 1–229.

Comodi, P., Liu, Y., Stoppa, F., Woolley A.R., 1999. A multi-method analysis of Si-, S- and REE-rich apatite from a new find of kalsilite-bearing leucitite (Abruzzi, Italy) *Mineralogical Magazine*, 63(5), 661-672.

Contreras-Reyes, E., Grevemeyer, I., Flueh, E.R., Scherwath, M., Heeseman, M., 2007. Alteration of the subducting oceanic lithosphere at the southern central Chile trench/outer rise. *Geochemistry, Geophysics, Geosystems*, 8, (7) http://dx.doi.org/10.1029/2007GC001632.

De Bono, A., 1998. Pelagonian margins in central Evia island (Greece). Stratigraphy and geodynamic evolution. PhD Thesis. Univ. Lausanne: http://www sst.unil.ch/publications/pdf/phd_debono.pdf

De Felipe, I.,Pedreira, D., Pulgar, J.A., Iriarte, E., M. Mendia, M., 2012. Petrography and C and O stable isotope composition of ophicalcites in the Western Pyrenees/Eastern Cantabrian Mountains: geodynamic implications. *EGU General Assembly 2012*, Vol. 14, EGU2012-12448.

Dercourt, J., Ricou, L. E., Vrielynck, B., 1993, Atlas Tethys palaeoenvironmental maps: *Paris, Gauthier-Villars*, p. 307

Deschamps, F., Godard, M., Guillot, S., Hattori, K., 2013. Geochemistry of subduction zone serpentinites: A review. *Lithos*, 178, 96–127.

Dick, H. J. B., Bullen, T., 1984. Chromian spinel as a petrogenetic indicator in abyssal and alpine-type peridotites and spatially associated lavas. *Contributions to Mineralogy and Petrology*, 86, 54-76.

Dollase, W.M., 1971. Refinement of the crystal structures of epidote, allanite and hancockite. *American Mineralogist*, 56, 447-464.

Douville, E., Charlou, J.L., Oelkers, E.H., Bienvenu, P., Jove Colon, C.F., Donval, J.P., Fouquet, Y., Prieur, D., Appriou, P., 2002. The rainbow vent fluids (36°14′N, MAR): the influence of ultramafic rocks and phase separation on trace metal content in Mid-Atlantic Ridge hydrothermal fluids, *Chemical Geology*, 184, 37 -48.

Dürr, S., Altherr, R., Keller, J., Okrusch, M., Seidel, E. 1978. The Median Aegean Crystalline Belt: Stratigraphy, structure, metamorphism, magmatism. In Alps, Apennines, Hellenides (eds H. Closs, D. H. Roeder and K. Schmidt), pp. 455–77. *IUGS report* no.38. Stuttgart: Schweizerbart.

Economou-Eliopoulos, M., Eliopoulos, D.G., 1999. Significance of a Spatial Association of High-Cr and High-Al Chromites for Their Genesis and Exploration, Extrait du Bulletin T. CXIX de l' Académie Serbe des Sciences et des Arts, *Classe des Sciences mathématiques et naturelles, Science naturelles*, 39, 123-140.

Elliot, J.S., 2002. Calcium phosphate biominerals. In M.J. Kohn, J. Rakovan and J.M. Hughes, Eds., Phosphates. *Reviews in Mineralogy and Geochemistry*, 48, Mineralogical Society of America, Washington, D.C. , 427–453pp.

Engin, T., Hirst, D.M., 1970. Serpentinization of harzburgites from the alpine peridotite belt of Southwest Turkey. *Chemical Geoogy*, 6, pp. 281-295.

Ernst, W.G., Liu, J., 1998. Experimental phase-equilibrium study of Al- and Ti-contents of calcic amphibole in MORB—A semiquantitative thermobarometer. *American Mineralogist*, 83, 952–969, 1998.

Escartin, J., Hirth, G., Evans, B., 1997. Effects of serpentinization on the lithospheric strength and the style of normal faulting at slow-spreading ridges. *Earth and Planetary Science Letters*, 151, 181–189.

Evans, B.W., Johannes, W., Oterdoom, H., Trommsdorf, V., 1976. Stability of chrysotile and antigorite in the serpentine multisystem. *Schweizerische Mineralogische und Petrographische Mitteilungen* 56, 79–93.

Exley, R.A., 1980. Microprobe studies of REE-rich accessory minerals: implications for Skye granite petrogenesis and REE mobility in hydrothermal systems. *Earth and Planetary Science Lett*ers,48, 97-110.

Exley, R.A., Mattey, D.P., Clague, D.A., Pillinger, C.T., 1986. Carbon isotope systematics of a mantle 'hot-spot': a comparison of Loihi seamount and MORB glasses. *Earth and Planetary Science Lett*ers, 78, 189-199.

Faupl P., Pavlopoulos A., Wagreich M., Migiros G. 1996. Pre-Tertiary blueschist terrains in the Hellenides: evidence from detrital mineral of flysch successions. *Terra Nova* 9, 186-190.

Ferrando, S., Frezzotti, M.L., Orione, P., Conte, R.C., Compagnoni, R., 2010. Late-Alpine rodingitization in the Bellecombe meta-ophiolites (Aosta Valley, Italian Western Alps): evidence from mineral assemblages and serpentinization-derived H_2-bearing brine. *International Geology Review*, 52, 1220–1243.

Ferrière J., Chanier F., Ditbanjong P., 2012. The Hellenic ophiolites: eastward or westward obduction of the Maliac Ocean, a discussion. *International Journal of Earth Sci*ences (Geol. Rundsch.), 101, (6), 1559-1580.

Festa, A., Pinib, G.A., Dilekc, Y., Codegonea, G., 2009. Mélanges and mélange-forming processes: a historical overview and new concepts. *International Geology Review*, 52, 10–12, p1040–1105.

Fitzgerald, S.,LEavENs, P.B., RuuNcor-o, A.L., NerrN, J.A.,1987. Crystal structure of a REE-bearing vesuvianite from San Benito County, California. *American Mineral*ogist, 12, 625-628.

Fitzgerald, S., Leavens, P.B., Nelen, J.A., 1992. Chemical variation in vesuvianite. *Mineralogy and Petrology*, 46, 163–178.

Fleury, J.J., 1980. Les zones de Gavrovo - Tripolitza et du Pinde - Olonos (Grece continentale et Peloponese du Nord): evolution d' une plate-forme et d' un bassin dans leur carde alpin. *Annales de la Société géologique du Nord*, 1, 651p., Lille.

Frondel, J.W., 1964. Variation of some rare earths in allanite. *Amer. Mineral*., 49, 1159-77.

Frost, B.R., Beard, J.S., 2007. On silica activity and serpentinization. *Journal of Petrology*, 48, 1351–1368.

Frost, B.R., Beard, J.S., McCaig, A., Condliffe, E., 2008. The formation of micro-rodingites from IODP hole U1309D: key to understanding the process of serpentinization. *Journal of Petrology*, 49, 1579–1588.

Früh-Green, G.L., Kelley D. S., Bernasconi S. M., Karson J. A., Ludwig K. A., Butterfield D. A., Boschi C., Proskurowski G., 2003. 30,000 years of hydrothermal activity at the Lost City Vent Field. *Science*, 301, 495–498.

Früh-Green, G.L., Connolly, J.A.D., Plas, A., Kelley, D.S., Grobéty, B., 2004. In: Serpentinization of o ceanic peridotites: Implications for geochemical cycles and biological activity. *American Geoph ysical Union*, Washington D.C., 144, 9-6.

Godfriaux, J., 1968. Etude géologique de la région de l' Olympe (Grèce). *Annales Géologiques de Pays Hellénique*, 19, 1-271.

Gartzos, 2004. Comparative stable isotope study of the magnesite deposits of Greece. *Bulletin of the Geological Society of Greece* vol. XXXVI, 2004.

Gartzos, E., Dietrich, V.J., Migiros, G., Serelis, K., Lymperopoulou, Th., 2009. The origin of amphibolite from metamorphic soles beneath the ultramafic ophiolites in Evia and Lesvos (Greece) and their geotectonic implication. *Lithos*, 108, 224-242.

Gimeno-Serrano, M.J., Sanz, L.F.A., Nordstrom, D.K., 2000. REE speciation in lowtemperature acidic waters and the competitive effects of aluminium. *Chemical Geology*, 165, 167–180.

Graessner, T., Schenk, V., 1999. Low-pressure metamorphismof Palaeozoic pelites in the Aspromonte, southern CalabriaConstraints for the thermal evolution in the Calabrian cross-section during the Hercynian orogeny. *Journal of Metamorphic Geology*, 17, 157–172.

Grant, J.A., 1986. The Isocon diagram — a simple solution to Gresens' equation for metasomatic alteration. *Economic Geology*, 81, 1976–1982.

Grant, J.A., 2005. Isocon analysis: A brief review of the method and applications. *Physics and Chemistry of the Earth.* 30, 997–1004.

Groat, L.A., Hawthorne, F.C., Ercit, T.S., 1992. The chemistry of vesuvianite.*Canadian Minerologist*, 30, 19-48.

Guernet, C., Robert, P., 1973. Sur l' existence de bauxites d' age jurassique en Eube´e (Gre´ce). *Comptes Rendus de l'Académie des Sciences*, 276, 885–887.

Haas, J.R., Shock, E.L., Sassani, D.C., 1995. Rare earth elements in hydrothermal systems: estimates of standard partialmolal thermodynamic properties of aqueous complexes of the rare earth elements at high pressures and temperatures. *Geochimica et Cosmochimica Acta*, 59, 4329–4350.

Halls, C., Zhao, R., 1995. Listwaenite and related rocks: perspectives on terminology and mineralogy with reference to an occurrence at Cregganbaun, Co. Mayo, Republic of Ireland. *Mineralium Deposita*, 30, 303-313.

Hammarston, J.M., Zen, E.A., 1986. Aluminum in hornblende: An empirical igneous geobarometer. *American Mineralogist*,71,1297-1313.

Harlov, D.E., Autstrheim, H., 2013. Metasomatism and the Chemical Transformation of Rock. The Role of Fluids in Terrestrial and Extraterrestrial Processes. *Springer* Heidelberg New York Dordrecht London.

Hatzipanagiotou, K., Tsikouras, B., 2001. Rodingite formation from diorite in the Samothraki ophiolite, NE Aegean, Greece. *Geological Journal*, 36, 93–110.

Hatzipanagiotou, K., Tsikouras, B., Migiros, G., Gartzos, E., Serelis, K., 2003. Origin of rodingites in ultramafic rocks from Lesvos island (NE Aegean, Greece). *Ofioliti*, 28, 13–23.

Hilairet, N., Reynard, B., 2009. Stability and dynamics of serpentinite layer in subduction zone. *Tectonophysics*, 465, 24–29.

Hinsken, T., Bröcker, M., Strauss, H., Bulle, F., 2017. Geochemical, isotopic and geochronological characterization of listvenite from the Upper Unit on Tinos, Cyclades, Greece. *Lithos*, 282–283, 281–297.

Hudson, J.D., 1977, Stable isotopes and limestone lithification: *Journal of the Geological Society*, London, 133, (6), 637-660.

Hynes, A., 1982. A comparison of amphiboles from medium- and low-pressure metabasties. *Contributions to Mineralogy and Petrology*, 81, 119-125.

Izbicki, J.A., Ball, J.W., Bullen, T.D., Sutley, S.J., 2008. Chromium, chromium isotopes and selected trace elements, western Mojave Desert, USA. *Applied Geochemistry*, 23, 1325–1352.

Jacobshagen, V., 1986. Geologie von Griechenland. Beitraege zur regionalen Geologie der Erde. *Gebrueder Borntraeger Verlag*, Berlin, 363 pp.

Johannes, W., 1970, Zur Entstehung von Magnesitvorkommen: Neues Jahrb. *Mineralogie Abh.*, 118, 274-825.

Kamenetsky, V.S., Crawford, A.J., Meffre, S., 2001. Factors Controlling Chemistry of Magmatic Spinel: an Empirical Study of Associated Olivine, Cr-Spinel and Melt Inclusions from Primitive Rocks. *Journal of Petrology*, 42, (4), 655-671.

Karkanas, P., 1987. Studu of the chrysotile asbestos deposit of Zidani, Kozani, and the occurence of tremolitic asbestos of Ano Agoriani, Othrys, Greece., Phd Thesis. National and Kapodistrian University of Athens (in Greek), 355pp.

Karkalis, C., Magganas, A., Koutsovitis, P., 2016. Petrological, mineralogical and geochemical data from the Eohellenic ophiolitic nappe in the island of Skyros, Greece. *Bulletin of the Geological Society of Greece*,2016 *Proc. of the 14th Intern. Conference*.

Kartashov, P.M., Ferraris, G., Ivaldi, G., Sokolova, E., McCammon, C.A., 2002. Ferriallanite-(Ce), CaCeFe3+AlFe2+[SiO4][Si2O7]O(OH), a new member of the epidote group: Description, X-ray and Mössbauer study. *Canadian Mineral*ogist, 40, 1641-1648.

Katsikatsos. G. 1970: Les formations triasiques de l'Eubée centrale. *Ann. géol. Pays hellen*. 22, 62-76.

Katsikatsos, G., Fytikas, M., Koukis, G., 1970. Geological Map of Greece, Kymi Sheet. *Institute of Geology and Mineral Exploration, Greece* (IGME).

Katsikatsos, G., Migiros, G., Triantaphyllis, M., Mettos, A., 1986. Geological Structure of Internal Hellenides (E. Thessaly-SW Macedonia. Euboea-Attica-Northern Cyclades Islands and Lesvos). IGME, *Geol. and Geoph. Res*., Special Issue, 191-212.

Katsikatsos, G. 1991a. Geological map of Greece, Aliveri sheet. *Greek Institute for Geologic and Minining Research*, Athens, Greece.

Katsikatsos, G. 1991b. Geological map of Greece, Rafina sheet. *Greek Institute for Geologic and Minining Research*, Athens, Greece

Katsikatsos, G., 1992. Geology of Greece. Athens: OPEB.

Katzir, Y., Matthews, A., Garfunkel, Z., Schliestedt, M., Avigad, D., 1996. The tectonometamorphic evolution of a dismembered ophiolite (Tinos, Cyclades, Greece). *Geological Magazine*, 133, 237– 254.

Keith M.L., Weber Y.N., 1964. Carbon and oxygen isotopic composition of selected limestone and fossils. *Geochimica et Cosmochimica Acta*, 28, 1787-1816.

Kelemen, P.B., Kikawa, E., Miller, D.J., Abe, N., Bach, W., Carlson, R.L., Casey, J.F., Chambers, L.M., Cheadle, M., Cipriani, A., Dick, H.J.B., Faul, U., Garces, M., Garrido, C., Gee, J.S., Godard, M.M., Graham, D.W., Griffin, D.W., Harvey, J., Ildefonse, B., Iturrino, G.J., Josef, J., Meurer, W.P., Paulick, H., Rosner, M., Schroeder, T., Seyler, M., Takazawa, E., 2004. Site 1275. In: Proceedings of the ocean drilling program; initial reports; drilling mantle peridotite along the Mid-Atlantic Ridge from 14 degrees to 16 degrees N; covering Leg 209 of the cruises of the drilling vessel JOIDES Resolution; Rio de Janeiro, Brazil, to St George, Bermuda; sites 1268–1275, 6 May-6 July 2003, vol Texas A&M University Ocean Drilling Program College Station, pp 167.

Kelemen, P. B., Matter, J., 2008. In situ carbonation of peridotite for CO_2 storage. *Proc. of the National Academy of Sciences of the United States of America*, 105(45), 17295-17300.

Kelemen, P. B., Matter, J., Streit, E. E., Rudge, J. F., Curry, W. B., Blusztajn, J., 2011. Rates and mechanisms of mineral carbonation in peridotite: Natural processes and recipes for enhanced, in situ CO_2 capture and storage. *Annual Review of Earth and Planetary Sciences*, 39, 545-576.

Kilias, A., Frisch, W., Avgerinas, A., Dunkl, I., Falalakis, G., Gawlick, H. J., 2010. Alpine architecture and kinematics of deformation of the northern Pelagonian nappe pile in the Hellenides, *Austrian Journal of Earth Sciences*, 103, 4–28.

Klein, F., 2009. Petrology of Serpentinites and Rodingites in the Oceanic Lithosphere. *Staats-und Universitätsbibliothek Bremen*.

Klein, F., Garrido, C.J., 2011. Thermodynamic constraints on mineral carbonation of serpentinized peridotite, *Lithos*, 126, 147–160.

Koutsovitis, D., 2009. Petrological and mineralogical study of the ophiolitic rocks in the region of East Othris. Phd Thesis. National and Kapodistrian University of Athens. 547 pp.

Koutsovitis, P., Magganas, A., Pomonis, P., Ntaflos, T., 2013. Subduction-related rodingites from East Othris, Greece: Mineral reactions and physicochemical conditions of formation, *Lithos*, 172-173, 139-157.

Laborda López, C.L., Sánchez-Vizcaíno, V., Marchesi, C., Gómez Pugnaire, M.T., Garrido, C.J., 2015. Preliminary Petrographic and Geochemical Study of Metarodingites from Cerro del Almirez (Betic Cordillera, S. Spain). *Revista de la sociedad española de mineralogía*, Macla, 20, 79-80.

Lemoine, M., Tricart, P., Boillot, G., 1987. Ultramafic and gabbroic ocean floor of the Ligurian Tethys (Alps, Corsica, Apennines): In search of a genetic imodel. *Geology*, 15, (7), 622-625.

Li, X.P., Rahn, M., Bucher, K., 2004. Metamorphic Processes in Rodingites of the Zermatt-Saas Ophiolites, *International Geology Review*, 46, 28–51.

Li X.P., Zhang, L., Wei, C., Al Y., Chen, J., 2007. Petrology of rodingite derived from eclogite in western Tianshan, China. *Journal of Metamorphic Geology*, 25, 363–382.

Li, X.P., Rahn, M., Bucher, K., 2008. Eclogite facies metarodingites: phase relations in the system SiO_2–Al_2O_3–Fe_2O_3–FeO–MgO–CaO–CO_2–H_2O: an example from the Zermatt-Saas ophiolite, *Journal of metamorphic Geology*, 26, 347–364.

Likhoidov, G.G., Plyusnina, L.P., 1992. Rodingites of northern Sakhalin and their physicochemical formation conditions. *Tikhookeanskaya Geologiya*. 2, 53–65 (in Russian).

Lips, A.L.W., White, S.H.Y., Wijbrans, J.R., 1988. 40Ar/39Ar Laser prebe direct dating of discrete deformational events: a continuous record of early Alpine tectonics in the Pelagonian zone, NW Aegean area, pGreece. *Tectonophysics*, 298, 133-153.

Magganas, A., Koutsovitis, P., 2015. Composition, melting and evolution of the upper mantle beneath the Jurassic Pindos ocean inferred by ophiolitic ultramafic rocks in East Othris, Greece, *International Journal of Earth Sciences*, 104, 1185-1207.

Maluski, H., Bonneau, M., Kienast, J.R., 1987. Dating the metamorphic events in the Cycladic area: 39Ar/40Ar data from metamorphic rocks of the island of Syros (Greece). *Bulletin de la Societe Geologique de France*, 8, (3), 5, 833-842.

Marakis, G., 1972. Rodingites in Serpentine of central and South Eubea Island (Greece). *Annales Géologiques des Pays Hélléniques*, 24, 241-246.

Marakis, G., 1972. Remarks on the mineral clinochlore from rodingites of Kimi, Euboea Island, Greece. *Neues Jahrbuch für Mineralogie Monatshefte*, 8, 345-349.

McCollom, T.M., Bach W., 2009. Thermodynamic constraints on hydrogen generation during serpentinization. *Geochimica et Cosmochimica Acta*,73,856–879.

McDonough, W. F., Sun, S.S., 1995. The composition of the Earth, *Chem. Geol*., 120, 223 – 253.

Meagher, E.P., 1980. Silicate garnets, In P. H. Ribbe, Ed., *Reviews in Mineralogy*, 5 Orthosilicates, p.25-66. Mineralogical Society of America, Washington, D. C.

Melfos V., Magganas A., Voudouris P., Kati M., 2009. The Mesozoic Larissa ophicalcite-serpentinite association in Eastern Thessaly, Greece: Mineralogical, geochemical and isotopic constraints for rocks formed in an Ocean-Continent Transition setting. *Geophysical Research Abstracts, EGU General Assembly 2009*, vol. 11, EGU2009-10797-2.

Menzies, M., 1974. The petrogenesis of the Makrirakhi ultramafic complex. Thesis. University of Cambridge.

Menzies, M., Long, A., Ingram, G., Tatnell, M., Janecky, D.R., 1993. MORB peridotite–seawater interaction: experimental constraints on the behaviour of trace elements, 87Sr/86Sr and 143Nd/144Nd ratios. In: Prichard, H.M., Alabaster, T., Harris, N.B.W., Neary, C.R. (Eds.), Magmatic processes and plate tectonics. *Geological Society Special Publications*, 76, 309–322.

Mével, C., 2003. Serpentinization of abyssal peridotites at mid-ocean ridges. *Comptes Rendus Géoscience*, 335, 825–852.

Migiros, 1986. The ophiolites of East Thessaly. I.G.M.E., *Geol. & Geoph. Res.*., Special Issue, 249-268 (in Greek, included extended Abstract and fig. legends in English).

Morimoto, N., Fabries, J., Ferguson, A.K., Ginzburg, I.V., Ross, M., Seifert, F.A., Zussman, J., Aoki, K., Gottardi, J., 1988. Nomeclature of Pyroxenes. *American Mineralogist*,73, 1123-1133.

Most, T., 2003. Geodynamic evolution of the Eastern Pelagonian zone in Northwestern Greece and the Republic of Macedonia. PhD Thesis, University of Tuebingen, Tuebingen, 195 pp.

Mountrakis, D., 1986. The Pelagonian zone in Greece: A polyphase deformed fragment of the Cimmerian continent and its role in the geotectonic evolution of the Eastern Mediterranean. *Journal of Geology*, 94, 335-347

Murzin, V.V., Chudnenko, K.V., Palyanova, G.A., Varlamov, A., Naumov, E.A., Pirajon, D.A., 2018. Physicochemical model for the genesis of Cu-Ag-Au-Hg solid solutions and intermetallics in the rodingites of the Zolotaya Gora gold deposit (Urals, Russia). *Ore Geology Reviews*, 93, 81-97.

Nakamura, N., 1974. Determination of REE, Ba, Mg, Na and K in carbonaceous and ordinary chondrites. *Geochimica et Cosmochimica Acta*, 38, 757-775.

Neal, C., Stanger, G.,1985. Past and present serpentinisation of ultramafic rocks; anexample from the Semail ophiolite nappe of northern Oman. In: Drever, J.I. (Ed.), The Chemistry of Weathering. D. Reidel Publishing Company, 249–275 pp.

Nickel, E.H., Mandarino, J.A., 1987. Procedures involving the I.M.A. Commission on New Minerals and Mineral Names, and guidelines on mineral nomenclature. *American Mineralogist*, 72, 1031-1042.

Nirta G., Moratti G., Piccardi L., Montanari D., Catanzariti R., Carras N. ,Papini M., 2015. The Boeotian flysch revisited: new constraints on ophiolite obduction in central Greece. *Ofioliti*, 40, 107– 23.

Normand, C., Williams-Jones, A.E., 2007. Physicochemical conditions and timing of rodingite formation: evidence from rodingite-hosted fluid inclusions in the JM Asbestos mine, Asbestos, Québec. *Geochemical Transactions*. 8, 11.

Norrell, G. T., Teixell, A., Harper, G.D., 1989. Microstructure of serpentinite mylonites from the josephine ophiolite and serpentinization in retrogressive shear zones, California. *Geological Society of America Bulletin*. 101: 637–682.

O'Hanley, D.S., Chernosky, J.V.JR., Wicks, F.J., 1989. The stability of lizardite and chrysotile. *Canadian Mineralogist*, 27, 483-493.

O'Hanley, D.S., Schandl, E.S., Wicks, F.J., 1992. The origin of rodingites from Cassiar, British Columbia, and their use to estimate T and P(H_2O) during serpentinization. *Geochimica et Cosmochimica Acta*, 56, 97–108.

O'Hanley, D.S., 1996. Serpentinites: records of tectonic and petrological history. *Oxford Monographs on Geology and Geophysics*, 34, 1–277.

Okay, A.I., Xu, S. T., Sengor, A.M.C. 1989. Coesite from the Dabie Shan eclogites, central China. *European Journal of Mineralogy*, 1, 595-598.

Okay, A.I., Işintek, I., Altiner, D. Özkan-Altıner, S., Okay, N., 2012. An olistostrome–mélange belt formed along a suture: Bornova Flysch zone, western Turkey. *Tectonophysics*, 568–569, 282–295.

O'Reilly, S., Griffin, W.L., 2013. Moho vs crust–mantle boundary: Evolution of an idea. *Tectonophysics*, 609, 535-546.

Ozawa, K., 1994. Melting and melt segregation in the mantle wedge above a subduction zone: evidence from the chromite-bearing peridotites of the Miyamori ophiolite complex, northeastern. *Journal of Petrology*, 35, 647-678.

Oze, C., Sharma, M., 2005. Have olivine, will gas: Serpentinization and the abiogenic production of methane on Mars. *Geophysical Research Letters*, 32,(10). DOI:10.1029/2005GL022691

Page, J.N., 1976. Serpentinization and alteration in an olivine cumulate from the Stillwater Complex, southwestern Montana. *Contribution to Mineralogy and Petrol*ogy, 54, 127-137.

Palandri, J.L., Reed, M.H., 2004. Geochemical models of metasomatism in ultramafic systems: serpentinization, rodingitization, and sea floor carbonate chimney precipitation. *Geochimica et Cosmochimica Acta*, 68, 1115–1133.

Palinkaš, L. A., Jurković, I., Garašić, V., Palinkaš, S.S., 2012. Genesis of vein-stockwork cryptocrystalline magnesite from the dinaride ophiolites. *Ofioliti*, 37,(1), 13-26.

Patzak M., Okrusch M., Kreuzer, H., 1994. The Akrotiri unit on the Island of Tinos, Cyclades, Greece, witness to a lost terrane of Late Cretaceous age. *N. Jah. Min. Ab*., 194, 211–218.

Papanikolaou, D., 1984. The three metamorphic belts of the Hellenides: a review and a kinematic interpretation, *Geological Society of London*, Special Publications, 17, 551-561.

Papanikolaou, D., 1986. Geology of Greece, National and Kapodistrian University of Athens (in Greek).

Papanikolaou, D.J., 1989. Geotectonic map of Greece IGCP 276 edn. *Geological Society of Greece*, Special Publication 1, Athens.

Papastamatiou, J., 1945. Sur les proprietes cristallographiques et chimiques du diopside prenant part a la constitution de quelques enclaves enallogenes recueillies sur un affleurement de serpentine pres de Kimi (lie d'Eubee). *Annales géologiques des pays helléniques*., 1, 129-138.

Paraskevopoulos, G., Kanakis, F., 1972. Η γένεσις των ελληνικών οφιτοασβεστίτων - Zur Genese der griechischen ophicalcite. *Bulletin of theGeological Society of Greece*, 9, 2, 413-451.

Parkinson, I., Arculus, R, 1999. The redox state of subduction zones: insights from arc-peridotites., *Chemical Geology*, 160, 409-423.

Pearce, J A., 1983. Role of the sub-continental lithosphere in magma genesis at active continental margins. In C.J Hawkesworth and M.J. Norry, Eds., Continental basalts and mantle xenoliths, p. 230-249. Shiva, Orpington (I-ondon), and Birkhauser Boston, Cambridge, Massachusett.

Pe-Piper, G., Piper, D.J.W., 2002, A synopsis of the geology of the Cobequid Highlands, Nova Scotia. Atlantic Geology, 38, 145-160.Pe-Piper, G. and Miller, L., 2002:Zeolite minerals from the North Shore of the Minas Basin, Nova Scotia. *Atlantic Geology*, 38, 11-28.

Pirajno, F., 2013. Effects of Metasomatism on Mineral Systems and Their Host Rocks: Alkali Metasomatism,Skarns, Greisens, Tourmalinites, Rodingites, Black-Wall Alteration and Listwanites. In Harlov D.E., Austrheim, H., (eds) Metasomatism and the chemical transformation of the rock: the role of fluids in terrestrial and extraterrestrial processes. Springer, Berlin, pp 203-251.

Pomonis, P., Karipi, S., Tsikouras, B.S., Hatzipanagiotou, K.,, 2008. Rodingite formation in ultramafic rocks from the Koziakas ophiolite, Western Thessaly, Greece: conditions of metasomatic alteration, geochemical exchanges and T–X (CO_2) evolutionary path. *The Canadian Mineralogist*, 46, 727–739.

Pomonis, P., Magganas, A., 2017. Petrogenetic Implications for Ophiolite Ultramafic Bodies from Lokris and Beotia (Central Greece) Based on Chemistry of Their Cr-spinels. *Geosciences*,7(1), 10. doi:10.3390/geosciences7010010.

Pohl, W., 1990. Genesis of magnesite deposits - models and trends. *Geologische Rundschau, 79*(2), 291-299.

Power, I.M., Wilson, S.A., Dipple1, G.M., 2013. Serpentinite Carbonation for CO_2 Sequestration. *Elements*, 9, 115-121.

Price, R.C., Gray, C.M., Wilson, R.E., Frey, F.A., Taylor, S.R., 1991. The effects of weathering on rare-earth element, Y and Ba abundances in Tertiary basalts from southeastern Australia. *Chemical Geology*, 93, 245–265.

Python, M., Ceuleneer, G., Ishida, Y., Barrat J.A., Arai, S., 2007 Oman diopsidites: A new lithology diagnostic of very high temperature hydrothermal circulation in mantle peridotite below oceanic spreading centres. *Earth and Planetary Sciences Letters*, 255, (3‐4), 289‐305.

Python, M., Yoshikawa, M., Shibata, T., Arai, S., 2011. Diopsidites and Rodingits: Serpentinisation and Ca Metasomatism in the Oman Ophiolite Mantle. from book Mafic Melt Emplacement During the Shock Deformation in the Subvolcanic Environment: Example from Tastau Volcanoplutonic Ring Complex, Eastern Kazakhstan (pp.401-435)

Plyusnina, L.P., Likhoidov, G.G., Zaraisky, G.P., 1993. Physicochemical formation conditions of rodingite from experimental data. *Petrologiya*,1,(5), 557–568.

Rai, D., Moore, D.A., Hess, N.J., Rosso, K.M., Rao, L., Heald, S.M., 2007. Chromium(III) hydroxide solubility in the aqueous K^+–H^+–OH^-–CO_2–HCO_3^-–CO_3^{2-}-H_2O system: A thermodynamic model. *Journal of Solution Chemistry*, 36, 1261–1285.

Raleigh, C.B., Paterson, M.S., 1965. Experimental deformation of serpentinite and its tectonic implications. *Journal of Geophysical Research*, 70, (16), 3965-3985.

Ranero, C., Morgan, J.P., McIntosh, K., Reichert, C., 2003. Bending-related faulting and mantle serpentinization at the Middle America trench. *Nature*, 425, 367–373.

Ranero, C., Villaseñor, A., Morgan, J.P., Weinrebe, W., 2005. Relationship between bendfaulting at trenches and intermediate-depth seismicity. *Geochemistry, Geophysics, Geosystems*, 6, (12).

Rassios, A.H.E., Moore, E.M., 2006. Heterogeneous mantle complex, crustal processes, and obduction kinematics in a unifield Pinods-Vourinos ophiolitic slab. In: A.H.F. Robertson and D. Mountrakis (eds), Tectonic Development of the Eastern Mediterranean region. *Geological Society of London*, Special Publication, 260, pp. 237-266.

Rice, J. M.,1977. Contact metamorphism of impure dolomitic limestone in the Boulder Aureole, Montana. *Contributions to Mineralogy and Petrology*, 59, 237–259

Rice, J.M., 1983. Metamorphism of rodingites. I. Phase relations in a portion of the system CaO- MgO-$A1_2O_3$-SiO_2-CO_2-H_2O. *American Journal of Science*, 283, (1), l2l-150.

Richardson, W.D., Pringle, N., Mosley, M.J., Westermark, B., Dubois Dalcq, M., 1988. A role for platelet-derived growth factor in normal gliogenesis in the central nervous system. *Cell*, 53, 309–319.

Ring, U.,J., Glodny,T., Will, T., Thomson, S.N., 2007. An Oligocene extrusion wedge of blueschist-facies nappes on Evia, Aegean Sea, Greece: Implications for the early exhumation of high-pressure rocks. *Journal of the Geological Society*, 164, 637–652.

Robertson, A.H.F., 1990. Late Cretaceous oceanic crust and Early Tertiary foreland basin development, Euboea, Eastern Greece. *Terra Nova*, 2, (4), 333-339.

Robertson, A.H.F., Shallo, M., 2000. Mesozoic-Tertiary tectonic evolution of Albania in its regional Eastern Mediterranean context. *Tectonophysics*, 316, 197-214.
Robertson, A.H.F., 2002. Overview of the genesis and emplacement of Mesozoic ophiolites in the Eastern Mediterranean Tethyan region. *Lithos*, 65, 1-68.
Roeder, P.L., MacArthur, D., Ma, X.P., Palmer, G.R., 1987. Cathodoluminescence and microprobe study of rare-earth elements in apatite. *American Mineralogist*, 72, 801-11.
Rollinson, H.R., 1993. Using Geochemical Data: Evaluation, Presentation, Interpretation, 1st Edition Pearson Education Limited.
Ronsbo, J.G., 1989. Coupled substitutions involving REEs and Na and Si in apatites in alkaline rocks from the Ilimaussaq intrusion, South Greenland, and the petrological implications. *American Mineralogist*, 74, 896 901.
Rubin, J.N., Henry, C.D., Price, J.G., 1993. The mobility of zirconium and other "immobile" elements during hydrothermal alteration. *Chemical Geology*, 110, 29–47.
Schandl, E.S., Mittwede, S.K., 2001. Evolution of the Acipayam (Denizli, Turkey) rodingites. *International Geology Review*, 43, 611–623.
Schermer, R.E., Lux, D.R., Burchfiel, B.C., 1990. Temperature-time history of subducted continental c rust, Mt. Olympos region, Greece. *Tectonics*, 9, 1165-1195.
Schermer, R.E., 1993. Geometry and kinematics of continental basement deformation during the Alpine orogeny, Mt. Olympos region, Greece. *Journal of Structural Geology*, 15, 571-591.
Schmädicke, E., Will, T.M., 2003. Pressure-temperature evolution of blueschist facies rock from Sifnos, Greece, and implications for the exhumation of high-pressure rocks in the central Aegean. *Journal of Metamorphic Geology*, 21, 799–811.
Schwartz, S., Allemand, P., Guillot, S., 2001. Numerical model of the effect of serpentinites on the exhumation of eclogitic rocks: insights from the Monviso ophiolitic massif (Western Alps). *Tectonophysics*, 42, 193–206.
Schroeder, T., Cheadle, M.J., Dick, H.J.B., Faul, U., Casey, J.F., Kelemen, P.B., 2007. Nonvolcanic seafloor spreading and corner-flow rotation accommodated by extensional faulting at 15N on the MidAtlantic Ridge: A structural synthesis of ODP Leg 209. *Geochemistry, Geophysics, Geosystem*, 8, (6), 1-16.
Schulte, M., Blake, D., Hoehler, T., McCollom, T., 2006. Serpentinization and its implications for life on the early Earth and Mars, *Astrobiology*, 6, 364–376.
Seyfried, W.E., Janecky, D.R., 1985. Heavy metal and sulfur transport during subcritical and supercritical hydrothermal alteration of basalt: Influence of fluid pressure and basalt composition and crystallinity. *Geochimica et Cosmochimica Acta*, 49, 2545–2560.
Shaked, Y., Avigad, D., Garfunkel, Z., 2000. Alpine high-pressure metamorphism at the Almyropotamos window (southern Evia, Greece). *Geological Magazine*, 137, 367-380.
Simantov, J., Economou, C., Bertrand, J., 1990. Metamorphic rocks associated with theCentral Euboea ophiolite (Southern Greece): some new occurrences. In: Malpas, J.,Moores, E.M., Panayiotou, A., Xenophontos, C. (Eds.), Oceanic Crust Analogues.Proceedings of the Symposium "Troodos 1987''. *Geological Survey Department, Ministry of Agriculture and Natural Resources, Nicosia, Cyprus*, 285 -293.
Sinton, J.M., Detrick, R.S., 1992. Mid-ocean ridge magma chambers. *Journal of Geophysical Research*, 97, 197–216.
Skliros, 2013. Διερεύνηση των συνθηκών σχηματισμού των εμφανίσεων μαγνησίτη Βάββδου και Γερακινής (Κεντρική Χαλκιδική) και μελέτη αξιοποίησης σε περιβαλλοντικές εφαρμογές. *Diploma Thesis*, Univerity of Patras. (in Greek)
Spear, F.S., Gilbert, M.C., 1984. Amphiboles in metamorphic rokc compositions- In Veblen, DR. & Ribbe, PH (eds). Reviews in mineralogy, 9B, Amphiboles: Petrology and experimental phase relations. *Mineralogical Society of America*, Washington, D.C., 268-278.
Spear, F. S., 1995. Metamorphic Phase Equilibria and Pressure-Temperature-Time Paths: New York, *Mineralogical Society of America*, 799 p.
Spray, J., Bebien, J, Rex, D.C., Roddick, J.C., 1984. Age constrains on the igneous and metamorphic evolution of the Hellenic-Dinaric ophiolites. *Geological Society London Special Publications*, 17, (1), 619-627.
Stakes, D. S., O'Neil, J. R., 1982. Mineralogy and stable isotope geochemistry of hydrothermally altered oceanic rocks. *Earth and Planetary Science Letters*, 57, (2), 285-304.
Stampfli, G.M., 1996. The Intra-Alpine terrain: a Paleotethyan remnant in the Alpine Variscides. *Eclogae Geologicae Helvetiae*. 89, (1), 13-42.

Stampfli, G.M., Mosar, J., Marchant, R., Marquer, D., Baudin, T., Borel, G., 1998. Subduction and obduction processes in the western Alps. In: A. Vauchez and R. Meissner (Eds.), Continents and their mantle roots. *Tectonophysics*, 296, (1-2), 159-204.

Stampfli, G.M. 2000. Tethyan oceans. In: E. Bozkurt, J.A. Winchester and J.D.A. Piper (Eds.), Tectonics and magmatism in Turkey and surrounding area. *Geological Society of London*, Special Publication, 173, 163-185.

Streckeisen, A. L., 1976. Classification of the common igneous rocks by means of their chemical composition: a provisional attempt. *Neues Jahrbuch für Mineralogie, Monatshefte*, 1976, H. 1, 1-15.

Stucki, A. Trommsdorff, V., Günther, D., 2001. Zirconolite in metarodingites of Penninic Mesozoic ophiolites, Central Alps. *Schweiz Mineralogische und Petrographische Mitteilungen*, 81, 257-265.

Thayer, T.P., 1966. Serpentinization considered as a constand-volume metasomatic process. *American Mineralogist*, 51, 685 -710.

Tracy, R. J., Robinson, P., Thompson, A.B., 1976. Garnet composition and zoning in the determination of temperature and pressure of metamorphism, central Massachusetts. *American Mineralogist*, 61, 762-75.

Tsikouras, B., Karipi, S., Rigopoulos, I., Perraki, M., Pomonis, P., Hatzipanagiotou, K., 2009. Geochemical processes and petrogenetic evolution of rodingite dykes in the ophiolite complex of Othrys (Central Greece). *Lithos*, 113, 540–554.

Tsikouras, B., Karipi, S., Hatzipanagiotou, K., 2013. Evolution of rodingites along stratigraphic depth in the Iti and Kallidromon ophiolites (Central Greece). *Lithos*, 175-157, 16-29.

Ulmer, P., Trommsdorff, V. 1995. Serpentine stability to mantle depths and subduction-related magmatism, *Science*, 268,858-861.

Valsami, E., Cann, J.R., 1992. Mobility of rare earth elements in zones of intensehydrothermal alteration in the Pindos ophiolite, Greece. In: Parson, L.M., Murton, B.J., Browning, P. (Eds.), Ophiolites and theirmodern oceanic analogues: *Geological Society*, Special Publication 60, London, 219–232 pp.

Van Hinsberg, V.J., Schumacher, J.C., Kearns, S., Mason, P.R.D., Franz, G., 2006. Hourglass sector zoning in metamorphic tourmaline and resultant major and trace-element fractionation. *American Mineralogist*, 91, 717–728.

Verma, S.P.,1992. Seawater alteration effect on REE, K, Rb, Sr, Th, Rb and Sr–Nb–Pb isotope systematics of mid-ocean ridge basalts. *Geochemical Journal*, 26, 159–177.

Veyland, A.,Dupont, L., Rimbault, J., Pierrard, J.-C., Aplincourt, M., 2000. Aqueous Chemistry of Zirconium(IV) in Carbonate Media. *Helvetica Chimica Acta*, 80, 414–427.

Wendlandt, R.F., Harrison,W.J.,1979. Rare earth partitioning between immiscible carbonate and silicate liquids and CO_2 vapour: results and implications for the formation of light rare-earth-enriched rocks. *Contributions to Mineralogy and Petrology*, 69, 409–419.

White, W.M., 2013. Geochemistry. 1st Edition. Wiley Blackwell.

Wicks, F.J., Whittaker, E. J. W., 1977. Serpentine textures and serpentinization. *Canadian Mineralogist*, 1, 5, 459-488.

Woodsworth, G.J., 1977. Homogenization of zoned garnets from politic schists. *Canadian Mineralogist*, 15, 230-242.

Wunder, B., Schreyer, W., 1997. Antigorite: high-pressure stability in the system $MgO–SiO_2–H_2O$ (MSH). *Lithos*, 41, 213–227.

Xypolias, P.,S., Kokkalas, 2003. "Upward extrusion and subsequent transpression as a possible mechanism for the exhumation of HP/LT rocks in Evia Island (Aegean Sea, Greece)." *Journal of Geodynamics*, 35, (3), 303-332.

Zharikov, Y., Lank, D.B., Cooke, F., 2007. Influence of landscape pattern on breeding distribution and success in a threatened Alcid, the marbled murrelet: model transferability and management implications. *Journal of Applied Ecology*, 44, 748–759.

12 Table of Figures

13 Appendix

List of Mineral Abbreviations

Allanite: Aln

Amphibole: Am

Andradite: Adr

Anorthite: An

Apatite: Ap

Aragonite: Arg

Calcite: Cal

Chlorite: Chl

Chrysotile: Ctl

Clinochlore: Clc

Clinopyroxene: Cpx

Diopside: Di

Dolomite: Dol

Epidote: Ep

Garnet: Grt

Grossular: Grs

Hydroandradite: Hadr

Hydrogrossular: Hgrs

H_2O: water

Lm: Lime

Lizardite: Lz

Magnetite: Mag

Orthopyroxene: Opx

Plagioclase: Pl

Prehnite: Prh

Quartz: Qtz

Serpentine: Srp

Spinel: Spl

Talc: Tlc

Vesuvianite: Ves